The use of supercritical carbon dioxide in Solid State Chemistry and basic structural investigations with chalcogenide halides of the third main group

DISSERTATION

Zur Erlangung des Grades eines Doktors

Der Naturwissenschaften

Vorgelegt von

Dipl. -Chem. Kledi Xhaxhiu

geb. am 20. 08. 1977 in Durrës

eingereicht beim Fachbereich 8

der Universität Siegen

Siegen 2005

Berichterstatter: Prof. Dr. H. -J. Deiseroth
Prof. Dr. H. Haeuseler
Mitglied der Promotionskommission: Prof. Dr. rer. Nat. Xin Jiang

Tag der mündlichen Prüfung: 23.11.2005

urn:nbn:de:hbz:467-1964

Acknowledgements

This work was completed in the time interval from March 2002 to September 2005 in the Department of Inorganic Chemistry, University of Siegen under the guidance of Prof. Dr. H. J. Deiseroth.

I would like to express my grateful thanks to Prof. Dr. H. J. Deiseroth for giving me the freedom on the selection of the working topics, for the exellent supervision and his amicable acquaintance.

Special thanks are dedicated to Dr. C. Reiner for the scientifical discussions, criticisms, suggestions and for the SEM and EDX investigations.

I would like to thank Dr. M. Schlosser for the Single crystal measurements, Dipl-Chem. Jens Schlirf and staat. gepr. Lebensmittelchemikerin Sylvia Wilnewski for the precious advices in the construction of several devices.

My special thanks are dedicated to Priv. Doc. Dr. L. Kienle for the HRTEM and SAED measurements.

My sincere acknowledgements are reserved to Prof. Dr. Schneider for his generous help and the fruitful discussions.

I would like to thank my working colleagues: Michael Wagener, Elmar Neumann, Krasimir Aleksandrov and all other members of the group of Inorganic Chemistry of the University of Siegen, whom I had the pleasure to work with.

I would like to thank Dipl. Ing. W. Büdenbender for the assistance and helpful discussions in several technical problems and Jennifer Hermann for the IR and Raman measurements.

In conclusion, I would like to dedicate my best thanks to my parents Sofika and Skënder as well as to my brother Jurgen for the continuous encouragement.

Abstract

On the use of supercritical carbon dioxide in Solid State Chemistry and basic structural investigations with chalcogenide halides of the third main group.

One of the tasks of this work was the exploration of the ability of supercritical CO_2 as a solvent and reaction environment in several reactions involving inorganic compounds of different natures. All attempts in this field were not successful. The use of $scCO_2$ as an educt for the permanent fixation of CO_2 (i.e. transformation of oxides or hydroxides in oxide carbonates or carbonates) seems to be a promising field of research.

A second focal point of this work was the preparation, characterisation and the structure determination of new solids in the ternary systems indium – chalcogen – halogen. The syntheses of In_5Ch_5X (Ch = S, Se; X = Cl, Br) and of derivative compounds were performed using the concept of building units. In_5Ch_5X represent four new mixed valence compounds crystallising in two different structure types, namely the chloride type (In_5Ch_5Cl, space group: $P2_1/m$) and the bromide type (In_5Ch_5Br, space group: $Pmn2_1$). In all these compounds indium occurs in three different oxidation states as In^+, covalent $(In\text{-}In)^{4+}$ dumbbells and In^{3+} suggesting the explicit formula $In_5Ch_5X = [In^+]\ [(In_2)^{4+}]\ 2[In^{3+}]\ 5[Ch^{2-}]\ [X^-]$. Beside the similarities remarkable differences were evident not only from the X-ray investigation but mainly from the real structure revealed from HRTEM investigations. The bromide-type compounds revealed ordered crystals. In contrast to that, the chloride-type compounds show several anomalies regarding the real structure, e.g. polylamellar intergrowth of polymorphs, twinning and nanoscale intergrowth of structurally similar compounds (In_5S_5Cl/In_6S_7).

A further topic of interest was the high temperature X-ray investigations of powdered samples $K_2In_{12}Se_{12}Te_7$, $K_2In_{12}Se_{19}$ and In_5Ch_5X (Ch = S, Se; X = Cl, Br). The process of lattice expansion revealed no phase transition for all these compounds within the studied temperature range. The coefficients of thermal expansion for each compound were determined.

Key words: reactions, $scCO_2$, indium chalcogenide halides, crystal structures, real structure, HRTEM, crystal defects, X-ray diffraction, high temperature investigations, expansion coefficient

Kurz-Zusammenfassung

Über die Verwendung des überkritischen Kohlendioxids in der Festkörperchemie und grundlegende Strukturuntersuchung mit Chalkogenidhalogeniden der dritten Hauptgruppe.

Eines der Ziele dieser Arbeit war die Erforschung der Eigung von überkritischem CO_2 als Lösungsmittel und Reaktionsmedium bei Reaktionen anorganischer Stoffe unterschiedlicher chemischer Natur. Alle Versuche auf diesem Gebiet waren nicht erfolgreich. Dagegen scheint die Verwendung des $scCO_2$ (sc = supercritical) als Edukt für die dauerhafte Fixierung von CO_2 (z.B. bei der Umwandlung von Oxyden oder Hydroxyden in Oxyde-Carbonate oder Carbonate) ein versprechendes Forschungsgebiet zu sein.

Ein zweiter Schwerpunkt der Arbeit war die Präparation, Charakterisierung und Strukturbestimmung neuer Feststoffe in den ternären Systemen Indium – Chalkogen – Halogen. Die Synthese von In_5Ch_5X (Ch = S, Se; X = Cl, Br) und abgeleiteter Verbindungen erfolgte auf Basis eines Baukastenprinzips. In_5Ch_5X repräsentieren vier neue gemischtvalente Verbindungen die in zwei unterschiedlichen Strukturtypen kristallisieren, nämlich im Chlorid-Typ (In_5Ch_5Cl, Raumgruppe: $P2_1/m$) und im Bromid-Typ (In_5Ch_5Br, Raumgruppe: $Pmn2_1$). In allen vier Verbindungen tritt Indium in drei Oxidationstuffen auf; in Form von In^+, kovalent gebundenen $(In\text{-}In)^{4+}$ Hanteln und als In^{3+} entsprechend der ionischen Formulierung: $In_5Ch_5X = [In^+]\ [(In_2)^{4+}]\ 2[In^{3+}]\ 5[Ch^{2-}]\ [X\text{-}]$. Neben diesen Ähnlichkeiten, sind deutliche Unterschiede nicht nur auf basis der Röntgenbeugungs Untersuchungen offensichtlich sondern hauptsächlich in der Realstruktur die durch HRTEM Untersuchungen aufgedeckt wurde. Die Bromid-Typ Verbindungen zeigen geordnete Kristalle. In Gegensatz zum Bromid-Typ zeigen die Chlorid-Typ Verbindungen mehrere Defekte in der Realstruktur, z.B. polylamellare Verwachsungen von Polymorphen, Verzwillingung und nanoskaligen Verwachsungen von strukturell verwandten Verbindungen (In_5Ch_5Cl/In_6S_7).

Ein weiteres interessante Thema waren die Hochtemperatur Röntgenuntersuchungen gepulverter Proben von $K_2In_{12}Se_{12}Te_7$, $K_2In_{12}Se_{19}$ und In_5Ch_5X (Ch = S, Se; X = Cl, Br). Der Verlauf der Zelleausdehnung zeigte für alle untersuchten Verbindungen innerhalb des untersuchten Temperaturbereiches keine Phasenübergänge. Für jede der untersuchten Verbindungen wurden die thermischen Ausdehnungskoeffizienten bestimmt.

Schlüsselwörter: Reaktionen, überkritisches CO_2, Indium Chalkogenidhalogenide, Kristallstrukturen, Realstruktur, HRTEM, Kristalldefekte, Hochtemperaturuntersuchungen, Ausdehnungskoeffizient

Contents

1 Introduction ……..... 1

1.1 Motivation…… 3

2 Experimental……. 5

2.1 Preparation procedure……..... 5

2.2 Characterisation……..... 7

2.2.1 Infrared spectroscopy measurements (MIR and FIR)…… 7

2.2.2 Raman spectroscopy measurements……..... 7

2.2.3 Thermal Analysis…… 8

2.2.4 X-Ray powder investigations…….. 8

2.2.5 Scanning Electron Microscopy (SEM) and Electron Beam Microanalysis (EBMA)…….. 9

2.2.6 Transmission Electron Microscopy (TEM)…… 9

2.2.7 X-ray single crystal analysis on STOE - IPDS single axis diffraction System……. 10

3 Reactions of some inorganic compounds in supercritical CO_2……. 12

3.1 Introduction……... 12

3.2 The definition of the supercritical fluid…… 13

3.3 The solubility in supercritical region…… 19

3.4 Overview of the method…… 22

3.5 Devices for the production of dry ice……... 23

3.5.1 The purifying subsystem……. 23

3.5.2 The metering subsystem……. 24

3.5.3 The ampoule…… 25

3.5.4 The autoclaves……..... 26

3.5.5 The measuring and releasing system…….. 27

3.5.6 The filling and sealing of the ampoule……... 29

3.5.7 The production of dry ice for counter pressure……... 30

3.6 Operating procedure…….. 31
3.7 Calculations…….. 31
3.8 Reactions in supercritical CO_2…….. 33
3.8.1 Optimisation of the system using CO_2…… 35
3.8.2 Testing the filled ampoules with dry ice……. 36
3.9 Experimental procedure…… 37
3.9.1 The comparison method…….. 37
3.10 Discussion of the results…….. 39
3.10.1 Dissolving ability of CO_2, attempts for the synthesis of ternary compounds using SnI_4…….. 40
3.10.2 Syntheses involving alkali metal carbonates and polar compounds……. 42
3.10.3 Attempts for the synthesis of the quaternary compound $Ag_6GeS_4Br_2$….. 47
3.10.4 Attempts for the substitution of In^+-species in the mixed valence compound In_5S_5Cl……. 48
3.10.5 Attempts for the synthesis of the compound In_5S_5I…….. 49
3.10.6 Searching for possible modifications of Se and Te…….. 50
3.10.7 Mercury (I) compounds…… 50
3.10.8 Hg_2Cl_2 – HgO……... 52
3.11 Conclusions…….. 57

4 New mixed valence chalcogenide halides of indium……... 58
4.1 Introduction……... 58
4.2 The compounds In_5Ch_5Cl (Ch = S, Se)……. 63
4.2.1 Preparation and properties of the samples…….. 63
4.2.2 Characterisation……... 64
4.2.3 Thermal analyses of In_5S_5Cl and In_5Se_5Cl…….. 70
4.2.4 Single crystal investigation of In_5Ch_5Cl (Ch = S, Se)…… 71
4.2.5 Single crystal investigations of In_5S_5Cl…….. 71
4.2.6 Single crystal investigation of In_5Se_5Cl……. 77
4.2.6.1 The chlorine position in the structure of In_5Ch_5Cl (Ch = S, Se)…. 81
4.2.7 Structure description of In_5Ch_5Cl (Ch = S, Se)……... 81

4.2.8 Discussion of inter-atomic distances…….. 88
4.2.9 The distribution of In^+ and $(In_2)^{4+}$ species around the edge-sharing double octahedra……. 92
4.3 The compounds In_5Ch_5Br (Ch = S, Se)…… 93
4.3.1 Preparation and properties of the samples…….. 93
4.3.2 Characterisation…….. 93
4.3.3 Thermal analysis of In_5S_5Br and In_5Se_5Br…….. 98
4.3.4 Single crystal investigation of In_5Ch_5Br (Ch = S, Se)…… 99
4.3.5 Single crystal investigations of In_5S_5Br…….. 99
4.3.6 Single crystal investigation of In_5Se_5Br…….. 102
4.3.6.1 The bromine position in the structure of In_5Ch_5Br (Ch = S, Se)… 104
4.3.7 Structure description of In_5Ch_5Br (Ch = S, Se)…….. 105
4.3.8 Discussion of the inter-atomic distances……. 110
4.3.9 The distribution of In^+ and $(In_2)^{4+}$ species around the edge-sharing double octahedra……. 114
4.4 A brief comparison of the structures…… 115
4.5 HRTEM investigations on In_5S_5Cl and In_5S_5Br and MAPLE calculations……. 116
4.5.1 The course of a HRTEM-investigation……... 116
4.5.2 The evaluation of the HRTEM-images……... 116
4.5.3 A general description of the SAED and HRTEM investigations in both structure- types…… 117
4.5.4 Polymorph intergrowth of In_5S_5Cl…….. 118
4.5.5 Polysynthetic twinning…… 122
4.5.6 Intergrowth of different compounds……... 127
4.5.7 Calculations of MAPLE values…….. 131
4.6 Substitution experiments…….. 133
4.7 The substitution of In^+ by Tl^+ in the compounds In_5Ch_5Cl (Ch = S, Se)…….. 139
4.7.1 Introduction……. 139
4.8 The Compounds $TlIn_4Ch_5Cl$ (Ch = S, Se)…… 139
4.8.1 Preparation and properties…….. 139
4.8.2 Characterisation…….. 140

4.8.3 Thermal analysis of $TlIn_4S_5Cl$ and $TlIn_4Se_5Cl$…….. 144

4.8.4 Single crystal investigation of $TlIn_4Se_5Cl$…….. 145

4.8.5 Structure description of $TlIn_4Se_5Cl$…… 148

4.8.6 Comparison of the interatomic distances of In_5Se_5Cl and $TlIn_4Ch_5Cl$….. 149

5 High temperature X-ray investigations…….. 151

5.1 Introduction……... 151

5.2 Thermal expansion of the lattice……... 152

5.3 The high temperature X-ray diffraction system…… 154

5.3.1 The high temperature attachment…… 156

5.3.2 Sample preparation……..... 157

5.3.3 Device accuracy…….. 158

5.3.4 Data evaluation……... 158

5.3.5 Calibration of the measuring device……... 158

5.4 The determination of temperatures……... 163

5.5 High temperature X-ray investigations of $K_2In_{12}Se_{12}Te_7$……. 166

5.5.1 Sample preparation……. 167

5.5.2 Room temperature measurements with double capillaries……. 171

5.5.3 The superstructure reflections……. 173

5.5.4 Determination of the expansion coefficients…….. 175

5.6 High temperature X-ray investigations of $K_2In_{12}Se_{19}$…….. 176

5.6.1 Sample preparation and measurement…… 177

5.7 Comparison of the thermal expansion of $K_2In_{12}Se_{12}Te_7$ and $K_2In_{12}Se_{19}$…….. 180

5.8 Investigation of the thermal behaviour of In_5S_5Cl, In_5S_5Br and In_5Se_5Cl, In_5Se_5Br…… 181

5.8.1 Discussion…….. 181

5.9 Lattice thermal expansion behaviour of In_5S_5Cl…….. 181

5.9.1 The sample preparation and measurement…….. 181

5.9.2 Thermal expansion coefficients of In_5S_5Cl and In_5Se_5Cl……... 185

5.9.3 Discussion of the results……. 186

5.10 Investigation of the thermal expansion of In_5S_5Br and In_5Se_5Br…….. 187

5.10.1 Sample preparation and measurement…… 187

5.11 Comparison of the results……. 193

6 Summary…… 195

7 References…….. 200

8 Appendix…… 213

8.1 Abbrevations……. 213

8.2 Definitions……. 214

8.3 Data for the reactions of some inorganic compounds in supercritical CO_2…….. 216

8.4 Data for the compounds In_5Ch_5Cl, In_5Ch_5Br (Ch = S, Se)……... 225

8.5 Data for the substitution experiments……... 234

8.6 Data for the compounds $TlIn_4Ch_5Cl$ (Ch = S, Se)…… 238

8.7 Data for the high temperature X-ray investigations…….. 240

8.8 Publications and posters…… 252

1 Introduction

The increasing requirements of the markets for new articles with attracting properties, have motivated chemists over centuries in their attempts to produce new materials which would benefit not only them but the whole society. The successful growth of the chemical industry according to the exigencies of the consumers led to the designation of new syntheses, which often involved the necessity for new solvents with a continuously increasing capacity to dissolve a wide range of compounds. To fulfil this purpose, different compounds with promising dissolving properties were synthesised, sometimes with completely unknown long-term effects on the life of our planet. In this sequential production race, a vast number of new syntheses directly influenced the human health. Many of them were associated with the production of harmful wastes and emission of poisonous gases. Others required increasing costs for treatment of the production wastes in compliance to the strengthening regulation.

With the increase of global population and the rise of the standards of living, many of these productive methods become unsustainable. In this context many chemist have perceived the need of an innovation, consisting of the replacement of many organic fuel-based solvents, especially halogenated organic solvents with harmless solvents that can be used as supercrtitical fluids SCFs [1, 2]. This attempt to use non toxic compounds, producing as little waste as possible and therefore causing a low environmental impact is called “Green Chemistry”.

The SCFs on the other hand offer great opportunities for different chemical processing beyond the environmental benefits. These opportunities are related with the facility to manipulate their solvent properties by manipulating pressure and temperature, which, sometimes lead to processes with less steps and less energy consumption.

In recent years one of the most preferred supercrtitical fluids is carbon dioxide. Except its chemical and physical properties (explained in details in chapter 3), its naturally occurrence and its abundant presence as a by-product of streams, power plants and industrial plants make it an attractive continuous phase for different applications. One of its first applications in industry as a substitute of organic solvents is related to its extraction capacity of different natural products widely used in food, pharmaceutical and biotechnological industry [3-9]. For the consumer, the products extracted by supercritical CO_2 are more acceptable than if they were extracted by dichloromethane or other organic solvents. Further studies and experiments on extraction using supercritical CO_2 presented that not only scents and oils could be extracted by this solvent but different elements their oxides and salts could be extracted too. Using supercritical CO_2 and organic ligands, metal ions of earth alkali metals [10], transition metals [11,12], lanthanides and actinides [13-15] were successfully

extracted. Nowadays this extraction method is seen as an alternative of purification of polluted soils from nuclear wastes, especially from uranium wastes [16].
The dissolving property of supercritical CO_2 is widely used in organic and polymer industries. Supercritical CO_2 is utilized as an alternative reaction medium for radical and ionic polymerisations [17-19], homogeneous and heterogeneous catalytic reactions [20, 21] and enzymatic reactions [22-24].

Simultaneously with the development of the new sustainable and promising synthesising methods, classical methods of syntheses are not vanishing but are enlarging the diversity of products with more attractive applications. One of these methods vastly applied and continuously improved is Solid State Chemistry which nowadays is finding exaltation due to the huge demand for new materials, especially from the electronic industry. Several solid materials classically synthesised, possess a variety of properties, e.g. electric (semiconductors, superconductors), magnetic etc. Dozen of researchers throughout the world, fascinated from these properties, found a close relation between them and the proper structure of the material.

The gathered experience has shown than not every possible combination of the selected atoms or atomic species would lead to a desired structure. The nature has arranged this process through several rules, depending not only on the ratio (quantity) of the involving species and the experimental conditions (i.e. pressure, temperature) but especially on their sizes, and coordination ability. Knowing these characteristics, a lot of compounds have been synthesised. Worth to mention here are the *chalcogenides* of the third main group elements, especially *indium chalcogendies*, where small differences in the preparation and treating conditions revealed a large number of binary compounds. Further researches including thalium and first group elements (K, Na, Rb, Cs) enlarged this spectrum with many ternary compounds. Surprisingly, in this wide variety of compounds, beside the normal valence compounds, a lot of mixed valence compounds could be obtained as well, each representing a new structural aspect. These new structures consist of interesting building units which constantly intrigue the creative "architects" to combine and manipulate them in new structures with unpredictable properties.
Recent studies carried out by Paashaus [98] revealed that some structural elements found in mixed valence compounds (of the third main group elements) are not typical only of the

binary or ternary chacogenides, since halogenes in the presence of chalcogenes could reveal the same.

1.1 Motivation

Inspired from the properties and the extended applications of $scCO_2$ in organic and polymer chemistry, inorganic chemists have employed it mainly as an effective *starting compound* in different syntheses. This work aims to test the dissolving abilities of $scCO_2$ by using it as a *reaction medium* in a variety of inorganic reactions. Therefore, one of the main requirements of this work deals with the projection and the construction of a serial of devices: a) for the measurement and manipulation of definite amounts of CO_2, b) for the reaction environment, c) for the protection and measurement of the working conditions (i.e. pressure and temperature). This task is followed by the most important purpose concerning the solubility and the reactions of several inorganic compounds ranging from fairly non polar molecular compounds (e.g. SnI_4) up to polar or ionic crystalline compounds (e.g. GeS, $CsCO_3$). This investigation includes also reactions which for different reasons failed in the normal solid reactions as well as searches for new modifications of chalcogenides like Se, Te.

The investigation of the system indium-chalcogenide awoke the interest of many researchers due to the versatile number of the found binary compounds. Among the normal valence compounds (e.g. InCh, In_2Ch_3 Ch = S, Se, Te) a variety of mixed valence compounds (e.g. In_4Ch_3, In_6Ch_7 Ch = S, Se, Te) with fascinating structural aspects could be obtained as well.
The determination of the mixed valence character of indium and the secrets of the structure invoked a great interest for a series of substitution of indium species mainly by alkaline metals (Na, K, Rb, Cs), thalium and rarely with d-elements (e.g. Cr). These substitutions, together with the previous substitution of indium in the normal valence compounds enlarged further the spectrum of ternary compounds.
The structural elements (building units) of these compounds attracted more attention. The possibility of their combination became and is still an investigative point. Further researches including this concept enriched the diversity of the mixed valence compounds, with the compounds MIn_5S_6 (M = Tl, K) [92, 95] and MIn_7Ch_9 (M = Rb, Cs; Ch = S, Se) [96, 97] which contain not only structural units of the previous compounds but two new characteristic building units as well. In the course of investigations on the mixed valence compounds, recent researches including other

elements of the third group and *halogens*, brought into light another group of compounds with interesting structure (M_3Te_3X, M = Al, Ga, In; X = Cl, Br, I) carrying the above concept.
Based on the concept of combining existing building units, new structures are expected. Therefore, the main tasks of this work relate to the investigations of the conditions for the syntheses of further new mixed valence compounds in the system; third group elements - chalcogenes - halogenes, emphasised especially on indium, determination of the structure(s) and necessary characterisations using several methods.

In the course of the investigation for new compounds in the system alkali metal - indium – chalcogenide, among others, Schlosser [122] synthesised the compound $K_2In_{12}Se_{19}$ which presented a complicated structure. The single X-ray crystal investigations performed by the author displayed the presence of ring-shape diffuse intensities around the Bragg positions *hkl* with $l = 2n + 1$. The occurrence of the ring-shaped diffuse intensities was caused by the cell duplication which arises due to the temperature dependent order-disorder transformation occurred by the dynamical disorder of the indium (In2/In3, see the comments of Schlosser [122]). The investigations performed by Schlosser displayed a continuous decrease of the intensities of the ring shaped diffuse reflections with temperature increase. At 673 K they disappeared. Four sequential measurements at 273 K, 295 K, 473 K, 673 K showed an approximately s-shaped dependence of the unit cell volume from temperature, followed by uncertainties about the behaviour of the lattice constants.
The substitution of seven selenium atoms by tellurim atoms brought into light the compound $K_2In_{12}Se_{12}Te_7$. This compound in contrast to $K_2In_{12}Se_{19}$ displays no ring-shaped diffuse intensities and is considered an ordered variant of $K_2In_{12}Se_{19}$.
Another important task of this work is to investigate the thermal behaviour (searching for possible physical anomalies and determination of the thermal expansion coefficients) of $K_2In_{12}Se_{19}$ and $K_2In_{12}Se_{12}Te_7$ by high temperature powder diffractometry and to compare the obtained results. The In frame of this work, the use of high temperature powder diffractometry is considered for investigations of other new compounds as well.

2. Experimental

2.1 Preparation procedure

To carry out the syntheses in this work several elements and binary educts were used. The majority of the employed educts was purchased while some others were synthesised and purified by solid state methods (annealing of homogenised mixtures of suitable solid educts). The provenience, consistence and the purity of the educts are listed in table 2.1.

Initially for the preparation of the ternary and quaternary compounds, elements and binary educts in stoichiometric proportions were used. Aluminium, gallium and indium as well as the chalcogenides, sulphur, selenium and tellurium were weighed under ambient conditions, while the elements as: Na, K, Tl and the air sensitive binary compounds $GaCl_3$, $GaBr_3$, $InCl_3$ $InBr_3$, InCl and InBr were stored and handled under inert atmosphere. The latter preparation of the ternary and quaternary compounds succeeded only from binary educts like: GaS, InS, In_2S_3, InSe, In_2Se_3, InCl, InBr, TlCl, TlBr which were weighed according to the stoichiometry, homogenised and pressed in pellets to enhance the reciprocal diffusivity and consequently the reactions velocity.

Generally 1g of solid educts is transferred into preheated and evacuated quartz ampoules. Samples containing Al, were treated differently. It is already known that aluminium reacts with the inner walls of the quartz ampoule, reducing SiO_2 to elementary Si. Therefore, to avoid an eventual by-reaction, aluminium oxide thimbles filled with the educts were encapsulated in preheated, evacuated and sealed quartz ampoules. The sealed ampoules were annealed over variable time periods at temperatures varying from 400°C to 600°C. When necessary the samples were heated up to 1000°C and then quenched in cold water. Afterwards the ampoules were opened in an inert atmosphere, the raw product was ground in an agate mortar and again annealed in preheated and evacuated ampoules. Sometimes, to obtain big crystals of the expected compounds, different temperature programs with variable heating and cooling rates were used.

Table 2.1: The constitution, origin and purity of the used chemicals.

Element / Compound	**Consistence**		**Producer**	**Purity**
Aluminium	Pieces	2.5-3.9 mm	Heraeus	99.999%
Cs_2CO_3	Powder		Chempur	99.9%
Chromium	Granules	0.7-3.5 mm	Balzers	99.99%
Gallium	Splatters		Aldrich	99.99%
Indium	Shot	tear drop	Chempur	99.999
$InCl_3$	Powder		Heraeus	99.999%
Iod	Crystals		Chempur	99.9
Potassium	Cylinder-shaped		Fluka	>98%
K_2CO_3	Powder		Merck	99.9%
KCl	Powder		Riedel-de Haën	>99%
Hg_2Cl_2	Powder		Merck	>99.6%
Hg_2Br_2	Powder		Merck	>99.6%
Hg_2I_2	Powder		Merck	>99.6%
HgO	Powder		Merck	>99%
RbCl	Powder		Ventron	99,9%
Rb_2CO_3	Powder		Chempur	99.9%
Selenium	Shot	1-3 mm	Fluka	99.995%
SeO_2	Powder		Merck	>98%
Sodium	Rods		Fluka	>99%
NaBr	Powder		Riedel-de Haën	>99%
NaCl	Powder		Riedel-de Haën	>99%
AgBr	Powder		Alfa	99.999
Ag_2S	Powder		Heraeus	>99%
Suflur	Pieces	< 7mm	Chempur	99.999%
Tellurium	Pieces		Chempur	99.999%
TlCl	Powder		Fluka	99,999%
TlBr	Powder		Merck	>99%

The processes of annealing and quenching the samples succeeded in self-made tube ovens, whose temperature was measured and controlled by Pt/Pt-Rh thermocouples. The thermocouples were externally controlled by programmable temperature controlling units.

2.2 Characterisation

2.2.1 Infrared spectroscopy measurements (MIR and FIR)

Infrared absorption spectra were recorded by a Bruker (Karlsruhe) Fourier Transform Interferometer IFS 113V. The measured range was 400 – 4000 cm^{-1} for the MIR (Middle infrared) region, and under 400 cm^{-1} for the FIR (Far Infrared) region with a resolution of ± 2 cm^{-1}. To perform MIR measurements, a very small amount of the fine powdered solid sample was mixed with dehydrated KBr and then pressed in thin pellets under high pressure. For the FIR measurements, the fine powdered sample was rubbed with Nujol yielding a viscose paste, which was layered over a polyethylene disc.
In either case, the measurements were recorded at room temperature under reduced pressure ($P \approx 10^3$ Pa). The obtained spectra were manipulated using the software OPUS 2.2 [P17].

2.2.2 Raman spectroscopy measurements

The Raman spectra were recorded by a Bruker Raman-Fourier-Transform-Spectrometer RFS 100/S with 180° adjustment. The measured range was 50 – 4000 cm^{-1} with a resolution of ± 2 cm^{-1}. The exciting radiation occurred with the 1064 nm line of an Nd-YAG laser.
To perform the measurements, small amounts of fine powdered samples were transferred into glass capillaries, which were sealed and measured at room- or at low temperature (liquid nitrogen, approx. 120 K). The measurements at low temperature were performed using a low-temperature cell (Bruker R 495).

2.2.3 Thermal Analysis

The Differential Thermal Analysis (DTA) is suitable for qualitative investigations of phase transitions and melting behaviours of solids. In this work, a measuring device "Linseis" (Type: DTA L-62) was employed. The sample and the reference (Al_2O_3) were enclosed in preheated evacuated and sealed quartz ampoules of 5 mm outer diameter and 10-20 mm length. The ampoules were placed into ceramic crucibles fixed on thermocouples. The samples were heated up to 700°C and cooled down to 50°C using a heating and cooling rate of 5°C/min. The registered temperature difference between the investigated compound and the reference is presented as a peak. With the Linseis software package [P16] the onset temperatures of the obtained peaks were determined. The calibration of the device was performed using the elements Sn, Zn and Ag in the region of 232 - 962°C.

2.2.4 X-Ray powder investigations

The X-Ray measurements for the characterisation of crystalline samples were performed with a powder diffraction device D5000 delivered from "SIEMENS" company (Karlsruhe). The device works with $CuK\alpha_1$-radiation (λ = 1.54051 Å) in transmission mode. For the measurements 50-100 mg of fine powdered sample was spread on a Mylar-foil (covered with a thin layer of silicon grease) and the foil was fixed on a flatbed holder.

The diffraction patterns were recorded by means of a "Braun" Position Sensitive Detector (PSD-50M) with an angular increment of 0.015° and a measuring time varying from 0.5 - 10 hours. The indexation of the reflections and their refinement was accomplished by the X-Ray data software package VISUAL X^{POW} [P14] and WIN X^{POW} [P15] delivered from the "STOE" company.

The temperature dependent measurements of powder samples were performed on a "STOE" transmission diffraction system type (STADI-P) with $CuK\alpha_1$-radiation. The temperature calibration was performed using an iridium standard (a = 3.8388 Å). The determination of the reflection positions for iridium sample was occurred through profile fitting of Lorentzian function by means of the program delivered by Toby [P18]. The dependence from each-other of plotted parameters was found by least square fitting using the software EXCEL from the software package OFFICE 2000.

2.2.5 Scanning Electron Microscopy (SEM) and Electron Beam Microanalysis (EBMA)

The determination of the samples morphology was performed with a CS44 SEM (Scanning Electron Microscope) delivered from the company CamScan (Cambridge) equipped with a Robinson BSE (**B**ack **S**cattering **E**lectron) and SE (**S**econdary **E**lectron) detector. Qualitative and quantitative elementary analysis were carried out with the DS-710 144-10 EDX (Energy Dispersive X-ray Spectroscopy) system delivered from EDAX (Cambridge) and the WDX-3PC (Wavelength Dispersive X-ray Spectroscopy) system delivered from Microspec (Freemont). With the EDX-system all wavelengths of the measuring range are collected simultaneously, while the WDX-system detects the different wavelengths step by step. The main differences between these methods are listed in the table 2.2. The measuring conditions for non conductive samples lead frequently to charging effects, therefore non conductive samples were vaporised with carbon or sputtered with a thin layer of gold.

Table 2.2: Comparison of the measuring characteristics of EDX and WDX.

Method	EDX	WDX
Detection limit [at %]	0.1 - 10 %	0.001 - 0.1 %
Accuracy [at %]	2 - 10 %	1 - 3 %
Measuring time	approx. 100 s	approx. 30 min
Detectable elements*	Na - U	C - U

* When using Be-window

2.2.6 Transmission Electron Microscopy (TEM)

The transmission electron microscope investigations were performed and evaluated in the Max Planck Institute for solid state research (Stuttgart), in the department of Prof. Dr. Dr. h.c. A. Simon by Dr. L. Kienle.

High **R**esolution **T**ransmission **E**lectron **M**icroscope (HRTEM) and **S**elected **A**rea **E**lectron **D**iffraction (SAED) images were performed with a Philips CM30ST device. The technical data are

summarised in table 2.3. For the SAED patterns a diaphragm has been used to limit the diffraction in a circular area with an approximate diameter of 1000 Å.

To obtain the required crystal size for these measurements, the samples were crushed under n-butanol in an agate mortar. The obtained suspension was dropped over copper grids in order to achieve crystallites in random orientation.

For all investigations, the sample carriers were fixed on a side-entry, double-tilt holder with a maximum tilt of ± 25° in two orthogonal directions. All images were recorded with a Multiscan CCD Camera (Gatan, Software: Digital Micrograph 3.6.1, Gatan).

Table 2.3: Technical data of the electron microscope Philips CM30ST.

Cathode material	LaB_6
Acceleration voltage	300 kV
Spherical Aberration constant	C_s = 1.15 mm
Spread of defocus	Δ = 70 Å
Illumination semiangle	1.2 mrad

The presence of amorphous layers on the surface of the investigated crystals, generate a small amount of noise. The latter has been reduced using an appropriate mask which filters the Fourier transforms. The simulation of HRTEM micrographs and SAED patterns was performed using the EMS program package [P1].

2.2.7 X-ray single crystal analysis on STOE - IPDS single axis diffraction system

The measurements of the reflection intensities were performed by means of the **I**mage **P**late **D**iffraction **S**ystem (IPDS) delivered from the "STOE" company (Darmstadt). For the measurements monochromatised (graphite monochromator) MoKα-radiation was used (λ = 0.71073 Å).

The respective crystal was fixed on the top of a glass capillary, which was fixed using modelling clay in a metal cylinder and mounted on the goniometer head. This device possess a single rotation axis (φ-axis) which corresponds to the goniometer axis. A microscope or a CCD camera was used for crystal centring. The image plate (BaBrF doped with Eu^{2+}) has a diameter of 350 mm and a

resolution of 0.0225 mm^2. The measuring parameters (the plate distance, φ-increment and the radiation time) were determined with respect to the cell dimensions and scattering intensity of the crystal.

After data collection, the reflections were visualised as points in the reciprocal space using the program RECIPE [P5]. This presentation allows the user to investigate several anomalies, e.g. twinning, superstructure etc. For the indexation, lattice refinement and data integration the programs INDEX [P3], CELL [P4] and INTEGRATE [P7] were used. The final refinement of the lattice was done according to the position of 8000, randomly over the whole measuring range of the distributed reflections using the least square method. For the data reduction and the numerical absorption correction the program X-RED [P10] was used. The face indexation and the optimisation for the numerical absorption correction based on symmetrical equivalent reflections and adequate face description was done using the program X-SHAPE [P9]. The crystal structures determination was performed according the Patterson method or by direct methods using the program SHELXS [P11]. The completion and the refinement of the structure models was attained through successive difference Fourier synthesis and the least square method for the whole matrix by the program SHELXL [P12]. The elaboration and the structure depiction were carried out by means of the program Diamond 2.1e [P13].

3 Reactions of some inorganic compounds in supercritical carbon dioxide

3.1 Introduction

Parallel to the extended use in organic and polymer chemistry, supercritical CO_2 has exalted great interests in inorganic chemistry too. Due to the tremendous versatility of supercritical carbon dioxide, a variety of inorganic synthesis (i.e. controlled hyrolysis or decomposition) have been carried out. Worth to mention here are the synthesis for the recovery of ZnS nanoparticles from reverse micelles [25], the production of TiO_2 nanoparticles and MgO submicron powders from the hydrolysis of titanium chelates [26, 27] and the decomposition of magnesium acetate in supercritical CO_2.

Beyond its dissolving properties, supercritical CO_2 can be regarded as a powerful reactant as well. Recently different authors have discovered the reactivity of supercritical CO_2 toward alkali and earth alkali metals. On the investigation of the reaction of metallic sodium and magnesium carbonate at 500°C Lou et al [28] presented the synthesis of large diamond crystals from the reduction of CO_2 released from the pyrolysis of magnesium carbonate. The CO_2 involved in the reaction was in the supercritical state due to the autogenic pressure inside the reaction vessel. In a latter study Lou et al [29] confirmed the formation of diamond microparticles and graphite as a byproduct even at 440°C from a direct reduction of supercritical CO_2 from metallic sodium. In a similar way Motiei et al [30] reported the synthesis of carbon nanotubes and nested fullerenes from the reduction of supercritical CO_2 with magnesium. These authors presented in details the advantages of this method toward the traditional less efficient methods.

The growth of world's industry during the last 50 years is associated with increasing emissions of CO_2 into the atmosphere which affects the "greenhouse effect". Over years chemists are fronting with this challenging problem and are developing different strategies to decrease the quantity of CO_2 production. A wide range of methods have been employed e.g. electrochemical [31, 32], photochemical [33, 34] etc. One of the largely experimented ways in this field consists on the permanent absorption of carbon dioxide by different minerals and its deposition as carbonates. Dahlin D. C et al [35] reported the conversion of CO_2 to carbonates by treating the aqueous solution

of Olivine, Serpentine and other magnesium silicates with supercritical CO_2, (efficiency up to 80%). Other researchers working in this field present also promising results [36, 37].

3.2 The definition of the supercritical fluid

The phase diagram of a single compound (Fig. 3.1) shows the state of matter dependent on pressure and temperature. The regions are divided by curved lines indicating the equilibria conditions between two phases: solid-liquid, solid-gas, liquid-gas. According to Gibbs' phase rule (3.1) for one component system,

$$\mathbf{P + F = 1 + 2} \qquad \mathbf{(3.1)}$$

where: P is the number of phases, F is the degrees of freedom. Each equilibrium curve has only one degree of freedom which might be the pressure or the temperature.

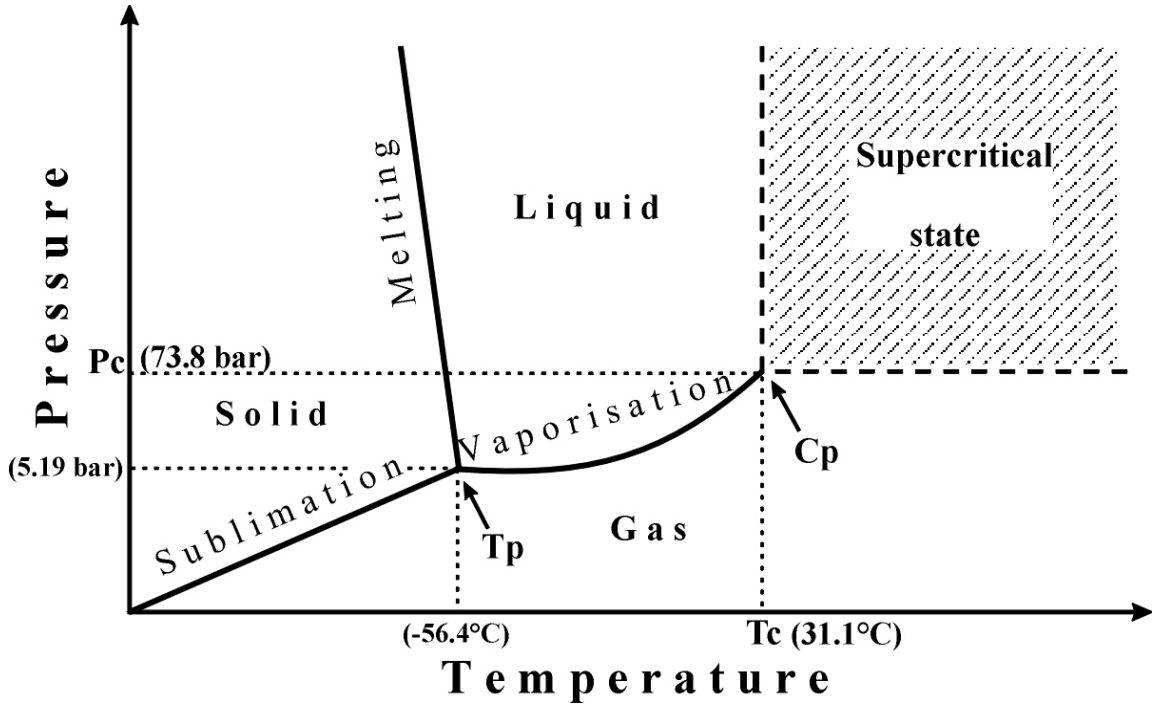

Fig. 3.1: The supercritical fluid diagram. Tp (triple point), Cp (critical point). The hatched region represents the supercritical state.

A possible change of one of them causes the change of the other parameter. The intersection of these three equilibria curves happens at one point, where all phases coexist. This is the triple point (TP), where no degrees of freedom exist (see equation 3.1). Following the vaporisation curve (gas-liquid equilibria), the further enhancements of pressure or temperature leads suddenly to another point, which is the border of a new state of matter. This point is the critical point, defined from critical pressure and critical temperature (see dashed lines in Fig. 3.1) and is characteristic for each compound. The region contoured from the critical parameters is called the supercritical region. Further enhancements of pressure and temperature within the supercritical region bring no liquefaction or gas formation. The state of matter within the hatched region (Fig. 3.1), differs from gases and liquids but shows properties of both. Therefore, the supercritical state of matter can be regarded as a liquid or gas heated and pressurised above its critical parameters (see Fig. 3.1). According to this statement, the features of supercritical fluid (Fig. 3.2) derive from those of gases and liquids and change gradually until the critical point, although some of them may change abruptly with increasing of pressure or temperature near the supercritical region.

.

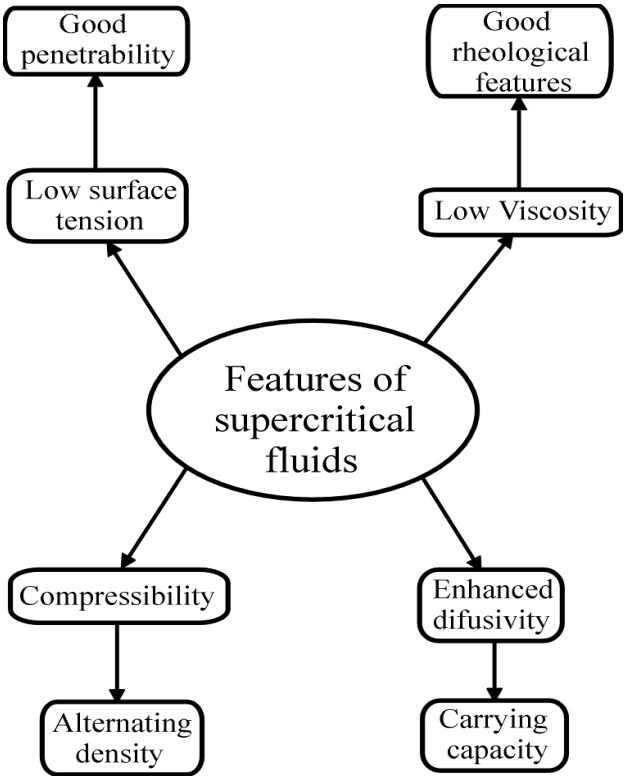

Fig. 3.2: Some features of supercritical fluids (SCF).

For a single component system only one phase exists in the critical region, therefore according to Gibbs' phase rule (3.1), the system has two degrees of freedom represented from the variables P and T. By changing these variables different values of densities and viscosities can be obtained, leading therefore to enhanced solubility of different compounds.

One of the most frequently asked questions relates to the reason of using $scCO_2$ (sc = supercritical) instead of other non hazardous inorganic or organic compounds which easily fulfil the purpose of supercritical fluid. A closer inspection of the table 3.1 shows that the critical values of scHCl (hydrochloric acid) change a little from $scCO_2$, the same analogy can be drawn for $scCH_4$ or scC_2H_6.

Table: 3.1 The most used supercritical fluids and their parameters.

Supercritical fluid	**Formula**	**P_c /bar**	**T_c /°C**	**d_c /kgm^{-3}**	**References**
Carbon dioxide	**CO_2**	**73.8**	**31.1**	**466**	**[38]**
Hydrogen chloride	HCl	82.6	51.5	420	[39 ,40]
Hydrogen bromide	HBr	85.5	90.0	-	[39]
Hydrogen iodide	HI	83.0	150.7	-	[39]
Amonia	NH_3	113.2	132.4	235	[40,41]
Water	H_2O	220.6	374.0	322	[42, 43]
Methane	CH_4	46.0	-82.6	163	[44]
Ethane	C_2H_6	48.7	32.2	207	[45, 46]
Methanol	CH_4O	80.8	239.5	273	[47]
Ethylenediamine	$C_2H_8N_2$	62.8	320	290	[48]

The use of supercritical carbon dioxide as a reaction medium is related not only to its critical values but also to a number of important properties presented in table 3.2 and Fig 3.3.

Table 3.2: Some thermodynamic and molecular properties of CO_2 [49].

Property	CO_2
Molar mass, M /kgmol^{-1}	44.010 x 10^{-3}
Critical pressure, P_C /bar	73.8
Critical temperature, T_C /K	304.1
Critical volume V_C /m3mol^{-1}	93.9 x 10^{-6}
Critical density, ρ_C /kgm^{-3}	466
Dipole moment, μ /Cm	0
Polarisability, α /m^3	2.65 x 10^{-30}
Lennard-Jones Potential Parameter, b_0 /Cm^{3}mol^{-1}	77.25

$b_0 = 2\pi N_A \sigma 3/3$, σ is the collision diameter (0.3941 nm)

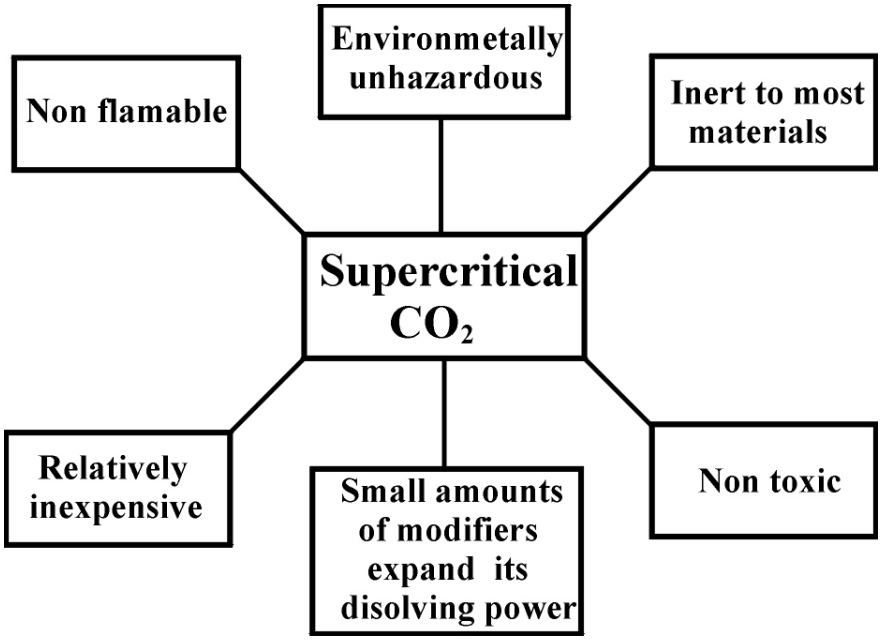

Fig. 3.3: Scheme of the main properties of supercritical carbon dioxide ($scCO_2$).

Some of the properties of $scCO_2$ e.g. the density are related directly to pressure and temperature. The density of $scCO_2$ at the critical point (d = 466 kgm^{-3}) is relatively high in comparison to the densities of other solvents used as supercritical fluids (see table 3.1).

The near-critical area of $scCO_2$ is characterised by a large compressibility. Because of the infinitely high compressibility at the critical point, even small thermal fluctuations lead to enormous fluctuations of density. Polyakoff & King [1] describe the rise of opalescence at the critical point due to this phenomenon. Moriyoshi et al [49] report that the density near the critical point changes abruptly with the pressure. At higher pressure and temperature (not far from the critical point) only a gradual change is observed (Fig. 3.4). The near-critical point area is the area with the enhanced density. A parallel shift of 50 K (303.15 K – 353.15 K) at the constant pressure P = 100 bar in the diagram presented in fig. 3.4 is associated with a density decrease down to one third of its initial value (from $\rho = 773.6$ kgm^{-3} at 303.15 K to $\rho = 221.2$ kgm^{-3} at 353.15 K).

At the critical point, due to the above mentioned properties, small fluctuations of temperature cause the drop of the speed of sound to a minimum, therefore the acoustic measurement is an important tool for its detection.

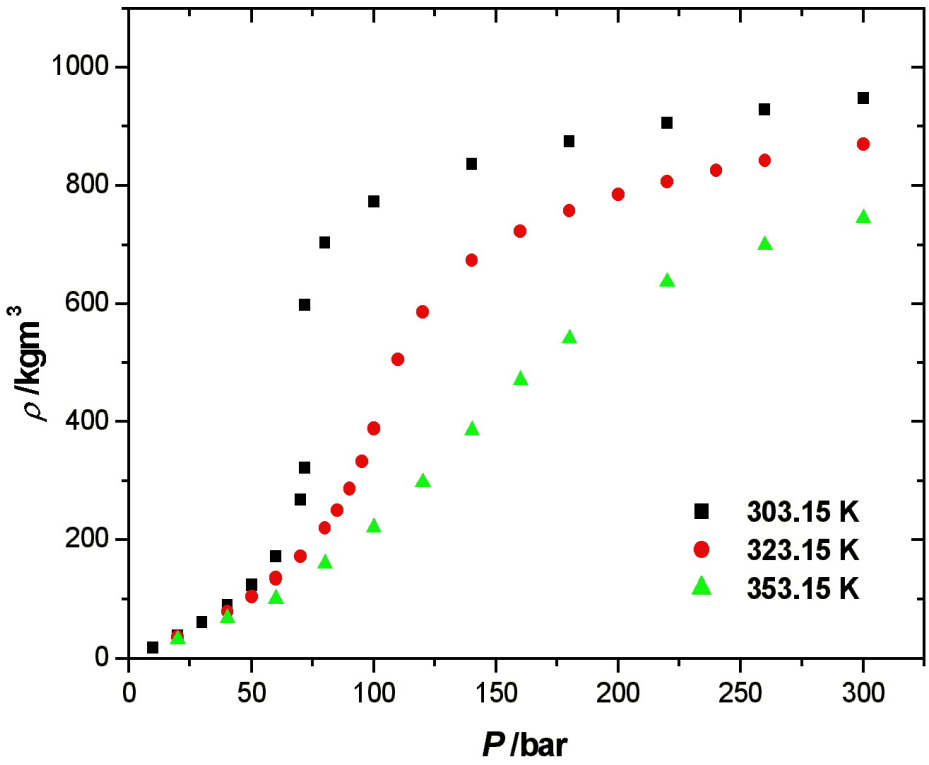

Fig. 3.4: Pressure dependence of the density of $scCO_2$ at three different temperatures [49].

Another property of $scCO_2$ which shows a relatively "strange" behaviour with pressure in the region near the critical point is the permittivity (ε) often expressed as relative permittivity (ε_r), $\varepsilon_r = \varepsilon / \varepsilon_0$. At temperatures near the critical temperature it displays a sharp profile and changes gradually with pressures at higher temperatures showing a parallelism to the density. Some typical values of the dependence of relative permittivity from pressure and temperature are presented by the diagram in fig. 3.5.

Regardless the drastic change of the relative permittivity near the critical point, $scCO_2$ preserves its non-polar nature even at high pressures and temperatures.

The advantage of using $scCO_2$ is presented not only through its density and dielectric constant behaviour but through its viscosity and diffusion coefficient (e.g. diffusion of CO_2 in solids) too. The viscosity of $scCO_2$ at the critical point is closer to the viscosity of gases in contrast to its diffusion coefficient which approaches the values of ordinary liquids (Table 3.3).

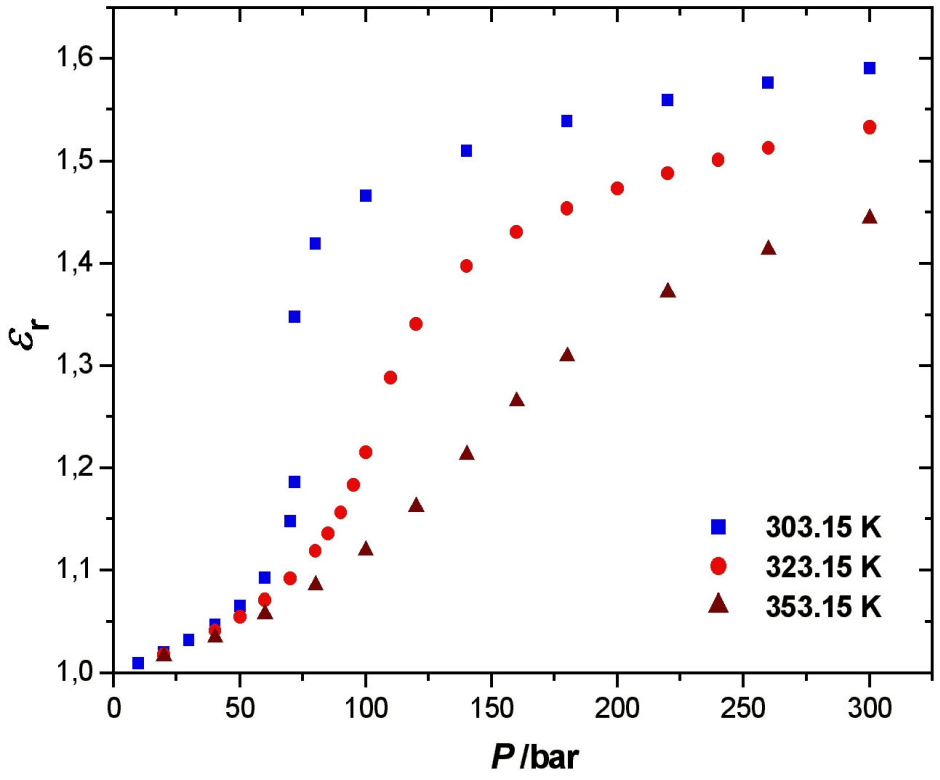

Fig. 3.5: Pressure dependence of relative permittivity of $scCO_2$ at three different temperatures [49].

Table 3.3: Comparison of the properties of supercritical CO_2 and those of ordinary gases and liquids [50].

Fluids	Density (kg/m^3)	Viscosity (g/m s)	Diffusion coefficient (m^2/s)
Gases	1 – 20	(1 – 3) x10^{-5}	(1 – 4) x 10^{-6}
Supercritical CO_2 T_c, P_c	466	3 x 10^{-5}	7 x 10^{-9}
Liquids	600 – 1600	(0.2 – 3) x 10^{-3}	(0.2 – 2) x 10^{-10}

Due to the enhanced diffusivity of $scCO_2$ by one order of magnitude and the mitigation of the viscosity by two orders of magnitude, supercritical CO_2 possess much more favourable mass transfer properties in comparison to that of the liquid solvents.

3.3 The solubility in supercritical region

Regarding the supercritical CO_2 as a gas compressed and heated over its critical values, its dissolving ability (so called "solvent power" according to Gidding & al. [51]) depends on two effects; namely the "physical effect" and the "chemical effect". The physical effect is defined by its actual pressure and temperature. Apart from this, the "chemical effect" unique to each compound, depends on its polarity, acid-base properties and the tendencies to build hydrogen bonding. Therefore the solubility parameter (δ_1) in relation to these effects can be expressed according to the equation (3.2):

$$\delta_1 = 1.25\sqrt{P_C}\,\frac{\rho_r}{\rho_{r(liq)}} \qquad \textbf{(3.2)}$$

Where: δ_1 is the solubility parameter of the supercritical fluid, P_C is the critical pressure of CO_2 (73.8 bar), ρ_r is the reduced density of the supercritical fluid, $\rho_{r(liq)}$ is the reduced density of CO_2 in the liquid state.

In the equation (3.2), the physical effect which reflects the distances between the molecules is strongly dependent on the reduced density, and is expressed from the ratio of reduced densities [$\rho_r/\rho_{r(liq)}$]. The reduced density itself (ρ_r) is the ratio between the actual density (ρ) and the critical density (ρ_C). The chemical effect may be merely attributed the factor 1.25 $P_C^{1/2}$.
Based on this knowledge, the solubility parameter depends strongly on the critical pressure and the reduced density of the fluid, in this case of $scCO_2$. Regarding the reduced density of liquids, an approximate value of 2.66 [51] is found.

A chemical reaction in supercritical carbon dioxide may take place when the educts have a good solubility. The solubility of the educts depends on the solubility parameter δ_2 which can be determined from the group contribution method [52, 53] if their structure is known. The method is based on the contribution of the vaporisation energy for each individual group (e.g. $-CH_3$, $-NH_2$, NO_2, -CN etc) and is expressed by equation (3.3):

$$\delta_2 = \sqrt{\frac{\sum_i (E_v)_i}{\sum_i v_i}} \qquad \textbf{(3.3)}$$

Where: δ_2 is the solubility of solute, $(E_v)_i$ and V_i is the vaporisation energy and molar volume of *i* component of the structure (for organic compounds the structure is divided into several building groups, and each group contributes the value of δ_2). Up to now detailed studies are accomplished for the determination of the solubility parameters mainly for organic compounds.

Based on thermodynamics, the Gibbs-Helmholtz equation (3.4) states that the dissolution of the solute in a solvent will take place when the free energy of mixing is negative ($\Delta G < 0$).

$$\Delta G = \Delta H - T\Delta S \qquad \textbf{(3.4)}$$

The determinating factor in the equation (3.4) is the heat of the mixing ΔH because the dissolution is a process associated with a large enhancement of entropy. Based on the dissolution power of the

supercritical fluid and the solubility of the solute, Hildebrand [54] defines the heat of mixing solvent-solute by the equation (3.5).

$$\Delta H = \phi_1\phi_2 (\delta_1 - \delta_2)^2 \quad \textbf{(3.5)}$$

In the equation (3.5) ΔH represents the heat of mixing between the solvent and solute, ϕ_1 and ϕ_2 are the partial volumes of the solvent and solute.

In order to have a negative free energy a small value of ΔH is needed, therefore, the difference between the solubility parameters of the solvent and solute should be relatively small. This means that the solvent and the solute must be almost of the same nature, e.g. both of them be polar or non-polar. In practice there exist different combinations of solvents and solutes. It might happen that the solute has the same nature as the solvent but a different density, in this case to achieve a good solubility the densities of the solvent and solute should approach. The supercritical fluids possessing high compressibility can tune their density over a wide range approaching in this way the density of the solute. Because of this ability they are often called solvents with adjustable dissolving power. When the solvent has a different nature from the solute, e.g. a non-polar solvent and a polar solute the use of co-solvents is required. Co-solvents may be small amounts of water, ammonia, mineral acids, acetone etc. By varying the kind and the amount (concentration) of the co-solvent the dissolution power of supercritical fluids can be adjusted.

It is also observed that the solubility of solid materials in supercritical fluids depends strongly on their vapour pressure *P*(sat) [55]. Organic salts show a wide range of solubility in supercritical fluids in contrast to the inorganic salts which show low solubility. Metal ions are almost insoluble, but researches have shown good solubility of metal ions bonded to organic ligands, examples of that are selective extractions of Sr, Cd, Pb and Hg [10-16].

3.4 Overview of the method

To perform the reactions in $scCO_2$ some basic components and equipments are required. The first component is the reaction medium CO_2 which will be transformed to $scCO_2$ by heating. It can be used as a gas, directly from the CO_2 bottle, as a liquid, from deep tube bottles or in its solid form as the dry ice. In the gas or liquid form CO_2 has been used successfully for several extractions and reactions followed by extractions. This method is very comfortable, but requires additional systems, sometimes complicated, to measure the quantity of CO_2 involved in the processes. For the purpose of this work, CO_2 from the gas state was transformed into dry ice by means of a converting system (Fig. 3.6). Solid CO_2 can be also obtained as trade product, but due to the purity requirements this choice was excluded. In the solid form the calculations and the manipulation of the amounts of CO_2 are more convenient for simple devices. A basic tool of the equipments necessary to carry out the reactions in $scCO_2$ is the reaction vessel (the autoclave).

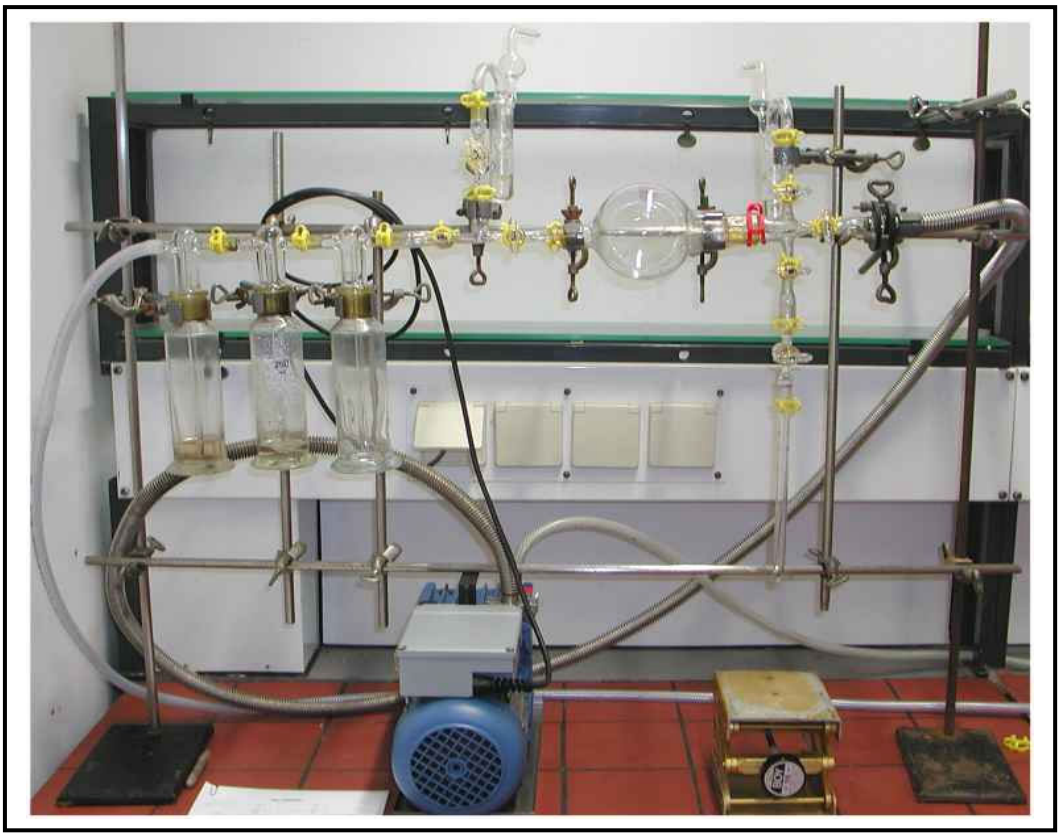

Fig. 3.6: The system for the production of defined amounts of dry ice.

Batch reactors for periodical use are projected, knowing that the time of the synthesis may wary from some hours up to one week or even more. The projection of autoclaves is accompanied by some auxiliary tools which are responsible for the indication of the reaction parameters and for the security of the system. A direct contact of the educts with the autoclave inner walls might lead to undesired by-reactions, which not only deteriorate the intended synthesis but can also corrode the autoclave (explained in details below). To overcome this trouble, a similar method based on the methods described by Rabenau [56] in his investigations using hydrothermal synthesis is employed. This method is based on using quartz ampoules as reaction vessels instead of autoclaves. First, the educts are transferred in quartz ampoules, which are then filled with CO_2 and finally sealed. The sealed quartz ampoules are placed inside the projected steel autoclave together with a counter-pressure agent (dry ice) to compensate the pressure inside the quartz ampoule. Finally the double system ampoule-autoclave is placed inside a drying oven to apply the necessary temperature for the transformation of solid CO_2 to $scCO_2$.

3.5 Devices for the production of dry ice

For the production of defined amounts of dry ice as reaction medium (inside the ampoule) or as counter-pressure (outside the ampoule) a CO_2 system was constructed (see fig. 3.6). It consists of four subsystems, namely the purifying subsystem, metering subsystem, ampoule and/or flask, and the evacuating pump.

3.5.1 The purifying subsystem

The purity of the $scCO_2$ plays an important role in the synthesis. Small amounts of impurities might have observable effects on the kinetics of the reactions. Therefore, for the purposes of this work, CO_2 with a purity of 99.999% was used, supplied from the company "Messer Griesheim". The CO_2-bottle was connected with the CO_2-system (see Fig. 3.6) by means of a plastic tube. The purifying subsystem served for the drying of CO_2 from traces of water coming mainly from the connections. Before entering in the metering subsystem, carbon dioxide passes through three

washing bottles, the middle washing bottle is filled with approx. 5 M sulphuric acid solution which serves as drying agent. For an effective drying, CO_2 bubbles through a porous material.

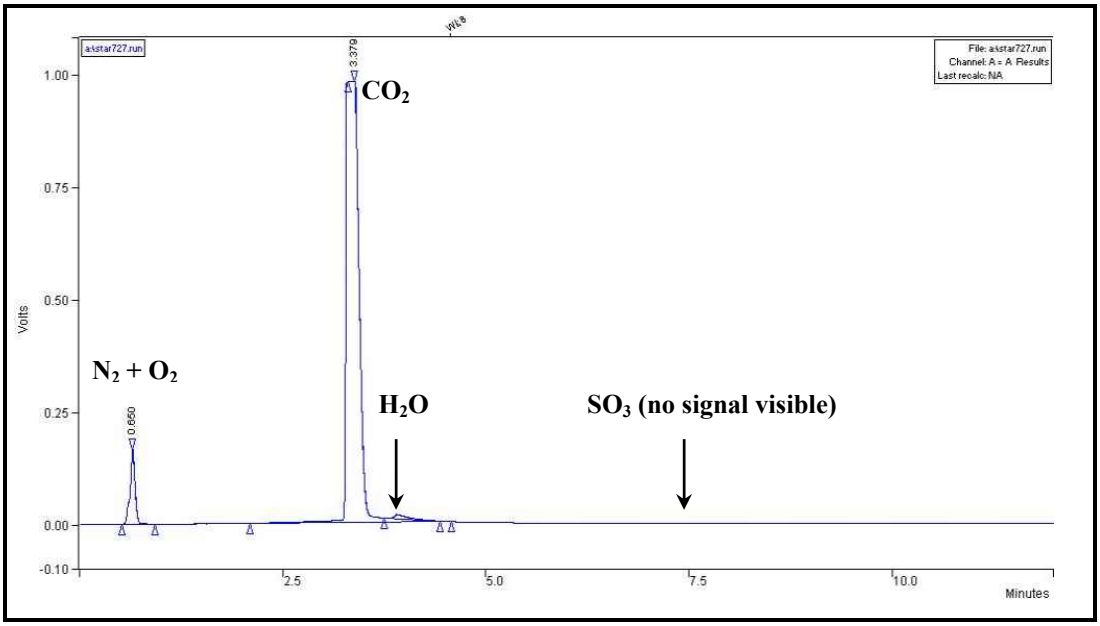

Fig. 3.7: A chromatogram section of CO_2 sample taken at the exit of the purifying system.

The purity of carbon dioxide after the purifying system was proved for traces of water and SO_3 (sulphur triioxide) by means of GC-TCD (Gas chromatograph equipped with thermal conductivity detector). To perform this, an air-bag equipped with a sealing valve was connected to the system. After purging the whole system several times, it was filled with CO_2 and closed. With a syringe, small amounts of samples were injected into the GC-TCD apparatus. The obtained result is displayed in fig. 3.7. The obtained chromatogram displayed a small trace of water and no traces of SO_3. A relatively small peak of air was detected, indicating the small amount of air entering the GC-FID apparatus during the injection process.

3.5.2 The metering subsystem

The metering system serves for the dosage of CO_2. It consists of six valves, two pressure outlets and a flask. The valves are used as restrictors and serve to keep the defined amount of CO_2 inside the system. The pressure outlets have the duty to keep a pressure equal to atmospheric pressure inside the system. The flask is an important part of the system's volume.

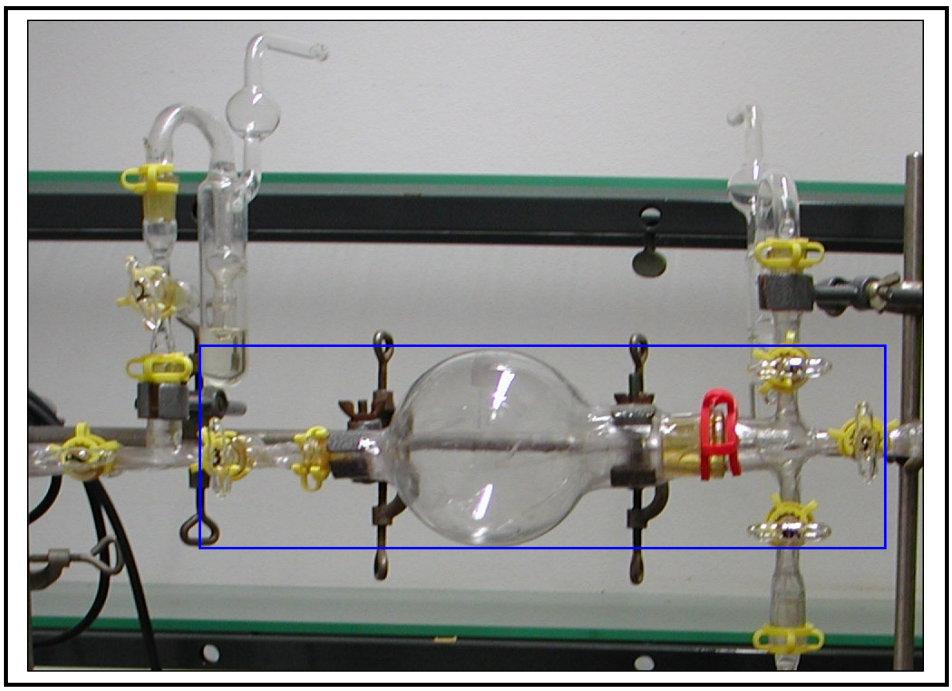

Fig. 3.8: Photograph of the metering system. The blue contoured part has the volume of 0.603 l.

In the fig. 3.8, this part is contoured with a blue rectangle and has a defined inner volume of 0.603 l, which corresponds to 1.095 g CO_2 at 20°C. This volume is determined by a simple analytical method. The part of the system was weighed empty and filled with water at 20°C, the difference of the weights revealed the mass of water inside the system and at the same time its volume.

3.5.3 The ampoule

The ampoule represents the third subsystem, the environment where the reaction takes place. For this purpose quartz ampoules were used, regardless of the reaction temperatures, which were less than 400°C. For such reaction temperatures, borosilicate glass ampoules could be used as well instead of quartz ampoules, but quartz in comparison to the latter shows a lower coefficient of expansion, which increases the stability during thermal changes.

The quartz glass ampoule employed for reactions in $scCO_2$ had a 12 mm outer diameter and a narrowing at 11.5 cm from its bottom which facilitates the sealing process (Fig. 3.9).

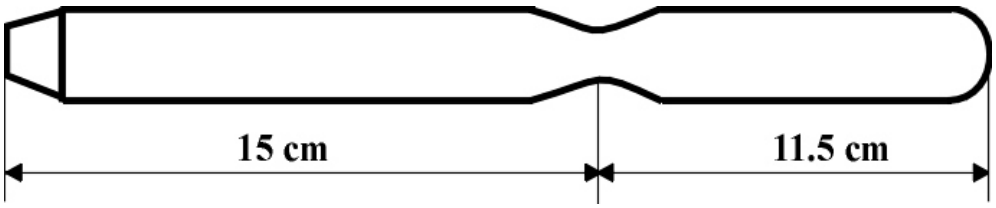

Fig. 3.9: The quartz ampoule used for high pressure CO_2 syntheses.

The ampoule is first filled with educts and subsequently with CO_2 (see the filling procedure), after that, it was sealed at the narrowing position. The outer and inner volume of the sealed ampoule depends from the accuracy of the sealing position along its narrowing.

For the determination of the inner volume, the ampoule was filled with distilled water at 20°C until the middle of the narrowing, and its water content was measured. After several times repetition for three prepared ampoules, a mean inner volume of 7.2 ml was obtained. Its outer volume is determined in a different way. The empty ampoule was filled partially with sand and sealed in the middle of the narrowing. The sealed ampoule was immersed in a cylinder filled with distilled water at a certain volume. The volume difference caused by the immersed ampoule gives the outer volume of the ampoule. This volume varied from 9.7 – 10.4 ml.

3.5.4 The autoclaves

The autoclaves are important parts of the high pressure system. They are regarded as a protector of the reaction vessel. Two different steel autoclave constructions were used for this purpose. They consist of stainless steel (Material 1.4571) vessels, O-rings and closing corks (see fig. 3.10). Each of them was projected to be used in the working conditions 400 °C and 400 bar (for detailed schematics of the autoclave used see figures 8.1-8.4 in appendix). The autoclave vessels consisted of steel cylinders each equipped with screw threads at the top. Two models of them were projected. The first one had the screw threads in the inner part of the body (Fig. 3.10a), the second one in the outer part (Fig. 3.10b). Their volumes were determined by filling them with water at 20°C were 101.5 and 115 ml respectively. Each autoclave was equipped with an O-ring which seals up the system.

Fig. 3.10: Steel autoclaves used for the $scCO_2$ reactions.

The closure of the autoclaves was done by the respective screw corks which consisted of the same material as the autoclaves. On the top of each cork connecting screws were mounted, making possible the connection of the autoclave with the measuring and releasing system.

3.5.5 The measuring and releasing system

To get continuous information about the counter-pressure during the high pressure reaction, and to release the counter-pressure gas after finishing the reaction another system was required. It consisted of three elements joined together by steel capillaries and screws (Fig. 3.11). These three elements of the system were the pressure gauge, the overpressure valve and the outlet valve. The latter two elements and the interconnection capillaries were delivered from the company "Swagelok". Two systems like this were built. Each autoclave was further connected to the respective measuring and releasing system by means of steel capillaries with 1/16" inner and 1/8" outer diameters. The pressure gauge displays the change of pressure with temperature during the heating and cooling process. Its maximal capacity was approx. 400 bar.

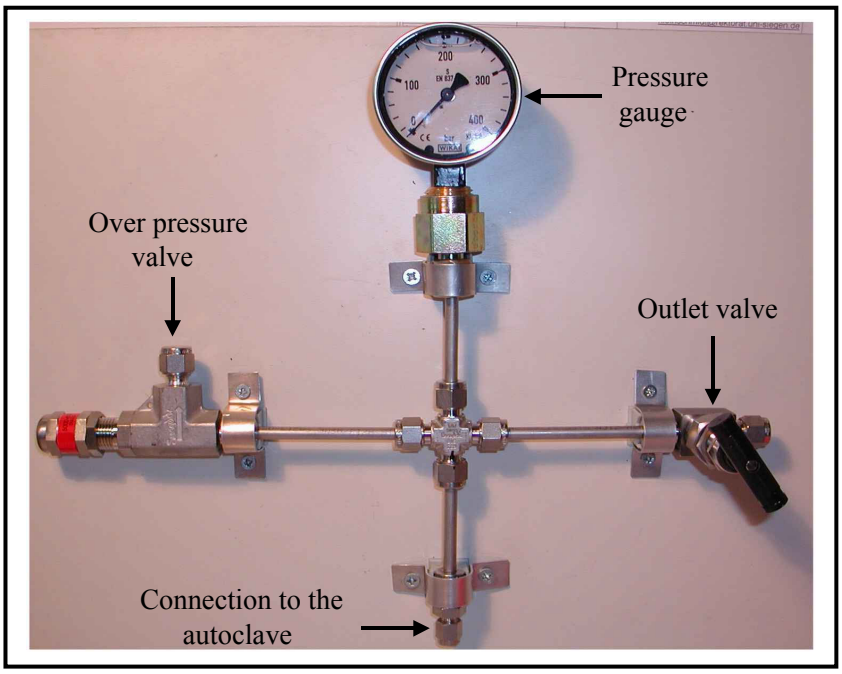

Fig. 3.11: The measuring and releasing system.

The overpressure valve is important for the security of system. Due to its adjustability, it can be adapted to the value of pressure considered as the maximum working pressure. The adjustment of the overpressure valves for both systems was done with CO_2. The maximum pressure for both overpressure valves was set to 400 bar. The outlet valve is intended for counter-pressure releasing after completing the reaction. To connect these three parts, steel tubes of 1/8" inner diameter were used.

$ScCO_2$ is a compressed gas and like each compressed gas it contains a high potential energy which can be released with catastrophic consequences. Therefore some precautions were taken into account while working with it. In order to prevent any possible explosion which might derive from the steel used for the autoclave construction or from the auxiliary parts, the autoclaves and the connected systems were pretested. For this test, an incompressible liquid (in our case water) was filled in the system and different pressures have been applied (pressure was generated from a hydraulic press). It was chosen water due to its lower potential energy in comparison to a compressed gas. For this experiment, the overpressure valve was removed from the system (see Fig. 3.11). Their screwing served for the connection to the hydraulic press.

The tests showed that both autoclaves could endure pressures about two times the maximum operating pressure, almost 800 bar for 5 minutes at 22°C. At higher pressures leaking at the joint parts were observed.

3.5.6 The filling and sealing of the ampoule

Firstly the weighted educts were transferred into a preheated and evacuated quartz ampoule. The filled ampoule was connected with the CO_2-filling equipment and the whole system was evacuated (see the procedure in appendix). The system was refilled with CO_2. During this time the connection valves of the ampoule with the system were kept closed. The bottom part of the ampoule was immersed in liquid nitrogen (Fig. 3.12a). When the pressure in the metering subsystem was equilibrated through the pressure outlets, the valves were reopened and the quantity of 603 ml contained in the metering system gradually solidified in the inner walls of the ampoule. According to the calculations, one filling of the ampoule was not enough to reach the required pressure (approx. 200 bar) inside, therefore, the filling procedure was applied two times, in order to obtain the desired pressure (see calculations).

The connecting valves were closed and the ampoule was carefully disconnected from the system, keeping its bottom part continuously immersed in liquid nitrogen. Several experiments performed to seal the ampoule after detaching it from liquid nitrogen failed as a consequence of the pressure inside it due to the sublimation of CO_2. To overcome this problem, a small metallic cylindrical vessel with a closed bottom and equipped at the top with three screws was used (Fig. 3.12b). The cylindrical vessel was previously filled with liquid nitrogen, then the bottom part of the ampoule was placed inside it and fixed by the screws. The presence of liquid nitrogen inhibits the sublimation of the solidified CO_2 when the narrowing part of the ampoule comes in contact with the flame. The sealed ampoule was carefully released from the fixing screws and placed in a dewar filled with liquid nitrogen. In this way the sealed ampoule could be preserved from explosion until the dry ice for counter-pressure was generated.

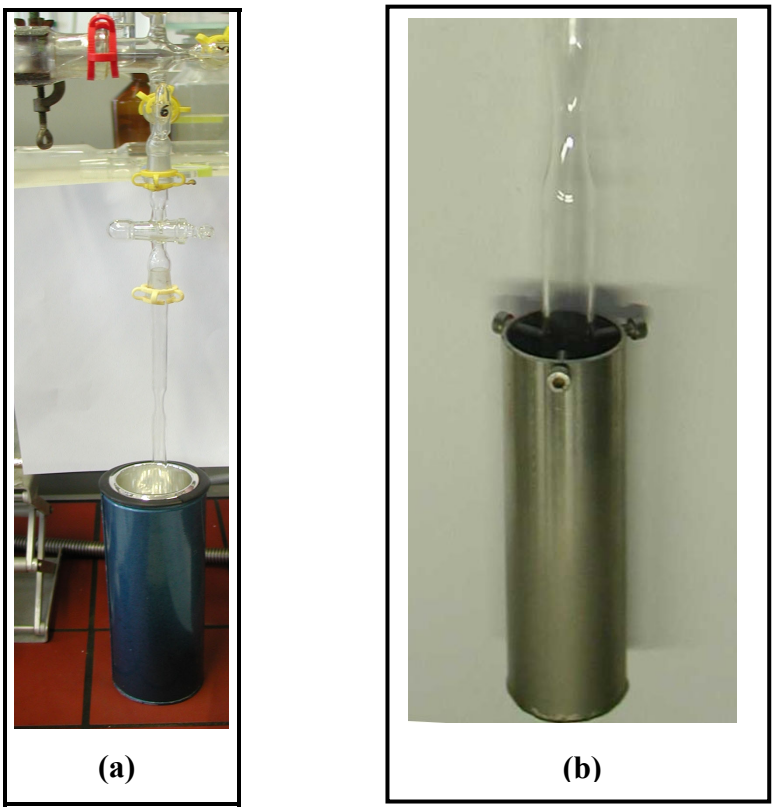

(a) **(b)**

Fig. 3.12: The ampoule filled with educts and partly immersed in liquid nitrogen (a). The ampoule fixed in the cylindrical vessel (b).

Before placing the ampoule inside the autoclave (batch reactor) the counter-pressure agent should be produced. As described above, dry ice was used as a counter-pressure agent, allthough in principle it is possible to use water, argon or nitrogen. The latter substances are not used due to the difference of their expansion coefficients compared to that of CO_2. This difference could lead to an explosion of the ampoule inside the autoclave caused by a pressure difference.

3.5.7 The production of dry ice for counter-pressure

The dry ice as a counter-pressure agent was produced in a similar way as the solid CO_2 inside the ampoule. The same system as in fig. 3.6 with a small modification was used. Instead of the ampoule, a 250 ml balloon was connected to the system. After evacuating and purging the system,

CO_2 was transferred in the system. Again liquid nitrogen was used to solidify CO_2 inside the balloon.

3.6 Operating procedure

The calculated (see calculations) amount of CO_2 was weighed fast (to avoid the condensation of water) on a balance using a polystyrene vessel and then transferred into the autoclave, where the filled and sealed ampoule was placed. The autoclave was closed and connected with the measuring and releasing system. A drying oven was employed to heat the autoclave. The measuring and releasing system was placed outside the oven due to the instabilities of its components at high temperatures. As mentioned above a capillary with 1/16" inner diameter connected the autoclave (inside the oven) with the measuring and releasing system (outside the oven). The purpose of choosing a thin capillary was related to the minimisation of the gas current inside it. The drying oven was equipped with a small aperture for an external thermometer. The enhancement of the temperature inside the oven was associated with a temperature increasing inside the autoclave and as a consequence of the ampoule inside it. Until the equilibria is reached, a temperature difference between the counter-pressure gas (CO_2) and the CO_2 inside the ampoule might occur. This temperature difference is associated with a pressure difference, which could cause the implosion of the ampoule if it would have surpassed 30 bar. The quartz ampoules used endure pressures up to 30 bar. The temperature was increased gradually until the desired value to avoid a huge difference of pressure inside the system. The autoclave with the ampoule inside stayed one to two weeks under the desired temperature (the supposed time for the completion of reaction). After this time the temperature was decreased gradually until reaching the room temperature. The outlet valve was opened only when the autoclave reached the room temperature, and the pressure inside it was gradually released. The pressure releasing was associated with the explosion of the ampoule.

3.7 Calculations

In the following part, the calculation of the necessary amount of CO_2 inside and outside (counter-pressure gas) the ampoule is described.

The international thermodynamic tables for carbon dioxide [38] give precious information about the dependence of pressure on temperature when the starting density of the CO_2 is known. Starting from the found density of CO_2 inside the sealed ampoule (6.80×10^{-3} mol ml^{-1}), it was possible to find out the approximate dependence of pressure from the heating temperature. More detailed informations are listed in appendix (table 8.1).

The above procedure considers only the ampoule and the CO_2 content in it. To calculate the quantity of CO_2 which should be transferred into the autoclave for counter-pressure, the equation (3.6) was used.

$$P_{in} = P_{out} \qquad \textbf{(3.6)}$$

Equation (3.6) states that the pressure inside the ampoule should be equal to the pressure outside it. The equation (3.6) can be fulfilled when the densities inside and outside the ampoule are equal.

$$\rho_{in} = \rho_{out} \Rightarrow m_{in}/V_{in} = m_{out}/V_{out} \qquad \textbf{(3.7)}$$

In the equation (3.7) the only unknown term is the mass of CO_2 which should be filled in the autoclave. The volume outside the ampoule is represented from the contribution of three terms for each system, respectively: the volume of the autoclave, the volume of the connecting capillary and the volume of the measuring system.

$$\mathbf{V_{out(1)} = V_{aut.(1)} + V_{cap.(1)} + V_{m.s.(1)}} \qquad \textbf{(3.8)}$$

$$\mathbf{V_{out(2)} = V_{aut.(2)} + V_{cap.(2)} + V_{m.s.(2)}} \qquad \textbf{(3.9)}$$

The inner volumes of autoclaves were determined by means of their water content at 20°C (similar to the procedure for determination of the inner volume of the ampoule). The volumes of the steel capillaries were calculated by knowing their inner diameter and length. The substitution of these values in the equations (3.8 and 3.9) revealed: $V_{out\,(1)} = 109.7$ ml, $V_{out(2)} = 121$ ml.

In this way, if the quantity of CO_2 inside the ampoule is known (dependent from environment's temperature) one can easily calculate the quantity of CO_2 outside it. Detailed information about these quantities for different temperatures is given in appendix (tables 8.2, 8.3).

The above described calculations are valid only for empty ampoules with inner and outer volume of approx. 7.2 and 10 ml respectively. The presence of educts in the ampoule decreases the inner volume. This volume decrease is associated with a density increase and as a consequence a higher amount of dry ice is needed outside the ampoule to balance the pressures. For the synthesis in $scCO_2$, 0.5 g educts were used corresponding approx. to a volume of 0.1-0.2 ml. The above calculations are repeated taking into account this volume (see table 8.3 in appendix).

3.8 Reactions in supercritical CO_2

It is mentioned above that the ampoule filled with the educts and CO_2 (dry ice) is placed inside the autoclave. To illustrate what happens with the dry ice inside the ampoule till it transforms into supercritical fluid the following explanation is used.

The sealed ampoule and the autoclave with its system represent a closed system, therefore according to thermodynamics they exchange with the surrounding only heat. At the beginning of the reaction the temperature inside the ampoule and outside is lower than the surrounding's temperature, causing a heat flow from the surrounding into the system. Inside the autoclave the process of sublimation will start (Fig. 3.13), in the ampoule, the same process happens, but displaced in time. This displacement of transition is explained through the low thermal conductivity of quartz. The process of transformation from dry ice into gas will continue as long as the temperature and pressure inside the system will increase until the liquid phase is formed. The whole transition is associated only by one degree of freedom (see the rule of phases), this means that the change of temperature is associated with the change of pressure inside the system. After reaching the triple point, further heating of the system generates an equilibrium between the liquid and gas phase (Fig. 3.13 state 2). This equilibrium exists until the critical point is reached. Near the critical point, the border between both phases (liquid-gas) fades (Fig. 3.13 state 3) and slowly one single phase is observed (Fig. 3.13 state 4). The transition from the triple point to the critical region is

associated with only one degree of freedom. This explanation takes into account the ideal case when the ampoule is filled only with CO_2. In practice, there might be several educts and the reaction products beside CO_2 in the ampoule, building a complex system.

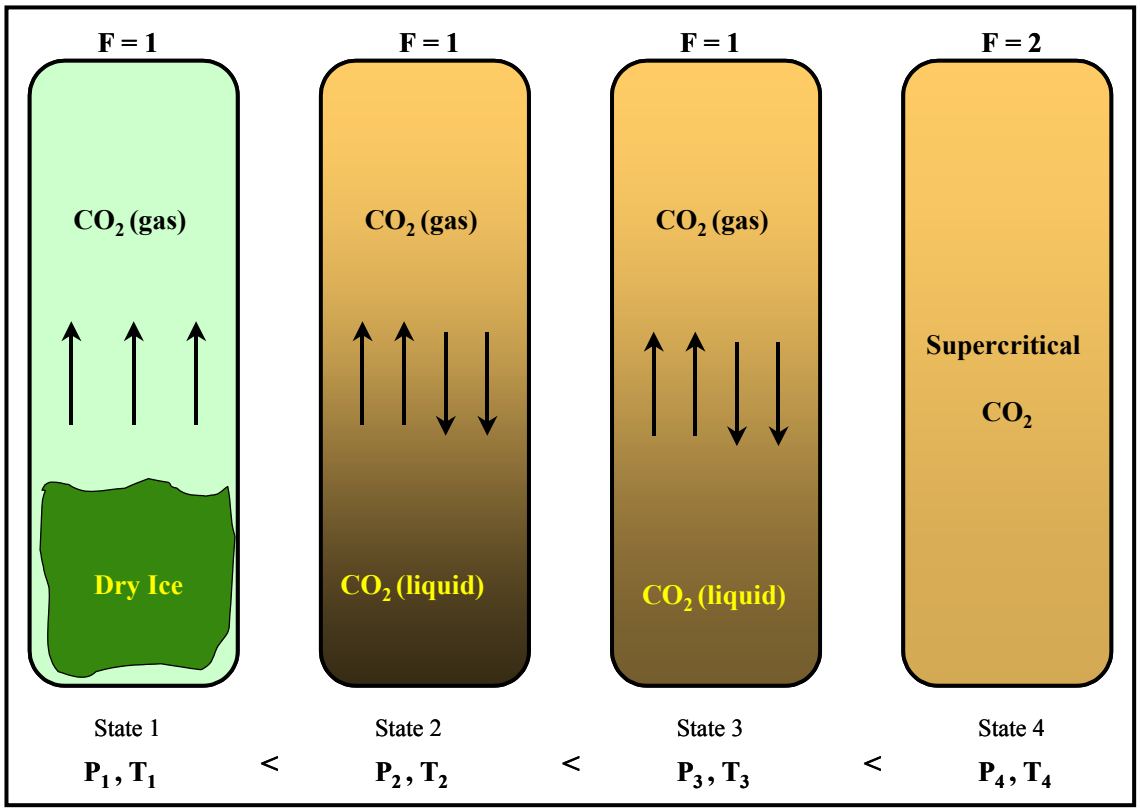

Fig. 3.13: Transition of dry ice into supercritical fluid inside a closed vessel.

If there is a solubility of the educts in the supercritical phase, the critical parameters of the solution will differ from the parameters of the pure solvent (CO_2). Jie Ke et al [57] investigated in their study concerning the change of the critical point during a chemical reaction in supercrititical CO_2, the process of the hydroformylation of propene using CO_2, H_2 and CO to obtain *n* and isobutyraldehyde. By experimenting different ratios of the starting compounds, they observed the decreasing of the critical point at higher ratios of H_2 and CO due to their lower critical parameters in comparison to CO_2, while the opposite was observed as the amount of butyraldehyde increased.

For the reactions in $scCO_2$ involving mainly solid inorganic educts, to enhance the mass transfer and the solubility, a large area of contact between the educts and $scCO_2$ should be created. Below the critical region very low or no solubility of solid educts is expected firstly, due to the existence of

different phases (gas – liquid - solid) and secondly due to the low ambient temperature. An enhanced solubility of the solid educts is expected in the critical or near-critical region.
According to the dissolved substances a displacement of the critical point mainly to high temperatures is expected. Therefore, a possible chemical reaction that might take place in the "new" critical region might be associated with the formation of a product which could be soluble as the participating educts or less soluble. In case of lower solubility of the product compared to the solubility of the educts, a faster conversion rate of the educts into product is expected. If the product will present similar solubility as the educts, only a certain rate of conversion might take place, until a saturated solution of the mixture educts-products can be obtained. After that, further amount of the educts will not be dissolved anymore in the fluid, and as a consequence no reaction will take place. In such cases to recover the formed product together with the dissolved educts, the change of the parameters of the fluid is required. The reactions in $scCO_2$ might be even more complex and in some cases might lead to the formation of species which are stable only in the critical conditions. The investigations of such products can be done only by in-situ measurements and are therefore beyond the scope of this work.

3.8.1 Optimisation of the system using CO_2

As the first step before starting the synthesis in supercritical fluid, the tightness and the security of both systems were tested. The previous test performed with water and the hydraulic press (see above) was followed by other tests using CO_2. To perform such experiments, the autoclaves were fully filled with dry ice and closed using O-rings made of special rubber. They were heated with different heating rates in a drying oven. The rubber as sealing material unfortunately exhibited limitations of the working conditions. At approx. 100°C the observed loss of pressure is obviously a problem of the O-ring material. Also the use of Teflon O-rings, projected for temperatures up to 250°C was unsuitable. The lack of elasticity, resulting mainly from the low initial temperature of the filled autoclave, led to loose autoclave. Attempts to use copper O-rings failed due to the hardness of this material. As an appropriate material Viton O-rings (fluoroelastomer) were successfully tested within a temperature range of RT -220°C. Temperatures higher than 250°C were associated with the loss of pressure in the system. Therefore the use of Viton O-rings limited the

upper temperature of the synthesis. The advantage of this material in comparison to the already tested materials lies in its elasticity, which persist for dynamic and static applications even at –23°C. Using Viton O-rings and fully filled autoclaves, pressures up to 400 bar could be achieved. At this pressure the overpressure valves of both systems were calibrated.

3.8.2 Testing the filled ampoules with dry ice

The choice of the gasket material and the calibration of the maximum working pressure of the system was followed by tests of the durability of the quartz ampoules at high pressures. The quartz ampoules were filled with CO_2 according to the procedure described in the appendix (Fig. 8.5, and steps of usage), sealed and placed inside the autoclave together with the calculated amount of CO_2 for the counter-pressure. The system was closed and placed in the oven. A fast heating rate up to 150°C (in less than one hour) displayed at the pressure gauge a rapid pressure increase which was followed by un abrupt decrease of pressure. After cooling down and releasing the pressure, a fine quartz sand was found inside the autoclave. The explosion of the ampoule happened as a consequence of the pressure difference outside and inside the ampoule. This pressure difference occurred due to the quick heating of the autoclave (quartz has a low heat conductivity). The observed decrease of pressure resulted from the cooling after the explosion of the ampoule.

To avoid this, a long stabilising time at ambient conditions (2-3 hours) and a slow heating rate (20°C/h) was used. This method showed promising results, but sometimes when heating up to 200°C, small deviation between the calculated and the observed pressure were observed leading to an explosion of the ampoule. The explosion of the ampoule can be assigned to two factors: a) the sealing accuracy which influences directly the outer volume of the sealed ampoule, b) the amount of CO_2 used for counter pressure.

The deviations between the observed and the calculated value of pressure derive mainly from the sublimation of CO_2 during the weighting and filling process. Therefore to compensate the loss, 1-2 g over the calculated amount were used. According to my own experience and the reports of Rabenau & Rau [58, 59] the counter-pressure can be even some hundred bar over the inner pressure. These tests were repeated for the ampoules filled with 0.5 g substance and CO_2. The volume difference caused by the presence of the educts has been taken into account.

3.9 Experimental procedure

The weighed educts (0.5 g) were transferred into a quartz ampoule. Air sensitive educts were handeld under inert atmosphere. Afterwards the ampoule was evacuated, filled with CO_2 (see filling procedure) and sealed. The sealed ampoule was placed inside the autoclave with the necessary amount of dry ice for counter-pressure. The autoclave was closed and left at ambient temperature for approx. 2 hours. Then, it was heated gradually (20°C / h) up to 200°C. The autoclaves remained at this temperature generally for one week if no pressure diminution was observed. Finally the system was cooled down to room temperature and gradually depressurised. Fast depressurisation rates often led to an ampoule explosion. The obtained sample (separated from glass splitter if necessary) was ground and then investigated by X-Ray diffraction, Raman and/or infra-red spectroscopy.

3.9.1 The comparison method

In order to distinguish whether a reaction depends on the presence of $scCO_2$, parallel synthesis was performed without CO_2. For such synthesis the same amount of educts was used. The quartz ampoule filled with educts was evacuated, sealed and heated. For some syntheses running with the autogenic release of CO_2 (e.g. decomposition of Rb_2CO_3) the sealed ampoule was not placed directly in the oven, but rather in a steel autoclave (Fig. 3.14) equipped with a Teflon insert. This autoclave served more as a protector in case of a possible explosion. No counter-pressure agent was used in such cases. Due to the pressure generated inside, great attention should be paid while removing the ampoule from the autoclave. By means of long tweezers and protecting gloves, the ampoule is firstly transferred into a container filled with liquid nitrogen. The ampoule remained immersed in liquid nitrogen for at least 10 minutes, then it was enwrapped with paper and quickly broken at its top. After the evaporation of dry ice, its solid content was ground and investigated by the methods described in the experimental procedure.

Fig. 3.14: Protecting autoclave used mainly for reactions occurring with autogenic CO_2 release (this kind of autoclave has been previously employed mainly for hydrothermal reactions).

3.10 Discussion of the results

Table 3.4: Educts, expected products, conditions and the obtained products.

No.	Educts	expected product	Conditions	Products
1	InI, SnI_4, C_3H_6O	$SnIn_2I_6$	100°C, 140 bar, 3d	SnI_2, InI_3
2	InI, SnI_4, In	$SnIn_3I_5$ (1)	200°C, 220 bar, 1w	Sn_2InI_5, SnI_2,
3	InI, SnI_4, In $C_4H_{10}O$	$SnIn_3I_5$	200°C, 225 bar, 2d	Sn_2InI_5, InI_2
4	Rb_2CO_3, SnI_4, I_2	Rb_2SnI_6 (1)	200°C, 220 bar, 1w	RbI_3, am.p.
5	Cs_2CO_3, SnI_4, I_2	Cs_2SnI_6	200°C, 220 bar, 1w	CsI_3, am.p.
6	K_2CO_3, SnI_4, I_2	K_2SnI_6 (1)	200°C, 220 bar, 1w	KI, KIO_3, am.p.
7	Rb_2CO_3, I_2	RbI_3 (1)	200°C, 225 bar, 1w	RbI, $RbIO_3$
8	Rb_2CO_3, SeO_2	Rb_2SeO_3 (1)	200°C, 230 bar, 1w	Rb_2SeO_3
9	Ag_2S, AgBr, GeS, S	$Ag_6GeS_4Br_2$	200°C, 230bar, 1w	Ag_3SBr
10	NaBr, In_2S_3, InS	$NaIn_4S_5Br$	240°C, 260 bar, 1w	-
11	In, S, I_2	In_5S_5I	200°C, 220 bar, 1w	In_2S_3, InI_2
12	In, S, I_2, CH_3OH	In_5S_5I	200°C, 225 bar, 1w	In_2O_3, In_2S_3, InI_2
13	In, S, $InCl_3$	In_5S_5Cl	200°C, 215 bar, 1w	InS, In_2S_3, InCl,
14	Se (trigonal)	Search for new modifications	200°C, 220 bar, 1w	-
15	Te (trigonal)	Search for new modifications	200°C, 220 bar, 1w	-
16	Hg_2Cl_2, Hg_2Br_2	$Hg_4Br_2Cl_2$ (1)	200°C, 220 bar, 1w	Hg_2Cl_2*Hg_2Br_2
17	Hg_2Cl_2, Hg_2I_2	$Hg_4Cl_2I_2$ (1)	200°C, 220 bar, 1w	Hg_2Cl_2*Hg_2I_2
18	Hg_2Br_2, Hg_2I_2	$Hg_4Br_2I_2$ (1)	200°C, 220 bar, 1w	Hg_2Br_2*Hg_2I_2
19	Hg_2Cl_2, HgO	$Hg_4O_2Cl_2$ (1)	200°C, 220 bar, 1w	$HgCO_3$*2HgO
20	HgO	$HgCO_3$	200°C, 220 bar, 1w	$HgCO_3$*2HgO
21	Hg_2Cl_2, HgO, H_2O	(2)	200°C, 220 bar, 1w	$Hg_4O_2Cl_2$,

(1) reactions run parallel to reactions with the same educts in evacuated ampoules,
(2) reactions run parallel to reactions with the same educts under hydrothermal conditions
am. p. abbreviation for amorphous product

3.10.1 Dissolving ability of CO_2, attempts for the syntheses of ternary compounds using SnI_4

In order to test the dissolving ability of $scCO_2$ and possible reactions which might take place in this fluid, firstly, educts with molecular nature and low melting points like SnI_4 [60] were employed. Additionally acetone was used as a co-solvent. The purpose of experiment 1 was to obtain the ternary compound $SnIn_2I_6$ in $scCO_2$ according to the reaction (3.10).

$$\mathbf{SnI_4 + 2InI \rightarrow SnIn_2I_6} \qquad \mathbf{(3.10)}$$

For this synthesis both solid educts were pulverised, weighed according to the stoichiometry and transferred into the quartz ampoule in an inert atmosphere. Acetone was added and then the ampoule was filled with CO_2 according to the described procedure.
The autoclave was opened under N_2 atmosphere (inside a glove bag). The depressurisation of the system caused the explosion of the ampoule. A red-brownish product was obtained. The collected sample was ground and measured on a X-ray diffraction system. SnI_2 and InI_3 instead of $SnIn_2I_6$ could be identified.

The second experiment in $scCO_2$ involved elemental indium in addition to the already used educts SnI_4 and InI. Using these educts it was aimed to produce $SnIn_3I_5$ [63] at 200°C and 220 bar according to the reaction (3.11).

$$\mathbf{SnI_4 + InI + 2In \rightarrow SnIn_3I_5} \qquad \mathbf{(3.11)}$$

At 200°C indium could serve as a reducing agent, reacting with SnI_4 to yield SnI_2 and InI. The latter products might further react in $scCO_2$ to yield the desired product. The preparation of the binary educts was done in an inert atmosphere. Elemental indium was used in form of small pieces. This reaction ran in parallel to another reaction involving the same educts, however, without CO_2. The XRD measurements of the product demonstrated the presence of Sn_2InI_5, InI and SnI_2. Therefore, it is assumed that tin tetraiodide has reacted with elemental indium.
The reaction without CO_2 also results in the formation of the ternary compound Sn_2InI_5, indicating that CO_2 has no influence. The synthesis of this ternary compound (Sn_2InI_5) has already been

reported by Beck [64]. He obtained it by using SnI_2 equilibrated with SnI_4, an excess of Sn and indium monoiodide at 350°C in an evacuated ampoule. Anyway my results demonstrate that Sn_2InI_5 can be partially obtained from the reaction SnI_4, InI and indium even at 200°C.

The above reaction was repeated again using 0.2 ml ethyl ether as co-solvent. The presence of this cosolvent should enhance the dissolving power of $scCO_2$. After annealing and pressurising the sample was kept at 200°C and approx. 225 bar for two days, the obtained product was similar to the previous one. The XRD measurement of the product again shows the presence of Sn_2InI_5 and InI_2 (Fig. 3.15).

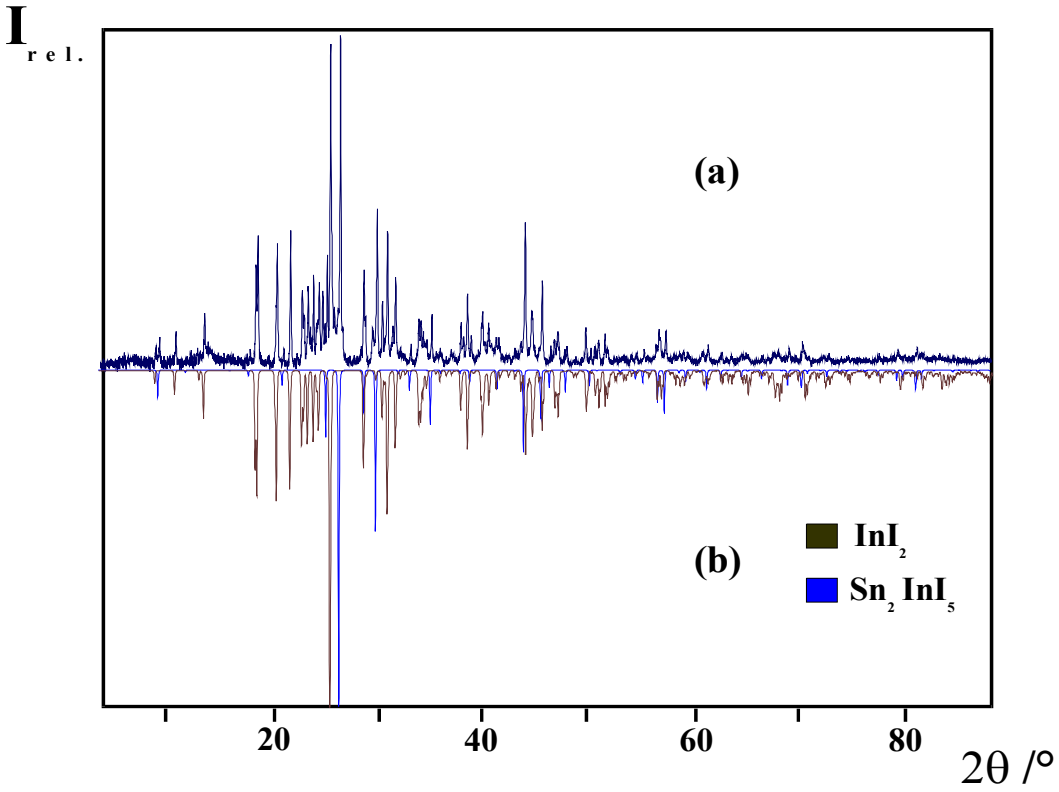

Fig. 3.15: Comparison of the patterns (a) of the measured sample with (b) the calculated patterns of InI_2, and Sn_2InI_5.

The above reactions displayed negligible activity of $scCO_2$ or the combination $scCO_2$/co-solvent in these reactions. All of them run also as solid state synthesis, where temperature and not the pressure plays the decisive role.

3.10.2 Syntheses involving alkali metal carbonates and polar compounds

In the next series of reactions in $scCO_2$ the educts have been alkali metal carbonates together with tin tetraiodide and iodine. The involved carbonates are crystalline ionic compounds, while tin tetraiodide and iodine are non polar molecular compounds. It is already known that iodine and SnI_4 dissolve well in non polar solvents (organic solvents). Thus, a high solubility could be expected in $scCO_2$ as well. The schematic of the intended reaction (3.12) was as follows:

$$\mathbf{M_2CO_3 + SnI_4 + I_2 \rightarrow M_2SnI_6 + by\text{-}products \quad (M = K, Rb, Cs)} \qquad \mathbf{(3.12)}$$

For these experiments (see table 3.4, reactions 4-6) the ampoules were annealed at 200°C, and approx. 220 bar for one week. The obtained products from syntheses in $scCO_2$ were crystalline, dark-brown in case of Rb_2CO_3 and Cs_2CO_3 and light-brown in case of K_2CO_3.
These experiments were accompanied by one simple high temperature reaction only (Rb_2CO_3, SnI_4 and I_2). The ampoule of this reaction was placed in a protecting autoclave (Fig. 3.14) due to the assumption that this reaction might produce CO_2. The obtained product was similar to the dark-brown products obtained by the synthesis in $scCO_2$.

Surprisingly, the X-ray diffraction analysis of the samples obtained from the above reactions in $scCO_2$ presented unexpected results. Instead of the expected ternary compounds, RbI_3 (Fig. 3.16) and CsI_3 could be identified for the reactions 4 and 5 (table 3.4). For the reaction 6 ($K_2CO_3/SnI_4/I_2$) the disproportionation products KI and KIO_3 were obtained (Fig. 3.17).

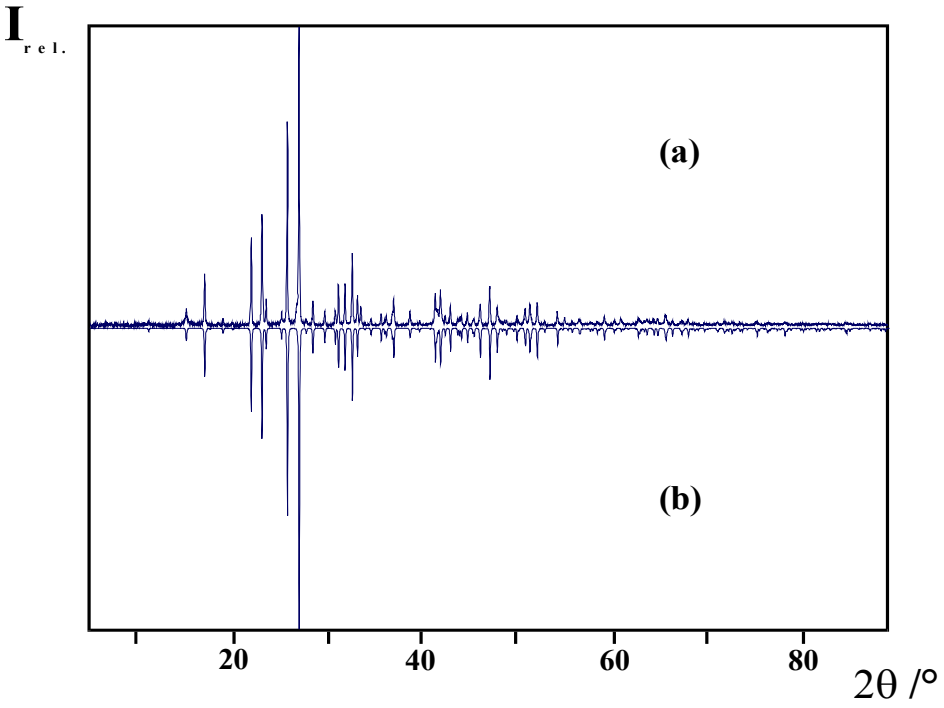

Fig. 3.16: Comparison of (a) the measured pattern of RbI_3 obtained from the reaction of Rb_2CO_3 with SnI_4 and I_2 in $scCO_2$ with (b) the calculated pattern of RbI_3.

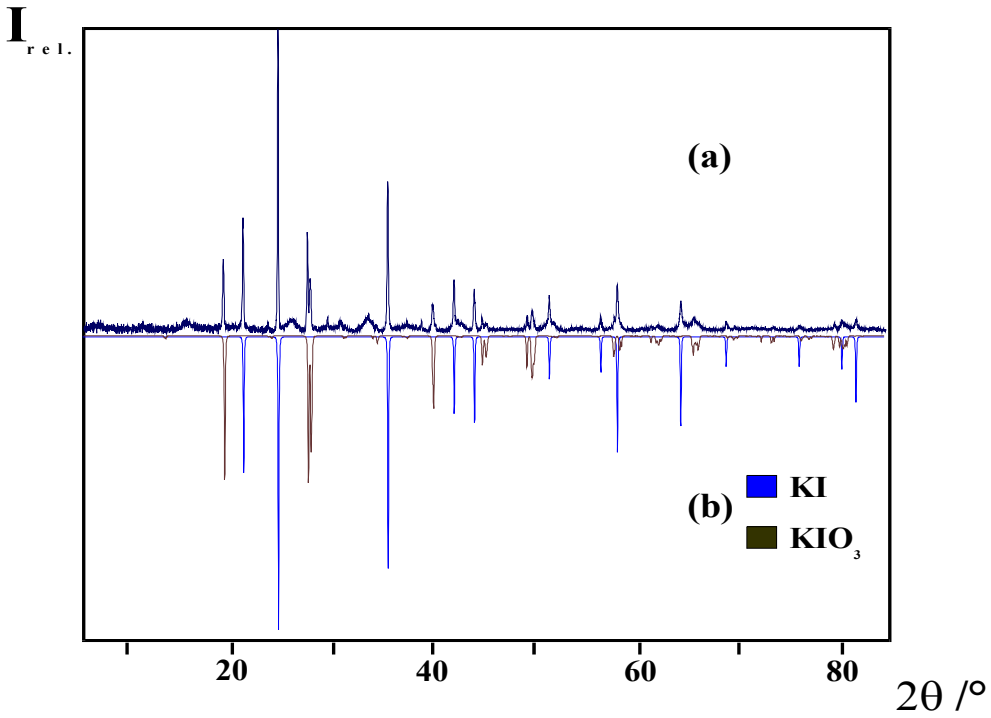

Fig. 3.17: Measured pattern (a) of the product of the reaction of K_2CO_3 with SnI_4 and I_2 in $scCO_2$ (b) the calculated patterns of KI and KIO_3.

The X-Ray measurements of the above samples did not display any traces of crystalline tin compounds, while the "solid state" reaction revealed again the same product (RbI_3), excluding therefore the role of $scCO_2$ in the mechanism of these reactions.

To investigate whether tin tetraiodide plays any role in the mechanism of the formation of MI_3 (M = Rb, Cs), two additional syntheses were projected, one in $scCO_2$ and the other as solid state reaction. The educts were rubidium carbonate and iodine. The X-Ray measurements of the obtained products show the presence of rubidium iodide and the presence of rubidium iodate (Fig. 3.18) and no RbI_3.

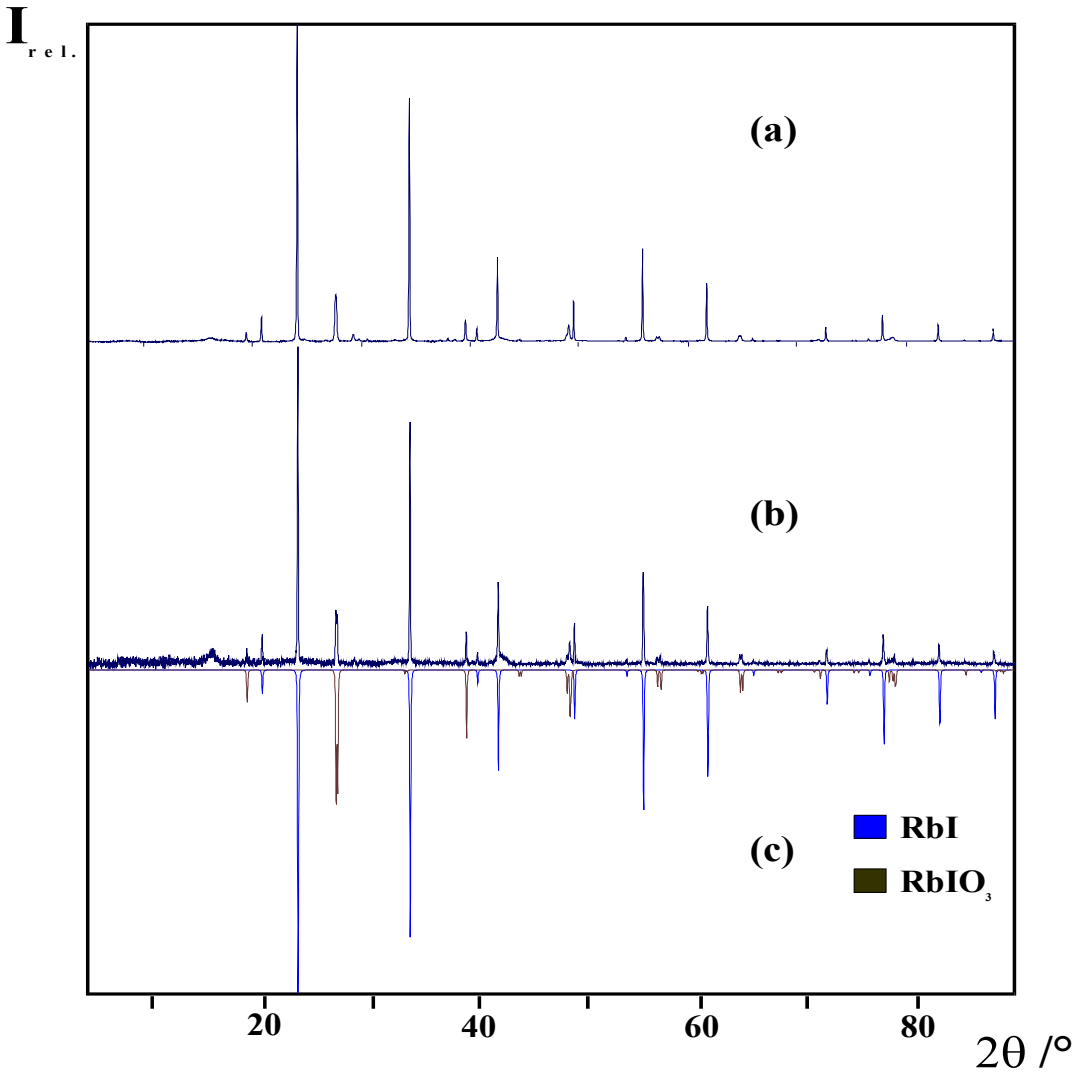

Fig. 3.18: Comparison of the patterns of the sample collected from high pressure reaction (a), solid state reaction (b), and the calculated ones RbI and $RbIO_3$ (c).

The reaction between rubidium carbonate and iodine can be either explained by a disproportionation of iodine and a decomposition of CO_3^{2-} (3.13), or by the presence of water according to equations 3.14 and 3.15.

$$\mathbf{3I_2 + Rb_2CO_3 \rightarrow 5RbI + RbIO_3 + CO_2} \quad \textbf{(3.13)}$$

$$\mathbf{I_2 + H_2O \rightarrow HI + HIO} \quad \textbf{(3.14)}$$

$$\mathbf{3HIO \rightarrow 2HI + HIO_3} \quad \textbf{(3.15)}$$

It was already discussed above that the CO_2 didn't contain water as impurity. To determine the water content of the educts, IR- and DTA-TGA measurements of the carbonates were performed (Fig. 3.19; 3.20).

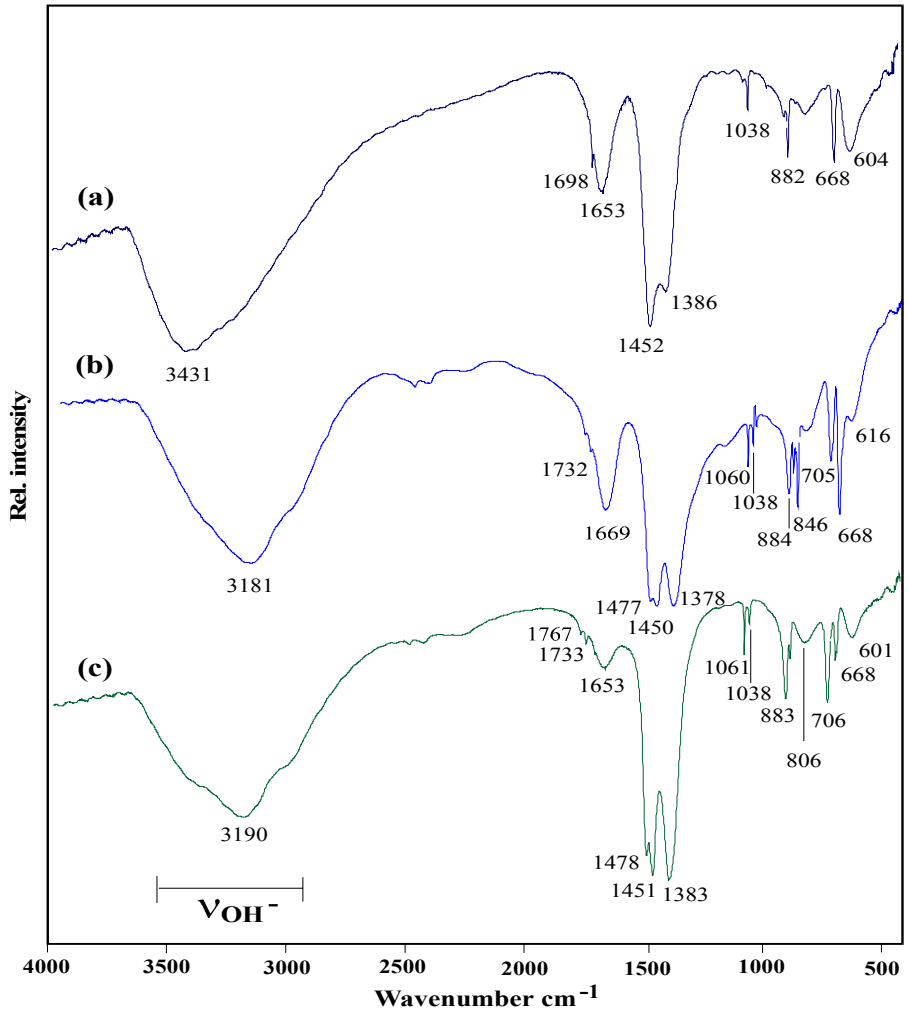

Fig. 3.19: IR-spectra recorded from a) K_2CO_3, b) Rb_2CO_3 and c) Cs_2CO_3.

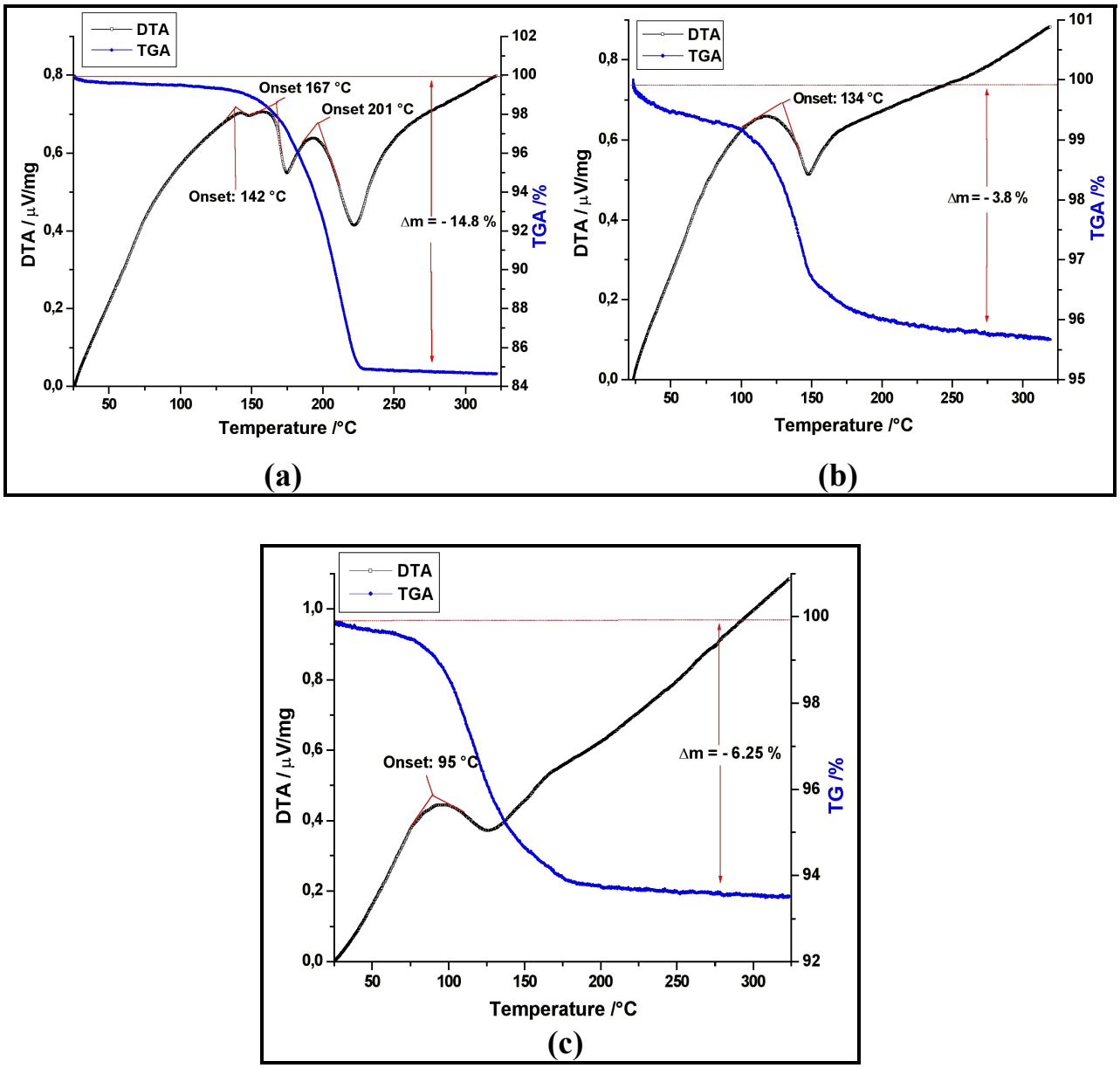

Fig. 3.20: DTA-TGA measurements of (a) Rb_2CO_3, (b) Cs_2CO_3 and (c) K_2CO_3.

The IR-measurements demonstrate the presence of absorbed and crystal water in all carbonates (broad ν_{OH-} bands in the range 3100 – 3400 cm^{-1} accompanied by δ_{H2O} around 1653 cm^{-1}). This was confirmed by the thermal analysis. The DTA-TGA measurements display the presence of a considerable quantity of water especially for Rb_2CO_3 and K_2CO_3. In the case of Rb_2CO_3 the water present is mainly crystal water (majority weight loss at temperatures over 150°C). In the case of

Cs_2CO_3 and especially K_2CO_3 (Fig. 3.23b, c), the crystal water was accompanied by higher amounts of absorbed water (weight loss at lower temperatures).

The previous experiments with the participation of SnI_4 displayed two important arguments:

1) the formation of rubidium and cesium triiodide occurred only when tin tetraiodide was present, independent of the presence of $scCO_2$
2) the formation of the triiodides was observed in case of rubidium and cesium but not in case of potassium

According to this mechanism, the reaction of tin tetraiodide with water might be possible (3.16):

$$\mathbf{SnI_4 + 4H_2O \rightarrow Sn(OH)_4 + 4HI} \qquad \mathbf{(3.16)}$$

The hydroiodic acid decomposes the carbonates, and the obtained iodides react with iodine to give the triiodides. This fact is reported by Tebbe [65] and Runsink [66], who obtained RbI_3 and CsI_3 using the respective iodides and an iodine rich ethanolic solution. In case of potassium this process is not favored due to the instability of KI_3 as solid.
In experiment 8, the reaction between Rb_2CO_3 and SeO_2 was investigated. Again the same product (Rb_2SeO_3) was obtained for the solid state and the supercritical syntheses. For these reactions the starting carbonate was dried (300°C for ten minutes in a dynamical vacuum) and the product has been treated under inert gas atmosphere because of its sensitivity toward air.

3.10.3 Attempts for the synthesis of the quarternary compound $Ag_6GeS_4Br_2$

A further reaction was tested based on the work of Wagener [67] who synthesised the compound $Ag_6GeS_4Br_2$, starting from the elements Ag, Ge, S and hydrobromic acid at a temperature of around 230°C and a pressure of approx. 5 bar. This compound belongs to the group of filled AlB_2 phases.
A trial to perform this reaction under the condition of $scCO_2$ starting from a powdered mixture of sulphur and binary compounds Ag_2S, AgBr, GeS (experiment 9) resulted in a dark grey product.

The X-ray measurement of the product shows the presence of non reacted educts and the ternary compound Ag_3SBr (Fig. 3.21).

Further investigations on this ternary compound (Ag_3SBr) revealed that it could be synthesised at 280°C in evacuated glass ampoules using an equimolar mixture of the binary compounds Ag_2S and AgBr (Reuter & Hardel [68]). Again the reaction in $scCO_2$ can be regarded simply as a solid state reaction between Ag_2S and AgBr.

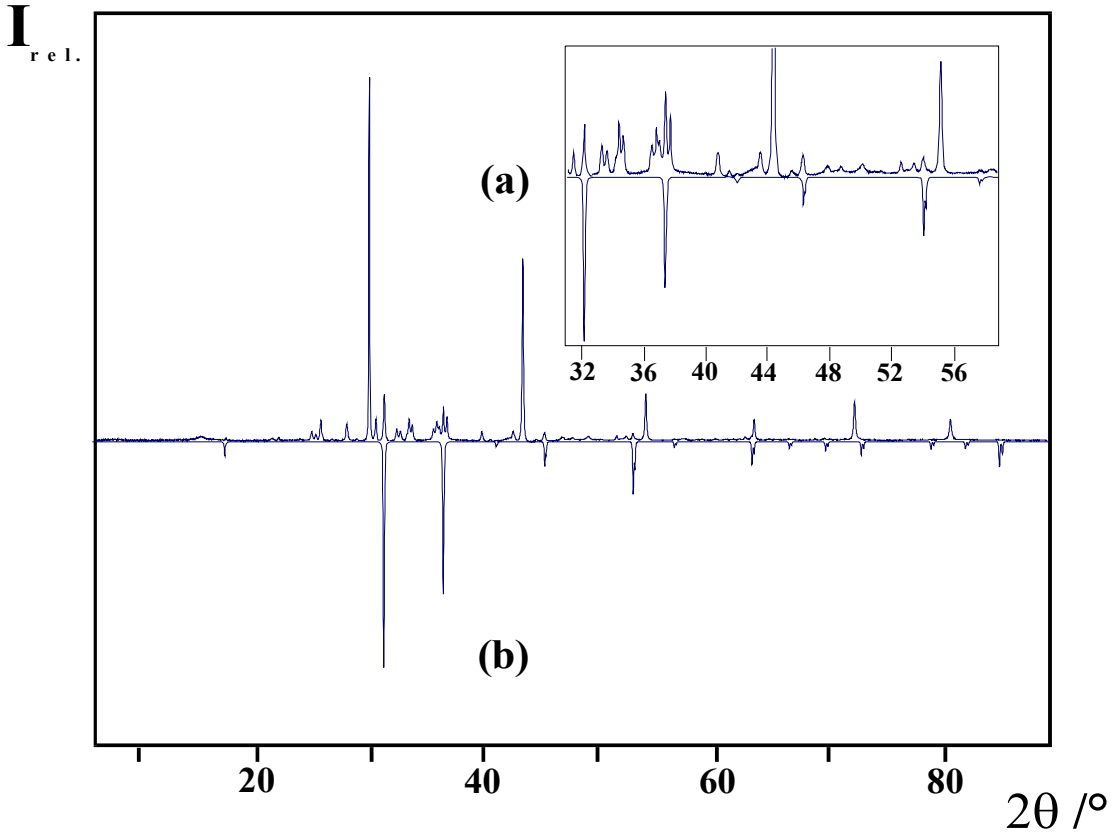

Fig. 3.21: Comparison (a) of the measured pattern obtained from the reaction between Ag_2S, AgBr, GeS and sulphur in $scCO_2$, with (b) the calculated pattern of Ag_3SBr.

3.10.4 Attempts for the substitution of In^+-species in the mixed valence compound In_5S_5Cl

One of the attempts to substitute In^+ in the mixed valence compound In_5S_5Cl (see chapter 6) with sodium, consisted in syntheses between InS [69], In_2S_3 [70] and NaBr to produce $NaIn_4S_5Br$ in

evacuated and sealed quartz ampoules at 500°C. This synthesis was thermodynamically unfeasible due to the high formation enthalpy of sodium bromide. It supposed that, the involvement of $scCO_2$ with its "special properties" might overcome this energetic barrier. At the same time this reaction shows the behaviour of ionic compound like NaBr in $scCO_2$.

To try this synthesis in $scCO_2$ (experiment 10), the binary educts InS, In_2S_3 (powdered) and sodium bromide (previously dried and stored under inert atmosphere) were employed (reaction 3.17).

$$\mathbf{NaBr + In_2S_3 + 2InS \rightarrow NaIn_4S_5Br} \qquad \mathbf{(3.17)}$$

The X-Ray measurement of the obtained product (brown coloured) displayed only the presence of non reacted educts. Under the applied conditions (240°C, 260 bar) no reaction took place, excluding therefore a possible solubility of any participating educts in $scCO_2$.

3.10.5 Attempts for the synthesis of the compound In_5S_5I

The reaction between In, S and InX_3 (X = Cl, Br) in evacuated quartz ampoules at 500°C, yielded two mixed valence compounds, namely In_5S_5Cl and In_5S_5Br (see chapter 4). Based on this observation, several attempts were carried out to synthesise In_5S_5I using the elements In, S and I_2 in evacuated ampoules. All the solid state syntheses performed at different temperatures did not yield this product. Two further attempts were carried out to obtain this product in $scCO_2$ (experiment 11; 12). The first reaction involved the elements and CO_2, the second one included additionally 0.2 ml methanol as cosolvent.

The reaction carried out without the presence of methanol (exp.11) yielded a brown product accompanied by un-reacted sulphur and indium. The brown product was a mixture of indium (III) sulphide and indium (II) idodide.

The reaction performed in the presence of methanol (exp.12) resulted in a grey product surrounding un-reacted indium and sulphur. This reaction is probably associated with the synthesis of

mercaptanes (methanthiol) due to the malodour of the product. The grey product consisted of indium (III) oxide associated by indium (III) sulphide and indium (II) idodide.

Binary educts and non reacted educts were also obtained from the reaction of In, S, $InCl_3$ in $scCO_2$ (experiment 13).

3.10.6 Search for possible new modifications of Se and Te [71-74]

The X-ray and Raman measurements of the products obtained from the respective reactions 14 and 15 performed at 200°C and 220 bar (one week), revealed only the trigonal starting modification for Selenium and Tellurium and no evidence for others.

3.10.7 Mercury (I) compounds

Another group of interesting compounds with respect to their behaviour in $scCO_2$ experiments was the mercury (I) halides (tab. 3.5; [75-79]).

Table 3.5: Some physical constants of the mercury (I) halides [75].

Property\ Compound	**Hg_2Cl_2**	**Hg_2Br_2**	**Hg_2I_2**
Melting point /°C	525	407	290
Sublimation temp /°C	383	345	140
Density /kg m^{-3}	7160	7307	7700
Solubility in water /gcm^{-3}	4×10^{-6}	2×10^{-4}	Very slightly soluble

These experiments focused on the investigation of the behaviour of Hg_2Cl_2, Hg_2Br_2 and Hg_2I_2 in supercritical CO_2 at 200°C and 215-225 bar.

These investigations revealed no reaction between the mercury (I) halides with the CO_2 and no decomposition according to the equilibrium (3.18) at the maximum established conditions.

$$\mathbf{Hg_2X_2 \leftrightarrow Hg^0 + HgX_2 \quad (X = Cl, Br, I)} \qquad \mathbf{(3.18)}$$

In accordance with the results for single mercury (I) halides just described, no reactions between different mercury (I) halides (exp. 16-18) could be observed (Fig. 3.22 and 3.23). Instead the reactions between Hg_2X_2 and Hg_2Y_2 ($X \neq Y$ = Cl, Br, I) in the presence of $scCO_2$ can be considered merely solid state reactions.

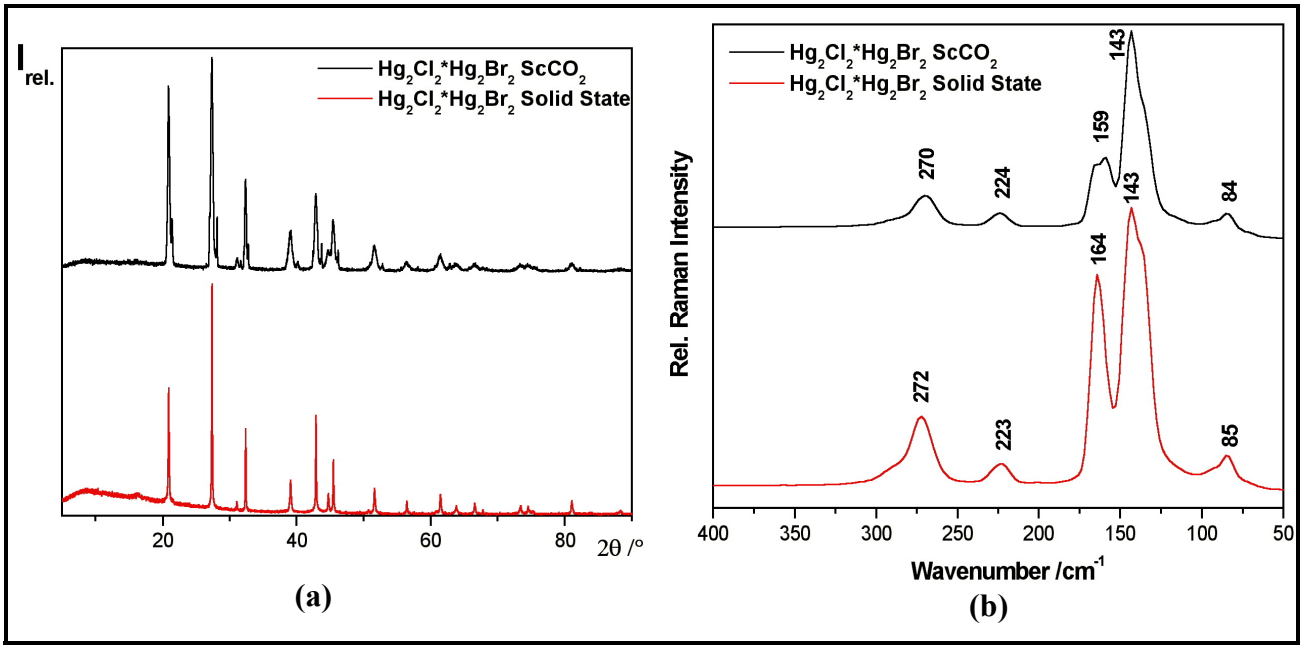

Fig. 3.22: Comparison of the data obtained from the product of the reaction between Hg_2Cl_2 and Hg_2Br_2 in supercritical CO_2 with the product obtained from solid state reaction a) diffraction patterns, b) Raman spectra.

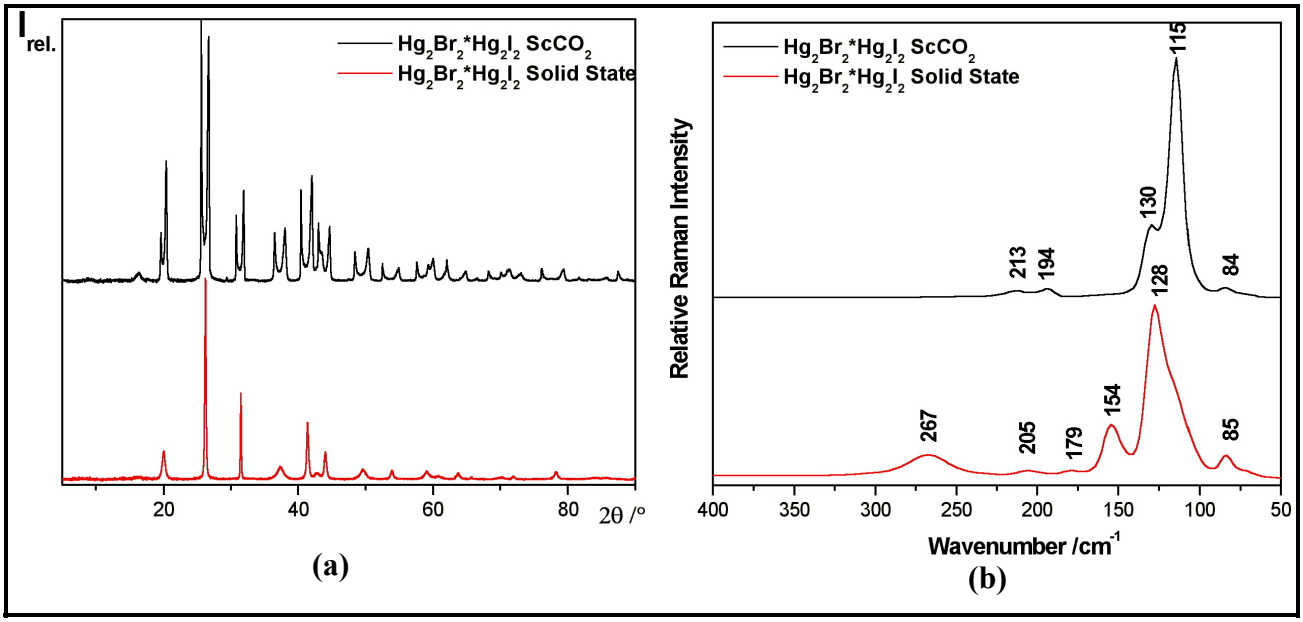

Fig. 3.23: Comparison of the data obtained from the product of the reaction between Hg_2Br_2 and Hg_2I_2 in supercritical CO_2 with the product obtained from solid state reaction a) diffraction patterns, b) Raman spectra.

3.10.8 Hg_2Cl_2 - HgO

Another binary system which has attracted the attention of many researchers is Hg_2Cl_2-HgO. In this system, mercury is found in two oxidation states, namely Hg(I) represented by Hg_2Cl_2 and Hg(II) represented by HgO. Up to now only a small number of mixed valence mercury compounds exists, mainly minerals [81]. Therefore, the investigation of this binary system in supercritical CO_2 was of special interest.

To carry out the experiment, equimolar amounts of Hg_2Cl_2 and HgO were used (experiment 19). The reaction conditions were approx. 200°C, 220 bar and the reaction time was one week. Again this synthesis was associated with a solid state reaction of the same educts.

The obtained products in both cases ($scCO_2$ and solid state synthesis) were pink coloured. The measured X-Ray patterns (Fig. 3.24) and Raman spectra recorded from the products of $scCO_2$ and solid state experiments displayed no reaction between the starting compounds. Anyway, a close inspection of the powder pattern obtained from the product of the $scCO_2$ reaction displayed some

reflections in addition to the starting compounds, (Fig. 3.25 arrow pointed) which do not appear in the pattern recorded from the product of the solid state reaction. A detailed investigation of these reflections evidenced the presence of mercury oxide-carbonate $HgCO_3$*2HgO.

It was shown with previous reactions (16-18) that mercury (I) chloride did not exhibit any reactivity with CO_2. Therefore the reaction for the formation of mercury oxide-carbonate has taken place between mercury (II) oxide and CO_2. The yield of this product under the present reaction conditions was quite low and did not influence the pressure inside the ampoule significantly. If the whole amount of HgO inside the ampoule would have reacted with CO_2, it might have led to a pressure decrease inside the ampoule of approx. 3 bars.

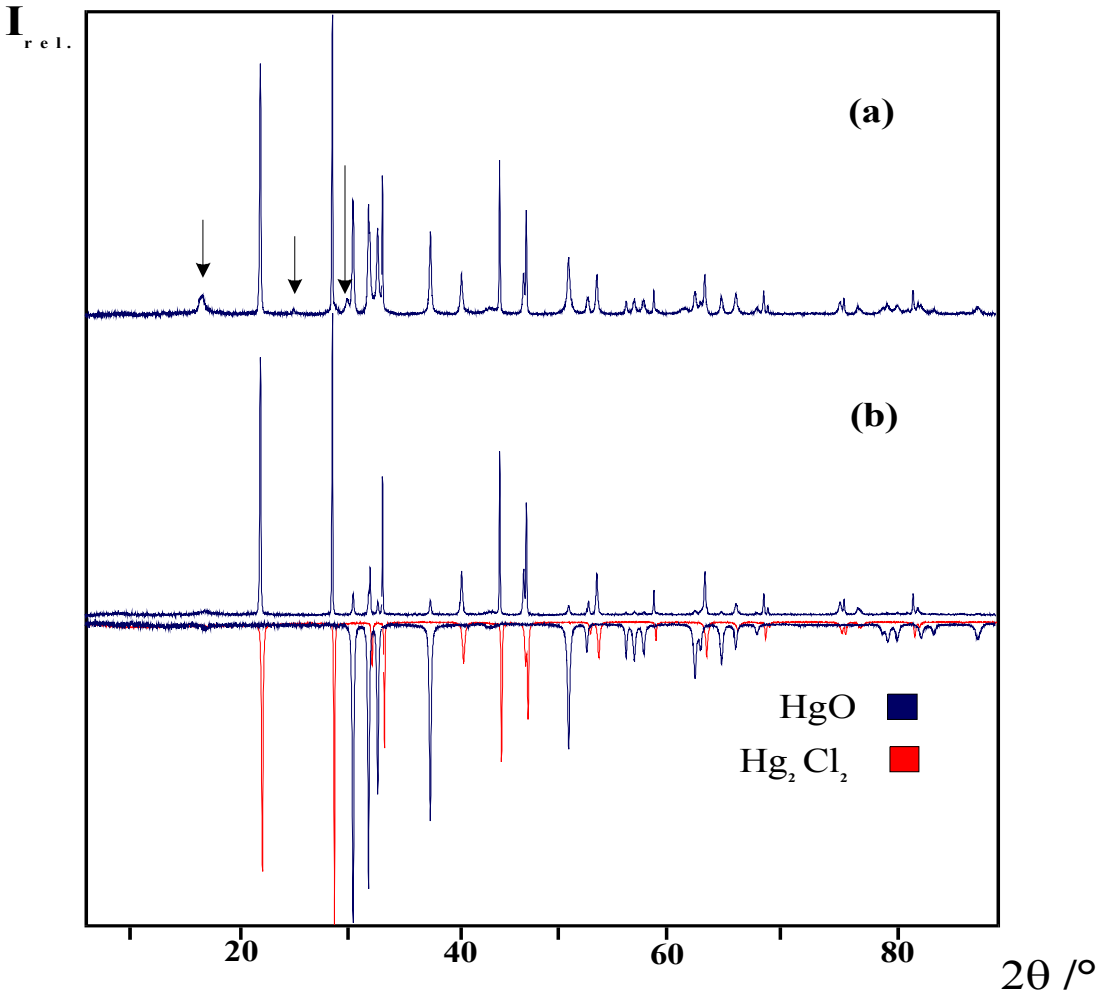

Fig. 3.24: Comparison of the diffraction patterns obtained from the reaction between Hg_2Cl_2 and HgO in a) $scCO_2$, b) solid state reaction with the starting compounds. (The marked peaks belong to $HgCO_3$*2HgO).

The formation of carbonates of different species starting from their oxides or hydroxides in pressurised or supercritical CO_2 has been reported by several researchers. Erhardt et al [82] reported the synthesis of carbonates of alkali metals and some transition metals from their solutions of hydroxides or oxides by the reaction with supercritical CO_2 at pressures ranging from 600-4500 atmospheres and temperatures varying from 100-400°C. In their report they explained the role of the pressure and temperature in the formation of carbonates. In a similar way Yanagihara et al [36, 37] reported the synthesis of the lanthanide carbonates from aqueous suspensions of the respective oxides at moderate pressures (68 – 240 atm) and low temperatures (25 – 50°C). The formation of carbonates from oxides is a phenomenon observed even at normal conditions, e.g. cadmium oxide reacts with the CO_2 of air to form $CdCO_3$ [83].

The evidence of a reaction between HgO and CO_2 (in supercritical state) awoke the interest for the production of $HgCO_3$ instead of mercury oxide-carbonate ($HgCO_3$*2HgO) obtained above. In experiment 20 (table 3.4) the reaction between HgO and CO_2 under the same conditions as in the experiment 19 was tested.

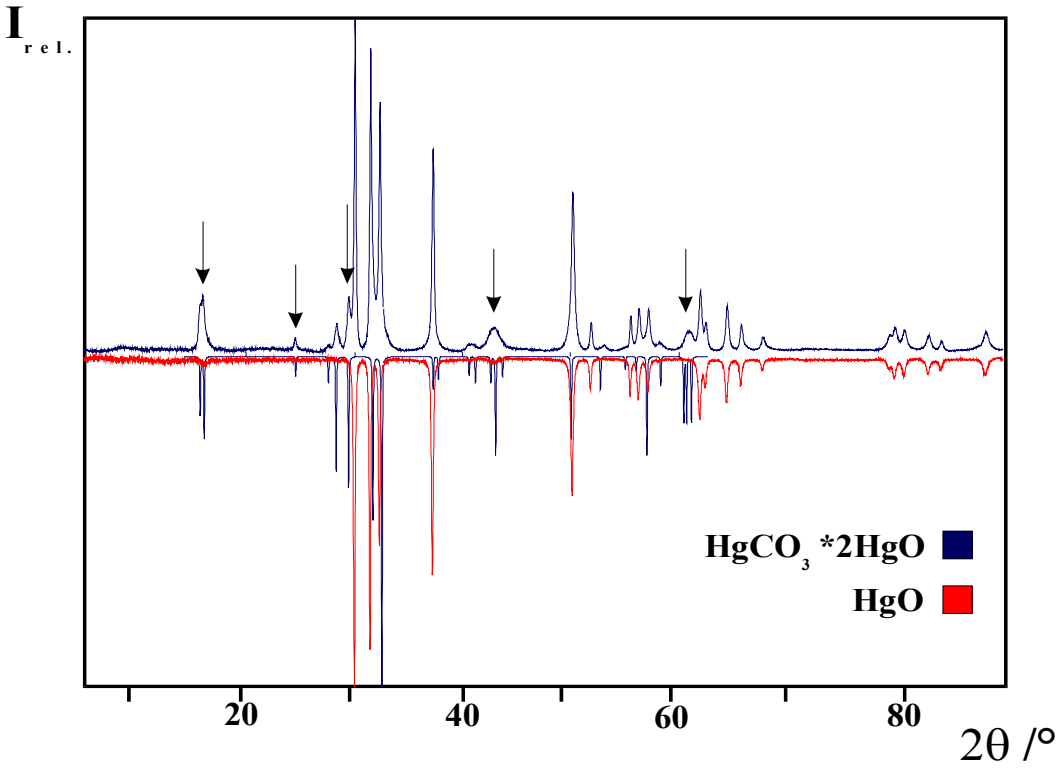

Fig. 3.25: Comparison of the diffraction pattern obtained from the reaction between HgO and CO_2 (above) with the calculated pattern of $HgCO_3$*2HgO and HgO.

This synthesis yielded a pink product, whose X-Ray diffraction and Raman measurements displayed again the formation of mercury oxide-carbonate instead of the expected mercury (II) carbonate (Fig. 3.25). The X-Ray diffraction pattern of the measured product displays also unreacted mercury (II) oxide in addition to mercury oxide carbonate (Fig. 3.25). The obtained IR spectra from the $HgCO_3$*2HgO - HgO mixture compared to the HgO spectra (Fig. 3.26) display not only the presence of the stretching vibrations (1375, 1299 cm^{-1}) belonging to the CO_3^{2-} group, but also a shifting of the Hg-O stretching vibrations (618, 476 cm^{-1} Fig. 3.27a) due to the incorporation of the group CO_3^{2-} in the structure.

The formation of $HgCO_3$*HgO in aqueous solution under CO_2 pressure of one bar has been reported by Bilinski et al [84], while Schlyapnikov et al, in their investigation about the solubility of HgO in aqueous solutions [85] reported its transformation to mercury oxide carbonate at higher CO_2 pressures.

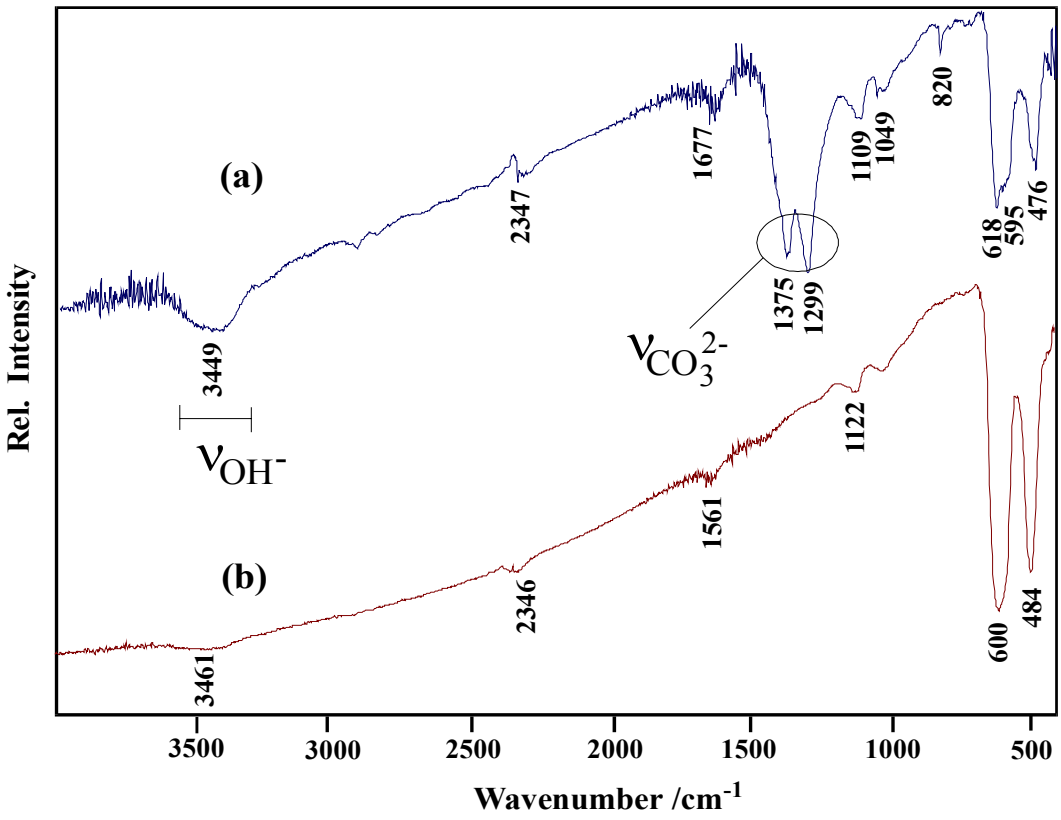

Fig. 3.26: Comparison of the Infra-Red spectra obtained a) from the product of the reaction between HgO and CO_2 in supercritical CO_2, b) HgO.

The experiment (19) between mercury (I) chloride and mercury (II) oxide occurred without the presence of water. It is already known that this system in the presence of water yields a mineral called terlinguaite ($Hg_4O_2Cl_2$) [86-87]. In this experiment 21 it is assumed that the presence of the CO_2 might have a possible impact on the equilibria that exist in this system, which could lead to a new mixed valence mercury compound.

To perform such an experiment in addition to the educts (Hg_2Cl_2, HgO), 0.5 ml of water were transferred in a quartz ampoule. The reaction conditions were 200°C, and approx. 220 bar for one week. For the comparison of the data obtained of the above experiment, a reaction of the same educts and water (the same amounts) running in parallel to the synthesis in $scCO_2$ was performed.
The products yielded from the supercritical CO_2 and hydrothermal-like reactions were brown-yellow. The X-Ray diffractions and Raman measurements (Fig. 3.27) of both products obtained consisted of terlinguaite ($Hg_4O_2Cl_2$) and partially non reacted mercury (I) chloride.

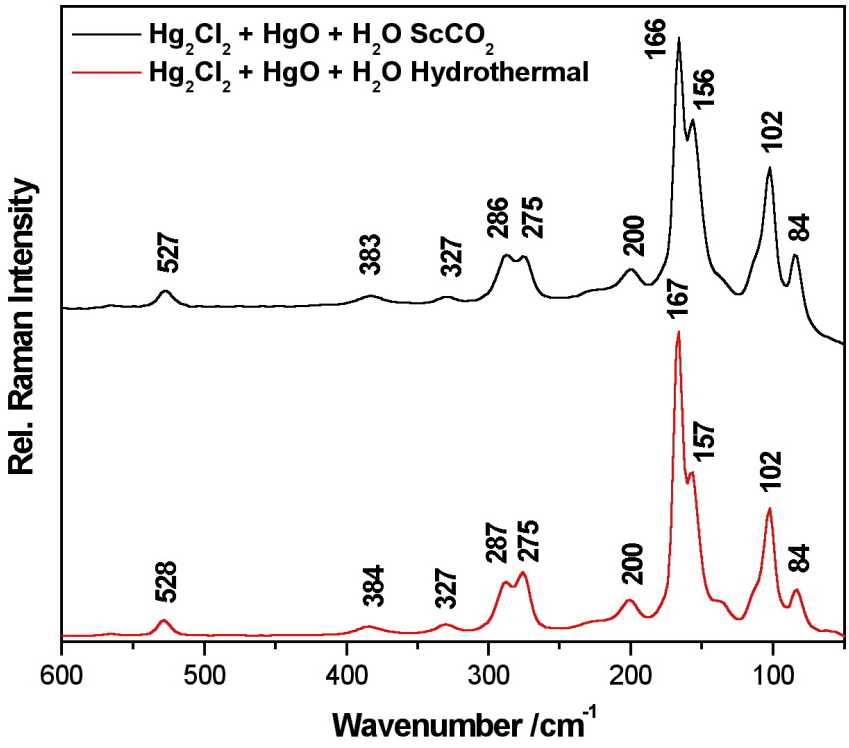

Fig. 3.27: Comparison of the Raman spectra obtained from the product of the reaction between Hg_2Cl_2, HgO and H_2O by a) supercritical CO_2 b) hydrothermal like synthesis.

Regardless of the presence of water and CO_2 in the ampoule, this reaction did not exhibit the formation of mercury oxide-carbonate. Therefore, this synthesis can be considered merely a hydrothermal reaction.

3.11 Conclusions

Several reactions between inorganic compounds of different nature were investigated in $scCO_2$. Applying temperatures varying from 100 to 200°C and pressures between 140-260 bar, it was aimed, to dissolve different species in $scCO_2$. It is supposed that the solvation of the inorganic species in $scCO_2$ and their subsequent reaction could lead to "new" compounds. The investigated syntheses presented in general no reaction caused by the presence of $scCO_2$ or tuned $scCO_2$. This behaviour indicated low or no solubility of the employed species in $scCO_2$ within the applied conditions. The role of the pressure in most of the synthesis was negligible; instead the temperature had the decisive role.

One of the application fields, which over years has attracted many researchers, consists in the permanent fixation of CO_2 from oxides or silicates to yield the respective carbonates. A similar example is presented above, and comprises the conversion of HgO into $HgCO_3$*2HgO in the presence of $scCO_2$. In these kinds of syntheses the pressure determines the rate of conversion of the starting compound into product and CO_2 is considered merely as an educt. Therefore, in such syntheses the application purpose of $scCO_2$ as solvent fades. Supercritical CO_2, despite of the vast applications as an authentic solvent in organic and polymer chemistry, due to its non polarity remains an improper solvent for inorganic synthesis.

4. New mixed valence chalcogenide halides of indium

4.1 Introduction

Some of the elements of the third main group, namely Al, Ga and in particular In appear in their compounds not only in the highest valence state M^{3+}. It exists a group of compounds where these elements are found simultaneously in different oxidation states. Focusing on indium as a representative of this group one can bear in mind the binary compounds In_6Ch_7 (Ch = S, Se) [88-91] as compounds where In possesses all its possible positive oxidation states, namely: In^+, formal In^{2+} and In^{3+}. The chalcogenides S and Se exhibit in these compounds their lowest oxidation state –2. Thus, as explained from Walther [89, 91] the sum formula of these compounds can be explicitly written in the following way: $[In^+]\ [(In_2)^{4+}]\ 3[In^{3+}]\ 7[Ch^{2-}]$. In the In_6S_7 structure type In^+ is located in three capped prismatic holes, the formal In^{2+}-ion forms with its neighbour In-In dumbbells, where each indium atom is coordinated from three sulphur atoms building ethane analogues units. In^{3+} occupies cis and trans edge-sharing octahedra. To get a further understanding in the structural properties of In_6Ch_7, several attempts have been done to substitute one of these individuals. The substitution of In^+ brought into light a series of ternary compounds with the composition MIn_5S_7 (M = Na, K, Tl) [93, 94]. As described from these authors, the In^+ position in these compounds is not fully occupied by the replacing atom M^+. Especially for K^+ and Tl^+ it is easy to understand because these ions have nearly similar radii to In^+. Thus the formula of these solids has to be given in the following form: $[M^+, In^+]\ [(In_2)^{4+}]\ 3[In^{3+}]\ 7[S^{2-}]$.

This structure type can be regarded as a series of repeating construction units. Considering a structure projection along [010], one can see that this structure is built up by two repeating building units (Fig. 4.1a). The first one (Fig. 4.1b) consists of cis and trans edge-sharing InS_6 octahedra layers connected to trigonal prisms. Each of the prisms shares two corners and one edge with octahedra of the octahedral layers. This building unit is further connected to the second repeating unit (Fig 4.1c), which consists mainly of cis and trans edge-sharing octahedra strands bonded to chains of ethane analogues In_2S_6 fragments.

Further investigations of mixed valence compounds in the system M – In – Ch (Ch = S, Se) lead to two new structure types, respectively: MIn_5S_6 (M = Tl, K) [92, 95] and MIn_7Ch_9 (M = Rb, Cs; Ch =

S, Se,) [96, 197], each of them containing a characteristic and a common interlayer. In the case of MIn_5S_6 (Fig. 4.2) the characteristic interlayer consists of $S_3In\text{-}InS_4$ units, comparable to the $S_3In\text{-}InS_3$ dumbbells, with the difference that one In atom of the dumbbell is coordinated by four sulphur atoms instead of three.

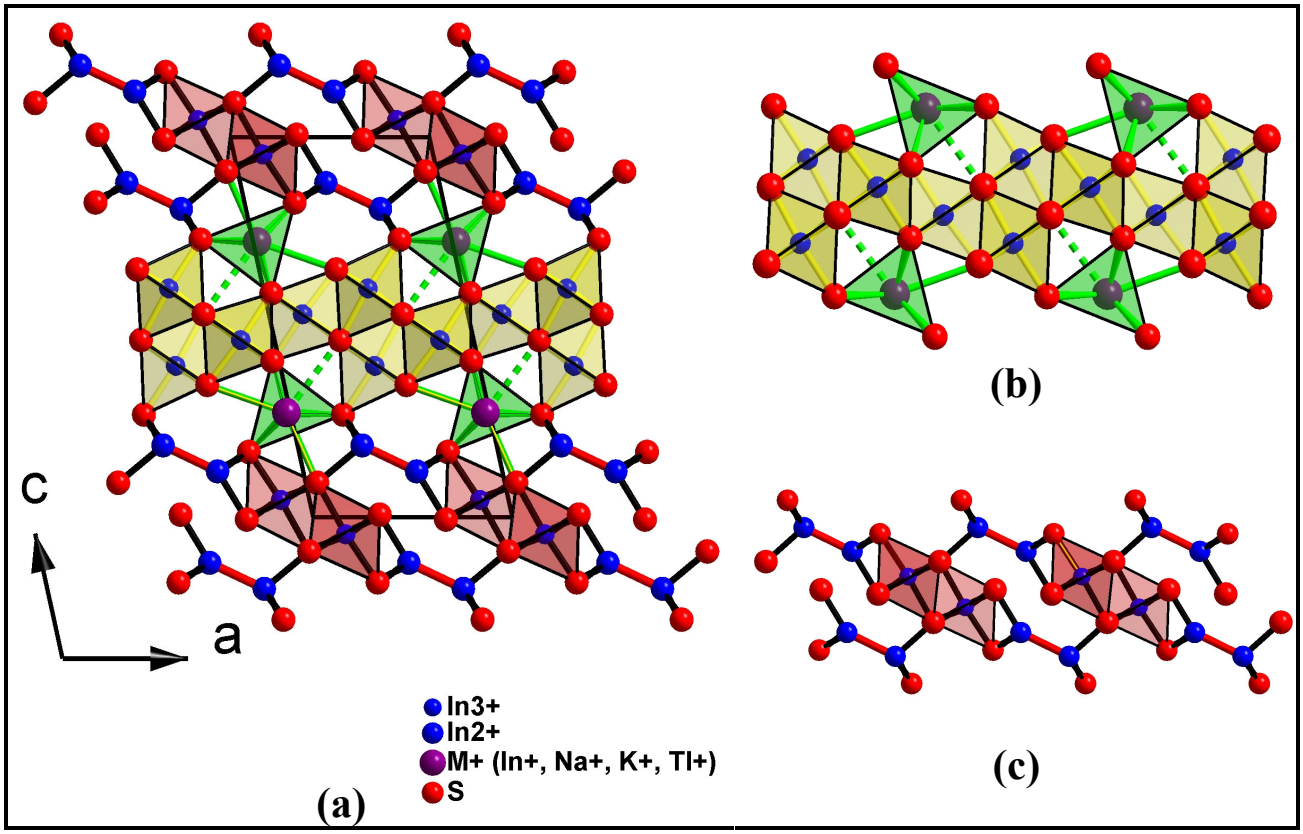

Fig. 4.1: (a) Crystal structure of MIn_5S_7 (M = In, Na, K, Tl), (b) construction unit build up by cis and trans edge-sharing InS_6 octahedra and trigonal prisms, (c) construction unit build up by cis and trans edge-sharing octahedra skeins bonded to chains of ethane analogues In_2S_6 fragments.

The $S_3In\text{-}InS_4$ units are further connected to trigonal prisms (Fig 4.2b) occupied by M^+ (and a small percentage of In^+). This building unit is bonded to the already known common unit reproducing the structure. The sum formula of the MIn_5S_6 structure type can be written in the following way: $[M^+]\ 2[(In_2)^{4+}]\ [In^{3+}]\ 6[S^{2-}]$.

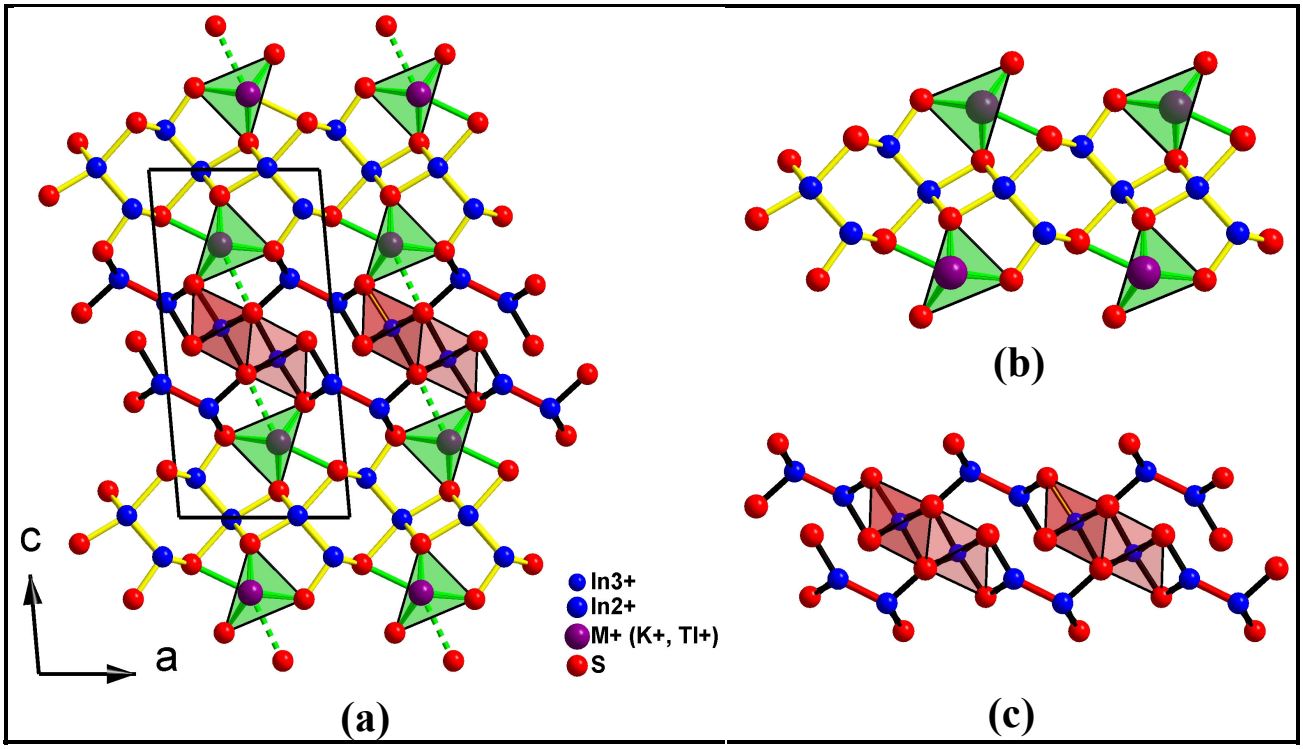

Fig. 4.2: Crystal structure of MIn_5S_6 (M = K, Tl). (b) Construction unit build up of S_3In-InS_4 dumbbells connected to trigonal prisms (c) common construction unit build up by cis and trans edge-sharing octahedra skeins bonded to chains of ethane analogues In_2S_6 fragments.

The third representative structure type of mixed valence indium chalcogenides, MIn_7Ch_9 (M = Rb, Cs; Ch = S, Se,), (Fig. 4.3) with its explicit sum formula $[M^+]\ 2[(In_2)^{4+}]\ 3[In^{3+}]\ 9[Ch^{2-}]$ [96, 97] again exhibits the above mentioned common unit. In this structure type the In^{3+} ions are simultaneously coordinated octahedrally and tetrahedrally, while the M^+ ions, because of their size, show a ninefold coordination (1 + 4 + 4). The characteristic interlayer contains InS_4 tetrahedra and MCh_9 polyhedra. The tetrahedra are centered by In^{3+} ions building InS_4 corner-sharing tetrahedra chains along [010]. The tetrahedra of the chains share common corners and edges with the M^+ polyhedra (Fig. 4.3b). Again the In^{2+} ions are part of the common interlayer (Fig. 4.3c) and have the same coordination as in the MIn_5Ch_7 structure type.

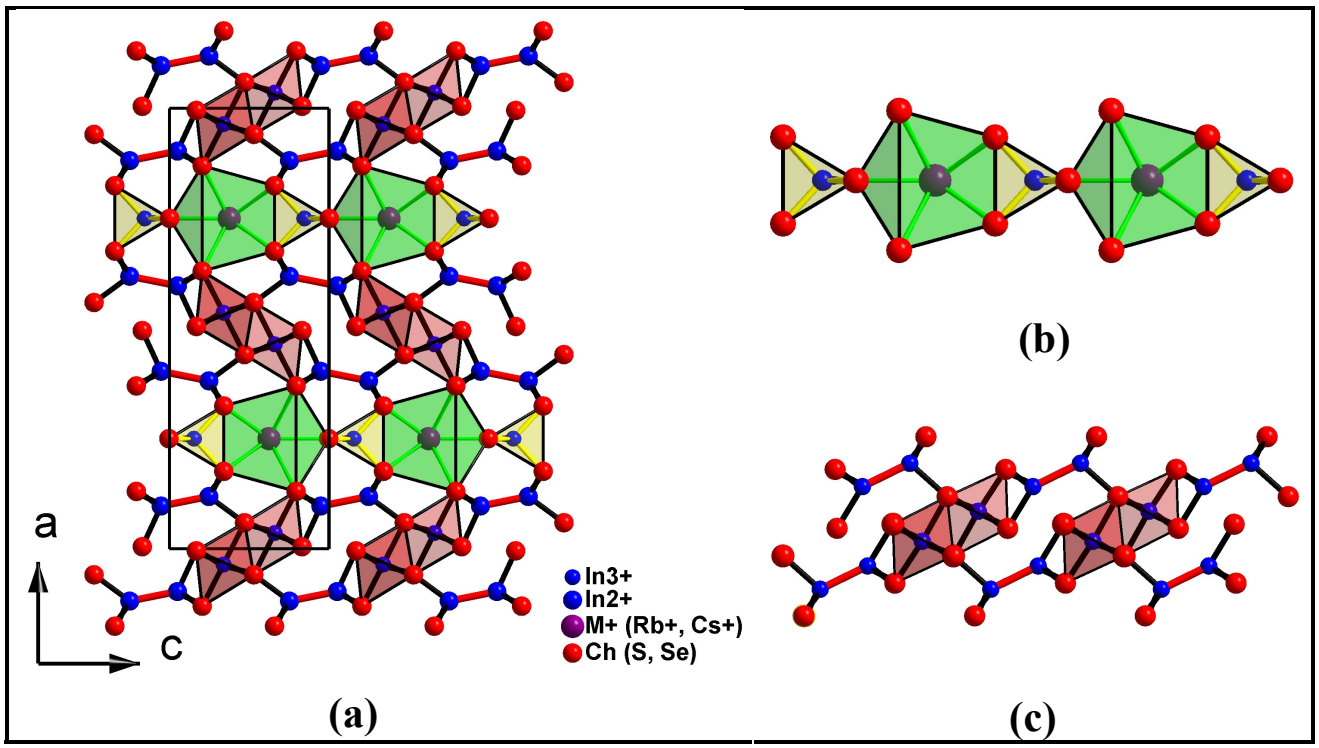

Fig. 4.3: (a) Crystal structure of MIn_7Ch_9 (M = Rb, Cs, Ch = S, Se), (b) construction unit build up by InS_4 corner-sharing tetrahedra chains which share corners and edges with MCh_9 polyhedra, (c) common construction kit build up of cis and trans edge-sharing octahedra skeins bonded to chains of ethane analogues In_2S_6 fragments.

In all the compounds mentioned above the common interlayer influences two lattice constants and thus the values of these lattice constants are nearly equivalent. The third one is defined by the characteristic interlayer of each structure type. This property is illustrated with three examples, each compound taken into consideration represents one of the mentioned structure types (see table 4.1) [93, 96].

Table 4.1: Lattice constants of three different compounds. Each one represents a structure type.

Lattice constants / Å	**KIn_5S_7** ($P2_1/m$)	**KIn_5S_6** ($P2_1/m$)	**$RbIn_7S_9$** ($Pmmn$)
a	**9.0847(4)**	**8.791(1)**	25.006(2)
b	**3.8872(1)**	**3.9070(3)**	**3.9082(3)**
c	17.3697(7)	17.504(2)	**8.9184(6)**

Investigating the pseudobinary systems MTe – MTeX (M = Al, Ga, In, X = Cl, Br, I) Paashaus [98] found intermediate ternary phases M_3Te_3X (M = Al, Ga, In, X = Cl, Br, I) (Fig. 4.4a) containing one dimensional "macromolecules" (Fig. 4.4b) in which ($Te_{3/3}M^{III}X$) trans corner-sharing tetrahedra chains share edges with cis and trans edge-sharing ($Te_{3/3}M_2^{II}Te_{3/3}$)-distorted "octahedra" (M_2-dumbells occupy "the centers" of the octahedra) skeins (Fig. 4.4b).

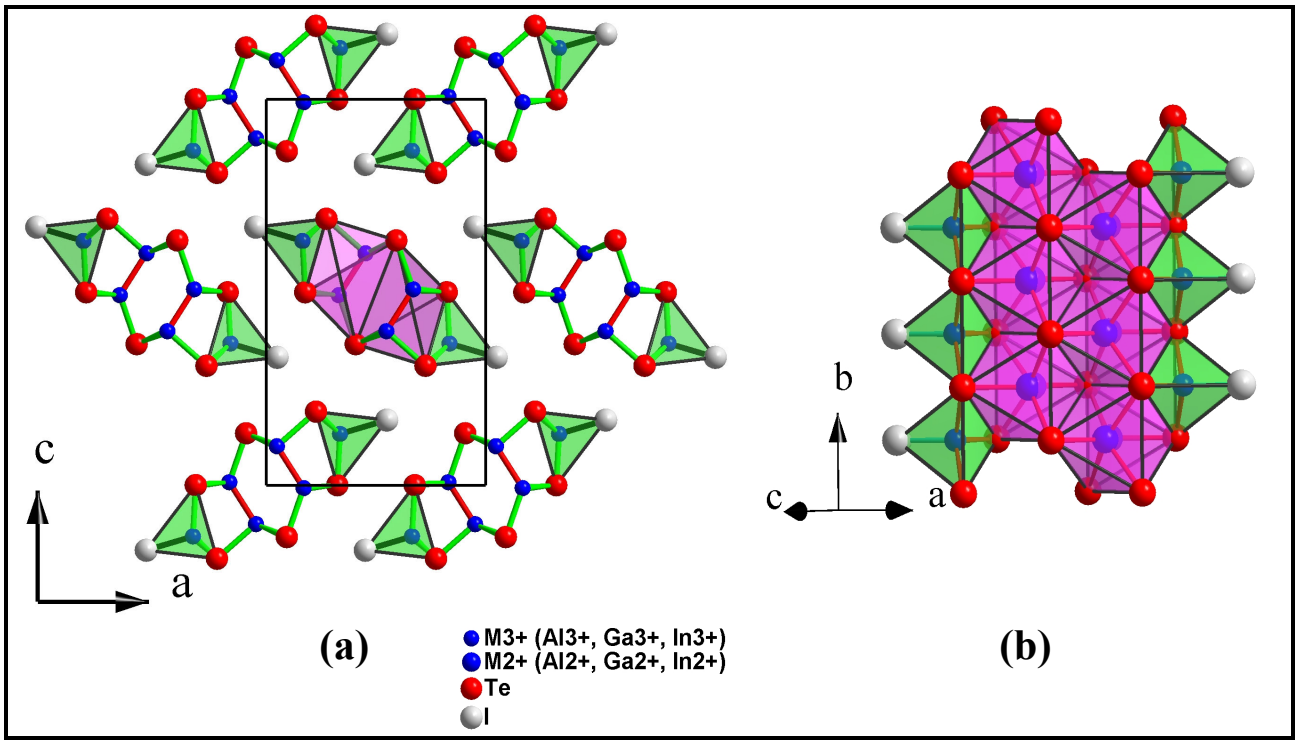

Fig. 4.4: (a) Crystal structure of the isotypic phases M_3Te_3X (M = Al, Ga, In, X = Cl, Br, I), projection along [010], (b) MTe_4 trans corner-sharing tetrahedra chains share edges with cis and trans edge-sharing octahedral skeins.

Writing the explicit formula of these compounds $[(M_2)^{4+}]$ $[M^{3+}]$ $3[Te^{2-}]$ $[X^-]$, the possible existence of other mixed valence ternary compounds is obvious. M^{3+} is tetrahedrally coordinated and the formal M^{2+} ions again build up M-M dumbbells which occupy distorted octahedral holes. In this structure type two structural elements of the previously discussed structure types can be observed, namely: trans corner-sharing tetrahedra chains (observed in the MIn_7Ch_9 type) and cis and trans edge-sharing ($Te_{3/3}Ga_2^{II}Te_{3/3}$)-distorted octahedra strands (observed in the common units of the above mentioned structures).

In the course of our investigations in the system In-Ch-X four further representatives of mixed valence indium chalcogenide halides have been obtained. These compounds show an equivalent sum formula, namely In_5Ch_5X (Ch = S, Se, X = Cl, Br). At the first glance, based on a comparison of lattice constants and the similar sum formulas one would assume the same structure for each of them with slightly different atomic positions deriving from the presence of different atoms. Detailed analysis revealed the existence of two significantly different independent structure types: the chloride-type (In_5Ch_5Cl) and the bromide-type In_5Ch_5Br (Ch = S, Se). Because of this structural difference each structure type will be treated separately and at the end a comparison of the structures will follow.

4.2 The compounds In_5Ch_5Cl (Ch = S, Se)

4.2.1 Preparation and properties of the samples

The syntheses of In_5Ch_5Cl was carried out by the reactions of a stoichiometric mixtures of the elements In, Ch (S, Se) and the binary compound $InCl_3$. $InCl_3$ was synthesized according to a procedure described by Templeton et al. [99]. The quartz ampoules were preheated and evacuated to remove traces of water adsorbed on the surface of the quartz ampoules. The elements In and Ch were transferred into the ampoules and the ampoules were repeatedly filled with argon and evacuated. The binary compound $InCl_3$ was added in an inert gas atmosphere (glove box). The ampoules were evacuated again. Before sealing the ampoules, their bottom part was immersed in liquid nitrogen to cool down the contents in order to avoid an early reaction. The samples were heated gradually up to 773 K and were held at this temperature for approximately one week.

Short ampoules (l = 4 cm; Ø = 1.2 cm) were preferred for these reactions, in order to avoid sublimation or transport reactions caused by a temperature gradient along the ampoule. The reactions in longer ampoules lead to a segregation of sulphur and InCl in the colder part of the ampoule.

In order to achieve bigger crystals, especially for single crystal measurements, a temperature program with a heating rate of 2 K/h was assumed. The samples were annealed for two weeks at 773 K and then slowly cooled down with a rate of 5 K/h up to 323 K. Reddish and dark brownish (for In_5Se_5Cl) needle-shaped crystals could be recognized even with naked eyes.

The preparation methods described above, often yielded inhomogeneous samples, especially in the case of In_5Ch_5Cl (Ch = S, Se). To avoid the presence of by-products, a third preparation procedure was applied. Instead of elements only binary compounds InCh [100, 101], In_2Ch_3 [102, 103] and InCl [98] were used as starting materials. The binary compounds were weighed in stoichiometric quantities in an inert gas atmosphere, mixed in an agate mortar and finally the mixtures were cold pressed. The obtained pellets were transferred into previously heated and evacuated quartz ampoules of 12 mm outer diameter. The ampoules were evacuated and sealed. The temperature program used to anneal them was the same as described above. The samples obtained in this way were nearly homogenous and bigger crystals were formed.

4.2.2 Characterisation

Under the optical microscope the obtained products In_5S_5Cl and In_5Se_5Cl consisted of fine red-brownish (in case of In_5S_5Cl) and dark-brownish (in case of In_5Se_5Cl) needle-shaped crystals with lengths up to some mm but with low diameters (max. 30 μm) (Fig. 4.5). The crystals of both compounds splice and inter-grow widely. They are accompanied by the binary solids In_6Ch_7(Ch = S, Se; black needle-shaped crystals) and in the case of In_5S_5Cl additionally In_2S_3 (red isometric crystals). The presence of these byproducts was proved by X-ray powder diffraction and EDX analysis.

The needle-shaped crystals of both compounds are investigated by SEM (scanning electron microscope).

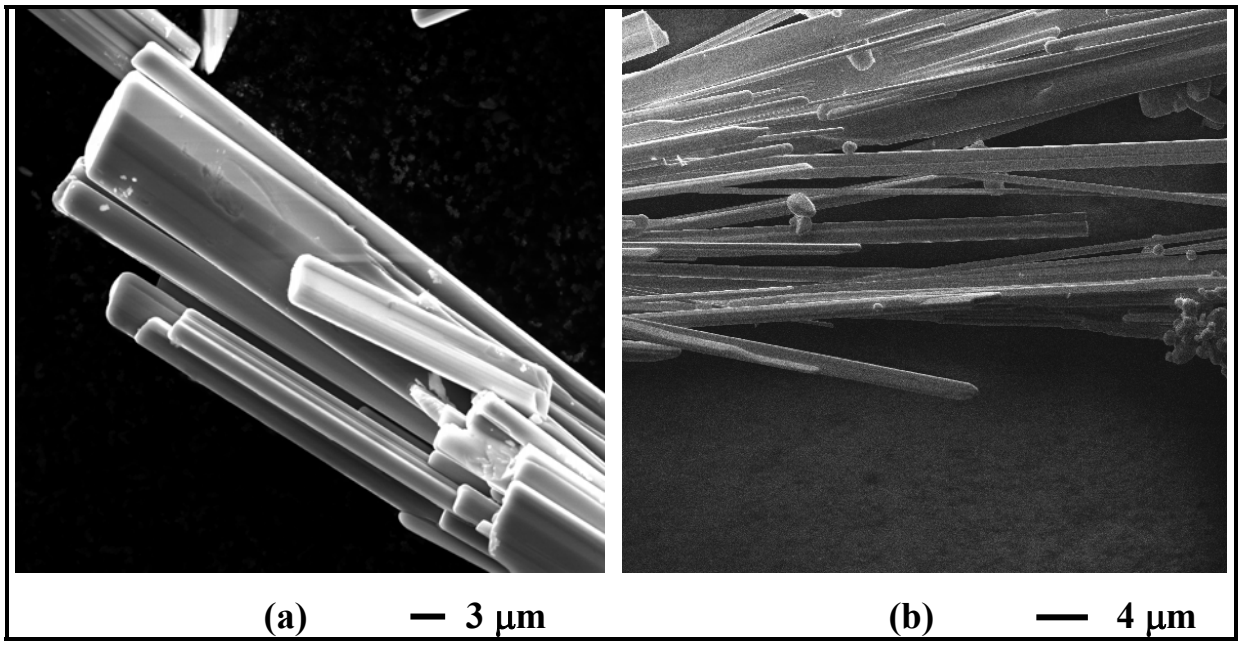

Fig. 4.5: SEM pictures of (a) In_5S_5Cl, (b) In_5Se_5Cl needles.

The qualitative elemental analysis with the EDX system shows for the red-brownish needle-shaped crystals the presence of indium, sulphur and chlorine while the darker needle-shaped crystals (In_6S_7) grown nearby contain only indium and sulphur (Fig. 4.7). For In_5Se_5Cl only the spectrum of the main product is shown (Fig. 4.6).

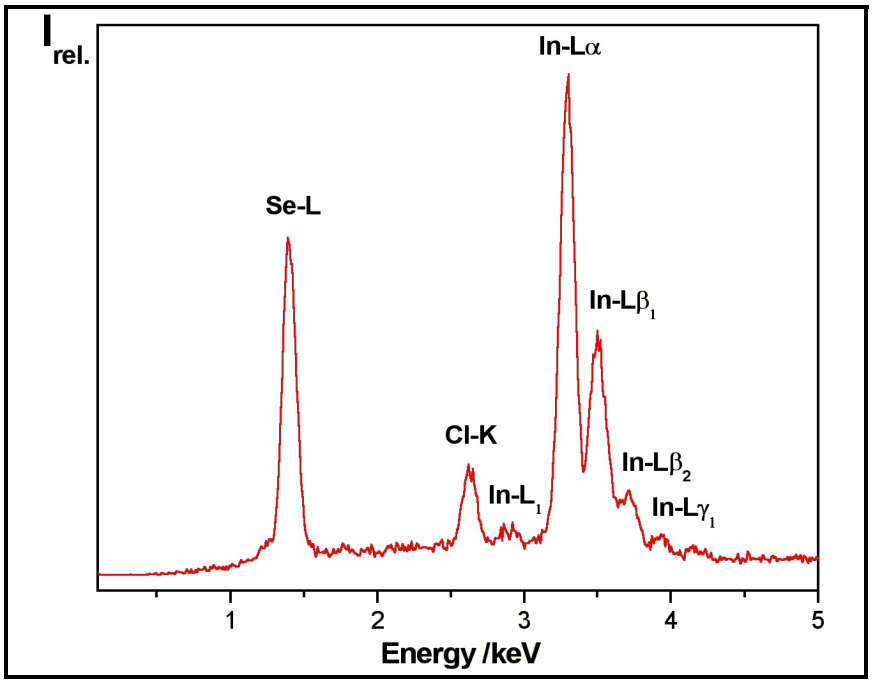

Fig. 4.6: EDX spectra of dark brown needle-shaped crystals of In_5Se_5Cl.

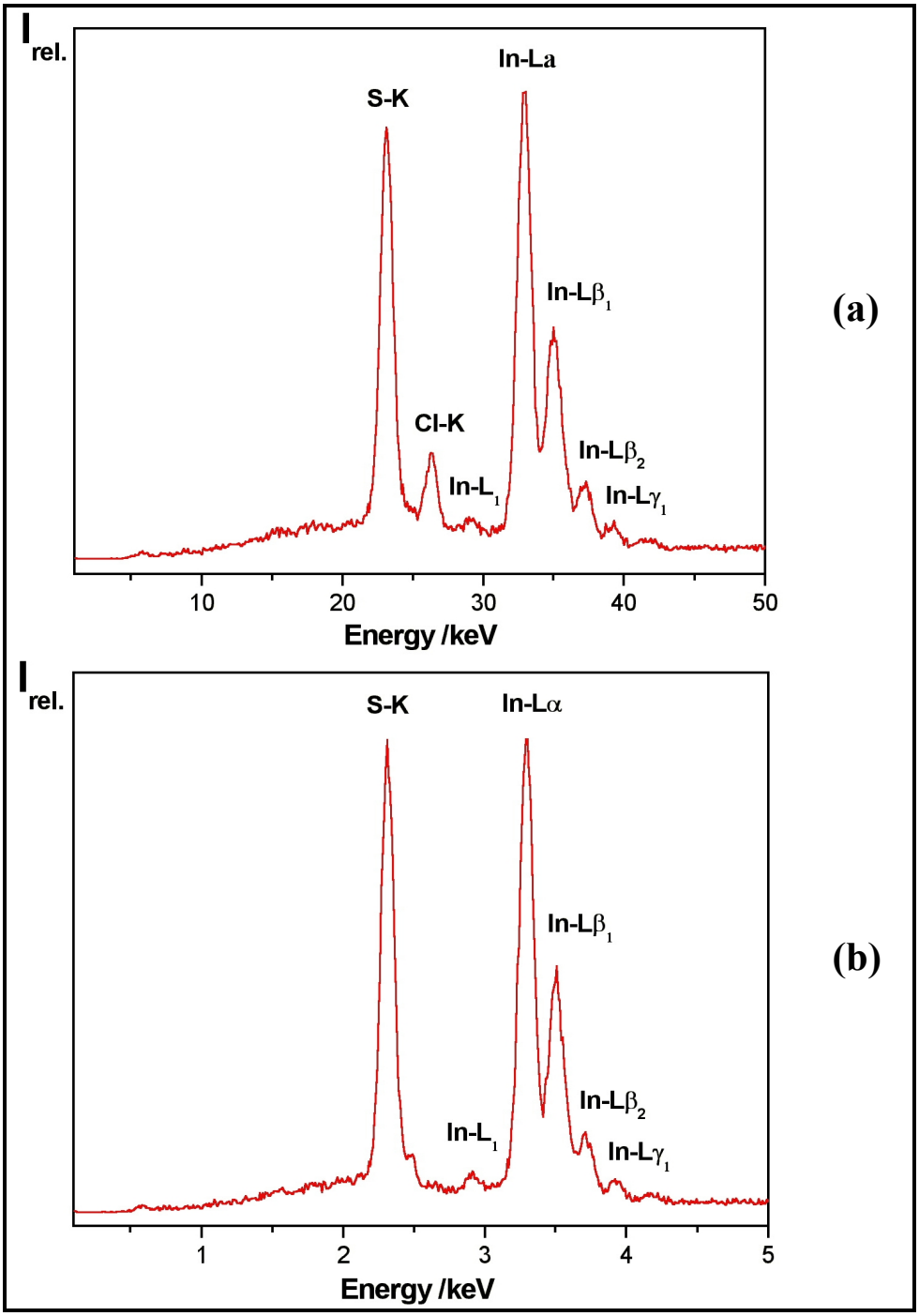

Fig. 4.7: EDX spectra of needle-shaped crystals (a) In_5S_5Cl (red crystals), (b) In_6S_7 (black crystals grown in the same ampoule).

A bulk of crystals from both samples was pulverized in an agate mortar and measured with the D5000 powder diffraction system. The measured diffraction patterns show good agreements with the calculated (single crystal data see below) diffraction patterns (Figures 4.8, 4.10).

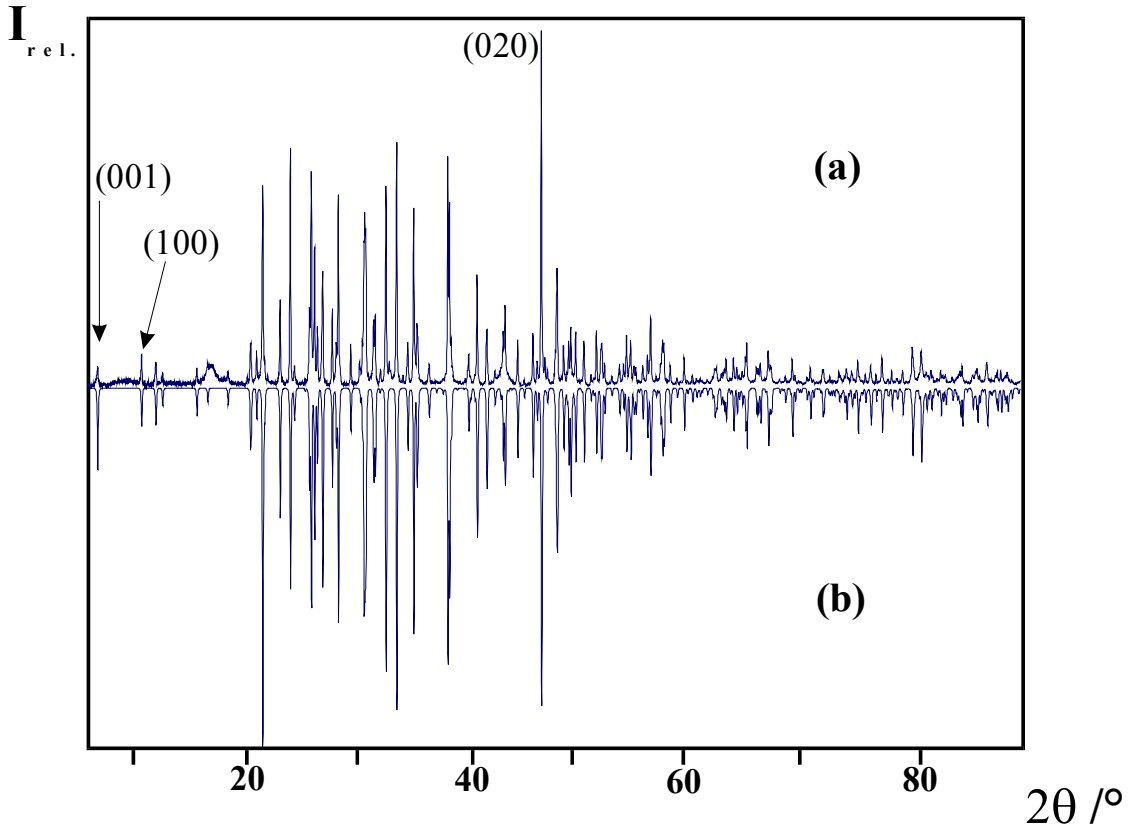

Fig. 4.8: Comparison of a measured powder diffraction pattern of In_5S_5Cl (a) with the powder pattern of In_5S_5Cl calculated from single crystal data (b).

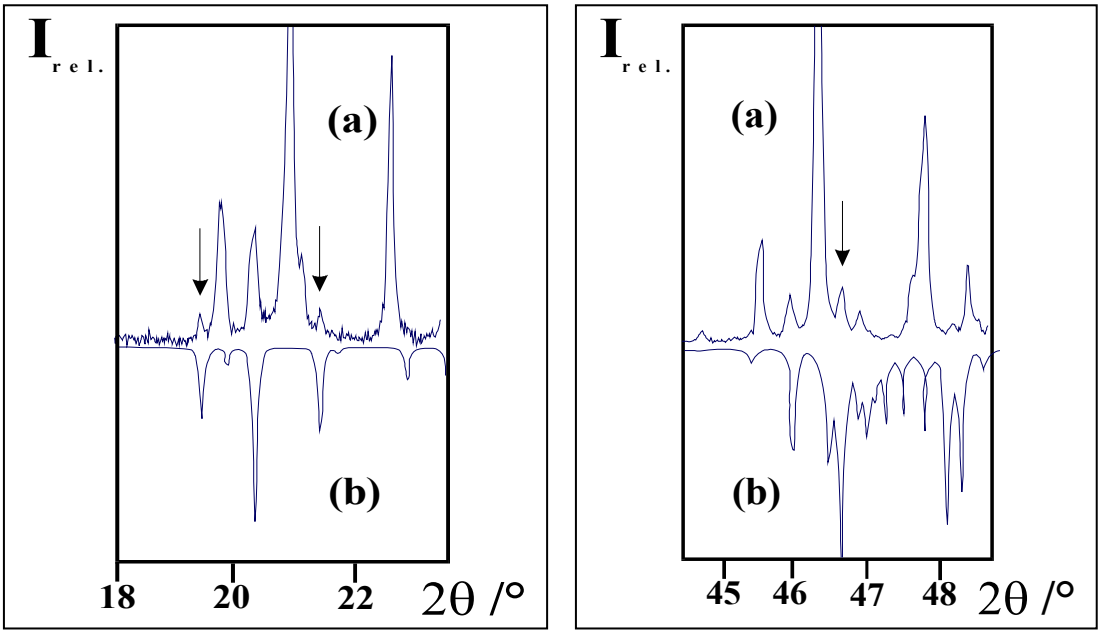

Fig. 4.9: Comparison of sections of a measured powder pattern of In_5S_5Cl (a) with the calculated powder pattern of In_6S_7 (b). The reflections marked by arrows belong to In_6S_7.

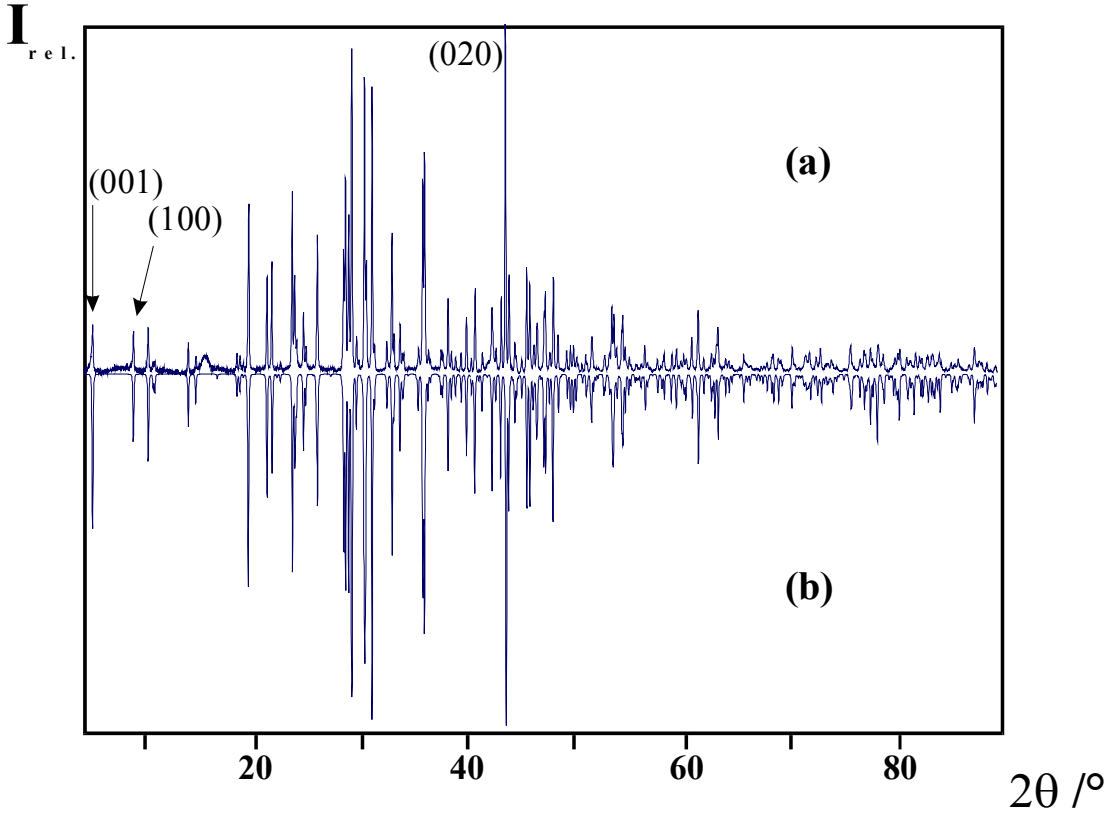

Fig. 4.10: Comparison of a measured powder diffraction pattern of In_5Se_5Cl (a) with the powder pattern of In_5Se_5Cl calculated from single crystal data (b).

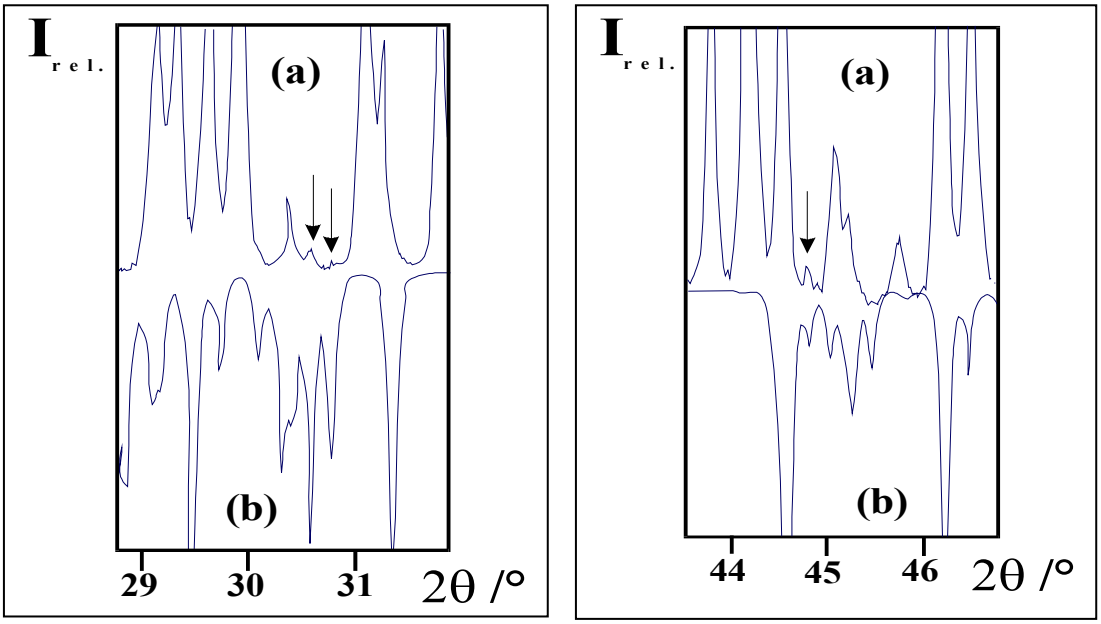

Fig. 4.11: Comparison of sections of a measured powder pattern of In_5Se_5Cl (a) with the calculated powder pattern of In_6Se_7 (b). The reflections marked by arrows belong to In_6Se_7.

The measured powder patterns of both compounds display some reflections deriving from impurities observed in the EDX measurements too, e.g. In_6S_7 in case of In_5S_5Cl and In_6Se_7 in case of In_5Se_5Cl (Fig. 4.9, 4.11).

Due to the needle shape of the crystals with a growth direction along [010] (Fig. 4.12) the powder diffraction measurements were influenced by texture effects. The measurements with the flatbed sample holder displayed increased intensities for the reflections with the indexes 0k0. In contrast to that, the intensities of the reflections with the indexes h00 and for 00l are decreased. This fact is demonstrated especially by the reflections with the indexes 001 and 020 in the case of In_5S_5Cl (Fig. 4.8) and by the reflection with the index 001 in the case of In_5Se_5Cl (Fig. 4.10).

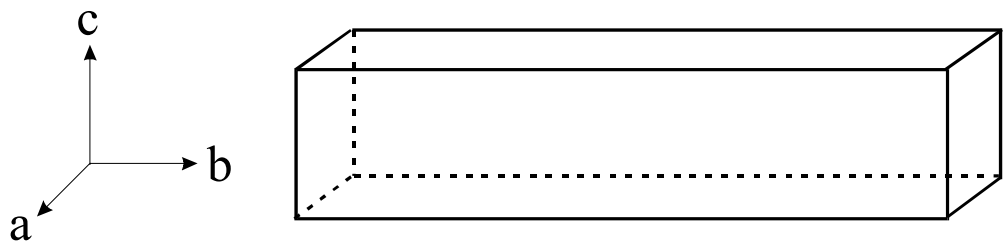

Fig. 4.12: Sketch of a needle-shaped crystal.

The reflections of both compounds could be indexed with a monoclinic primitive cell. The refined lattice parameters from the powder diffraction measurements for both analysed compounds are listed in the table 4.2. The list with the refined cell parameters of In_5Se_5Cl and the indexed lines with the respective intensities is given in appendix (table 8.4).

Table 4.2: Refined lattice constants from powder patterns for the compounds, In_5S_5Cl and In_5Se_5Cl.

Compound	**a** /Å	**b** /Å	**c** /Å	**β** /°	**V** /Å^3
In_5S_5Cl	8.9376(6)	3.9165(2)	14.984(1)	93.663(5)	523.42(4)
In_5Se_5Cl	9.2391(3)	4.0951(1)	15.2920(6)	92.743(3)	577.91(2)

4.2.3 Thermal analyses of In_5S_5Cl and In_5Se_5Cl

The results of the thermal analysis for the new solids are presented in Fig. 4.13.

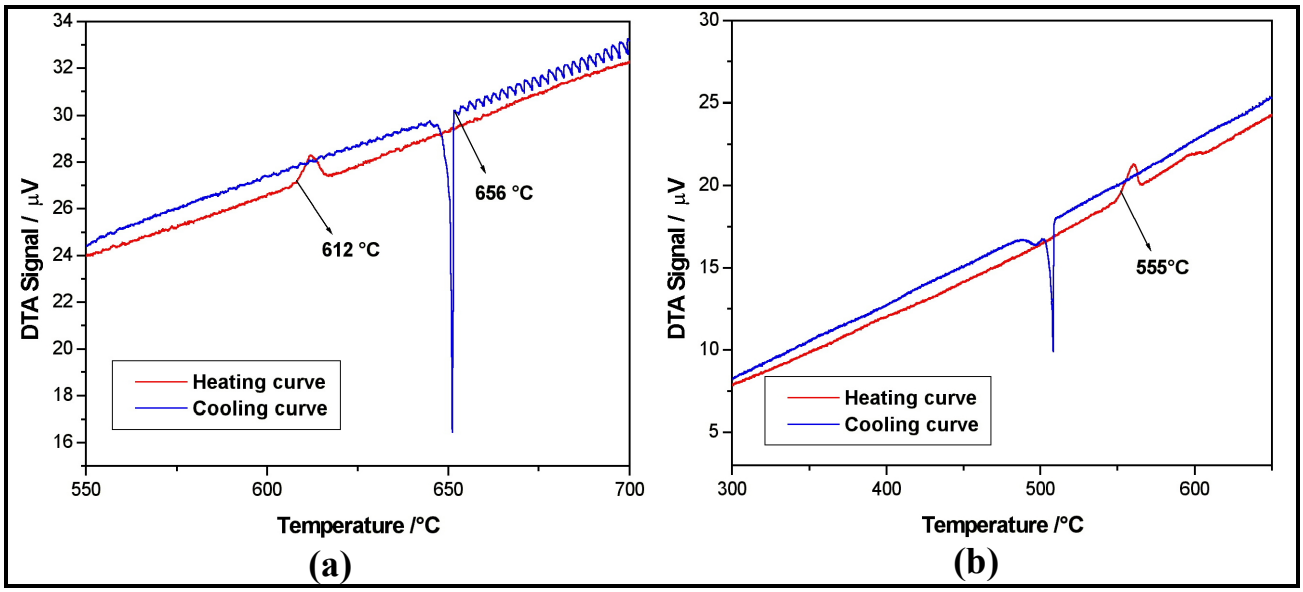

Fig. 4.13: Sections from DTA-measurement of the compounds a) In_5S_5Cl and b) In_5Se_5Cl. The heating curve shows an endothermic effect (a) at 612 °C for In_5S_5Cl and (b) at 555 °C for In_5Se_5Cl. The cooling curve shows two exothermic effects in case of In_5Se_5Cl.

In_5S_5Cl and In_5Se_5Cl are relatively stable in air. The melting behaviour of both compounds, In_5S_5Cl and In_5Se_5Cl was investigated by means of differential thermal analysis (DTA). Sections of the DTA measurements of these compounds are presented in fig. 4.13. The heating curve in case of In_5S_5Cl displays an endothermic effect at approx. 612°C (Fig. 4.13 a). Its cooling curve displays an exothermic effect at 655°C which corresponds to an unusually high solidifying temperature. To investigate this phenomenon, the X-ray powder diffraction of the post-DTA sample was performed. It displayed mainly the presence of In_6S_7 (m.p. 656°C [89]).

In the case of In_5Se_5Cl (Fig. 4.13 b), the heating curve displays two effects. One endothermic effect at approximately 555 °C followed by a broad effect. The cooling curve presents two exothermal effects at 510 and 502°C respectively. The powder pattern of the post-DTA sample confirmed only the presence of In_5Se_5Cl.

To endorse these investigations, high temperature powder diffractions of both compounds were carried out. These investigations (see chapter 5) displayed a gradual decompositions to In_2S_3 and In_2Se_3 for In_5S_5Cl and In_5Se_5Cl respectively. Based on these analyses an incongruent melting behaviour can be concluded for both compounds.

4.2.4 Single crystal investigation of In_5Ch_5Cl (Ch = S, Se)

For the single crystal investigation of In_5S_5Cl and In_5Se_5Cl, needle-shaped crystals from both compounds were chosen under an optical microscope and fixed with the help of grease on the top of a glass capillary. The capillary was fixed on a goniometer head and the measurement was carried out on a STOE IPDS diffraction system.

4.2.5 Single crystal investigations of In_5S_5Cl

The obtained measured data from the IPDS system were further analysed by the STOE IPDS Program package [P1]. After visualising the reflections with the program EXPOSE [P2], the reflections were indexed (INDEX [P3] and CELL [P4]) in a monoclinic cell. A closer inspection of the reciprocal space with the help of the program RECIPE [P5] showed that not all reflections could be indexed in this monoclinic cell.

The remaining reflections were indexed again, showing the already found monoclinic lattice but with a different orientation matrix in comparison to the first one. The program RECIPE [P5] displays both lattices in the reciprocal space overlapping and interpenetrating to each other (Fig. 4.14). The investigated crystal In_5S_5Cl consisted of two individuals with comparable intensities.

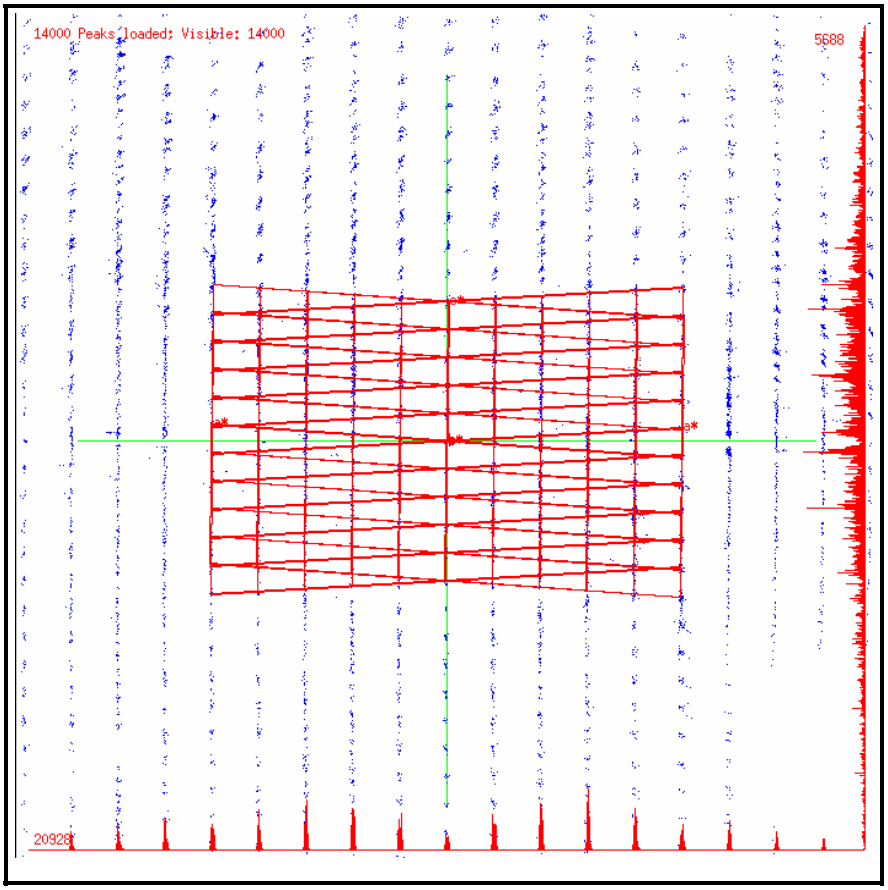

Fig. 4.14. Projection of the reciprocal space along [010]* for a twinned crystal of In_5S_5Cl. The measured reflection positions are exhibited as blue points. The penetrating reciprocal lattices corresponding to the twinning individuals are highlighted. The volume ratio between the twin individuals was approximately 1:1.

Several crystals of In_5S_5Cl were measured and the obtained reflections positions in the reciprocal space were investigated for particularities. All of them presented similar systematic twinning.

Using the program SPACE [P6], reciprocal planes (*hkl*) were calculated from imaging plate data. The obtained results revealed that the reflections (*h0l)* with $h = 5n$ (n = 0, 1, 2, …) superimpose (Fig. 4.15) while all further reflections (*h0l*, $h \neq 5n$) of both twinning individuals appear separately, indicating that, the twinning can be described as a twinning by reticular pseudo-merohedry.

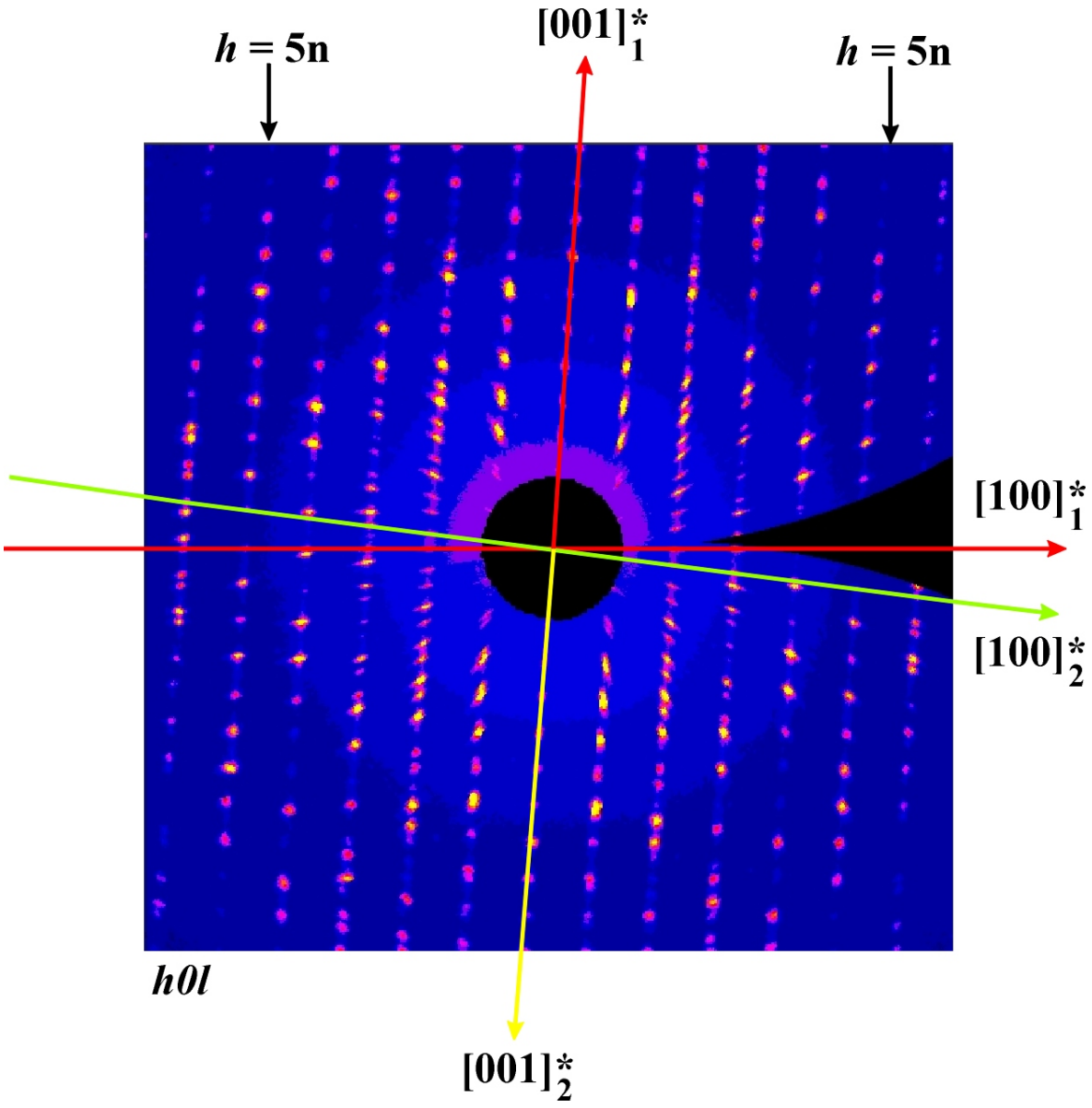

Fig. 4.15: Simulated precession of the plane (*h0l*) calculated from the obtained data by the program SPACE [P6]. The reflections (yellow dots) (hkl) *h* = 5n (n = 0, 1, 2…) overlap.

The penetrating reciprocal lattices of the twin individuals based on the analysis of the reciprocal space and on the information delivered from the calculated reciprocal planes about the coinciding reflections (*h0l*) *h* = 5n are presented additionally in figure 4.16.

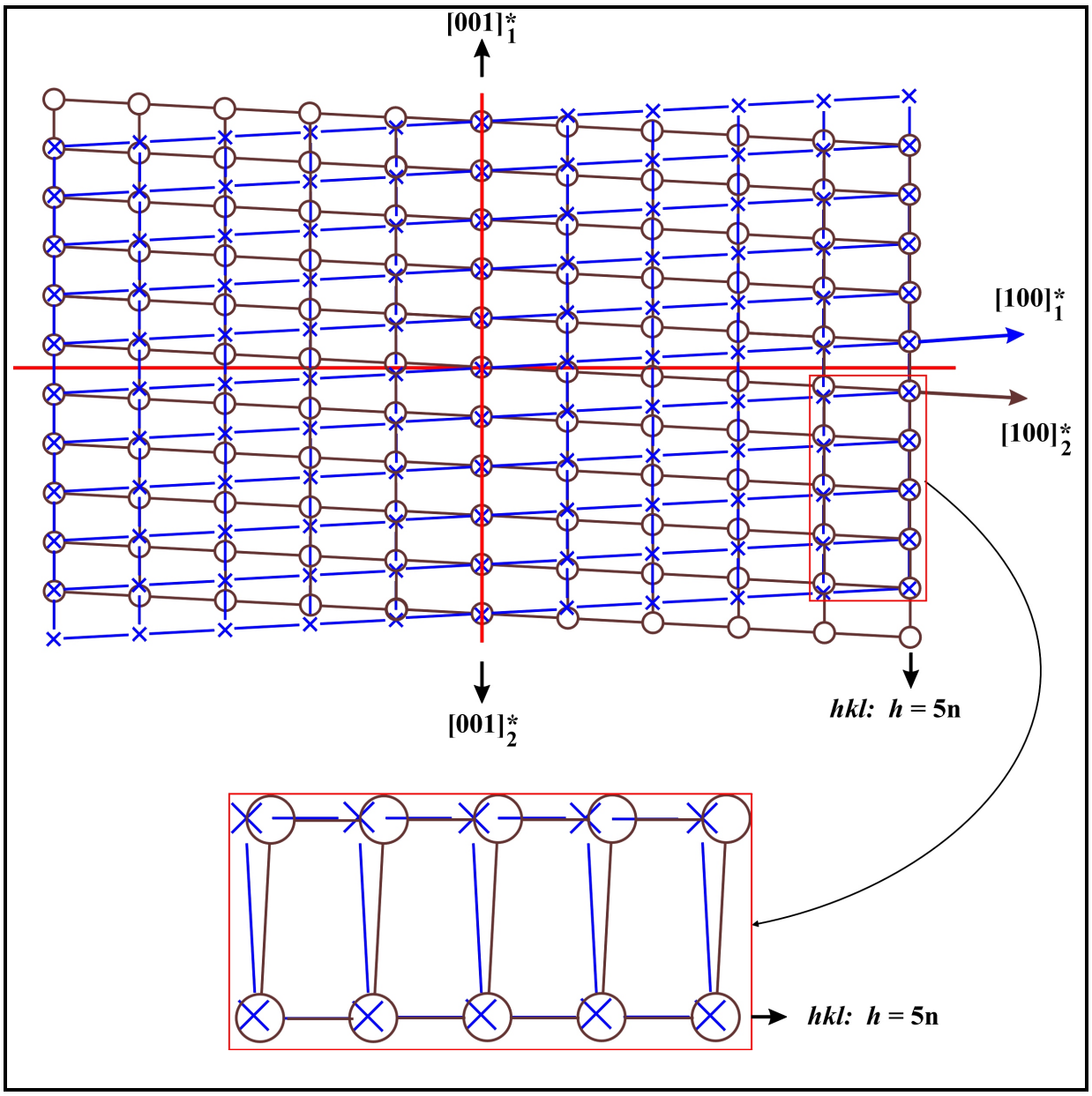

Fig. 4.16: The penetrating reciprocal lattices of the twinning individuals of In_5S_5Cl which can be described as a twinning by reticular pseudo-merohedry. The reflections hkl, $h = 5n$ don't coincide exactly (the magnified section within the red rectangle displays this fact), while the reflections *hkl*, $h \neq 5n$ are presented separately. (**O:** reflections belonging to the first individual (*hkl*, $h \neq 5n$), **x:** reflections belonging to the second individual (*hkl*, $h \neq 5n$), **⊗:** nearly overlapping reflections (*hkl*, $h = 5n$, $n = 0, 1, 2, \ldots$).

The data were integrated using the program TWIN [P7] which suppressed the completely or partly overlapping reflections of the twin domains leading to an incomplete data set. The obtained data sets of both individuals were corrected for Lorenz and polarisation effects. The crystal-face indexation was performed with a CCD-camera [P8] and optimised using the program X-SHAPE [P9]. The numerical absorption correction based on an adequate number of symmetrically equivalent reflections was done using the program X-RED [P10].

The row conditions for reflections (*0k0*) with $k = 2n$ represent a screw axis parallel to [010] ($2_1 \parallel b$). This condition for reflection leads to two different space groups, respectively: $P2_1$ (non centrosymmetric) and $P2_1/m$ (centrosymetric). A structure solution performed by the program SHELXS [P11] using direct methods is possible in both space groups, but the best figures of merit are obtained after the refinement (SHELXL [P12]) in the space group $P2_1/m$. The presentation of the distribution of the normalized structure factors by means of E-statistic and N(Z)-test suggested the centrosymetric space group $P\ 2_1/m$.

After the structure refinement, the R-values ($R_1 = 0.0982$, $wR_2 = 0.2348$) and the Fourier residuals ($\rho_{max.} = 3.406$ e/Å^3, $\rho_{min.} = -4.401$ e/Å^3) were relatively high. This probably arise from the obtained incomplete data set (a huge number of the overlapping reflections of both twin individuals were cancelled during the simultaneous integration) and from a variety of crystal defects discussed in details below.

The measuring parameters and important results of the last refinement cycle are listed in table 4.3. The final positional coordinates of the atoms together with their standard deviations, the isotropic and anisotropic temperature factors are listed in tables 4.4 and 8.5 (in appendix).

Table 4.3: Important parameters for the X-ray single crystal investigation of In_5S_5Cl.

Sum formula	**In_5S_5Cl**
Formula weight /gmol^{-1}	M = 769.85
Temperature /K	T = 293(2)
Wavelength /Å	Mo$K\alpha$, γ = 0.71073
Space group	$P2_1/m$ (No. 11)
Crystal dimension /mm	0.48 × 0.03 × 0.01
Cell dimensions /Å, /°	a = 8.927(1) b = 3.9062(5) c = 14.951(2) β = 93.48(2)
Volume /Å^3	V = 520.4(1)
Formula units per unit cell	Z = 2
Density (calculated) /gcm^{-3}	ρ = 4.913
Absorption coefficient /mm^{-1}	μ = 12.102
F(000)	684
Diffractometer	IPDS (Stoe), oriented graphite monochromator
Scan type	φ
Measured θ range /°	3.45 ≤ θ ≤ 31.68
Index ranges	-12 ≤ h ≤ 13 -5 ≤ k ≤ 5 -21 ≤ l ≤ 22
Measured reflections	2056
Independent reflections	1044 (R_{int} = 0.0725)
Completeness to θ /%	52.5
Absorption correction	Numerical [P8, P10]
Structure solution	Direct methods [P11]
Structure refinement	Full-matrix least-squares on F^2 [P12]
Data/restraints/parameters	1044 / 0 / 68
Goodness-of-Fit on F^2	1.225
R values [$I \geq 2\sigma(I)$]	R_1 = 0.0840, wR_2 = 0.2288
R values (all data)	R_1 = 0.0982, wR_2 = 0.2348
Final Fourier residuals / eÅ^{-3}	$\rho_{max.}$ = 3.406, $\rho_{min.}$ = -4.401

Table 4.4: Position, equivalent isotropic displacement parameter U_{eq} and occupancy factors for In_5S_5Cl. The standard deviations are given in brackets.

Atom	Position	*x*	*y*	*z*	U_{eq} /Å^2	*sof*
In1	2e	0.6575(3)	¾	0.4455(2)	0.0096(6)	1
In2	2e	0.1344(4)	¾	0.0638(2)	0.0136(7)	1
In3	2e	-0.0423(4)	¼	0.3565(2)	0.0161(7)	1
In4	2e	0.2360(3)	¼	0.2914(2)	0.0111(7)	1
In5	2e	-0.3829(5)	¼	0.1575(3)	0.030(1)	0.96(2)
Cl	2e	0.327(1)	¼	0.0055(7)	0.014(2)	1
S1	2e	0.467(1)	¼	0.3994(7)	0.008(2)	1
S2	2e	0.834(1)	¼	0.5024(7)	0.009(2)	1
S3	2e	0.318(1)	¾	0.2002(7)	0.008(2)	1
S4	2e	-0.033(1)	¼	0.1023(7)	0.010(2)	1
S5	2e	0.792(1)	¾	0.2983(7)	0.011(2)	1

The occupancy of each atomic position was proved and resulted fully occupied within the threefold calculated standard deviation. The above presented data were obtained from the last refinement cycle where all the occupancy factors except In5 were set to full occupancy. In5 is also fully occupied within the calculated standard deviation (see table 4.4).

4.2.6 Single crystal investigation of In_5Se_5Cl

Beside the structural investigations performed on the crystals of the compound In_5S_5Cl, similar investigations were carried out on the dark-brown crystals of In_5Se_5Cl. The comparison of the lattice parameters obtained from the powder diffraction measurements (see table 4.2) leads to the assumption that In_5Se_5Cl crystallises isotypic to In_5S_5Cl.

For In_5Se_5Cl, similar to In_5S_5Cl, several crystals were measured on the IPDS. The collected data sets were analysed for anomalies by the program RECIPE [P5]. The measured crystals of In_5Se_5Cl presented systematic reticular pseudo-merohedrical twinning similar to In_5S_5Cl.

For the data set obtained from the crystal of In_5Se_5Cl it was proceded in the same way as in the case of In_5S_5Cl. The data were integrated by using the program TWIN [P7]. The overlapping reflections were detected automatically and cancelled from the data set. The measured crystal of In_5Se_5Cl consisted of two twinned domains with an approximate volume ratio between the main domain and the twinned domain of 3:1.The intensities of the main individual were corrected for Lorenz and polarisation effects. The crystal-face indexation was performed with a CCD-camera [P8] and optimised using the program X-SHAPE [P9]. The numerical absorption correction, based on an adequate number of symmetrical equivalent reflections, was done using the program X-RED [P10].

The reflection conditions for reflections *0k0* with $k = 2n$ represent a screw axis parallel to [010] ($2_1 \parallel b$). leading to the space groups $P2_1$ and $P2_1/m$. The final refinement data presented also high R-values ($R_1 = 0.0860$, $wR_2 = 0.2346$) and high Fourier residuals ($\rho_{max.} = 3.980$ e/Å^3, $\rho_{min.} = -4.532$ e/Å^3) which can be attributed to the incomplete data set and to crystal defects. The measuring parameters and the results of the last refinement cycle are listed in table 4.5. The final positional coordinates of the atoms together with their standard deviations, the isotropic and anisotropic temperature factors are listed in tables 4.6 and 8.6 (in appendix).

Table 4.5: Important parameters for the X-ray single crystal investigation of In_5Se_5Cl.

Sum formula	**In_5Se_5Cl**
Formula weight /gmol^{-1}	M = 1004.35
Temperature /K	T = 293(2)
Wavelength /Å	Mo$K\alpha$, γ = 0.71073
Space group	$P2_1/m$ (No. 11)
Crystal dimension /mm	0.46 × 0.03 × 0.02
Cell dimensions /Å, /°	a = 9.23058(8) b = 4.0866(3) c = 15.294(2) β = 92.47(1)
Volume /Å^3	V = 576.36(9)
Formula units per unit cell	Z = 2
Density (calculated) /gcm^{-3}	ρ = 5.787
Absorption coefficient /mm^{-1}	μ = 25.809
F(000)	864
Diffractometer	IPDS (Stoe), oriented graphite monochromator
Scan type	φ
Measured θ range /°	$3.39 \le \theta \le 30.35$
Index ranges	$-12 \le h \le 11$ $-5 \le k \le 5$ $-21 \le l \le 21$
Measured reflections	5209
Independent reflections	1515 (R_{int} = 0.1383)
Completeness to θ /%	77.1
Absorption correction	Numerical [P8, P10]
Structure solution	Direct methods [P11]
Structure refinement	Full-matrix least-squares on F^2 [P12]
Data/restraints/parameters	1515 / 0 / 68
Goodness-of-Fit on F^2	1.101
R values [$I \ge 2\sigma(I)$]	R_1 = 0.0790, wR_2 = 0.2289
R values (all data)	R_1 = 0.0860, wR_2 = 0.2346
Final Fourier residuals / eÅ^{-3}	$\rho_{max.}$ = 3.980, $\rho_{min.}$ = -4.532

Table 4.6: Position, equivalent isotropic displacement parameter U_{eq} and occupancy factors for In_5Se_5Cl. The standard deviations are given in brackets.

Atom	Position	*x*	*y*	*z*	U_{eq} /Å^2	*sof*
In1	2e	0.6599(2)	¾	0.4451(1)	0.0140(4)	1
In2	2e	0.1308(2)	¾	0.0633(1)	0.0209(5)	1
In3	2e	-0.0472(2)	¼	0.3484(1)	0.0173(5)	1
In4	2e	0.2312(2)	¼	0.2915(1)	0.0122(4)	1
In5	2e	**-0.3947(3)**	¼	**0.1456(2)**	**0.0370(9)**	**0.94(1)**
Cl	2e	0.3267(6)	¼	0.0027(4)	0.023(1)	1
Se1	2e	0.4671(2)	¼	0.3966(1)	0.0106(5)	1
Se2	2e	0.8374(2)	¼	0.5031(2)	0.0126(5)	1
Se3	2e	0.3201(2)	¾	0.1964(2)	0.0112(5)	1
Se4	2e	-0.0414(2)	¼	0.1040(2)	0.0150(5)	1
Se5	2e	0.7892(2)	¾	0.2902(2)	0.0130(5)	1

For the structure refinement of In_5Se_5Cl it was proceded in the same way as for In_5S_5Cl. A slight under occupancy of In5 (*s.o.f.* = 0.94) reveals the composition $In_{4.96}Se_5Cl$ (table 4.6). A similar case is observed in the structure of In_6S_7 [92] where In5 corresponding to In^+ shows an occupancy of *sof* = 0.88 and therefore the composition $In_{5.88}S_7$. In this compound and in In_5S_5Cl, $(In_2)^{4+}$-species have a similar coordination as In^+ (see below), thus, it is supposed that a partial occupation of In5 position might be addressed to this species.

These particular (unusual) crystal structures of the mixed valence indium chalcogenide halides In_5Ch_5Cl (Ch = S, Se) possess a comparable monoclinic metric and are isotypic. They crystallise in the space group $P2_1/m$. All the atoms are located on a mirror plane, special position 2e with y = ¼ and ¾ respectively.

The observation of the isotropic parameters in both compounds, displays that In3 and especially In5 show significantly higher equivalent isotropic displacement parameter in comparison to the other atoms. Similarly, enhanced displacement parameters for In3 and In5 corresponding respectively to formal In_2^{4+} and In^+ are observed and discussed by Walther [92] in the course of investigation about the compounds In_6S_7 and In_6Se_7.

4.2.6.1 The chlorine position in the structure of In_5Ch_5Cl (Ch = S, Se)

The localisation of chlorine atoms in the structure of In_5Ch_5Cl based on the X-ray single crystal investigation is almost impossible due to the small difference in the numbers of electrons between S and Cl. To solve this problem, the single crystal investigation of In_5Se_5Cl is considered where the obvious difference in the number of electrons for Se and Cl allows the distiction. The distribution of the chlorine atoms in the structure agrees with the explanation based on the concentration of the local positive and negative charge (see the explanation about the coordination of In1, In2) and is considered to be the same for In_5S_5Cl.

4.2.7 Structure description of In_5Ch_5Cl (Ch = S, Se)

In_5Ch_5Cl respectively: In_5S_5Cl and In_5Se_5Cl crystallise monoclinic in the space group $P2_1/m$ (No. 11) with two formula units in the unit cell. Both of them are mixed valence compound, where, indium occurs in three different oxidation states, In^+, formal In^{2+} and In^{3+} respectively together with Ch^{2-} and Cl^-. The explicit formula of these compounds can be written in the following way:

$$\mathbf{In_5Ch_5Cl = [In^+]\ [(In_2)^{4+}]\ 2[In^{3+}]\ 5[Ch^{2-}]\ [Cl^-]}$$

The three different indium species exhibit characteristic local coordinations. For a better understanding of the structure, the direction along [010] is considered (Fig. 4.17a). In^+ occupies three capped trigonal prismatic holes. The trigonal prims share faces with each other, building chains along *b* (Fig. 4.17b). The In^{2+} builds with its neighbored In^{2+} covalent bonded dumbbells $(In_2)^{4+}$, where each indium atom is further coordinated by three chalcogenide atoms forming ethane analogue units in eclipsed conformation (Fig. 4.17d). In^{3+} is octahedrally coordinated. The octahedra build cis and trans edge-sharing double octahedra chains along the *b* axis. In this structure type, two kinds of edge-sharing octahedra double-chains are observed.

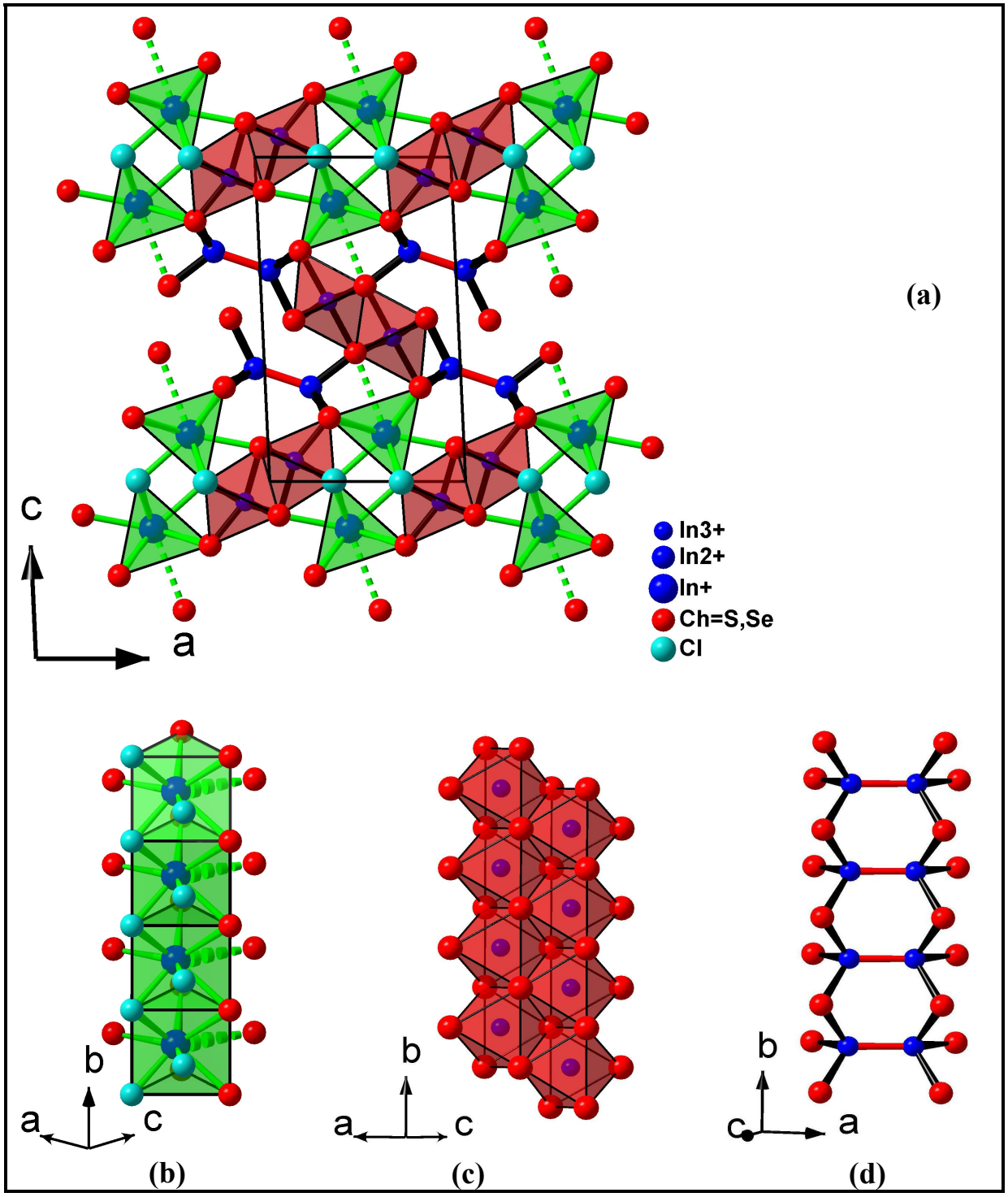

Fig. 4.17: (a) Projection of the structure of In_5Ch_5Cl (Ch = S, Se) along [010]
(b)-(d) Characteristic structure fragments of In_5Ch_5Cl
(b) Face-sharing three capped trigonal prisms
(c) Cis and trans edge-sharing octahedral double chains ($InCh_6$)
(d) Ethane analogue chains built up by In_2S_6-units

In the first one the octahedra are built up by 6 chalcogenid atoms ($InCh_6$ Fig. 4.17c), in the second one, the octahedra are built by four chalcogenid and two halogenid atoms ($InCh_4Cl_2$ Fig. 4.18).

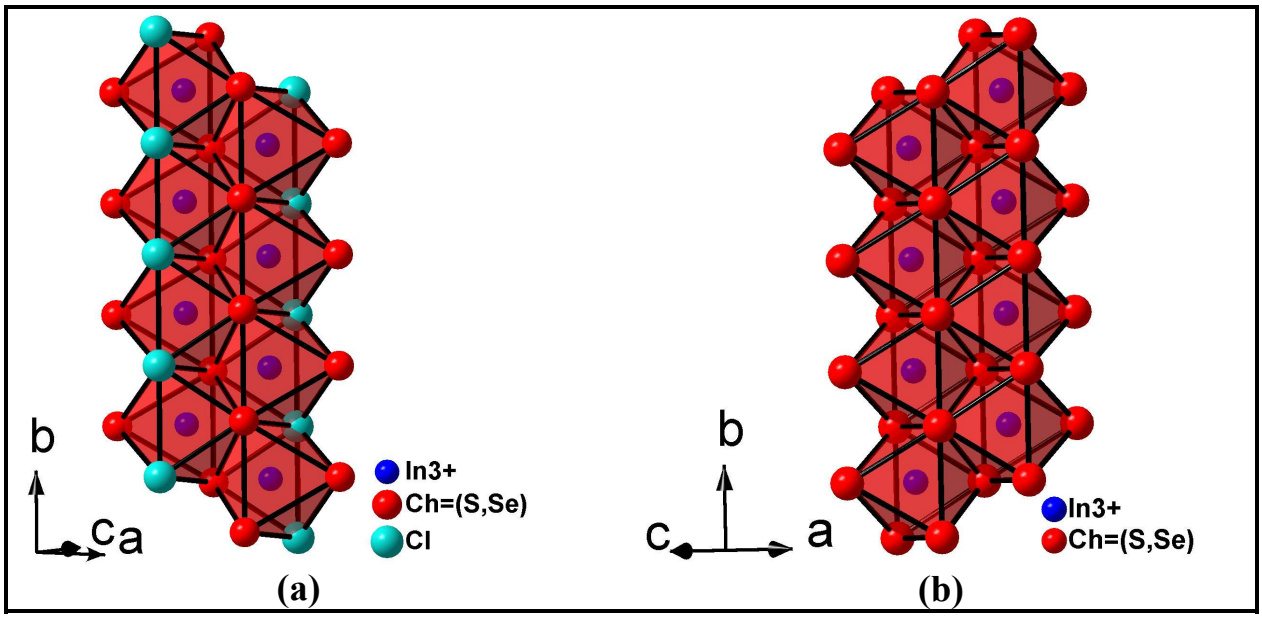

Fig. 4.18: Cis and trans edge-sharing octahedra double-chains, made by (a) $InCh_4Cl_2$-octahedra, (b) $InCh_6$-octahedra (Ch = S, Se).

The cis and trans edge-sharing $InCh_6$-octahedra double chains are bonded mainly to the ethane analogues In_2Ch_6-fragments while the cis and trans edge-sharing $InCh_4Cl_2$-octahedra double chains prefer to share edges and corners with the trigonal prismatic units centred by In^+.

Similar to the mixed valence binary and ternary indium chalcogenides mentioned above (Fig. 4.1-4.4), this structure is built up by two different repeating building units regarded as two dimensional motives. One motif is characteristic for this kind of structure and the other one is common for other structures too (Fig. 4.19). The characteristic motif is built up from cis and trans edge-sharing $InCh_4Cl_2$/$InCh_4Cl_2$ octahedra double-chains which share edges and corners with the three capped trigonal prismatic units occupied by In^+ species (Fig. 4.19b).

The common motif is similar to the mixed valence binary and ternary indium chalcogenides mentioned above, thus, made of cis and trans edge-sharing octahedra double-chains bonded to

chains of ethane analogues In_2S_6 fragments (Fig. 4.19c). Again the common motif influences two lattice constants and, therefore, the values of these lattice constants are nearly equivalent. The third one is determined by the characteristic interlayer (table 4.7).

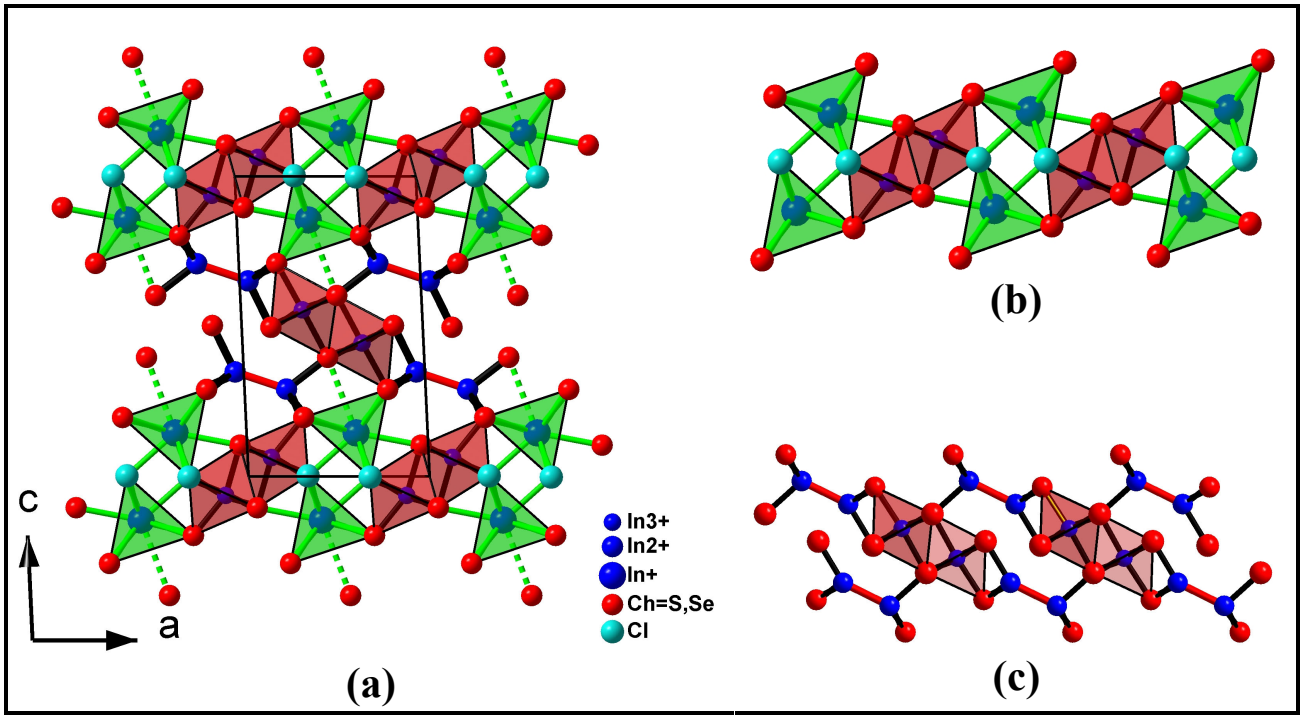

Fig. 4.19: (a) Projection of the structure of In_5Ch_5Cl (Ch = S, Se) along [010], (b) the characteristic construction motif build up by cis and trans edge-sharing $InCh_4Cl_2$ octahedra double chains sharing edges and corners with trigonal prismatic units, (c) the common motif build up of cis and trans edge-sharing octahedra skeins bonded to chains of ethane analogues In_2S_6 fragments.

.

Table 4.7: The lattice constants of different compounds. Each compound represents a different structure type which contains the common motif. * data taken from Walther [92] and Reiner [96].

Lattice constants /Å	In_6S_7*	KIn_5S_7*	KIn_5S_6*	$RbIn_7S_9$*	In_5S_5Cl	In_5Se_5Cl
a	**9.090(2)**	**9.0847(4)**	**8.791(1)**	25.006(2)	**8.927(1)**	**9.23058(8)**
b	**3.8894(5)**	**3.8872(1)**	**3.9070(3)**	**3.9082(3)**	**3.9062(5)**	**4.0866(3)**
c	17.166(3)	17.3697(7)	17.504(2)	**8.9184(6)**	14.951(2)	15.294(2)

A detailed observation of the $(In_2)^{4+}$coordination spheres shows, that its first and second sphere together are in good agreement with the first coordination sphere of In^+ (Fig. 4.20).

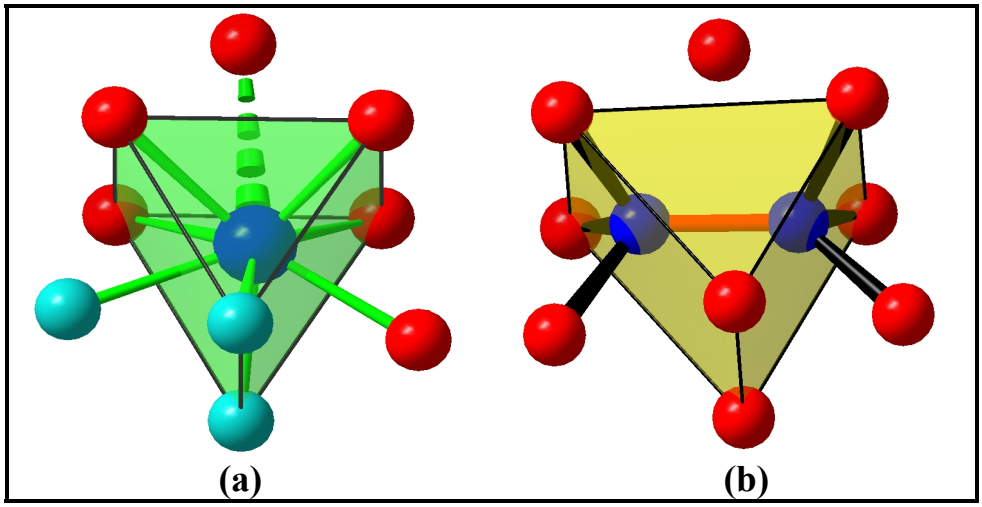

Fig. 4.20: First and second coordination sphere of (a) In^+ and (b) $(In_2)^{4+}$ in the structure of In_5Ch_5Cl.

Visualising the $(In_2)^{4+}$-species in trigonal prismsmatic coordination, the projection of the structure of In_5Ch_5Cl along [010] presented in fig. 4.17 transforms into a mosaic, where every double octahedra (edge-sharing octahedral double chains = double octahedra according to their appearance in the selected projection, fig. 4.21) is surrounded by six triangles (trigonal prisms = triangle due to the appearance in the selected projections, fig. 4.21). A detailed view of the structure reveals two different kinds of triangle environments around the double octahedra. On the one hand the double $InCh_4Cl_2$-octahedra are surrounded from four triangles centred by In^+ species and two other triangles centred by $(In\text{-}In)^{4+}$ dumbbells, thus briefly: (4:2 = $4\times In^+$, $2\times(In_2)^{4+}$ fig. 4.22a). On the other hand the double $InCh_6$-octahedra are surrounded from two triangles centred by In^+ species and four other triangles centred by $(In\text{-}In)^{4+}$ dumbbells, (2:4 = $2\times In^+$, $4\times(In_2)^{4+}$ fig. 4.22b) thus an inversed coordination in comparison to the double $InCh_4Cl_2$ octahedra.

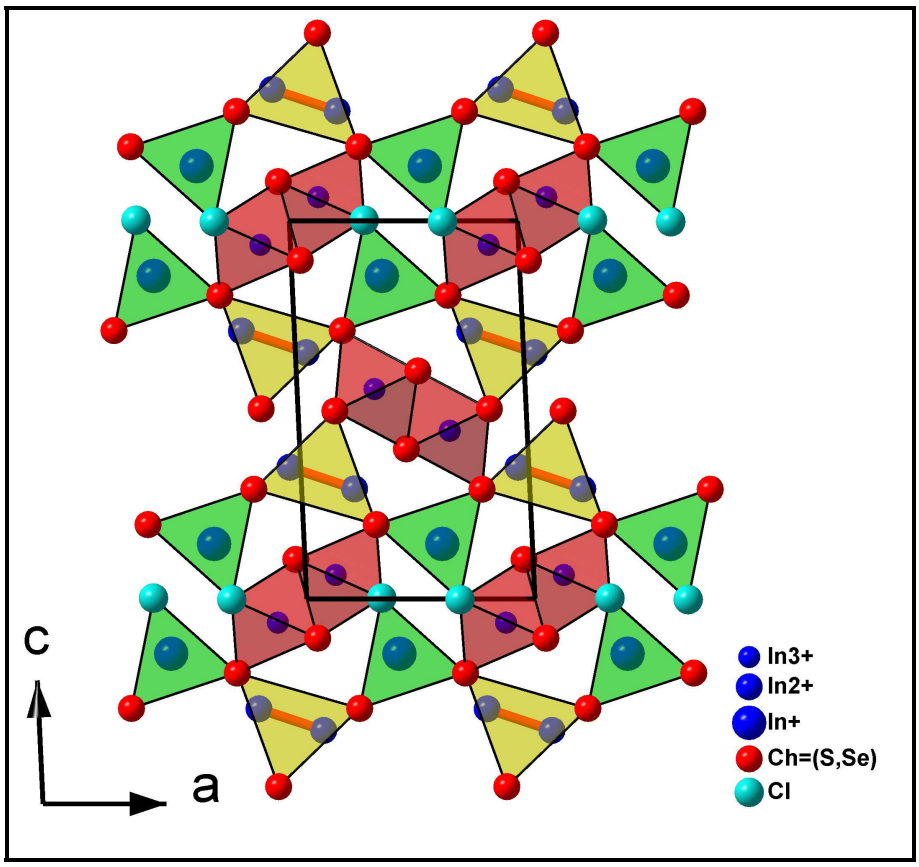

Fig. 4.21: Projection of the In_5Ch_5Cl structure along [010]. Every double $InCh_4Cl_2$/ $InCh_6$ double octahedra is surrounded by six triangles.

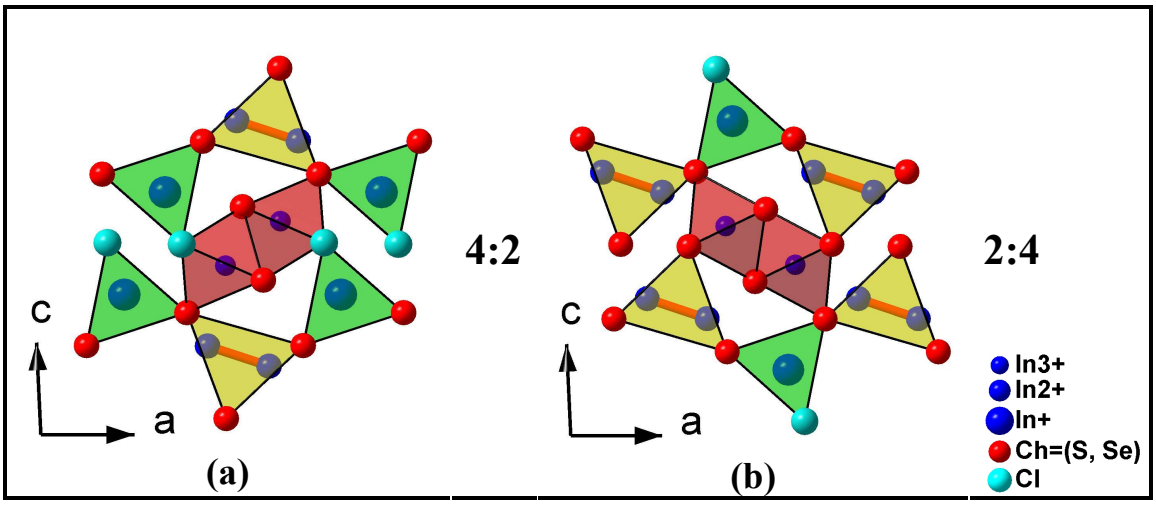

Fig. 4.22: (a) Double $InCh_4Cl_2$ octahedra surrounded by four triangles centred by In^+ species and two other triangles centred by $(In\text{-}In)^{4+}$ dumbbells. (b) double $InCh_6$ octahedra surrounded by two triangles centred by In^+ species and four other triangles centred by $(In\text{-}In)^{4+}$ dumbbells.

Based on this evidence the structure of In_5Ch_5Cl can be topologically described by means of two consequent repeating layers perpendicular to [1 0 10], where

1.- The first layer consists of double octahedra with 4:2-arrangement (Fig. 4.23a)

2.- The second layer consists of double octahedra with 2:4-arrangement (Fig. 4.23b)

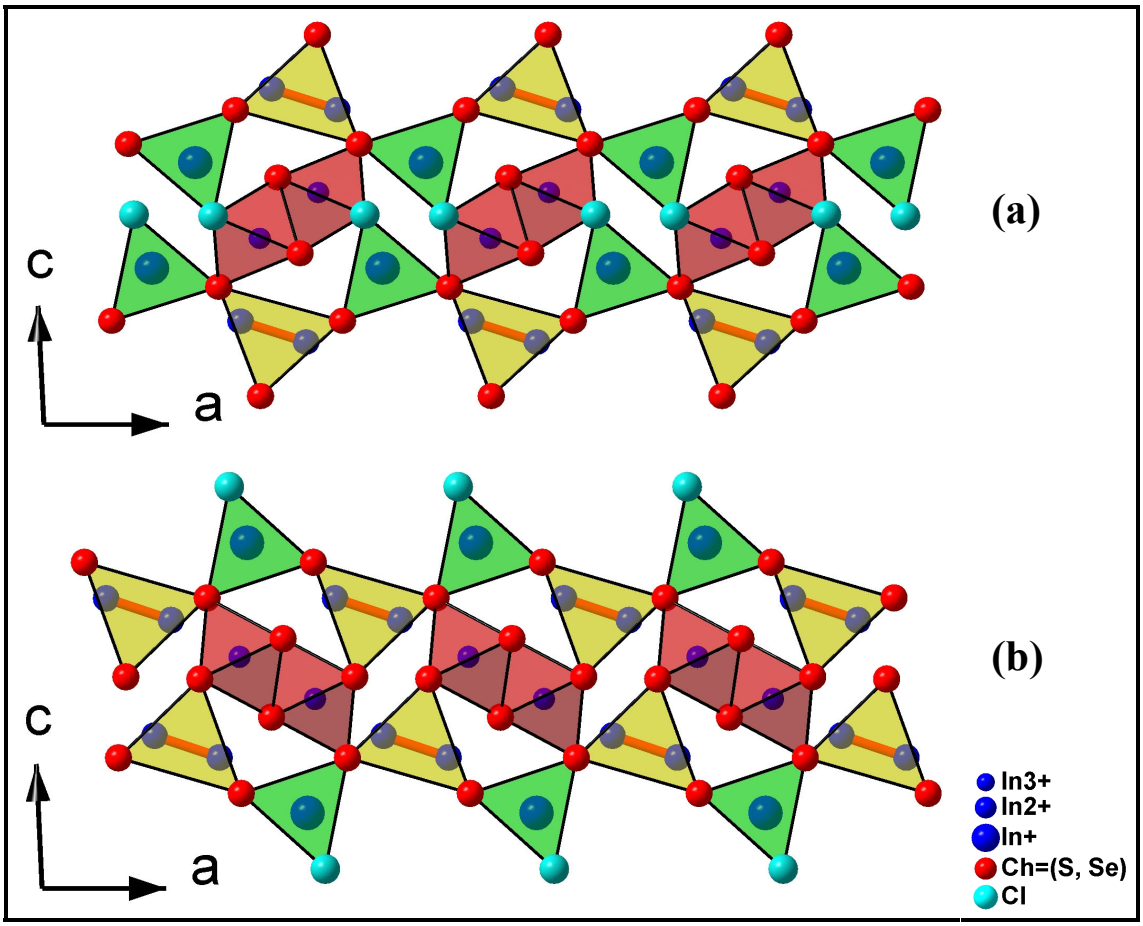

Fig. 4.23: Projection of the topologically regarded layers of In_5Ch_5Cl structure. a) layer 1 built up of octahedra with 4:2 arrangement, b) layer 2 built up of octahedra with 2:4 arrangement.

Topologically regarded in this case, means that parts of one layer belong at the same time to the adjacent layer, in other words, the layers share common parts.

4.2.8 Discussion of inter-atomic distances

Interatomic distances up to 4.1 Å and their standard deviations obtained from the last refinement are listed in table 4.8. The interatomic angles are listed in table 8.9 in appendix.

Table 4.8: Inter-atomic distances in the isotypic compounds In_5S_5Cl and In_5Se_5Cl. * In3 and In4 have a formal charge of +2.

Atom	anion	In_5S_5Cl /Å	In_5Se_5Cl /Å
In1 (In^{3+})	- S/Se5	2.57(1)	2.798(3)
	- S/Se2 (2×)	2.620(7)	2.743(2)
	- S/Se1	2.63(1)	2.734(3)
	- S/Se1 (2×)	2.653(7)	2.789(2)
In2 (In^{3+})	- S/Se3	2.54(1)	2.625(3)
	- S/Se4 (2×)	2.544(7)	2.678(2)
	- S/Se4 (2×)	2.59(1)	2.654(3)
	- Cl (2×)	2.776(7)	2.907(5)
In3* ($In)^{2+}$	- S/Se2	2.50(1)	2.636(3)
	- S/Se5 (2×)	2.571(7)	2.671(2)
	- In4	2.723(4)	2.748(2)
In4* ($In)^{2+}$	- S/Se3 (2×)	2.517(7)	2.658(2)
	- S/Se1	2.54(1)	2.651(3)
In5 (In^{+})	- Cl (2×)	3.187(9)	3.136(6)
	- S/Se5 (2×)	3.206(9)	3.410(3)
	- S/Se4	3.28(1)	3.350(4)
	- Cl	3.34(1)	3.303(7)
	- S/Se3 (2×)	3.398(9)	3.447(3)
	- S/Se1	3.93(1)	4.098(4)

In In_5Ch_5Cl, the coordination polyhedra around In^+ are similar to the polyhedra of In^+ in MIn_5S_7 (M = In, Na, K, Tl) [93, 94], but the three caped trigonal prisms are built up by chalcogenid and chloride ions. The prism itself is built up by four chalcogenid atoms and two chloride ions (Fig. 4.24).

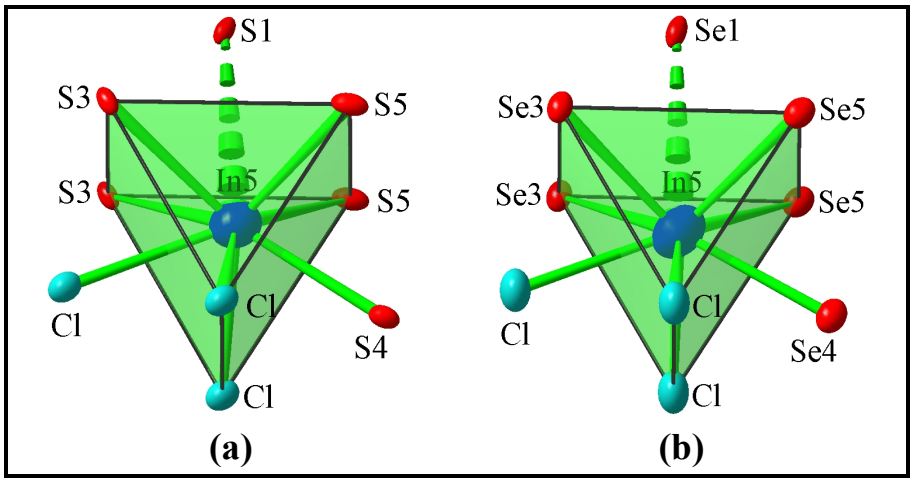

Fig. 4.24: Coordination spheres of In^+ species in (a) In_5S_5Cl and (b) In_5Se_5Cl. The presented ellipsoids are shown with a probability of 90%.

The inspection of the inter-atomic distances listed in table 4.10 reveals that the longest ones are those between In5 and Ch/Cl $d_{In5\text{-}Cl}$ = 3.34 Å (In_5S_5Cl), 3.30 Å (In_5Se_5Cl) and $d_{In\text{-}Ch1}$ = 3.93 Å (In_5S_5Cl), 4.10 Å (In_5Se_5Cl). The latter two distances $d_{In5\text{-}Ch1}$ are significantly larger than others (almost 4 Å), suggesting therefore a coordination of 8 +1 for In5.

In3 and In4 are coordinated by three chalcogenide atoms building an ethane analogue In_2Ch_6 unit (Fig. 4.25). These units are typical building units for the compounds InS [100], InSe [101], and are found in a vast number of mixed valence compounds, some of which such as MIn_5S_6, MIn_5Ch_7, MIn_7Ch_9 [93-95] are discussed above.

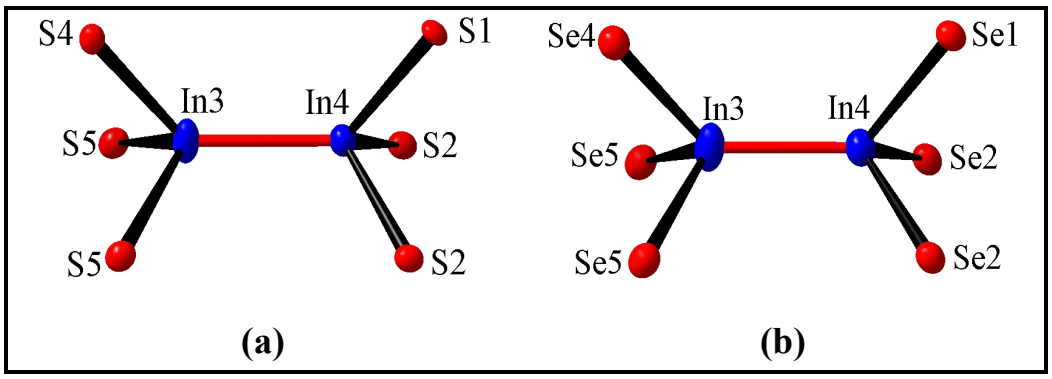

Fig. 4.25: Coordination spheres of the $(In_2)^{4+}$ dumbbells (a) In_5S_5Cl and (b) In_5Se_5Cl. The presented ellipsoids are shown with a probability of 90%.

A comparison of the distances between the covalent bonded In3 and In4 in these solids and In-In distances in other ternary compounds which contains these units shows a good agreement (table 4.9). Anyway, these distances are somehow shorter compared to the distances between In-In atoms in InCh (Ch = S, Se).

Table 4.9: Interatomic distances between In-In and In-Ch (S, Se) in some solids which contain In_2Ch_6 dumbbells in their structures.

Compound	$d_{In\text{-}In}$	$d_{In(a)\text{-}Ch}$	$d_{In(b)\text{-}Ch}$	References
InS	2.7684(9)	2.549	2.549	[100]
In_6S_7	2.742 (9)	2.554	2.559	[88]
KIn_5S_6	2.7221(9)	2.545	2.549	[93]
$RbIn_7S_9$	2.731(1)	2.532	2.532	[96]
In_5S_5Cl	**2.723(4)**	**2.554**	**2.524**	
InSe	2.771(1)	2.634	2.633	[104]
In_6Se_7	2.760(2)	2.674	2.685	[90]
In_5Se_5Cl	**2.748(2)**	**2.659**	**2.656**	

Concerning the average distances between indium and chalcogenide atoms ($d_{In\text{-}Ch}$) in In_2Ch_6 dumbbells, they are also in a good agreement with the analogue distances of similar units found in some other solids (see table 4.9).

In1 and In2 are octahedrally coordinated. In1 is coordinated by six chalcogenides (Fig. 4.26) while In2 is coordinated by four chalcogenides and two chloride atoms (Fig. 4.26). In this structure type the octahedra centered by In1 are pared between them (share a common edge), the same is observed for octahedra centred by In2. Concerning the distances between indium and the anions in the considered octahedra (table 4.8), In2-Cl exhibits the longest distance (2.776 Å, In_5S_5Cl and 2.907 Å In_5Se_5Cl) while In2-Ch3 the shortest indium-chalcogenide distances 2.54 Å (In_5S_5Cl) and 2.625 Å (In_5Se_5Cl). The average distances between In and Ch in the $InCh_4Cl_2$ octahedra (2.562 Å for In_5S_5Cl, 2.658 Å for In_5Se_5Cl) are shorter than the average distances in the $InCh_6$ octahedra (2.624 Å and, 2.766 Å). This difference in the distances can be explained based on the coordination of In1 and In2 respectively. The sum of the negative charges of the first coordination sphere of the $InCh_6$ octahedra [6 x (-2)] is higher compared to the corresponding sum of the $InCh_4Cl_2$ octahedra [4 x (-2) + 2 x (-1)], therefore, the lower negative charge around In2 atom is associated with a higher attraction force of indium toward the chalcogenid atoms, shortening the bonding distance between them.

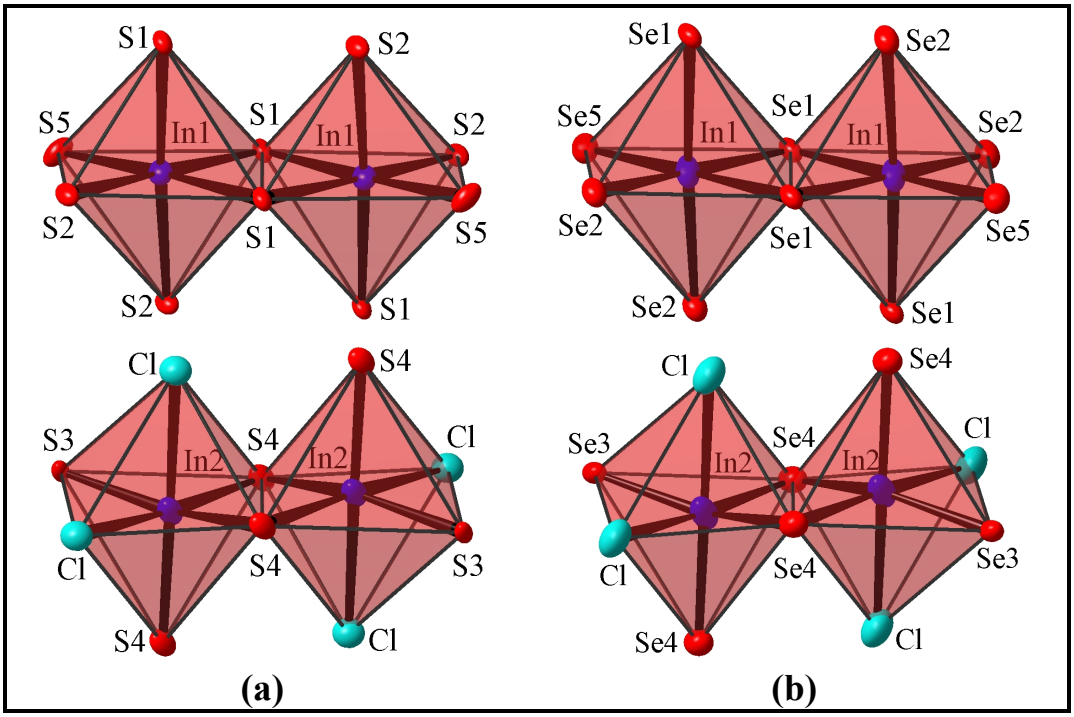

Fig. 4.26: Coordination spheres of In^{3+} in (a) In_5S_5Cl and (b) In_5Se_5Cl. The presented ellipsoids are shown with a probability of 90%.

The average In-Ch (Ch = S, Se) distances in the $InCh_6$-octahedra are comparable with analogues distances in other solids which contain octahedrally coordinated species (see table 4.10).

Table 4.10: Average In-Ch distances in some solids which contain $InCh_6$-octahedra.

In_2S_3	In_6S_7	KIn_5S_6	$RbIn_7S_9$	In_5S_5Cl	$NaInSe_2$	In_6Se_7	In_5Se_5Cl
2.628	2.643	2.624	2.627	2.624	2.758	2.767	2.766

4.2.9 The distribution of In^+ and $(In_2)^{4+}$ species around the edge-sharing double octahedra

The distribution of the triangles centred by In^+ and/or $(In_2)^{4+}$ around $InCh_4Cl_2/InCh_6$ double ocahedra can be explained based on the local charge compensation. Because of the lower local negative charge around the $InCh_4Cl_2$ double octahedra, they favour less positive charged triangles as neighbours (4x centred by In^+ and two 2x centred by $(In_2)^{4+}$, fig. 4.20a while the higher negative charged $InCh_6$ double octahedra favour more positive charge triangles (2x centred by In^+ and 4x centred by $(In_2)^{4+}$, fig. 4.20b). In other words, the difference in negative charge around $InCh_4Cl_2$ or $InCh_6$ double octahedra influences the surrounding ratio of the triangles (trigonal prisms) centred by In^+ and $(In_2)^{4+}$ species.

The above description brings to light only the "average" structure of In_5Ch_5Cl obtained from the X-ray measurement. Further structural anomalies investigated by HRTEM accompanied by SAED and other techniques are presented together with the bromide-structure investigations in the chapter 4.5.

4.3 The compounds In_5Ch_5Br (Ch = S, Se)

4.3.1 Preparation and properties of the samples

The synthesis of In_5Ch_5Br (Ch = S, Se) was performed similarly to the synthesis of In_5Ch_5Cl, based on the reaction of a stoichiometric mixture of the elements In, Ch (S, Se) and the binary compound $InBr_3$. The binary compound $InBr_3$ was synthesised according to the procedure described by Paashaus [98]. The quartz ampoules were treated previously as described for In_5Ch_5Cl. $InBr_3$ was added in an inert atmosphere (glove box). The samples were heated gradually up to 773 K and were held in this temperature for approximately one week.

Bigger crystals, especially for single crystal measurements were achieved by using a temperature program with a relatively small temperature increment (2 K/h). The samples were annealed for two weeks at 773 K and then slowly cooled down with a temperature decreasing rate of 5 K/h until 323 K.

Again the presence of byproducts could be minimised using the binary compounds InCh [100-101], In_2Ch_3 [102-103] and InBr [98] as starting materials. The binary compounds were weighed in stoichiometric amounts in an inert gas atmosphere, mixed in an agate mortar and finally the mixtures were pressed in pellets. The obtained pellets (<12 mm diameter) were transferred into previously heated and evacuated quartz ampoules. The ampoules were evacuated, sealed and heated using the same temperature program.

4.3.2 Characterisation

The obtained products In_5S_5Br and In_5Se_5Br consisted of fine red-brownish (in case of In_5S_5Br) and dark-brownish (in case of In_5Se_5Br) needle-shaped crystals with lengths of a few milimeters and small diameters (max. 30 μm).

Crystals of each compound were investigated using an electron microscope and the recorded SEM images are presented in fig. 4.27.

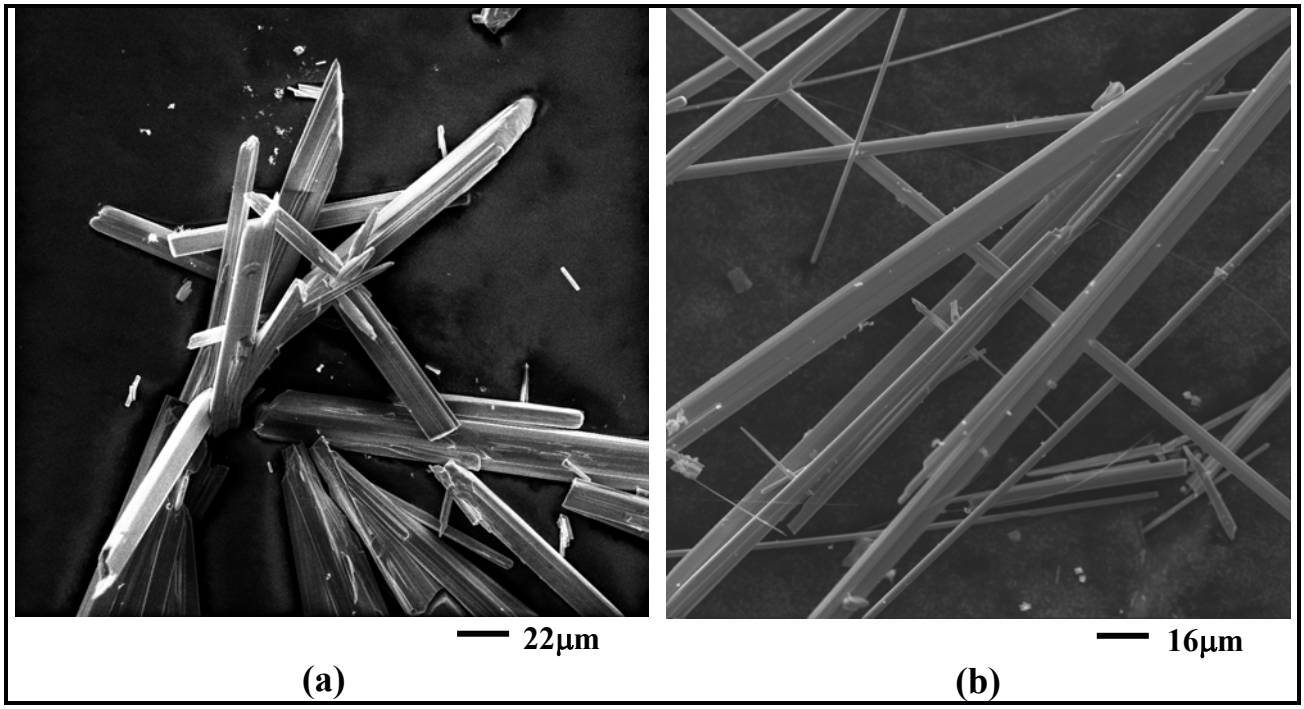

Fig. 4.27: SEM pictures of (a) In_5S_5Br, (b) of In_5Se_5Br needle-shaped crystals.

The qualitative elemental analysis based on EDX measurements for the red-brownish needle-shaped crystals displayed the presence of indium, sulphur and bromine (Fig. 4.28). The dark-brownish needle-shaped crystals of In_5Se_5Br displayed the respective elements too. Because of the small difference in the number of electrons between Se and Br, an overlapping of the Br-L line and the Se-L line occurs (Fig. 4.29). The presence of both elements could be confirmed by their Kα lines in the EDX spectrum and/or WDX analysis. The recorded EDX spectra are presented in figures 4.28, 4.29.

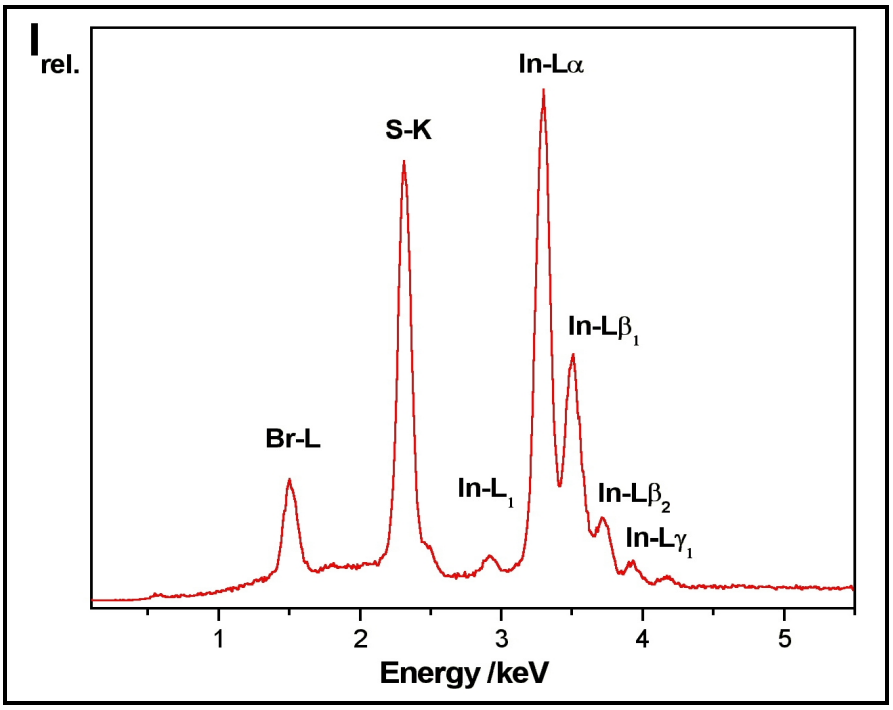

Fig. 4.28: EDX spectrum of needle-shaped red-brownish crystals of In_5S_5Br.

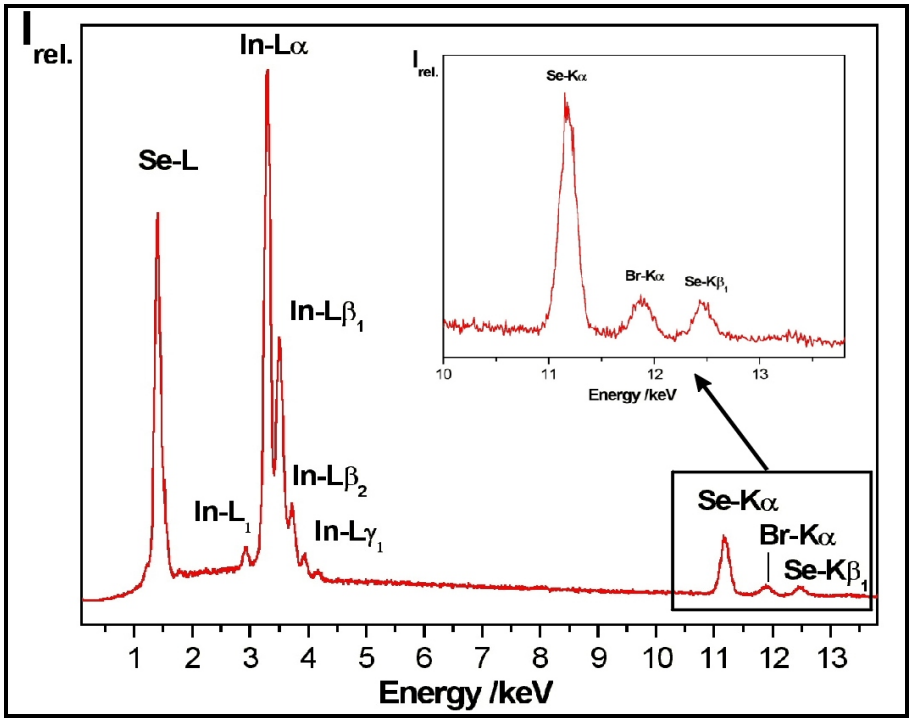

Fig. 4.29: EDX spectrum of the dark-brown needle-shaped crystals of In_5Se_5Br, for a better visualisation the section from 11.5-14 keV is magnified. The Br-L line overlaps with the Se-L line, the presence of bromine is confirmed by the Br-Kα line.

Crystals of both samples were ground and measured on a D5000 powder diffraction system. The measured diffraction patterns are in a good agreement (except the intensities of the reflections) with the calculated diffraction patterns from single crystal data (Fig. 4.30 and 4.31).

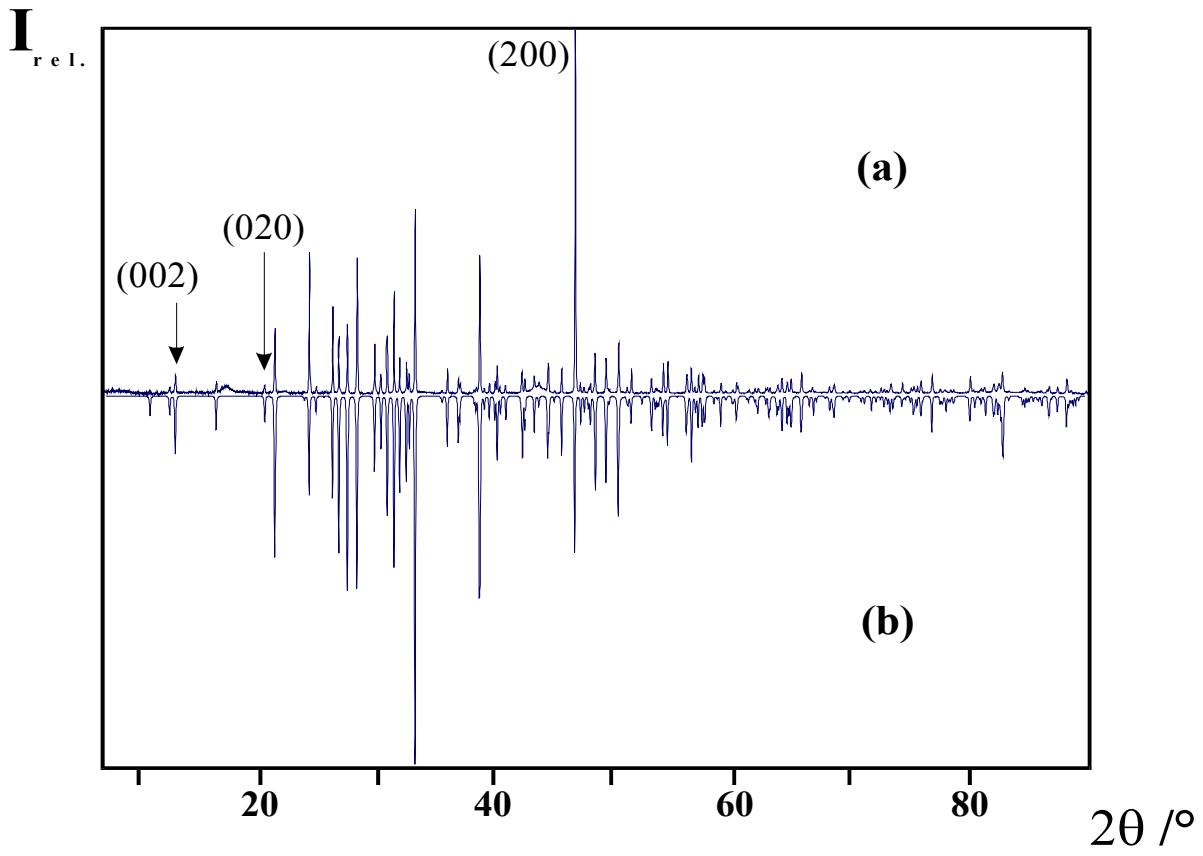

Fig. 4.30: Comparison of a measured powder diffraction pattern of In_5S_5Br (a) with the powder pattern of In_5S_5Br calculated from single crystal data (b).

The intensity differences between the measured and calculated powder patterns of both compounds are caused by the morphology of the crystals (needle shape crystals) similarly as in case of In_5Ch_5Cl. Based on the growth direction (*a*-axis), increased intensities for the reflections with the indexes h00 are observed (based on the cell choice). In opposite to that, the intensities of the reflections with the indexes 0k0 and 00l are decreased. This fact is demonstrated especially by the reflections with the indexes 200, 020 and 002 in the case of In_5S_5Br (Fig. 4.30) and the reflection with the index 200 in the case of In_5Se_5Br (Fig. 4.31).

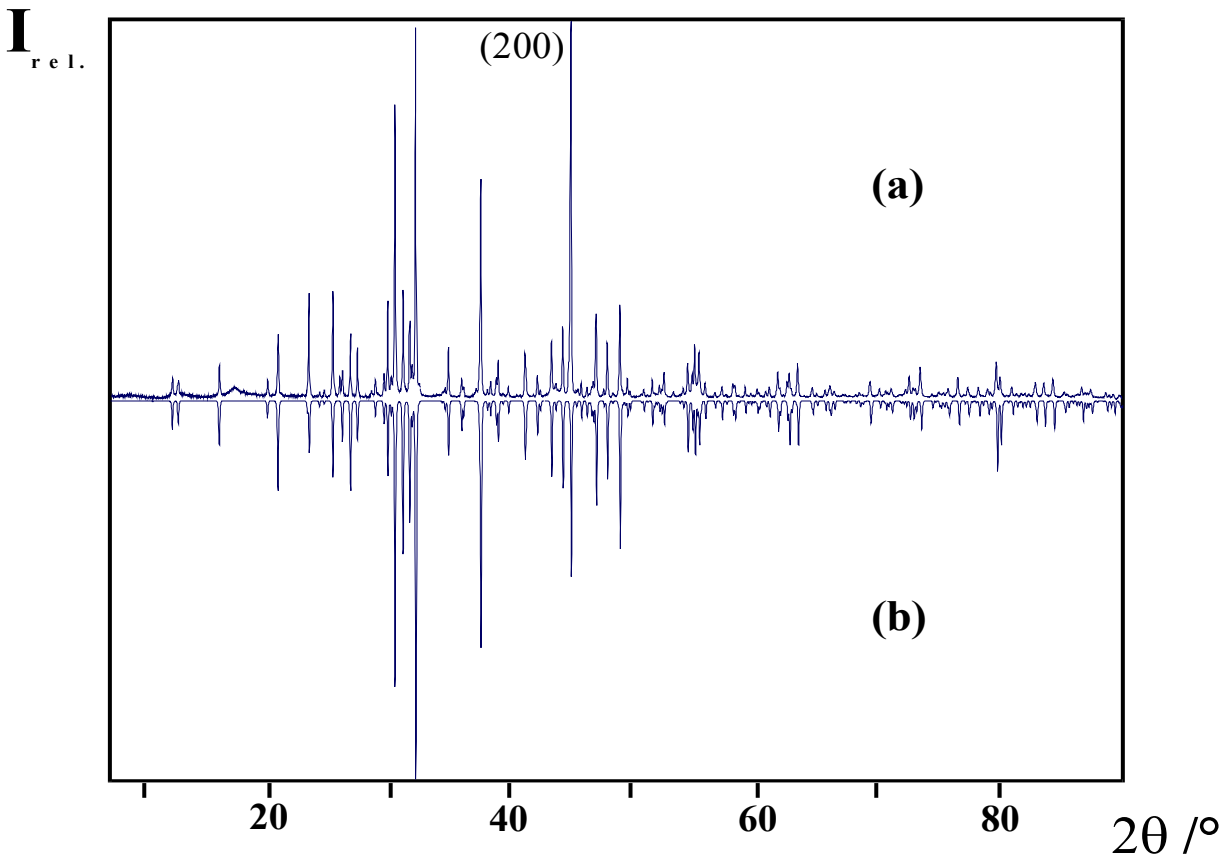

Fig. 4.31: Comparison of a measured powder diffraction pattern of In_5Se_5Br (a) with the powder pattern of In_5Se_5Br calculated from single crystal data (b).

The reflections of both compounds can be indexed in a orthorhombic primitive cell with the lattice constants listed in table 4.11.

Table 4.11: Refined lattice constants from powder patterns for the compounds In_5S_5Br and In_5Se_5Br.

Compound	a /Å	b /Å	c /Å	V /Å^3
In_5S_5Br	3.935(1)	9.088(1)	14.852(1)	531.06(1)
In_5Se_5Br	4.096(1)	9.339(1)	15.254(1)	583.56(3)

4.3.3 Thermal analyses of In_5S_5Br and In_5Se_5Br

Thermal investigations of both compounds In_5S_5Br and In_5Se_5Br were performed by DTA and by high temperature powder diffraction measurements. The results obtained from the DTA are presented in figure 4.32, while the high temperature powder diffraction investigations are explained in chapter 5.

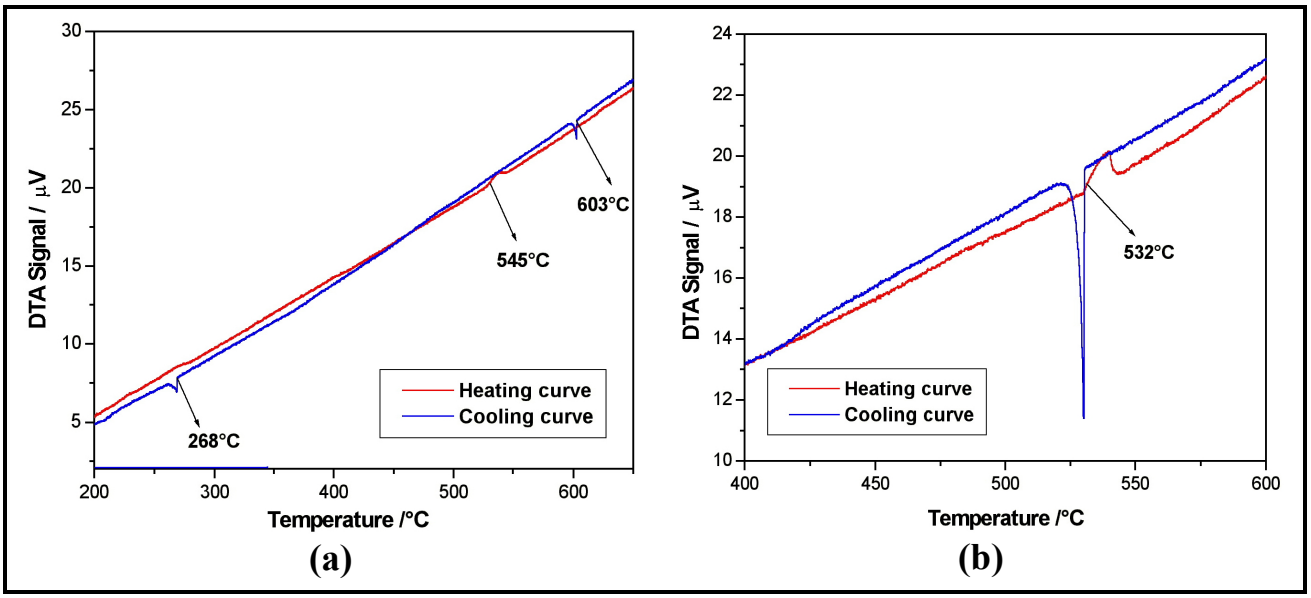

Fig. 4.32: Sections of the DTA-curves of In_5S_5Br and In_5Se_5Br. The heating curve shows an endothermic effect (a) at 545 °C for In_5S_5Br and (b) at 532 °C for In_5Se_5Br (the cooling curve shows two exothermic effects in case of In_5S_5Br and only one exothermic effect in case of In_5Se_5Br).

Similar to In_5Ch_5Cl both compounds are relatively stable in air. The thermal behaviour of In_5S_5Br investigated by DTA presents an endothermic effect at 545 °C in the heating curve and two exothermic effects in the cooling curve. The compound melts incongruently. According to the applied heating regime (5°C/min) the decomposition products are In_6S_7 (m.p. 603 °C, Fig. 4.32a) and InBr (m.p. 268°C, Fig. 4.32a). The decomposition of this compound into In_2S_3, InS and InBr is confirmed by the high temperatures powder diffraction analysis. In case of In_5Se_5Br (Fig. 4.32b) only one endothermic effect is observed in the heating curve (532 °C) and one exothermic effect in the cooling curve. Regardless this behaviour, the compound melts incongruently similarly to the other already discussed compounds.

4.3.4 Single crystal investigation of In_5Ch_5Br (Ch = S, Se)

For the single crystal investigation needle-shaped crystals of both compounds were chosen under an optical microscope and fixed with the help of grease on top of a glass capillary. The capillary was fixed on a goniometer head and measured on a STOE IPDS diffraction system.

4.3.5 Single crystal investigations of In_5S_5Br

The obtained data for In_5S_5Br were further analysed by the STOE IPDS Program package [P1]. After visualizing the reflections by the program EXPOSE [P2], the reflections were indexed (INDEX [P3] and CELL [P4]) in an orthorhombic cell. A close inspection of the reciprocal space (RECIPE [P5]) showed no anomalies like twinning, superstructure etc.

The data were integrated using the program INTEGRATE [P7]. The obtained data set has been corrected for Lorenz and polarisation effects. The crystal-face indexation was performed with a CCD-camera [P8] and optimised using the program X-SHAPE [P9]. The numerical absorption correction based on an adequate number of symmetrically equivalent reflections using the program X-RED [P10].

The zonal reflection condition (*h0l*) $h + l = 2n$ is represented by the symmetry element n⊥b, the row condition for reflections *h00* $h = 2n$ and *00l* $l = 2n$ respectively by 2_1 ll a and 2_1 ll c. These reflection conditions lead to the space groups, *Pmmn* (centrosymmetric) and $Pmn2_1$ (non centrosymmetric). Structure solution and the refinement were carried out in both space groups, but satisfactory results were obtained only from the latter one. The E-statistic and N(Z)-test, support the presence of a non centrosymmetric structure. The structure was refined as an inversion twin with fractional contribution of 0.38(2).

Compared to the chloride-type compounds, the structure refinement revealed quite satisfactory R-values ($R_1 = 0.0312$, $wR_2 = 0.0553$) and lower Fourier residuals ($\rho_{max.} = 2.030$ e/Å^3, $\rho_{min.} = -1.459$ e/Å^3). The measuring parameters and the results of the last refinement cycle are listed in table 4.12. The positions and the equivalent isotropic displacement parameters as well as the anisotropic displacement parameters are listed in tables 4.13 and 8.7 (in appendix).

Table 4.12: Important parameters for the X-ray single crystal investigation of In_5S_5Br.

Sum formula	**In_5S_5Br**
Formula weight / $gmol^{-1}$	$M = 814.31$
Temperature / K	$T = 293(2)$
Wavelength / Å	Mo$K\alpha$, $\gamma = 0.71073$
Crystal System	orthorhombic
Space group	$Pmn2_1$ (No. 31)
Crystal dimension / mm	$0.10 \times 0.02 \times 0.01$
Cell dimensions / Å	$a = 3.9201(3)$ $b = 9.0562(8)$ $c = 14.812(1)$
Volume / $Å^3$	$V = 525.83(8)$
Formula units per unit cell	$Z = 2$
Density (calculated) / gcm^{-3}	$\rho = 5.143$
Absorption coefficient / mm^{-1}	$\mu = 15.522$
$F(000)$	720
Diffractometer	IPDS (Stoe), oriented graphite monochromator
Scan type	φ
Measured θ range / °	$3.55 \leq \theta \leq 31.65$
Index ranges	$-5 \leq h \leq 5$ $-12 \leq k \leq 13$ $-21 \leq l \leq 21$
Measured reflections	5062
Independent reflections	1954 ($R_{int} = 0.0288$)
Completeness to θ / %	99.4
Absorption correction	Numerical [P8, P10]
Structure solution	Direct methods [P11]
Structure refinement	Full-matrix least-squares on F^2 [P12]
Data/restraints/parameters	1954 / 1 / 69
Goodness-of-Fit on F^2	1.012
R values [$I \geq 2\sigma(I)$]	$R_1 = 0.0248$, $wR_2 = 0.0534$
R values (all data)	$R_1 = 0.0312$, $wR_2 = 0.0553$
Final Fourier residuals / $eÅ^{-3}$	$\rho_{max.} = 2.030$, $\rho_{min.} = -1.459$

Table 4.13: Atomic coordinates, isotropic displacement parameters U_{eq} and occupancy factors for In_5S_5Br.

Atom	Wyck.	*x*	*y*	*z*	U_{eq} /Å^2	*sof*
In1	2a	0	0.88739(6)	0.40219(3)	0.0110(1)	1
In2	2*a*	½	0.60634(6)	0.52634(3)	0.0114(1)	1
In3	2*a*	½	0.18662(6)	0.30168(4)	0.0148(1)	1
In4	2*a*	½	0.47837(6)	0.25593(3)	0.0104(1)	1
In5	2*a*	½	**-0.14118(9)**	**0.11158(5)**	**0.0280(3)**	**0.946(4)**
Br	2*a*	0	0.40267(9)	0.45688(5)	0.0127(2)	1
S1	2*a*	½	0.7016(2)	0.3608(1)	0.0080(3)	1
S2	2*a*	½	0.4343(2)	0.6621(1)	0.0092(3)	1
S3	2*a*	0	0.7715(2)	0.5652(1)	0.0088(3)	1
S4	2*a*	½	1.0612(2)	0.4541(1)	0.0088(3)	1
S5	2*a*	0	1.0296(2)	0.2501(1)	0.0105(3)	1

The occupancy of each individual position was proved and resulted fully occupied within the three fold standard deviation, except of In5 which is slightly under occupied (table 4.13). This slight under occupancy (*s.o.f.* = 0.946) reveals the composition $In_{4.946}S_5Br$. A similar case to this is observed in the structures of In_5Se_5Cl (see above).

Comparable to In_5Ch_5Cl (Ch = S, Se), the $(In_2)^{4+}$-species have a similar coordination to In^+. Hence, it is supposed that a partial occupation of the In5 position by $(In_2)^{4+}$ could lead to the reduced occupancy of that position.

4.3.6 Single crystal investigation of In_5Se_5Br

The single crystal data of In_5Se_5Br were analysed similarly to In_5S_5Br. The reflections could be indexed orthorhombically. The investigation of the reciprocal space using the program RECIPE [P5] presented no anomalies.

The data were integrated using the program INTEGRATE [P7] and corrected for Lorenz and polarisation effects. The crystal-face indexation was performed with a CCD-camera [P8] and optimised using the program X-SHAPE [P9]. The numerical absorption correction based on an adequate number of symmetrical equivalent reflections was done using the program X-RED [P10].

The condition for reflections similarly as in the case of In_5S_5Br, are consistent with two space groups: *Pmmn* and $Pmn2_1$. A structure solution performed by the program SHELXS [P11] using direct methods is possible in both space groups, but the best R-factors are obtained again from the solution and the refinement (SHELXL [P12]) in the space group $Pmn2_1$. The distribution of the normalized structure factors obtained by means of E-statistic and N(Z)-test suggested the non centrosymetric space group $Pmn2_1$. The structure of was refined as an inversion twin with a fractional contribution of 0.49(2). The structure refinement revealed quite satisfactory R-values (R_1 = 0.0357, wR_2 = 0.0800) and Fourier residuals ($\rho_{max.}$ = 2.010 e/Å^3, $\rho_{min.}$ = -1.861 e/Å^3) similar to In_5S_5Br. The measuring parameters and the results of the last refinement cycle are listed in table 4.14. The positions and the equivalent isotropic displacement parameters as well as the anisotropic displacement parameters are listed in tables 4.15 and 8.8 (in appendix).

Table 4.14: Important parameters for the X-ray single crystal investigation of In_5Se_5Br.

Sum formula	**In_5Se_5Br**
Formula weight / gmol^{-1}	M = 1048.81
Temperature / K	T = 293(2)
Wavelength / Å	Mo$K\alpha$, γ = 0.71073
Crystal System	orthorhombic
Space group	$Pmn2_1$ (No. 31)
Crystal dimension / mm	0.20 × 0.03 × 0.01
Cell dimensions / Å	a = 4.0932(3) b = 9.3331(7) c = 15.251(2)
Volume / Å^3	V = 582.60(8)
Formula units per unit cell	Z = 2
Density (calculated) / gcm^{-3}	ρ = 5.979
Absorption coefficient / mm^{-1}	μ = 28.733
F(000)	900
Diffractometer	IPDS (Stoe), oriented graphite monochromator
Scan type	φ
Measured θ range / °	3.45≤ θ ≤ 30.30
Index ranges	-5 ≤ h ≤ 5 -13 ≤ k ≤ 13 -21 ≤ l ≤ 21
Measured reflections	6605
Independent reflections	1951 (R_{int} = 0.0468)
Completeness to θ / %	99.2
Absorption correction	Numerical [P8, P10]
Structure solution	Direct methods [P11]
Structure refinement	Full-matrix least-squares on F^2 [P12]
Data/restraints/parameters	1951 / 1 / 69
Goodness-of-Fit on F^2	1.207
R values [$I \geq 2\sigma(I)$]	R_1 = 0.0323, wR_2 = 0.0790
R values (all data)	R_1 = 0.0357, wR_2 = 0.0800
Final Fourier residuals / eÅ^{-3}	$\rho_{max.}$ = 2.010, $\rho_{min.}$ = -1.861

Table 4.15: Atomic coordinates, isotropic displacement parameter U_{eq} and occupancy factors for In_5Se_5Br.

Atom	Wyck.	*x*	*y*	*z*	U_{eq} /Å^2	*sof*
In1	2a	0	0.8945(1)	0.40437(6)	0.0158(2)	1
In2	2a	½	0.6060(1)	0.52379(6)	0.0171(2)	1
In3	2a	½	0.1943(1)	0.30369(7)	0.0194(2)	1
In4	2a	½	0.4765(1)	0.25430(6)	0.0152(2)	1
In5	2a	½	-0.1462(2)	0.11299(9)	0.0324(4)	0.968(6)
Br	2a	0	0.4073(2)	0.4552(1)	0.0175(3)	1
Se1	2a	½	0.7059(1)	0.35849(8)	0.0113(3)	1
Se2	2a	½	0.4284(1)	0.65933(8)	0.0116(3)	1
Se3	2a	0	0.7750(2)	0.56870(8)	0.0125(3)	1
Se4	2a	½	1.0711(2)	0.45941(9)	0.0136(3)	1
Se5	2a	0	1.0342(2)	0.24864(9)	0.0138(3)	1

Similar to the compounds treated above, the occupancy of each individual position was proved and resulted fully occupied within the calculated standard deviation. In this compound even In5 position can be considered fully occupied (*s.o.f.* = 0.968(6) table 4.15) within the threefold standard deviation.

In analogy to the above discussed compounds, in this compound the isotropic displacement parameter of In5 is significantly higher in comparison to the other atoms.

4.3.6.1 The bromine position in the structure of In_5Ch_5Br (Ch = S, Se)

The localisation of bromine atoms in the structure of In_5Ch_5Br is based on the X-ray single crystal investigation of In_5S_5Br. In case of In_5Se_5Br the determination is almost impossible due to the small difference in the number of electrons between selenium and bromine atoms. The distribution of the

bromine atoms in the structure agrees with the explanation based on the concentration of the local positive and negative charge and is considered to be the same for In_5Se_5Br.

4.3.7 Structure description of In_5Ch_5Br (Ch = S, Se)

Both compounds In_5S_5Br and In_5Se_5Br crystallize in the orthorhombic crystal system in the space group $Pmn2_1$ (No. 31) with two formula units in the unit cell. Based on the nomenclature proposed by Robin [105], these compounds can be classified in the first group of mixed valence compounds similar to In_5Ch_5Cl, where, indium occurs in three different oxidation states: In^+, formal In^{2+} and In^{3+}. The chalcogen atoms and bromine possess their lowest oxidation numbers [Ch^{2-}] and [Br^-]. In analogy to the chloride-type compounds, the explicit formula of these compounds can be written in the following way:

$$\mathbf{In_5Ch_5Br = [In^+]\ [(In_2)^{4+}]\ 2[In^{3+}]\ 5[Ch^{2-}]\ [Br^-]}$$

For a better comparison with In_5Ch_5Cl, the structure is projected along [100] (Fig. 4.33a). Concerning the description of each indium species in In_5Ch_5Br, there is a close analogy to the chloride structure. In^+ is located in three capped trigonal prismatic holes, the trigonal prisms themselves share common faces with each other building units along [100] (Fig. 4.33b). Each In^{2+} builds with its neighbored In^{2+} covalent bonded dumbbells $(In_2)^{4+}$, where each indium atom is further coordinated by three chalcogenides. The resulting ethane analogue units (eclipsed conformation) form chains along [100] (Fig. 4.33d). In^{3+} is octahedrally coordinated, similar to the chloride-type compounds. The octahedra build cis and trans edge-sharing double octahedra chains along the short *a* axis (Fig. 4.33c). In contranst to the chloride-type, this structure type shows only one kind of edge-sharing octahedra double-chain, namely $InCh_6$-$InCh_4Br_2$ (Fig. 4.33c). Different from In_5Ch_5Cl, in this structure there is one building unit playing the role of the common and characteristic motif.

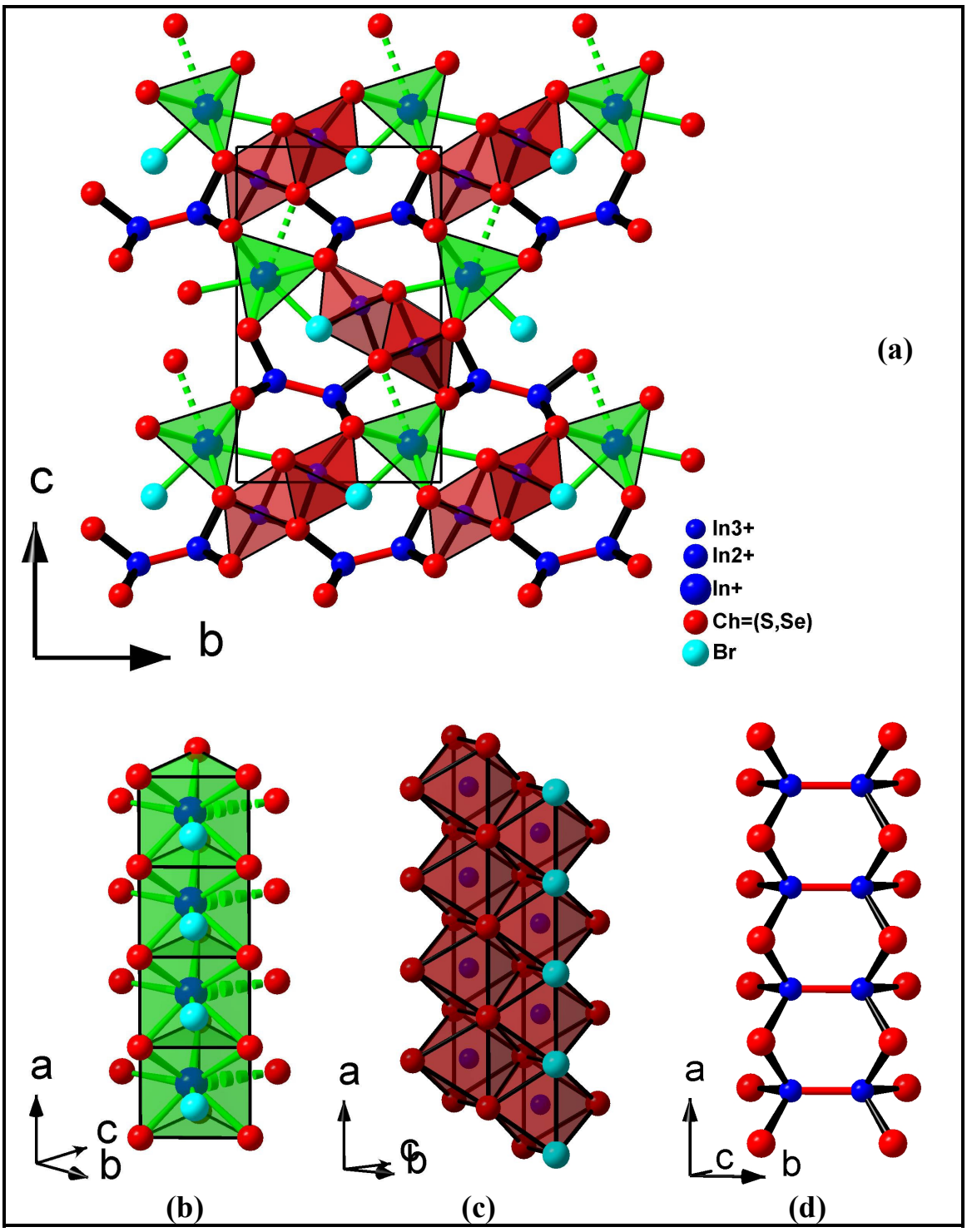

Fig. 4.33: (a) Projection of the structure of In_5Ch_5Br (Ch = S, Se) along [100]
(b)-(d) Characteristic structure fragments of In_5Ch_5Br
(b) Face-sharing three capped trigonal prisms
(c) Cis and trans edge-sharing octahedra double chains ($InCh_6$ and $InCh_4Br_2$)
(d) Ethane analogue chains built up by In_2S_6-units

This building unit consists of trans edge-sharing octahedra double-chains $InCh_6$-$InCh_4Br_2$, bonded to chains of ethane analogue In_2S_6 fragments and at the same time sharing edges and corners with the trigonal prismatic units occupied by In^+ species (Fig. 4.34b,c).

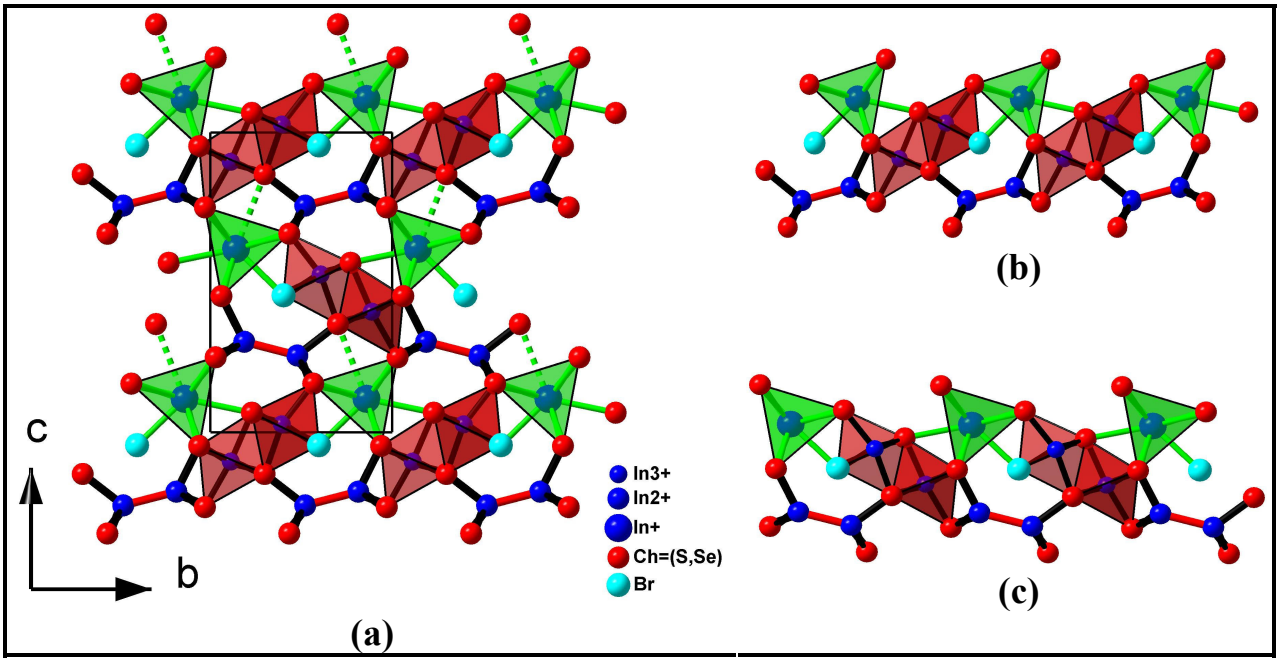

Fig. 4.34: (a) Projection of the structure of In_5Ch_5Br (Ch = S, Se) along [100], (b) and (c) building units build up by cis and trans edge-sharing octahedral double chains $InCh_6$ and $InCh_4Br_2$ sharing edges and corners with trigonal prismatic units and with chains of ethane analogue In_2S_6 fragments.

This construction unit can be regarded as an intermediate of the construction units observed in the structure of In_5Ch_5Cl (Fig. 4.19b,c), where, a row of $(In\text{-}In)^{4+}$ dumbbells bonded to edge-sharing octahedra double-chains is substituted by a row of trigonal prisms. This characteristic explains the similarity between the lattice constants of the four species (see table 4.16).

Table 4.16: The space groups and lattice parameters of the four new compounds In_5Ch_5X (Ch = S, Se; X = Cl, Br; taken from X-ray single crystal measurements).

Compound	Space group	a / Å	b / Å	c / Å	β /°	V / Å^3
In_5S_5Cl	$P2_1/m$	8.927 (1)	3.9062(5)	14.951 (2)	93.48 (2)	520.4 (1)
In_5S_5Br	$Pmn2_1$	3.9201(3)	9.0562(8)	14.812(1)	90	525.83(8)
In_5Se_5Cl	$P2_1/m$	9.2306(1)	4.0866 (3)	15.294(2)	92.47(1)	576.36(9)
In_5Se_5Br	$Pmn2_1$	4.0932(3)	9.3331(7)	15.251(2)	90	582.60(8)

For a comparison of the lattice constants it should be taken into account that the lattice constant *a* of the chloride-type is comparable with the lattice constant *b* of the bromide-type and vice versa. Similarly as in the chloride-type structure, the first and second coordination sphere of In^+ are in good agreement with the coordination sphere of $(In_2)^{4+}$ (Fig. 4.35).

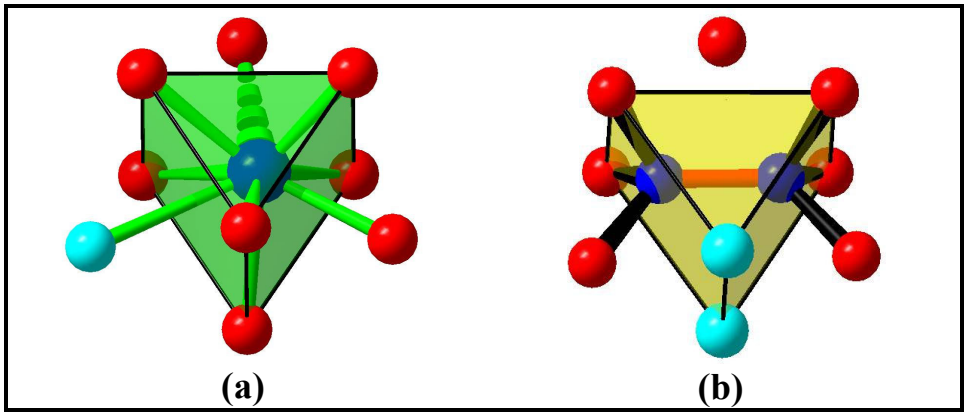

Fig. 4.35: First and second coordination sphere of (a) In^+ and (b) $(In_2)^{4+}$ species in the structure of In_5Ch_5Br.

In a projection along [100] the bromide-type structure (In_5Ch_5Br) can be regarded as a mosaic where every edge sharing octahedra double-chain $InCh_6$-$InCh_4Br_2$ (in the projections presented as double octahedra) is surrounded by six trigonal prisms (presented as triangles in the selected projection, figure 4.36).

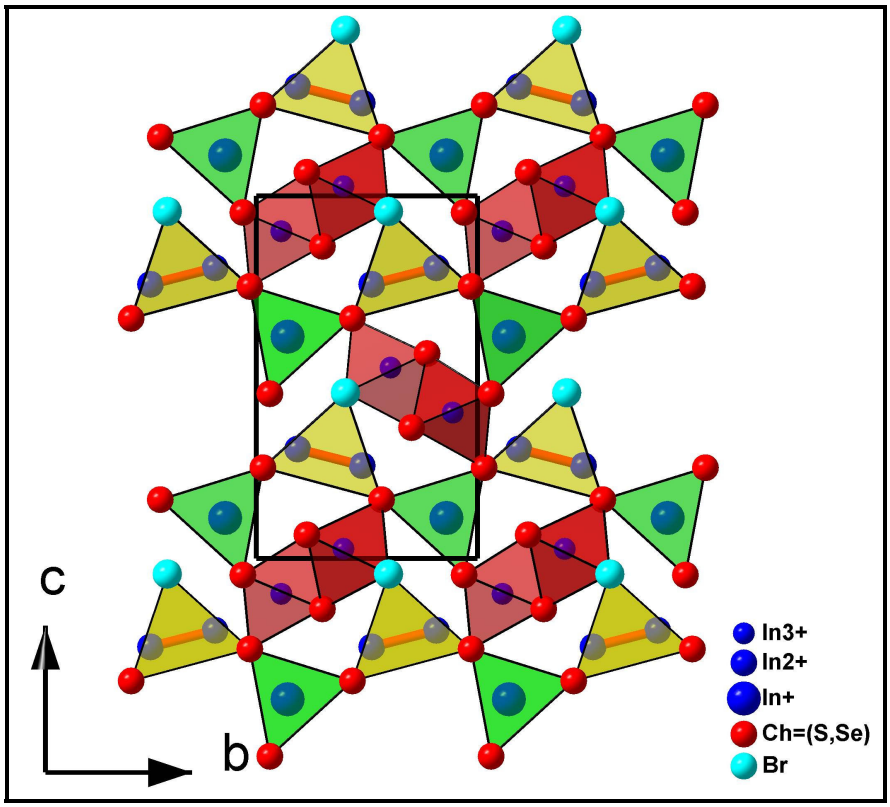

Fig. 4.36: Projection of the In_5Ch_5Br structure along [100]. Each double octahedra is surrounded by six triangles.

In contrary to the chloride-type structure where two different kinds of triangle environments around the double octahedra are found (4:2 and 2:4 respectively), this structure, surprisingly displays only one kind of triangle environment, namely 3:3.

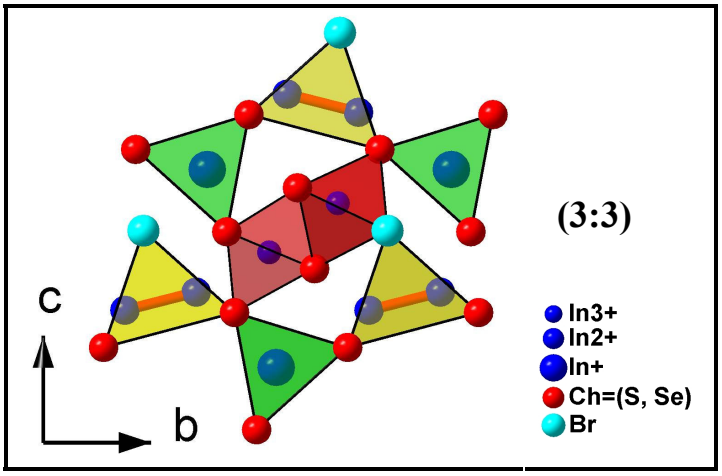

Fig. 4.37: (a) Double octahedra surrounded by three triangles centred by In^+ and three other triangles centred by $(In\text{-}In)^{4+}$ dumbbells.

Three of the trigonal prisms surrounding double octahedra are centred by In^+ and three by $(In_2)^{4+}$ dumbbells (Fig. 4.37).

In analogy to the chloride-type structure, the bromide type structure can be described by topological layers perpendicular to [001]. In contrast to the chloride type where the whole structure can be represented by two different layers, the bromide type shows only one kind of layer (Fig. 4.38).

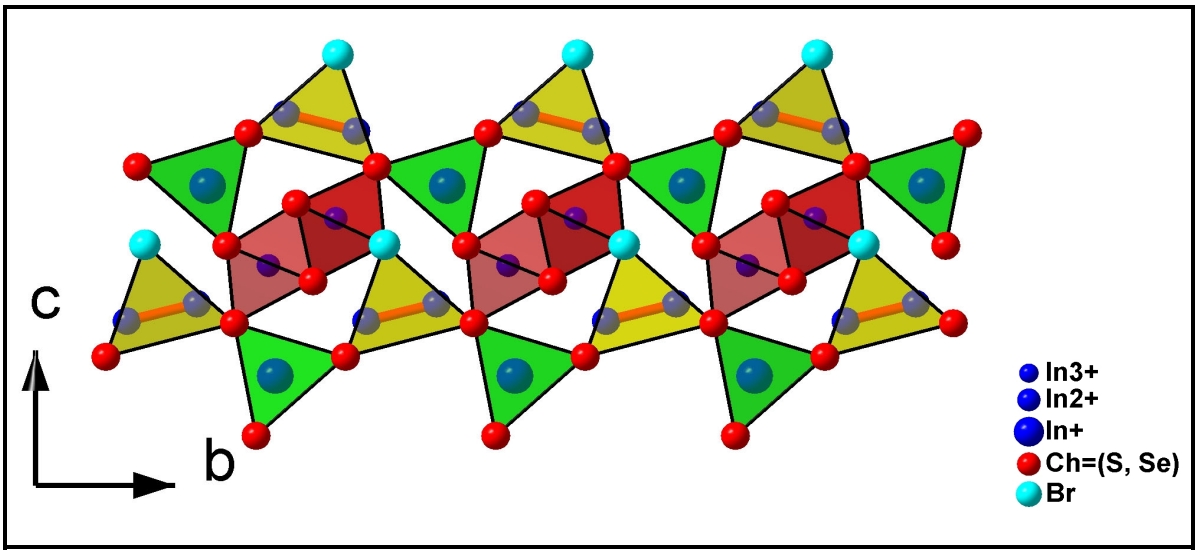

Fig. 4.38: Projection of the topological layer of the In_5Ch_5Br structure type.

4.3.8 Discussion of the inter-atomic distances

Interatomic distances up to 4 Å and their standard deviations for both compounds In_5S_5Br and In_5Se_5Br obtained from the last refinement are listed in table 4.17. The interatomic angles are listed in the table 8.10 in appendix.

Table 4.17: Inter-atomic distances in the isotypic compounds In_5S_5Br and In_5Se_5Br. * In3 and In4 have a formal charge of +2.

Atom	anion	In_5S_5Br /Å	In_5Se_5Br /Å
In1 (In^{3+})	- S/Se5	2.595(2)	2.710(2)
	- S/Se4 (2×)	2.628(1)	2.758(1)
	- S/Se3	2.631(2)	2.742(2)
	- S/Se1 (2×)	2.655(1)	2.789(1)
In2 (In^{3+})	- S/Se3 (2×)	2.532(1)	2.673(1)
	- S/Se2	2.544(2)	2.649(2)
	- S/Se1	2.600(2)	2.689(2)
	- Br (2×)	2.8815(7)	2.953(1)
In3* ($In)^{2+}$	- S/Se4	2.527(2)	2.639(2)
	- S/Se5 (2×)	2.540(1)	2.670(1)
	- In4	2.728(1)	2.739(2)
In4* ($In)^{2+}$	- S/Se2 (2×)	2.530(1)	2.660(1)
	- S/Se1	2.549(2)	2.667(2)
In5 (In^{+})	- S/Se4 (2×)	3.133(2)	3.189(2)
	- S/Se5 (2×)	3.231(2)	3.362(2)
	- Br	3.295(1)	3.425(2)
	- S/Se2 (2×)	3.384(2)	3.410(2)
	- S/Se3	3.418(2)	3.529(2)
	- S/Se1	3.955(2)	3.990(2)

Again, the coordination polyhedra around In^+ (In5) in In_5Ch_5Br are similar to the polyhedra of In^+ in MIn_5S_7 (M = In, Na, K, Tl) [93, 94] and in In_5Ch_5Cl. In this structure-type In^+ is three caped trigonal prismatic coordinated from chalcogenid and bromide atoms (Fig. 4.39). The prism itself is built up only by chalcogenid atoms: 2x Ch2, 2x Ch5 and 2x Ch4 (Fig. 4.39). The interatomic distances In5- chalcogenid/bromide are listed in table 4.17.

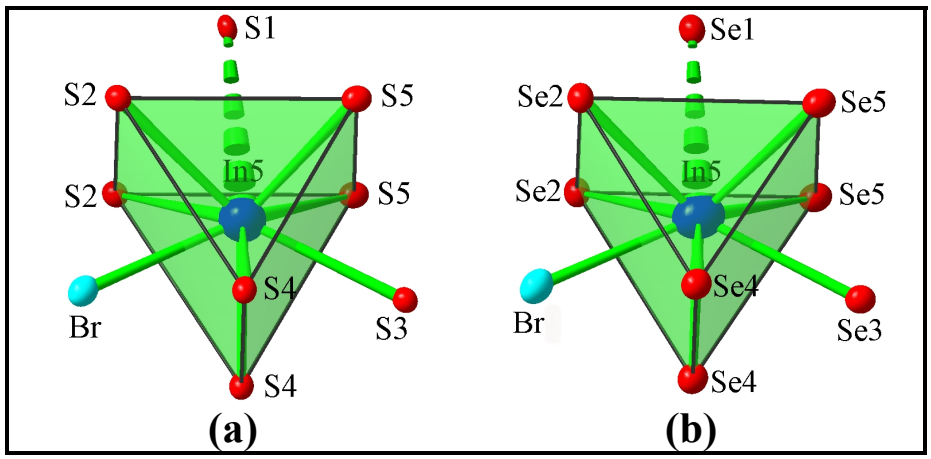

Fig. 4.39: Coordination spheres of In^+ species in (a) In_5S_5Br and (b) In_5Se_5Br. The presented ellipsoids are shown with a probability of 90%.

The longest observed distances are those between In5 and Ch1. These distances are almost equal to 4 Å, and thus the coordination number of In5 (In^+) can be described as 8+1.

In3 and In4 build with each other and six chalcogen atoms ethane analogue dumbbells In_2Ch_6, (Fig. 4.40). A comparison of the interatomic distances of these species in both structure types shows a good agreement between them (table 4.18).

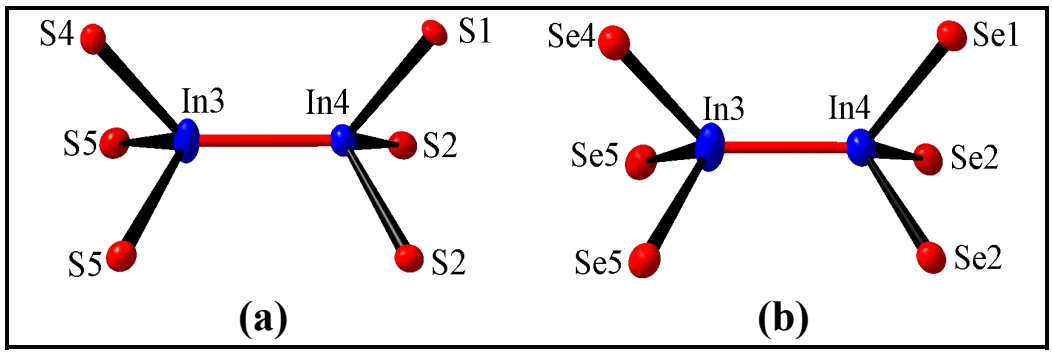

Fig. 4.40: Coordination spheres of the $(In_2)^{4+}$ dumbbells in (a) In_5S_5Br and (b) In_5Se_5Br. The presented ellipsoids are shown with a probability of 90%.

Table 4.18: Comparison of the interatomic distances of the In_2Ch_6 units in the new solids: In_5S_5Cl, In_5S_5Br, In_5Se_5Cl, In_5Se_5Br.

Compound	$\bar{d}_{In\text{-}In}$ (Å)	$\bar{d}_{In(a)\text{-}Ch}$ (Å)	$\bar{d}_{In(b)\text{-}Ch}$ (Å)
In_5S_5Cl	2.723(4)	2.554	2.524
In_5S_5Br	2.728(1)	2.536	2.536
In_5Se_5Cl	2.748(2)	2.659	2.656
In_5Se_5Br	2.739(2)	2.660	2.662

In analogy to the In_5Ch_5Cl structure, In1 and In2 are octahedrally coordinated. In1 is coordinated by six chalcogen atoms, while In2 has four chalcogen and two bromine neighbours (Fig. 4.41). Unlike the chloride-type structure, in the bromide-type structure the octahedra centred by In1 are pared (share a common edge) with octahedra centred by In2. Therefore instead of two kinds of double octahedra $InCh_6$-$InCh_6$ and $In_2Ch_4X_2$-$In_2Ch_4X_2$ observed in the chloride-type (Fig. 4.26), in the bromide-type a "hybrid" of these pairs is observed, namely $InCh_6$-$In_2Ch_4X_2$.

Similar to the chloride-type compounds, the average distances between indium and chalcogenides in bromine containing octahedra are significantly shorter compared to the octahedra without bromine atoms ($d_{In2\text{-}Ch}$ = 2.552 Å (In_5S_5Br) and 2.671 Å (In_5Se_5Br) compared to $d_{In1\text{-}Ch}$ = 2.632 Å (In_5S_5Br) and 2.757 Å (In_5Se_5Br)).

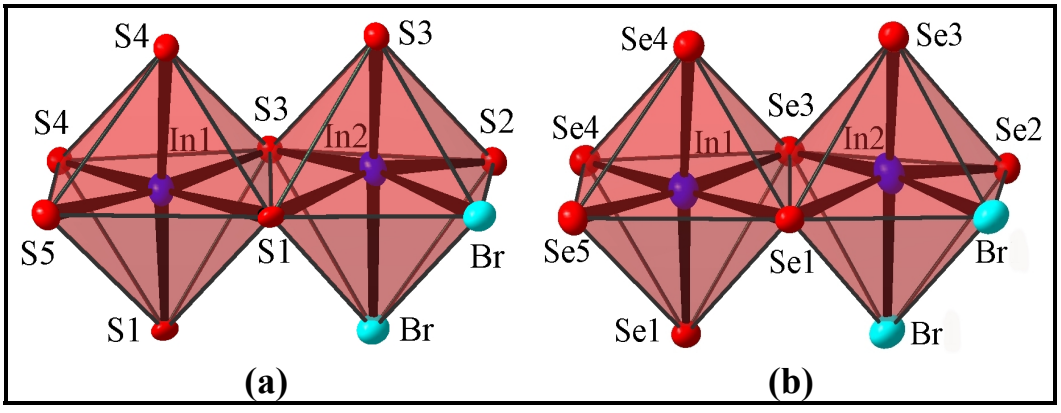

Fig. 4.41: Coordination spheres of In^{3+} in (a) In_5S_5Br and (b) In_5Se_5Br. The presented ellipsoids are shown with a probability of 90%.

4.3.9 The distribution of In^+ and $(In_2)^{4+}$ species around the edge-sharing double octahedral

In the bromide-type structure the distribution of the triangles centred by In^+ and/or $(In_2)^{4+}$ around $InCh_6$-$InCh_4Cl_2$ double octahedra is 3:3. As explained above, in the bromide-type structure only one kind of double octahedra exists, observed as a "hybrid" of the double octahedra existing in the chloride-type structure. Based on this explanation, the negative charge surrounding the double octahedra of the bromide-type structure is the average of the negative charge in both kinds of double octahedra of the chloride-type structure, therefore the environment of triangles centred by In^+ and $(In_2)^{4+}$ around these double octahedra is the average of the triangle environments observed in the chloride-type structure, schematically presented in figure. 4.42.

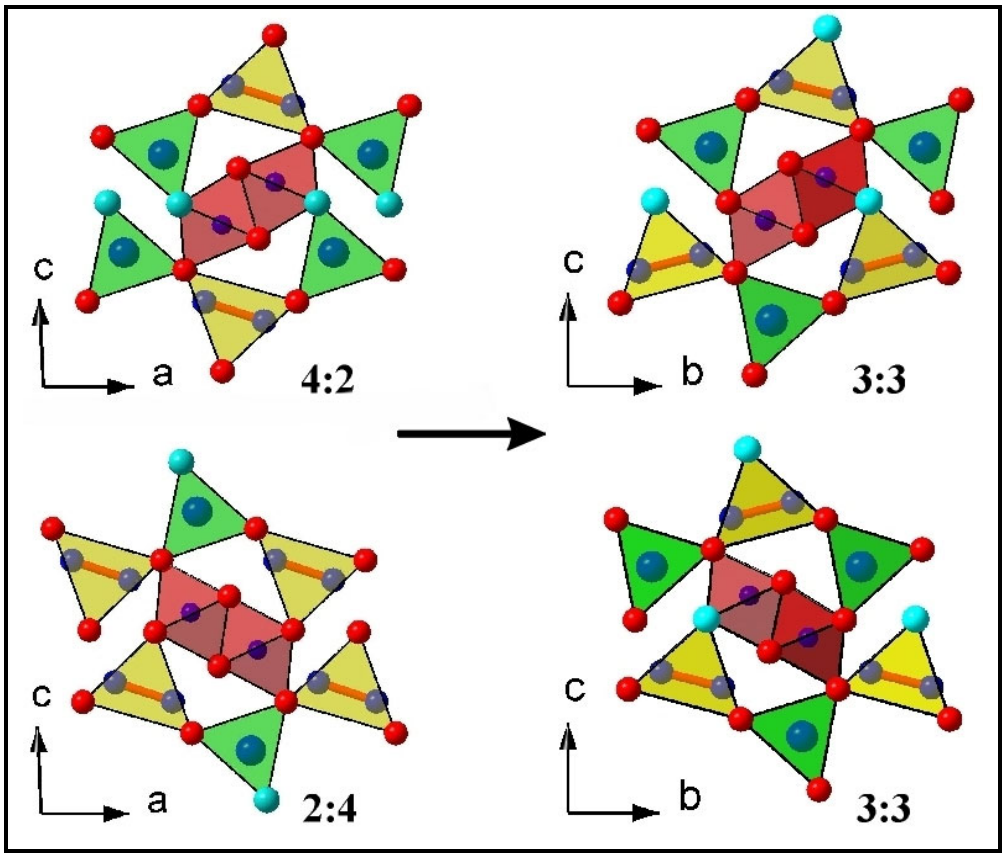

Fig. 4.42: Structural fragments of the chloride-type structure (4:2, 2:4 arrangements) and the bromide-type structure (3:3 arrangements). Focused on the distribution of the triangles centred by In^+ and $(In_2)^{4+}$, the structural fragment 3:3 of the bromide-type can be regarded as an "hybrid" (average) of the structural fragment of the chloride-type.

4.4 A brief comparison of the structures

A comparison of the results of the X-ray experiments of the In_5Ch_5Cl and In_5Ch_5Br structure-types (Fig. 4.43) shows great differences (table 4.19) derived especially from the anomalies of the chloride-type compounds. Regardless of the X-ray anomalies, the structures themselves present very close features. For a better comprehension of these differences and similarities, detailed HRTEM (High Resolution Raster Electron Microscope) investigations were carried out.

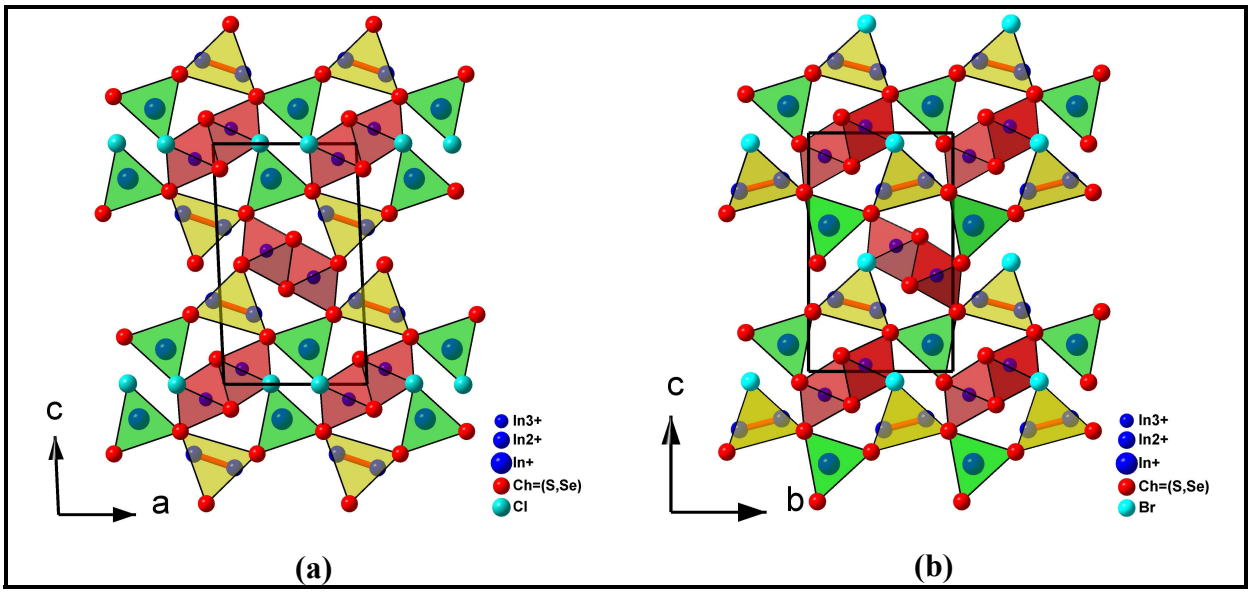

Fig. 4.43: Projection of the structures of (a) In_5Ch_5Cl along [010], and (b) In_5Ch_5Br along [100].

Table 4.19: Comparison of selected single crystal data obtained from the compounds In_5Ch_5Cl, In_5Ch_5Br (Ch = S, Se).

In_5Ch_5Cl (chloride-type)	**In_5Ch_5Br (bromide-type)**
Monoclinic ($P2_1/m$)	Orthorhombic ($Pmn2_1$)
Reticular pseudomerohedrical twinning	Inversion twinning
High R-values	Satisfactory R-values
In_5S_5Cl: $R_1 = 0.0982$, $wR_2 = 0.2348$	**In_5S_5Br**: $R_1 = 0.0312$, $wR_2 = 0.0553$
In_5Se_5Cl: $R_1 = 0.0860$, $wR_2 = 0.2346$	**In_5Se_5Br**: $R_1 = 0.0357$, $wR_2 = 0.0800$
High Fourier residuals	Low Fourier residuals
In_5S_5Cl: $\rho_{max.} = 3.406$ e/Å^3, $\rho_{min.} = -4.401$ e/Å^3	**In_5S_5Br**: $\rho_{max.} = 2.030$ e/Å^3, $\rho_{min.} = -1.459$ e/Å^3
In_5Se_5Cl: $\rho_{max.} = 3.980$ e/Å^3, $\rho_{min.} = -4.532$ e/Å^3	**In_5Se_5Br**: $\rho_{max.} = 2.010$ e/Å^3, $\rho_{min.} = -1.861$ e/Å^3

4.5 HRTEM investigations on In_5S_5Cl and In_5S_5Br and MAPLE calculations

4.5.1 The course of a HRTEM-investigation

At the initial stage of **HRTEM** (**H**igh **R**esolution **T**ransmission **E**lectron **M**icroscopy) observations, the orientation of thin crystallites must be determined by electron diffraction. The exact alignment of the investigated area with respect to the electron beam can be applied by means of electron diffraction through the employment of a **SAED** (**S**elected **A**rea **E**lectron **D**iffraction) aperture. Based on the adjusted orientation, high resolution micrographs along the defined zone axes can be obtained. Other zone axes can be adjusted by tilting the samples systematically. Due to the geometry of the objective lens, the tilts are limited to a maximum angle of about 30°.

4.5.2 The evaluation of the HRTEM-images

The interpretation of HRTEM images is not straightforward in any case, due to the influence of the CTF (Contrast Transfer Function) on HRTEM micrographs. The latter is particularly determined by lens aberrations, thickness of the sample and the focussing conditions. Changing the defocus value causes defined modifications of the CTF. It is therefore necessary to record images from each orientation with several defocus values (i. e. defocus series). One important step of HRTEM observations consists in the reproduction (image matching) of a complete defocus series based on the simulated images (e.g. multiple-slice procedure). However, even micrographs recorded under special conditions are important. Images which are recorded in the so called Scherzer defocus are not affected by gaps in the CTF. Therefore a direct correlation between HRTEM micrographs and structure projection can be achieved.

Using the theory of weak phase object approximation (WPOA), which states that the intensity of an object is proportional to its transparency, one can conclude that the black spots in those images relate to columns of atoms and white spots, to hollow spaces between the atoms. Based on this

theory the interpretation of the images can be facilitated when compared with the projections of the real structure.

The HRTEM measurements for the purpose of this work were performed in cooperation with the research group of Prof. Dr. Dr. h. c. mult. Simon (MPI Stuttgart) by Priv. -Doz. Dr. L. Kienle. More detailed information about the HRTEM measurements of these compounds (except what is mentioned here) is presented in the habilitation thesis of Mr. Kienle.

4.5.3 A general description of the SAED and HRTEM investigations in both structure-types

The HRTEM measurements were associated with the SAED and EDX measurements. The latter two, are auxiliary investigation methods and can be applied to supply the evidence of the lamellar real structures as well as to determine the composition in selected areas of the chosen crystal. For the HRTEM investigations one representative of each structure-type was considered, namely In_5S_5Cl for the chloride-type and In_5S_5Br for the bromide-type. Regardless of the similarities of the average structures described in details above, In_5Ch_5Cl and In_5Ch_5Br display noticeable differences in their real structures. These differences are listed as follows:

The SAED patterns of In_5S_5Br displayed only sharp reflections accompanied by a perfectly ordered real structure. All the patterns could be indexed based on the lattice parameters obtained from the X-ray investigation. The experimental and the simulated SAED patterns show a good agreement. The EDX measurements recorded in different areas within the investigated crystal exhibited no significant fluctuation of stoichiometry. The occurrence of the perfectly ordered real structure is confirmed by the HRTEM investigations. In accordance to the determined structure by X-ray measurements, the recorded HRTEM micrographs displayed the presence of layers with 3:3 arrangements in all the investigated crystals of In_5S_5Br. These arrangements are depicted as bright oval contrast in the micrographs.

In contrast to In_5S_5Br, the real structure of In_5S_5Cl presented a variety of anomalies which are derived from the two-dimensional order of the real structure. Beside the existence of the 4:2 and 2:4 arrangements (observed from the average structure) the HRTEM images and the SAED patterns

evidenced the existence of layers with 3:3 arrangements within the structure (this is not observed in the average structure determined by X-ray measurement). In addition, the presence of polymorphic intergrowth of layers with different arrangements, the polysynthetic twinning and the intergrowth of large separated domains containing In_6S_7 was observed. The latter observation was also supported by the EDX measurements (significant fluctuations of stoichiometry within the investigated crystal). These anomalies are described in details below.

4.5.4 Polymorph intergrowth of In_5S_5Cl

The average structure of In_5S_5Cl determined by the X-ray investigations displays only the presence of the alternating layers with 4:2 and 2:4 arrangements. HRTEM confirmed the existence of the layers with such arrangements only in small domains of the structure. In the simulated micrograph of figure 4.44a the existence of these arrangements is presented by regular and deformed S-shaped contrasts.

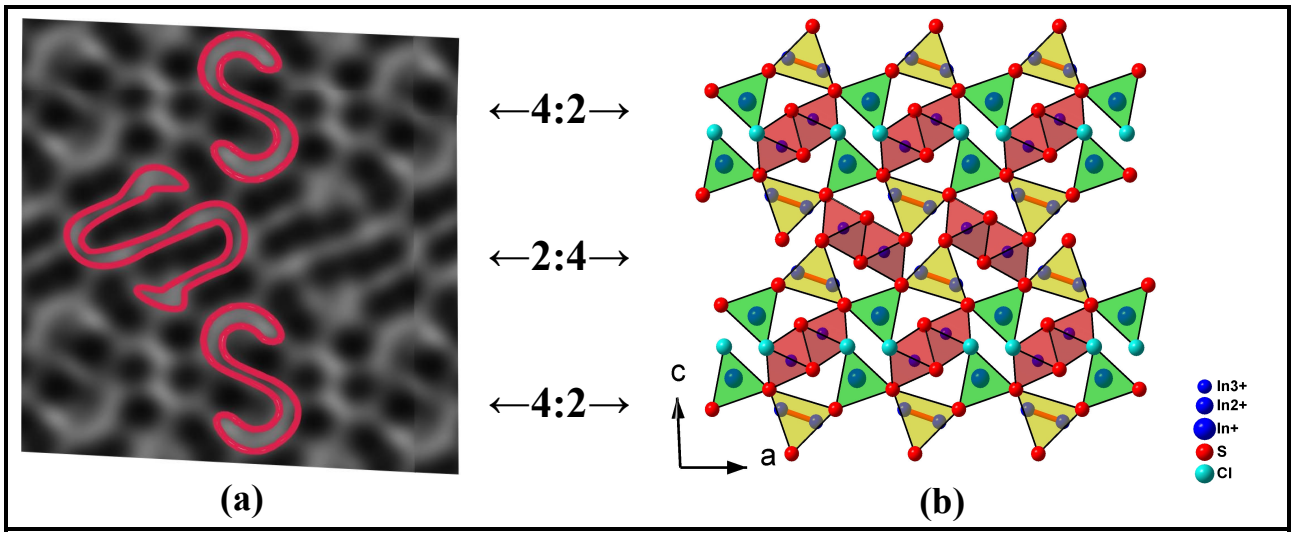

Fig. 4.44: (a) simulated micrograph of In_5S_5Cl along [010] (Δf = -55nm, t = 2 nm), the grey S-shaped contrasts explain the respective arrangement 4:2 and 2:4. For a better visualisation some of these S-shaped contrasts are marked in red, (b) projection of the structure of In_5S_5Cl along [010].

The regular S-shaped contrast belongs to the 4:2 arrangement while the deformed S-shaped contrasts correspond to the 2:4 arrangements.

In the real structure of In_5S_5Cl the periodic repetition of the layers with 4:2 and 2:4 arrangements is not continuous but interrupted by thin layers (lamellas) with 3:3 arrangements. The existence of these layers is presented by oval contrasts (see micrograph in fig. 4.45a). Only in rare cases the crystals display larger domains of one polymorph (see fig. 4.45).

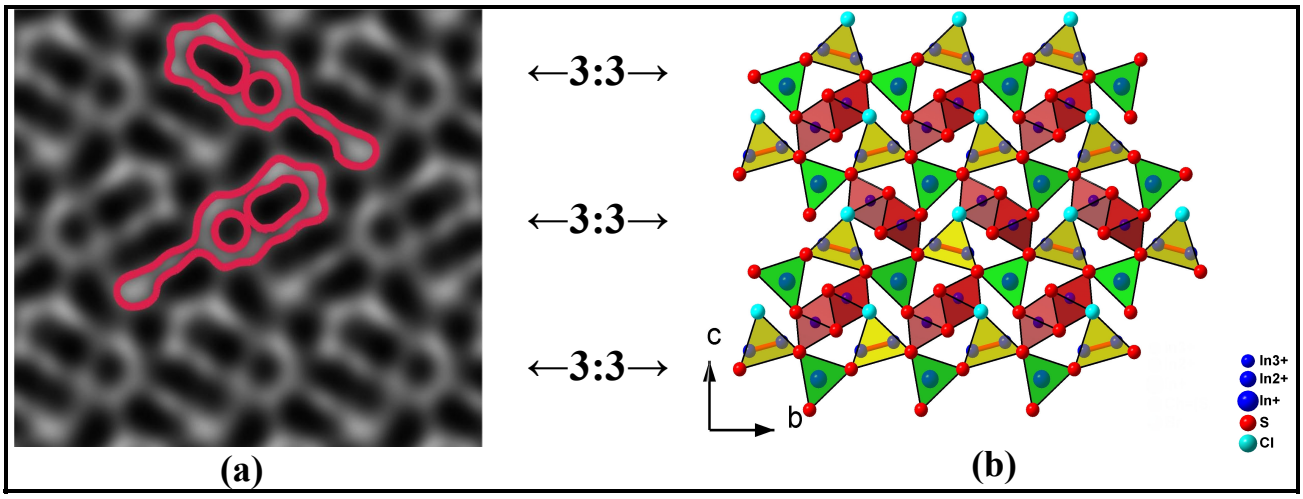

Fig. 4.45: (a) simulated micrograph of In_5S_5Cl along [-100] (Δf = -55nm, t = 2 nm), the grey oval-shaped contrasts explain the 3:3 arrangements. For a better visualisation two of these oval-shaped contrasts are marked in red. (b) fragment of the real structure of In_5Ch_5Cl.

At first glance the presence of 3:3 arrangements in the In_5S_5Cl-structure can be supposed to be derived from Br-impurities but EDX analysis displayed no traces of bromine.

As mentioned above, the SAED patterns recorded from separated or multiple domains proved the presence of the 3:3 arrangements. The diffraction patterns of $[010]_{mon}$ show characteristic splittings of the reflections deriving from the superposition of the orthorhombic and monoclinic domains. The latter was proved by the reproduction of the simulated patterns based on their superposition.

The simultaneous presence of layers with 3.3 arrangements beside the alternating layers with 4:2 and 2:4 arrangements could be realised by two different kinds of boundaries between the layers. These are:

a) boundaries between layers containing 3:3 and 2:4 arrangements (Fig. 4.46a)

b) boundaries between layers containing 3:3 and 4:2 arrangements (Fig. 4.46b)

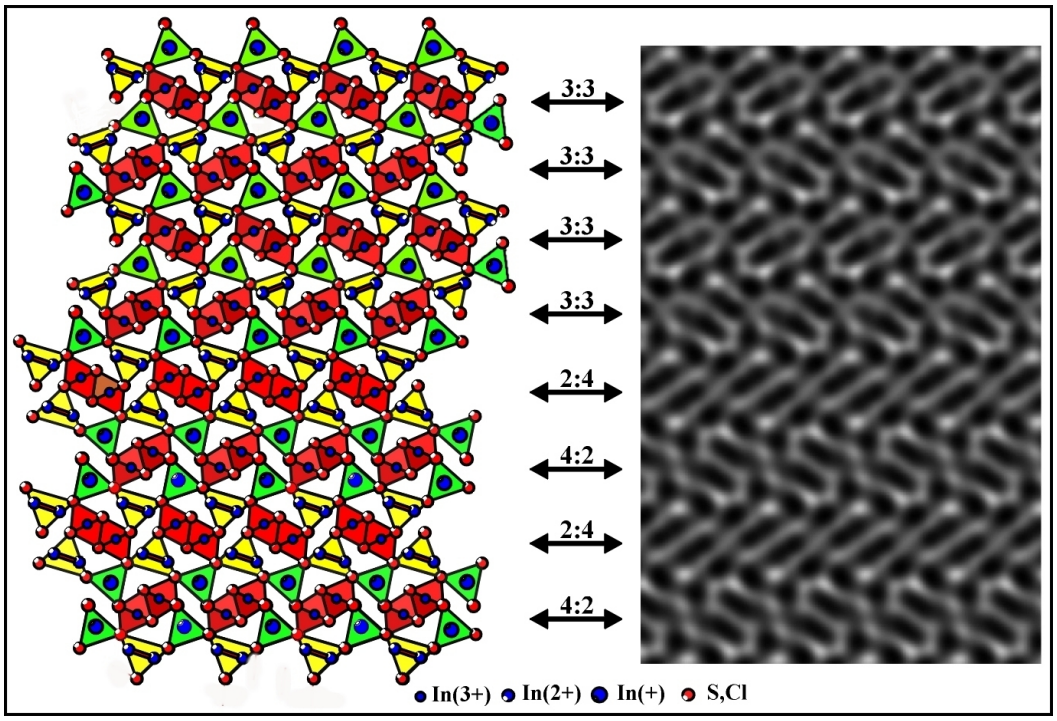

(a)

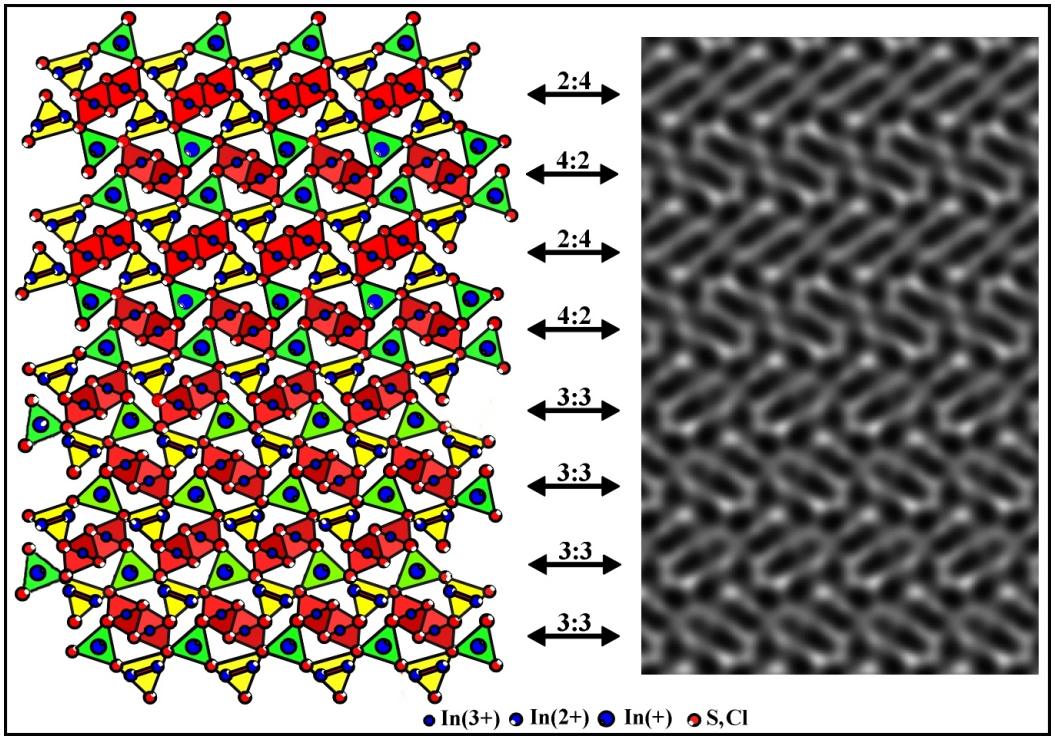

(b)

Fig. 4.46: Fragments of the structure showing two possible intergrowth of the polymorphs (left) the respective simulated HRTEM micrographs (right). a) Intergrowth with the boundary between layers with 3:3 and 2:4 arrangements, b) Intergrowth with the boundary between layers with 3:3 and 4:2 arrangements.

The simulated HRTEM micrographs (right) show deformed and regular S-shaped contrasts (at boundary) corresponding to 2:4 (Fig. 4.46a) and 4:2 (Fig. 4.46b) arrangements, both fitting well with the bright oval contrasts (3:3 arrangements).

The compatibility of the layers at the boundaries is excellent. This compatibility originates not only from the close similarity between the arrangements, but also from the close similarity of the lattice constants of the monoclinic and orthorhombic polymorphs (the lattice constants of the orthorhombic polymorph of In_5S_5Cl have been determined by SAED patterns recorded on separated domains of differently oriented crystals: a_{ortho} ~3.91 Å, b_{ortho} ~ 8.93 Å, c_{ortho} ~14.92 Å).

The occurrence of the lamellar intergrowth is displayed by the distinctive stripes observed in the bright field image (Fig. 4.47a). Further diffraction measurements of the selected area show the presence of the diffuse streaks generated from the nanoscale intergrowth (Fig. 4.47b).

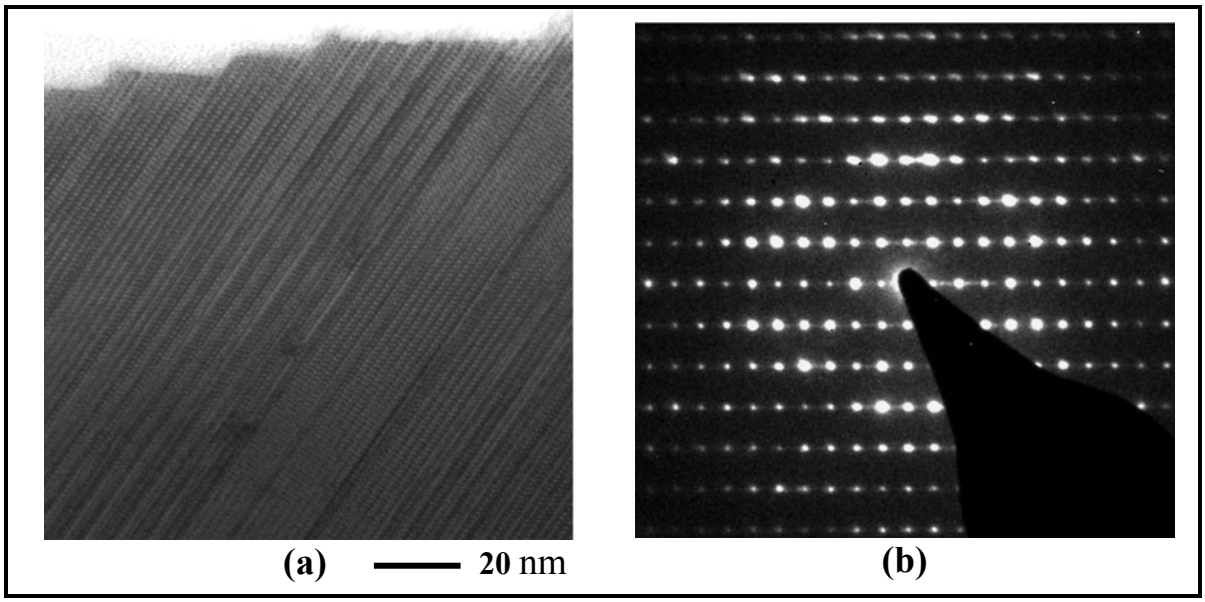

Fig. 4.47: (a) Bright-field image of In_5S_5Cl showing the lamellar intergrowth, (b) SAED pattern of In_5S_5Cl along $[100]_{orthorhombic}$.

The latter is confirmed by the HRTEM investigation of this region, which displayed mostly the presence of 3:3 arrangements (oval contrasts), intersected by layers of 2:4 and 4:2 arrangements (s-shape contrasts) (Fig. 4.48). Again, the simulated (left) and experimental (right) micrographs correlate well.

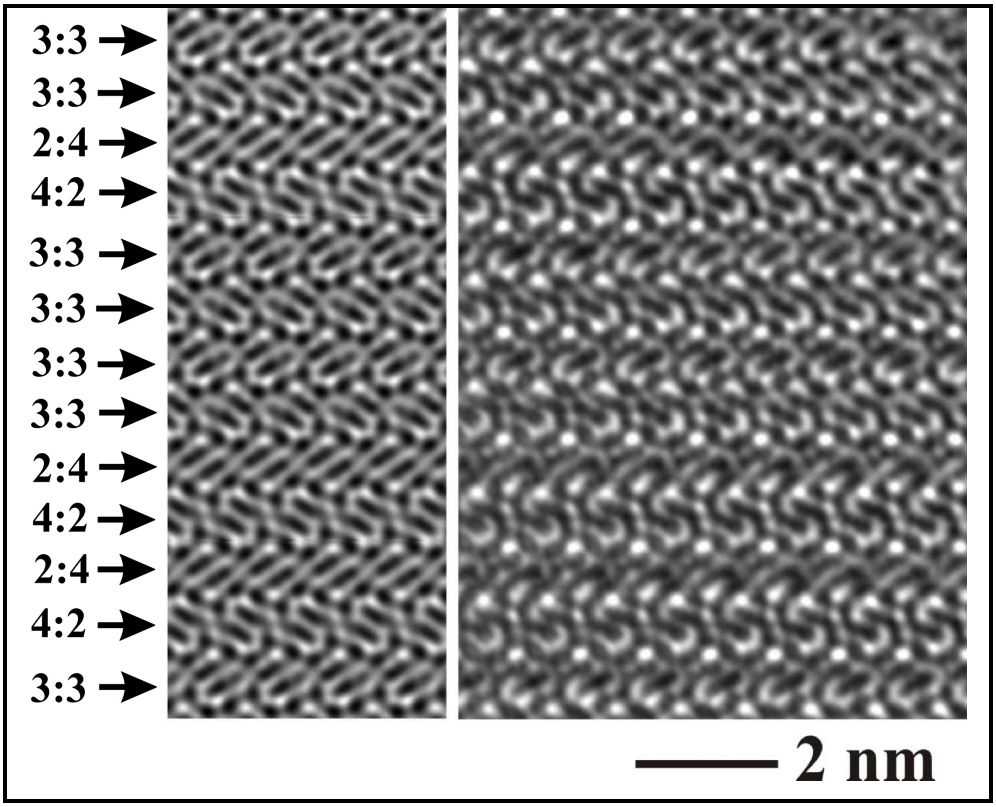

Fig. 4.48: Intergrowth of polymorphs containing orthorhombic and monoclinic layers, $[100]_{orthorhombic}$. Experimental (right) and simulated (left, Δf = -60 nm, t = 2 nm) HRTEM micrograph.

4.5.5 Polysynthetic twinning

The single crystal X-ray investigation of In_5S_5Cl shows the occurrence of twinning in all the investigated crystals. As mentioned in chapter 2, this twinning can be described by reticular pseudomerohedry, because the reflections *h0l* with *h* = 5n coincide. Regardless of the precious information about the twinning obtained from the X-ray investigations, several detailed uncertainties persist regarding the atomic structure of the twin boundary. To perform such investigations different techniques are considered.

Firstly, a dark field image of the small area of the investigated crystallite using strong diffractions contrast displays the presence of layers (bright or dark stripes fig. 4.49). These lamellas are aligned perpendicular to $[1\ 0\ 10]_{monoclinic}$ and their thickness ranges from 2 to 500 nm.

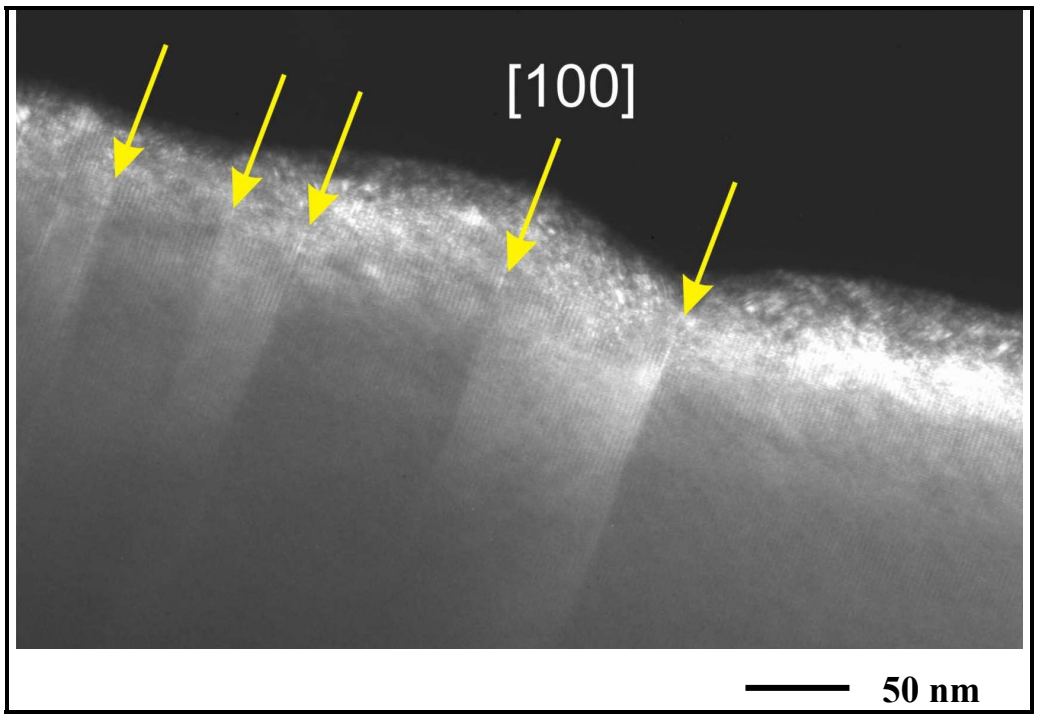

Fig. 4.49: Dark field image of a small area of the investigated crystallite displaying the presence of polysynthetic twinning, zone axis $[010]_{monoclinic}$. The yellow arrows point the boundary of the stacked lamellas.

The lamellas are separated and the sequentially recorded SAED patterns of the neighbouring lamellas display different orientations (Fig. 4.50).

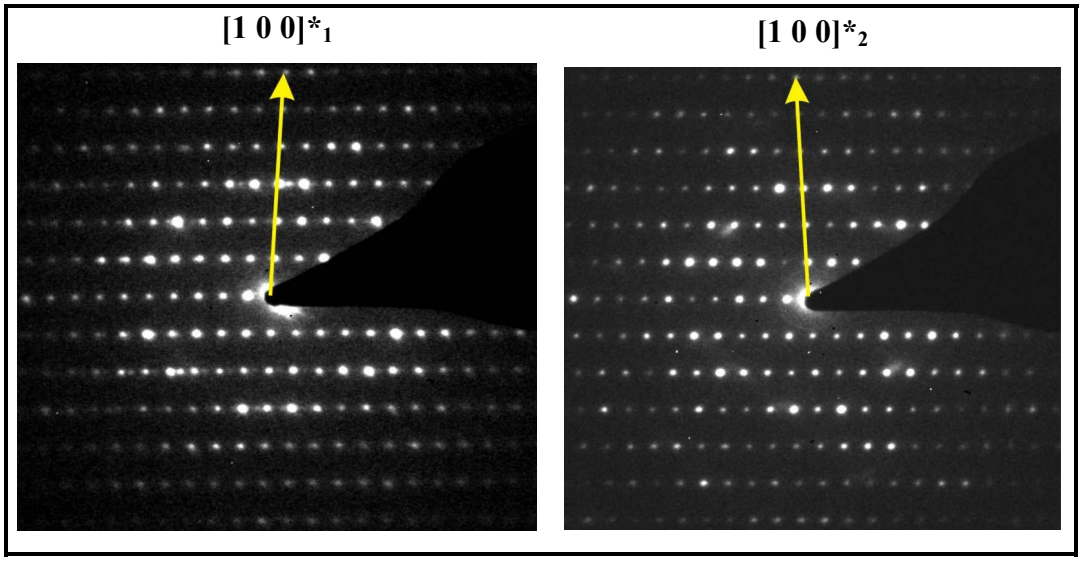

Fig. 4.50: SAED patterns of two neighbouring lamellas with different orientations in the zone axis $[010]_{monoclinic}$.

Secondly, the HRTEM investigation of two twinned domains orientated along [001] (Fig. 4.51) displays mainly the presence of the characteristic S-shaped contrasts. The S-shaped contrasts above and below the twin boundary represent the layers with 4:2 arrangements and 2:4 arrangements (Fig. 4.51 left). Surprisingly the twin boundary itself contains neither S-shaped nor deformed S-shaped contrast but oval contrasts resulting from 3:3 arrangements (Fig. 4.51).

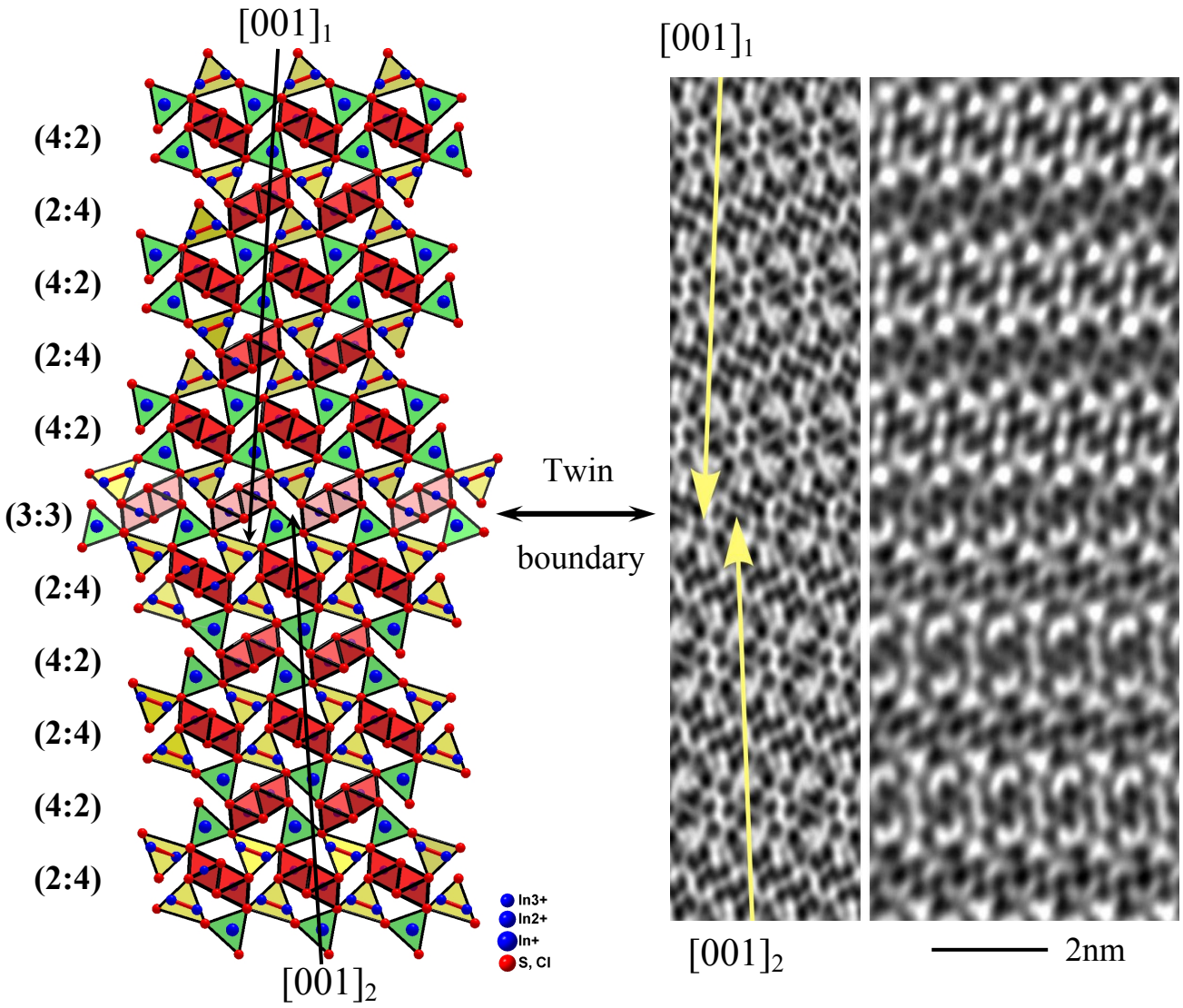

Fig. 4.51: Twinning of In_5S_5Cl. The 3:3 layer represents the twin boundary between 4:2 layer (above) and the 2:4 layer(below). The two monoclinic cells are shifted toward each other. At the simulated micrograph (middle, Δf = -60nm, t = 2nm) the domain shifting is emphasised by the yellow arrows.

The position of the neighbouring twinned lamellas, exhibits a shift of approximately $0.44a_{mon}$ depicted by black and yellow arrows in the projection of the real structure (left) and in the simulated HRTEM micrograph (right), respectively. A detailed investigation revealed that this single layer exactly at the twin boundary causes the shift of the domains. The shift is necessary to realise a perfect match of both domains.

The experimental HRTEM images of the twinned domains recorded at different defocus values show a good agreement with the respective simulated micrographs (Fig. 4.52). A better visualisation is presented by the experimental and simulated micrograph in the figure 4.52c (defocus value $\Delta f = -45$). The layer with 3:3 arrangements (oval contrasts pointed by arrow) between the layers with 4:2 (above) and 2:4 (below) arrangements represents the twin boundary.
The occurrence of the layer with 3:3 arrangements between the layers with 4:2 and 2:4 arrangements is observed above at the polymorphic intergrowth and at the same time at the polysynthetic twinning. This fact confirms once more the good compatibility between layers with different arrangements.

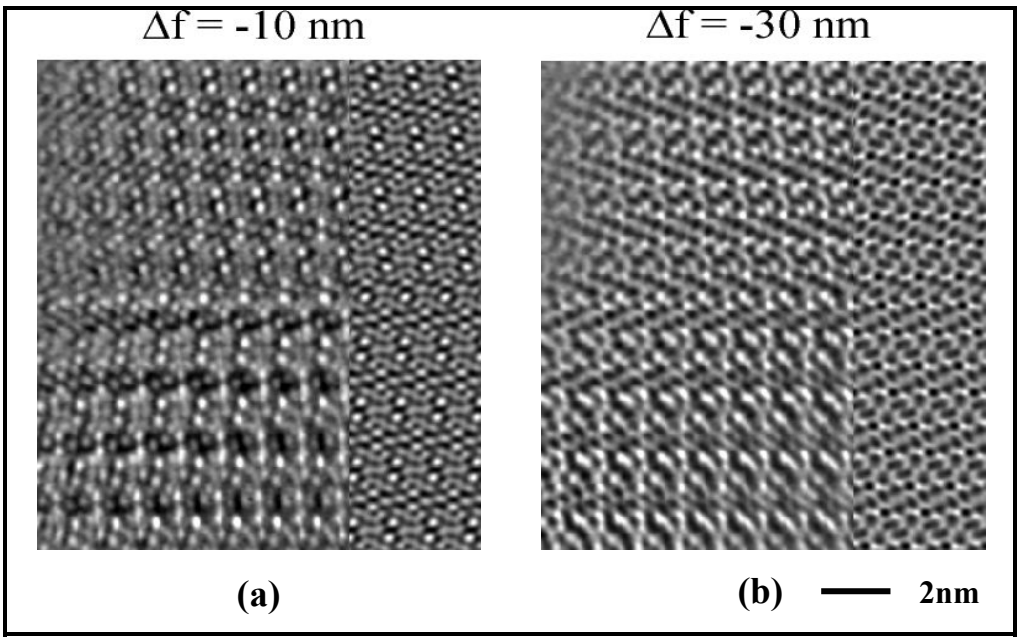

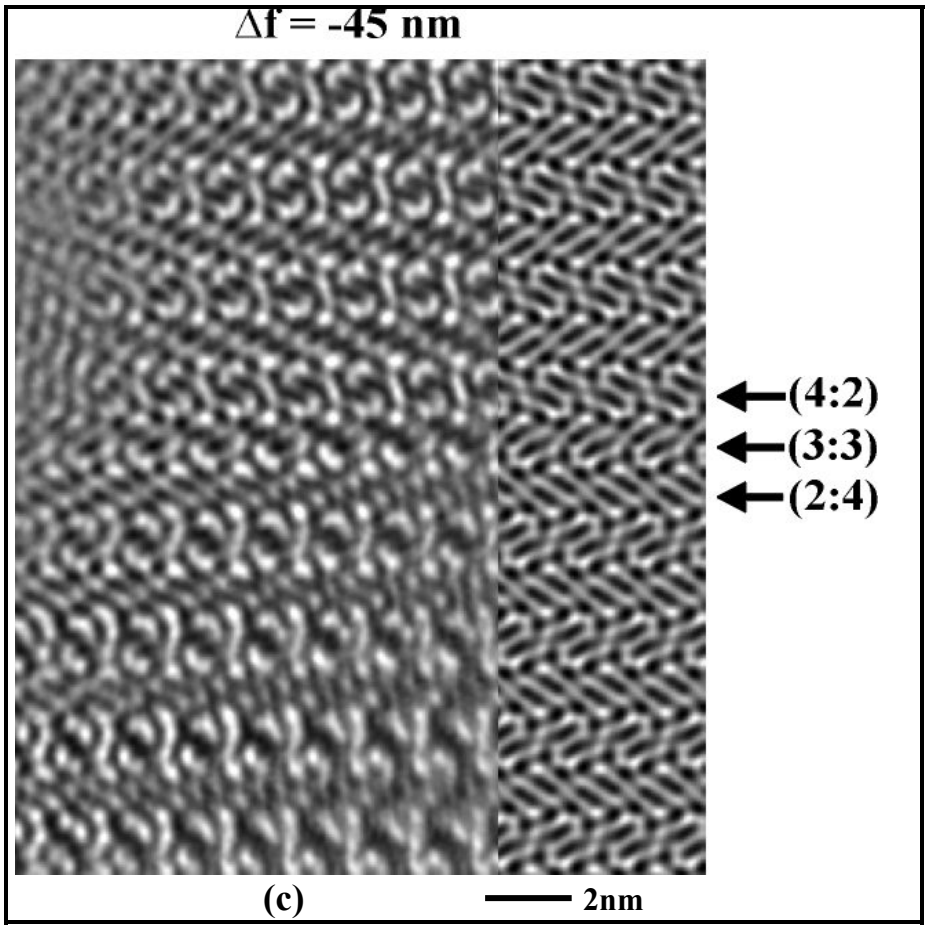

Fig. 4.52: Series of HRTEM images with different defocus value Δf (left) and their simulated micrographs (right). The presence of the layer with 3:3 arrangements at the twin boundary is displayed magnified in figure c.

4.5.6 Intergrowth of different compounds

The synthesis of In_5S_5Cl revealed an inhomogeneous product accompanied by In_6S_7. Both compounds, In_5S_5Cl and In_6S_7 have similar morphologies (needle-shaped), crystallographic parameters (see table 4.20) and crystallise in a common space group ($P2_1/m$). Another similarity between these compounds is related to the ability of twin formation. Hogg & Duffin [88] report this phenomenon in nearly all the investigated crystals of In_6S_7.

Table 4.20: The space group and the lattice parameters of the compounds In_5S_5Cl and In_6S_7.

Compound	S. Group	a /Å	b /Å	c /Å	β /°	V /Å^3
In_5S_5Cl	$P2_1/m$	8.949(1)	3.9169(5)	14.985(3)	93.66(1)	524.20(9)
In_6S_7	$P2_1/m$	9.090(5)	3.887(1)	17.705(4)	108.20(5)	577.64(8)

Beyond these similarities, a close inspection of the structure of In_6S_7 (projection along [010] Fig. 4.53) shows an additional similarity to the structure of In_5S_5Cl concerning the building layers. Both structures contain layers with 2:4 arrangements. The existence of this common feature in both structures and the similar characteristics mentioned above could facilitate an intergrowth of both compounds.

To prove the existence of the intergrowth of both compounds, the composition of several crystals of In_5S_5Cl was analysed by EDX measurements performed with a Philips CM30ST (scanning mode).
In figure 4.54a a dark field image of an analysed crystal is presented. The Cl-K mapping of this crystal exhibits the existence of two regions (Fig. 4.54b), one containing chlorine (dark contrast), and the other not (light contrast).

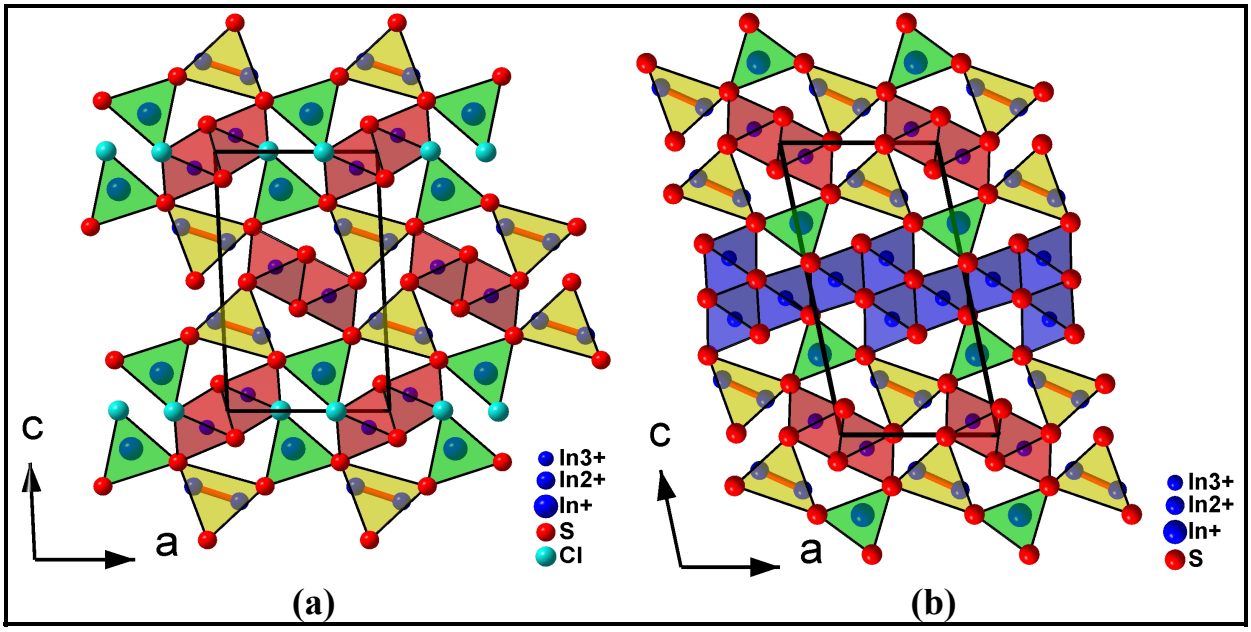

Fig. 4.53: Projection of the structures of (a) In_5S_5Cl, (b) In_6S_7 along [010].

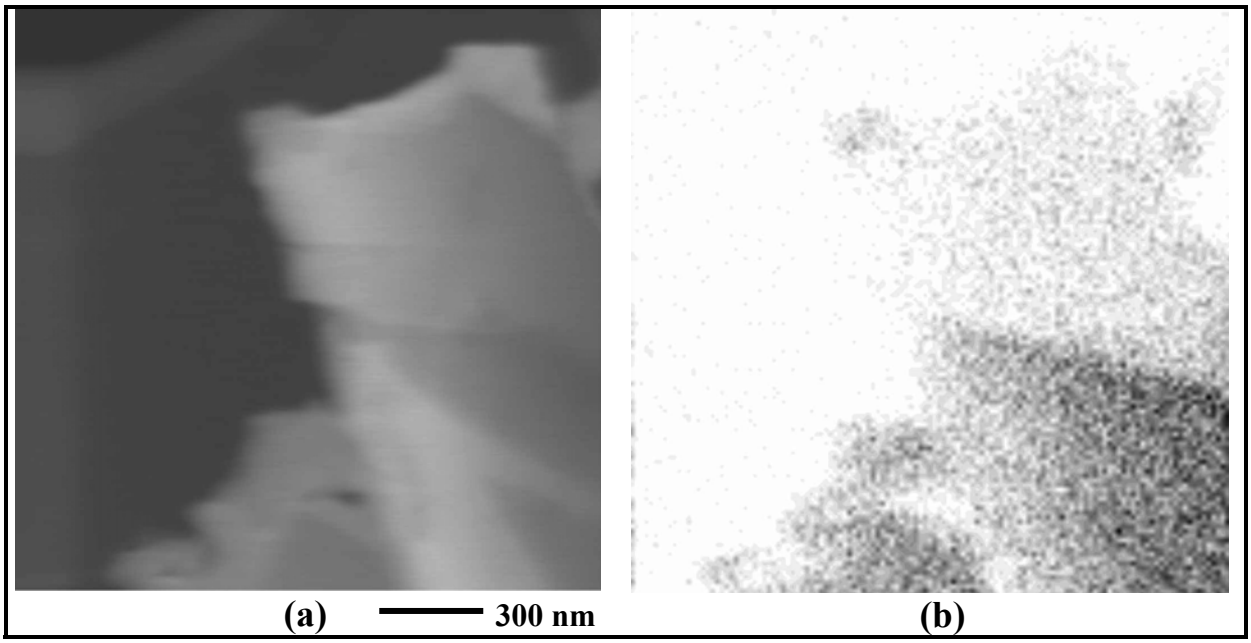

Fig. 4.54: (a) Dark field image of an In_5S_5Cl crystal, (b) Cl-Kα mapping (EDX) of the investigated crystal showing a chlorine rich area (dark contrast).

As evidenced by the quantification of point analysis the chlorine rich region (Fig. 4.54b) belongs to the compound In_5S_5Cl, while the other region represents In_6S_7. In order to obtain further

information about these regions (marked by yellow circles and centred with numbers 1 and 2), SAED patterns of both were recorded.

The SAED pattern of the region 1 displays no anomalies but only sharp reflections (Fig. 4.55(1)) while the region 2 exhibits the presence of the twinning (Fig. 4.55(2)).

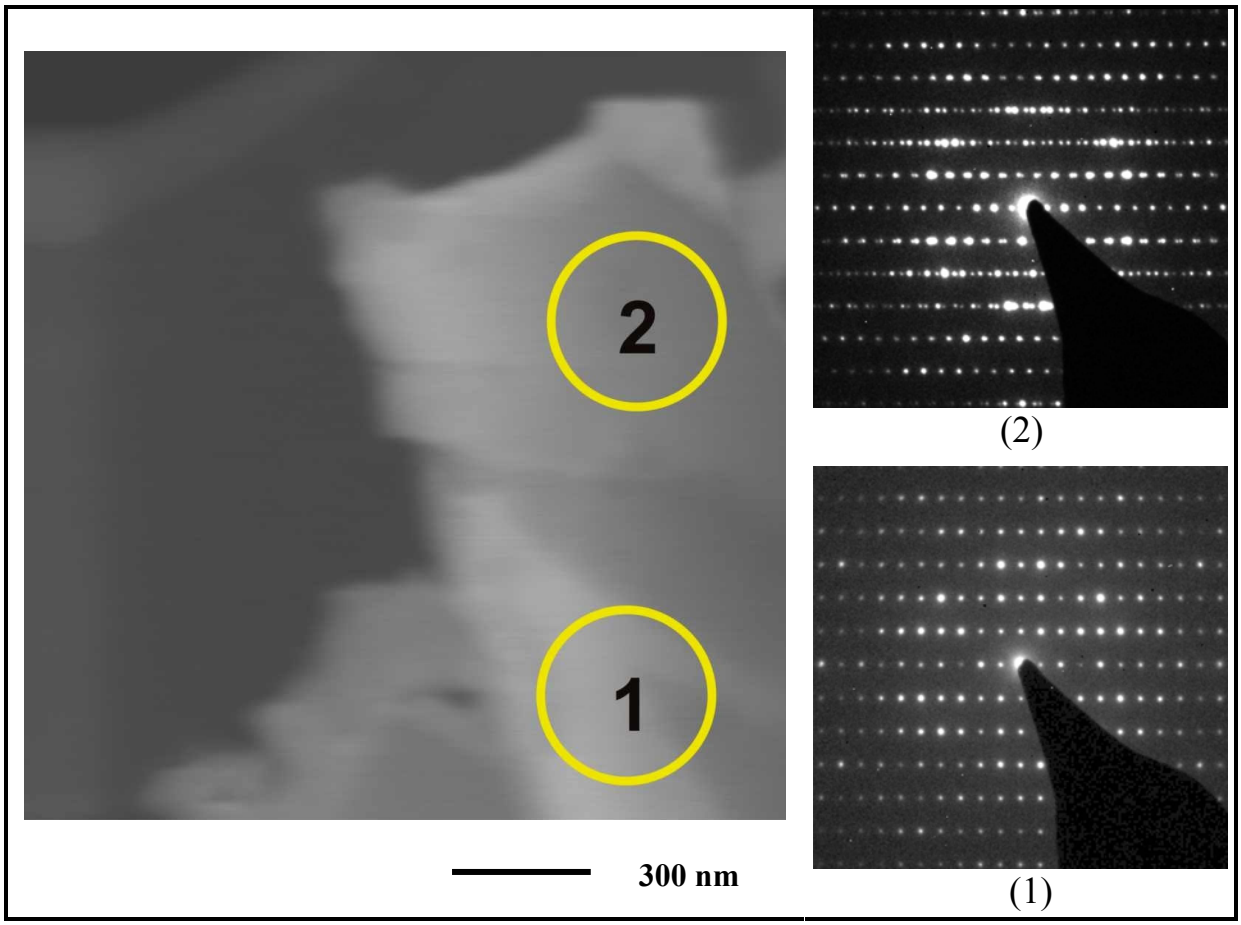

Fig. 4.55: Dark field image of an investigated crystal. SAED patterns of: (1) region containing a domain of In_5S_5Cl, (2) region containing twinned domains of In_6S_7.

The HRTEM image recorded from a small area between the regions 1 and 2 shows mainly monoclinic layers of In_6S_7 grown together with orthorhombic layers of In_5S_5Cl (Fig. 4.56). The orthorhombic layers of In_5S_5Cl are perturbed by two monoclinic layers of the same compound. The presence of a large domain of orthorhombic In_5S_5Cl between the monoclinic domains of In_6S_7 (twinned) and In_5S_5Cl leads to an almost perfect SAED pattern of the region where this domain is

located (Fig. 4.55 (1)). The occurrence of the boundary between the layers with 3:3 arrangements of the In_5S_5Cl and the layers with 2:4 arrangements of In_6S_7 confirms the good compatibility. Therefore, it can be concluded that a good compatibility exists not only between layers with different arrangements of one compound, but also between similar layers found in other compounds too.

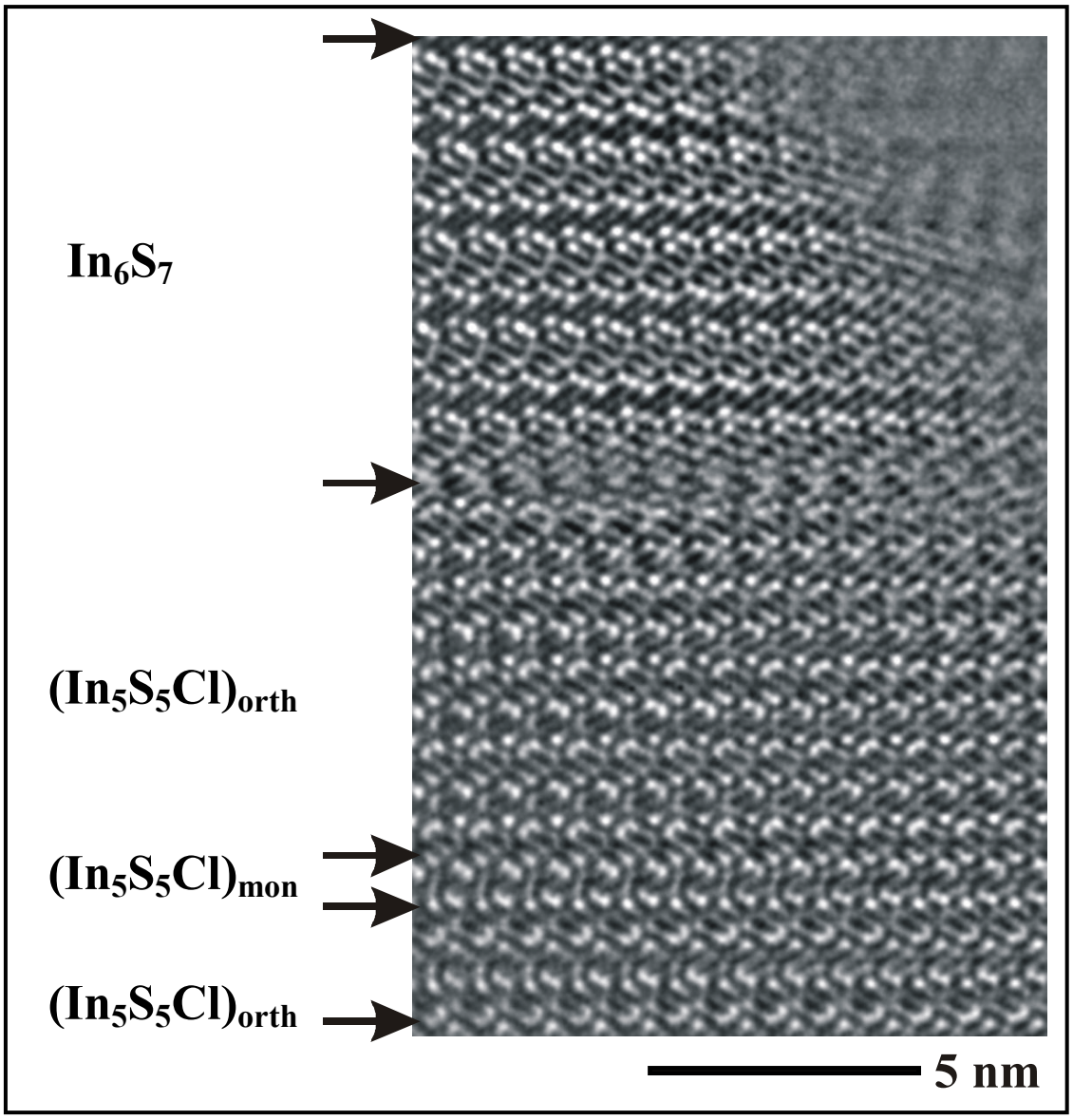

Fig. 4.56: Experimental micrograph of the investigated crystal of In_5S_5Cl, (Δf = -60 nm, thickness 5 nm).

4.5.7 Calculations of MAPLE values

The MAPLE (**M**adelung **P**art of **L**attice **E**nergy) [106-108] calculation represents a tool to check the validity of the structure. The correctness of the found structure can be judged by comparing the MAPLE value of the synthesised compound (ternary or polynary) with the sum of the MAPLE values of binary compounds. If the polynary compound has a similar nature to the binary compounds (e. g. ionic) and if the environments of the ions in these compounds are similar, a difference between the MAPLE values not higher than 1 % can be expected.
In the following, the calculated MAPLE values (MAPLE 4 [P19]) of the compounds In_5S_5Cl, In_5Se_5Cl, In_5S_5Br and In_5Se_5Br are compared with the MAPLE values of the corresponding binary compounds according to equation (4.1).

$$\mathbf{MAPLE(In_5Ch_5X) = MAPLE(In_2Ch_3) + 2\ x\ MAPLE(InCh) + MAPLE(InX)} \qquad \mathbf{(4.1)}$$

$$\mathbf{Ch = S, Se, and\ X = Cl, Br}$$

The results from these comparisons are listed in the table 4.21 and tables 8.11-8.13 in appendix. Deviations of 1% and 0.72 % were observed in the case of In_5S_5Cl and In_5Se_5Br. The comparison of In_5Se_5Cl and In_5S_5Br with the sum of binary compounds displayed deviations higher than 2% (see appendix). The observed discrepancy of approx. 2% can be dedicated firstly to the structural differences of the considered species (differences in the coordination spheres) and secondly to the bonding situation of indium in the ternary and in the binary compounds (two indium atoms of each considered ternary compound are covalently bonded like in InCh (Ch = S, Se) and InX (X= Cl, Br). Haas & Jansen [109] report deviations up to 4.7 % for the comparison of the compounds with different structural properties and bonding nature. The obtained MAPLE values are quite satisfactory confirming the correctness of the considered structures.

Table 4.21: MAPLE values in kcal mol^{-1} of In_5S_5Cl compared with β-In_2S_3 [110], InS [100] and InCl [111].

Atom	**n**	**binary**	**ternary**	**n x Δ[1)]**
In1	1	885.9332[a)]	832.3960	-53.5372
In2	1	877.4353[b)]	875.1993	-2.2360
In3	1	385.0382[d)]	328.1525	-56.8857
In4	1	385.0382[d)]	341.8242	-43.2140
In5	1	86.7901[e)]	149.9421	63.1520
S1	1	446.6314[c)]	443.0187	-3.6127
S2	1	446.6314[c)]	473.9330	27.3016
S3	1	446.6314[c)]	396.2415	-50.3899
S4	1	384.9244[d)]	462.0516	77.1272
S5	1	384,9244[d)]	387.1657	2.2413
Cl	1	86.3743[e)]	78.7052	-7.6691
		∑ = 4816.3523	∑ = 4768.6298	∑ = -47.7225 → **1%**

[1)] ternary – binary, [a)] from In_2S_3 [(CN 6) + (CN 4)], [b)] from In_2S_3 (CN 6), [c)] from In_2S_3 (mean value), [d)] from InS, [e)] from InCl.

4.6 Substitution experiments

In the course of the investigations about the existence of further mixed valence compounds several experiments were performed based on the selective substitution of elements in In_5Ch_5X (Ch = chalcogen; X = halogen).

The substitution experiments were carried out in three directions; the substitution of In-species, the substitution of chalcogenides and the substitution of halides.

The mixed valence character of these compounds In_5Ch_5X offers three different substitution possibilities of indium species, namely, the substitution of: a) In^+, b) $(In_2)^{4+}$, c) In^{3+}. In a similar way several substitutions can be applied for the chalcogenides and halides respectively (see table 4.22).

Table 4.22: The possibilities of substitution in In_5Ch_5X.

Ions in In_5Ch_5X	**Substituting ion**
In^+	K^+, Na^+, Rb^+, Tl^+, Ba^{2+}, Sr^{2+}
$(In_2)^{4+}$	$(Al_2)^{4+}$, $(Ga_2)^{4+}$
In^{3+}	Al^{3+}, Ga^{3+}, Tl^{3+}, Cr^{3+}
S^{2-}	Se^{2-}
Se^{2-}	Te^{2-}
Cl^-, Br^-	I^-

Not every ion can be exchanged by another ion with the same oxidation state. To perform reasonable substitutions some properties of the "candidate" ions like radius and coordination number (CN) should be taken into account. The distribution of the effective radii and the respective coordination numbers of selected ions are presented in figures 4.57, 4.58. The performed substitutions are listed in table 8.14 in appendix.

For the substitution of In^+-species in In_5Ch_5X several ions with the same coordination number and similar radii were employed. The substituting ions were mainly those of the alkali metals, the earth alkaline metals and Tl^+.

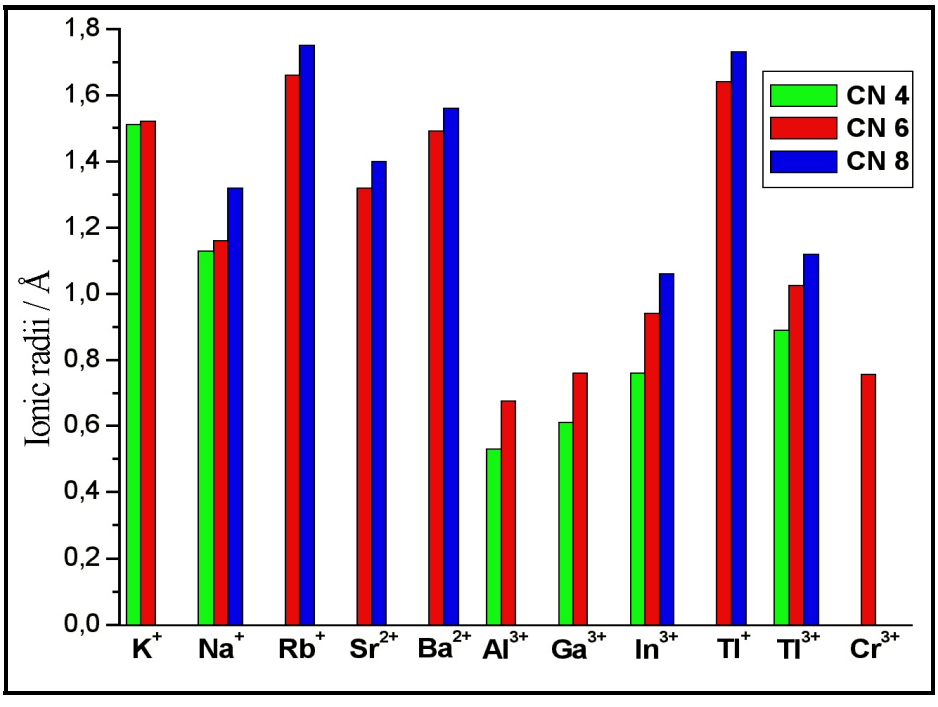

Fig. 4.57: The effective ionic radii for selected ions according to Shannon [115]. The coordination number is presented by different colours (see legend).

It is assumed that the substitution of In^{+} with an earth alkaline metal ion leads to vacancies in the structure due to the charge compensation. The evidence of the substitution of In^{+} species by bivalent ions (Sn^{2+}, Pb^{2+}) is already reported by Walter [92] in the compounds $Sn_xIn_{6-2x}Se_7$ and $Pb_xIn_{6-2x}Se_7$.

The reactions for the substitution of In^{+} in In_5Ch_5X by alkali metals were carried out using their halides (previously treated) or directly the elements as educts. The earth alkaline elements Sr, Ba were used in form of their sulphides. For all these substitution experiments only the formation of binary products such as In_6S_7 and InS was observed. This phenomenon can be explained by the high affinity of alkali or earth alkaline metals toward the halides and the high formation enthalpy of these compounds.

Further syntheses involving thalium or thalium (I) halides as educts, yielded the mixed crystals $TlIn_4S_5Cl$ and $TlIn_4Se_5Cl$ which are explained in details below (reactions 7, 9, see table 8.14 in apppendix). Instead of the expected $TlIn_4S_5Br$ only TlBr, InS and In_2S_3 could be obtained.

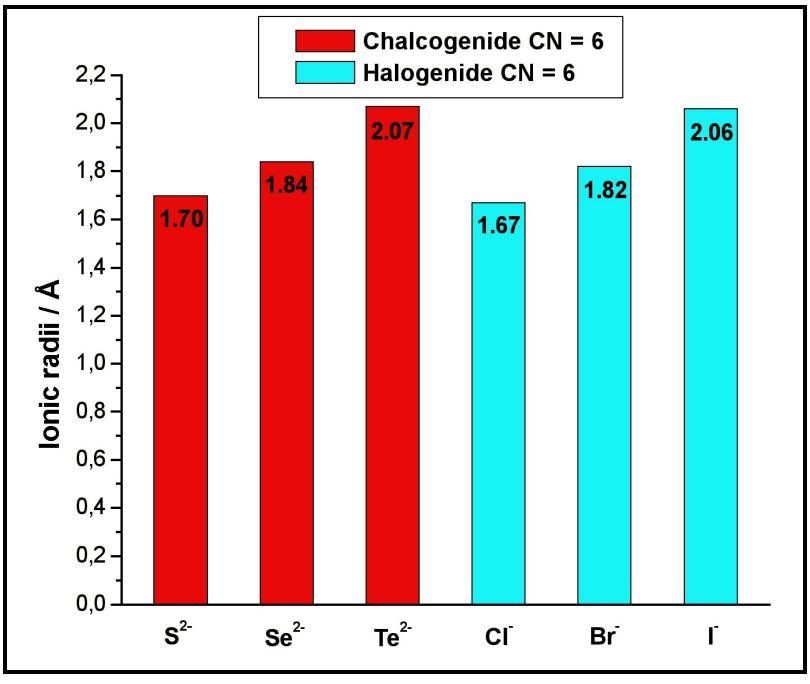

Fig. 4.58: The effective ionic radii for selected chalcogenide and halogenid ions according to Shannon [115].

Attempts to substitute the $(In_2)^{4+}$ species involved mainly the third group elements, Al and Ga (reactions 11-16, see table 8.14 in appendix). These substitution reactions were performed based on the existence of several compounds which contain covalent Al-Al or Ga-Ga bonds (reported by Paashaus & Kniep) [102].

Moreover, In^{3+}-species (CN = 6; octahedrally coordinated) were substituted by elements of the third group and Cr (reactions 11-18, see table 8.14). The effective radii of these ions are comparable to that of In^{3+} (Al^{3+} = 0.675 Å, Ga^{3+} = 0.76 Å, In^{3+} = 0.94 Å, Cr^{3+} = 0.755 Å) in their octahedral coordination.

Most of the syntheses involving Al and Ga yielded binary or ternary chalcogenides (ternary chalcogenides in the case of a partial substitution of binary compounds e.g. $Al_xIn_{(6-x)}S_7$) and binary halides $MHal_x$ (x =1-3). Traces of the latter could not be detected by X-ray powder diffraction, due to their enhanced sensitivity toward moisture. For such measurements the sample was ground in an inert atmosphere and measured shortly (20 min) between two foils welded together. Some of the samples were measured in capillaries.

The substitution of one In^{3+} by Cr^{3+} in In_5Se_5Cl (reactions 18) yielded a quarternary compound ($In_4In_xCr_{(1-x)}Se_5Cl$; see diffraction pattern in figure 4.59). Attempts to obtain a similar quarternary compound in the case of In_5S_5Cl failed.

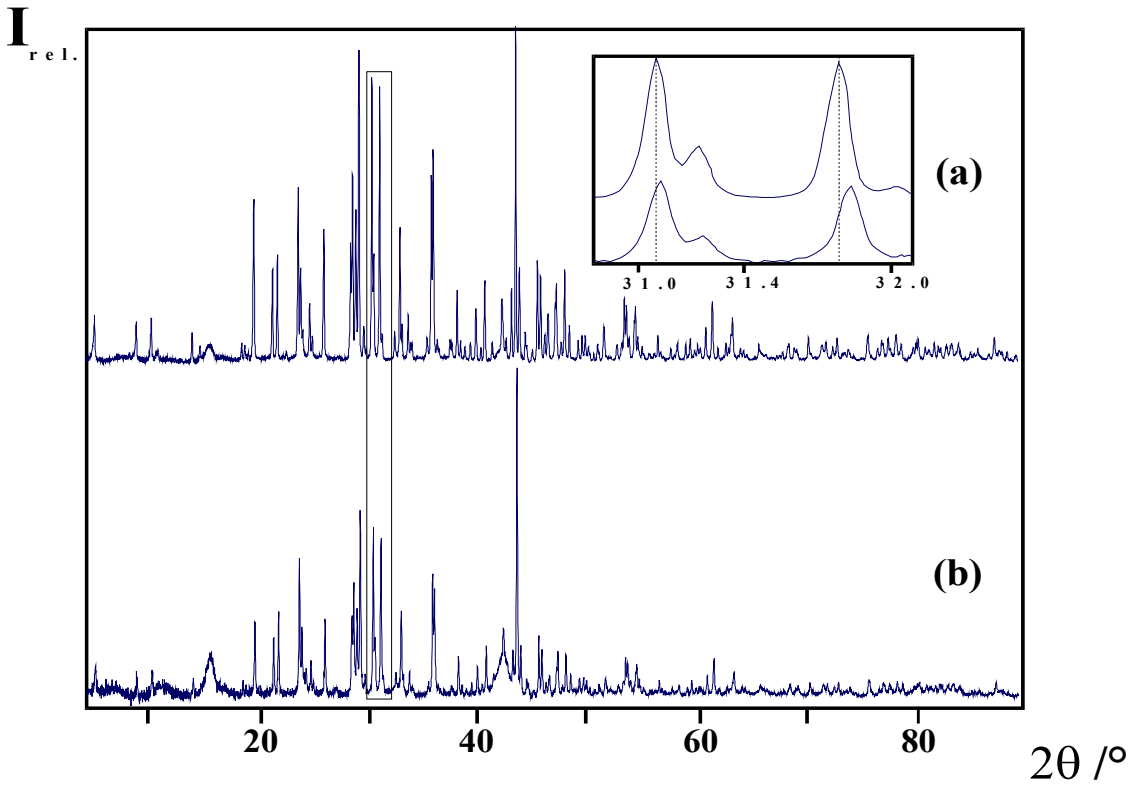

Fig. 4.59: Comparison of the measured powder diffraction patterns of: a) In_5Se_5Cl and b) $In_{(5-x)}Cr_xSe_5Cl$. For a better visualisation of the shift to the greater 2θ values a magnification of the contoured section (31.0 – 32.0 in 2θ) is shown at the top-right.

Table 4.23: Comparison of the refined lattice constants for the compounds In_5Se_5Cl and $In_4In_xCr_{(1-x)}Se_5Cl$.

Compound	a /Å	b /Å	c /Å	β /°	V /Å^3
In_5Se_5Cl	9.2391(3)	4.0951(1)	15.2920(6)	92.743(3)	577.91(2)
$In_4In_xCr_{(1-x)}Se_5Cl$	9.2352(9)	4.0947(3)	15.289(2)	92.741(7)	577.49(6)

The comparison of the diffraction patterns of In_5Se_5Cl and $In_4In_xCr_{(1-x)}Se_5Cl$ exhibits a slight shift to higher 2θ values for the latter. This shift is confirmed by the refined lattice constants (see table 4.23).

In addition to substitution of indium species, further substitutions have been carried out, namely the substitutions of chalcogenides and halides. Similarly such substitutions were performed based on the criteria of radii and coordination number of the substituting atoms (see table 4.23). The first attempt to the complete substitution of sulphur atoms in In_5S_5X by selenium atoms yielded the

compounds In_5Se_5X. Attempts for a complete substitution of selenium by tellurium atoms failed, and instead of In_5Te_5X, the binary compounds InTe or In_7Te_{10} were obtained (see reactions 22, 23). The partial substitution of sulphur by selenium atoms in both compounds; In_5S_5Cl and In_5S_5Br, yielded the respective mixed crystals ($In_5S_{2.5}Se_{2.5}Cl$; $In_5S_{2.5}Se_{2.5}Br$, reactions 19, 20). The powder diffractions and the lattice constants determined by single crystal X-ray diffraction measurement are listed in appendix (Fig. 8.6; table 8.15). The partial substitution experiments have shown that a part of the selenium atoms can be substituted by tellurium atoms. A representative of these substitutions is ($In_5Se_{(5-x)}Te_xBr$) obtained from the experiment 21. The obtained diffraction pattern of the latter shows a shift to low 2θ angles (see Fig. 4.60) confirming the substitution of smaller Se-atoms by bigger Te-atoms.

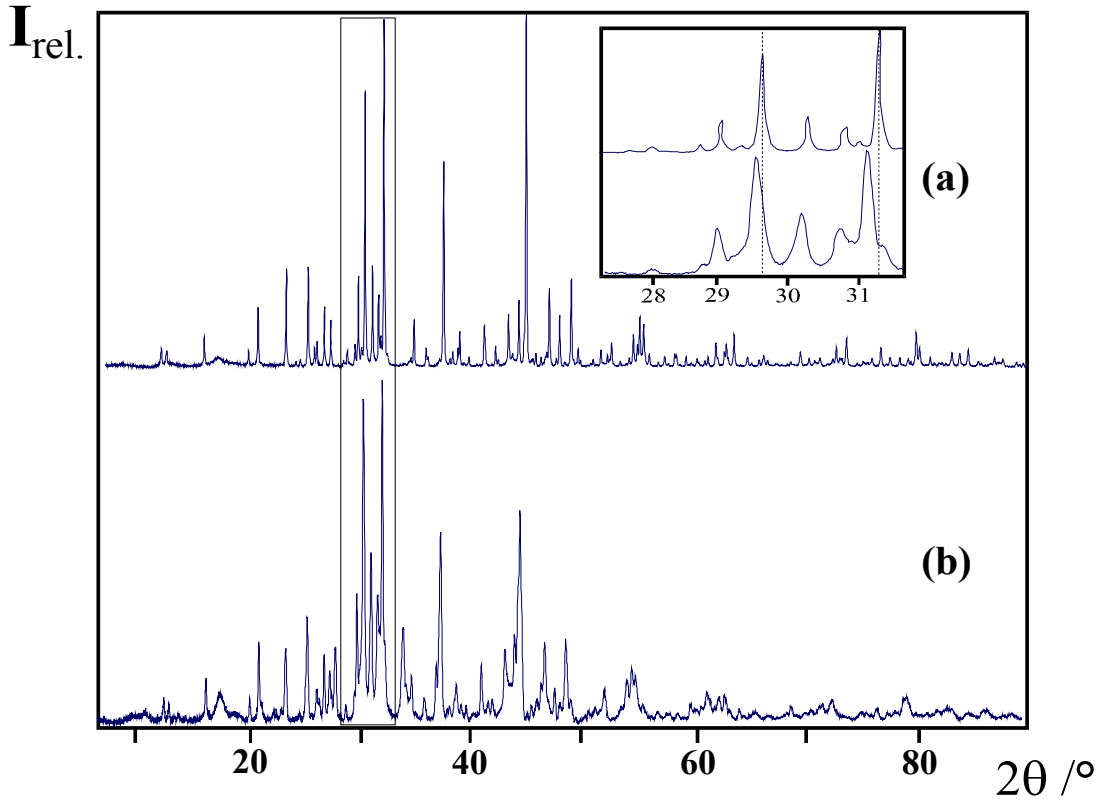

Fig. 4.60: Comparison of the measured powder diffraction patterns of: a) In_5Se_5Br and b) $In_5Se_{(5-x)}Te_xBr$. For a better visualisation of the reflections shifting to the smaller 2θ values, a magnification of the contoured section (31.0 – 32.0 in 2θ) is shown at the top-right.

The attempts for a complete substitution of chlorine by bromine atoms yielded the new compounds In_5Ch_5Br (Ch = S, Se). The substitution experiments evidenced that even mixed crystals of chlorides and bromides ($In_5Ch_5Cl_{(1-x)}Br_x$) could be obtained (reactions 24, 25). The powder patterns and the characteristics of these mixed crystals are presented in fig. 8.6 and table 8.15 in appendix.

Further attempts for the complete substitution of bromine by iodine atoms (reactions 26, 27) did not yield the expected ternary compound In_5Ch_5I. Instead of the latter, the binary compounds InCh, In_2Ch_3, In_6Ch_7 and InI were obtained.

The complete substitution of selenium atoms by tellurium atoms, and of bromine by iodine atoms did not take place probably due to the spatial hindrance caused from the size of these ions.

Further experiments (exp. 28-32) concerning the complete substitution of indium atoms or the substitution of simultaneously two not equal atoms (e.g. In, Se through Al, Te) did not reveal the expected compounds.

4.7 The substitution of In^+ by Tl^+ in the compounds In_5Ch_5Cl (Ch = S, Se)

4.7.1 Introduction

Earlier experience of substitutions of In^+-species by the cations Tl^+, K^+, and Na^+ in the mixed valence compounds In_6Ch_7 (Ch = S, Se) resulted in the characterisation of the new compounds: $TlIn_5S_7$, $TlIn_5Se_7$ [94], KIn_5S_7, $NaIn_5S_7$ [93].

The previous chapter showed that the mixed valence character of the compounds In_5Ch_5Cl (Ch = S, Se) leads to a number of possible substitutions of the respective species. This section deals properly with two compounds $TlIn_4S_5Cl$, $TlIn_4Se_5Cl$, obtained from the substitution of In^+ by Tl^+-species in the respective compounds In_5S_5Cl and In_5Se_5Cl. The ionic radius of Tl^+ in sulphides, is reported by Shannon (denoted as doubtful) to be around 1.45 Å [115]. Anyway, this value is lower than the value predicted previously (1976) from him (1.65 Å) for coordination number 6 (in oxides) and slightly higher compared to the size of In^+ (1.32 Å) [92].

4.8 The Compounds $TlIn_4Ch_5Cl$ (Ch = S, Se)

4.8.1 Preparation and properties

The preparation of the mixed valence compounds $TlIn_4S_5Cl$ and $TlIn_4Se_5Cl$ was carried out using the binary compound TlCl and elements In, S, Se in a similar way as In_5Ch_5Cl (annealing temperature 450°C). The obtained samples consisted of extremely thin yellow-orange needle-shaped crystals in case of $TlIn_4S_5Cl$ and grey needle shaped ones (similar to In_5Se_5Cl) in case of $TlIn_4Se_5Cl$. The attempts for thicker crystals in case of $TlIn_4S_5Cl$ lead to different syntheses conditions, considering the preparation mode and the temperature optimisation.

At least two different synthesising ways were tried, firstly starting from elements and $InCl_3$ and secondly, from the stoichiometric proportions of the binary educts like TlCl, InS and In_2S_3 (pressed in pellets). Further applied strategies involved temperature gradients, where the samples prepared in both ways were heated with a heating ratio 2 K/h up to 450°C, annealed at this temperature for two

weeks and then cooled down to room temperature with a cooling rate of 5K/h. All these strategies didn't yield thicker crystals for single crystal X-ray investigations.

4.8.2 Characterisation

The yellow-orange needle shaped crystals of $TlIn_4S_5Cl$ had a length varying from some millimeters up to one centimeter and diameters of a few micrometers (see Fig. 4.61), while the crystals of $TlIn_4Se_5Cl$ have a similar morphology as the crystals of the compound In_5Se_5Cl. Two recorded SEM (scanning electron microscope) images of the crystals of $TlIn_4S_5Cl$ are presented in fig. 4.61.

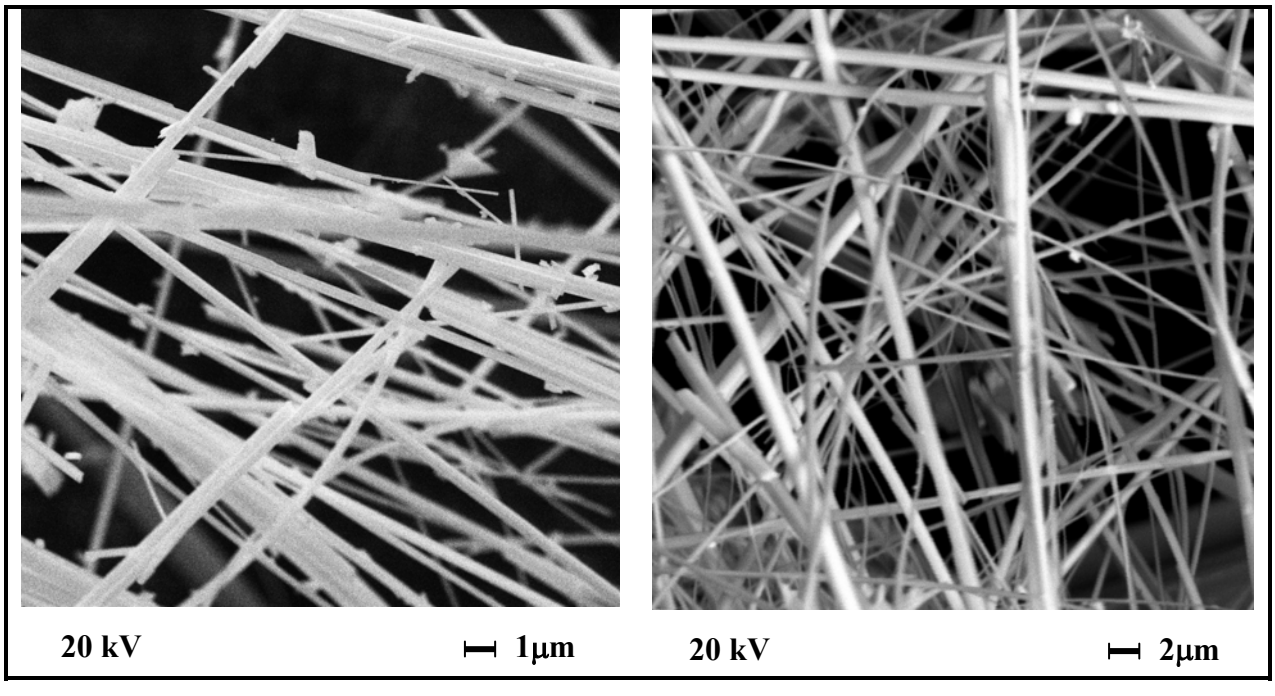

Fig. 4.61: SEM of the yellow-orange crystallites of $TlIn_4S_5Cl$.

The qualitative evidence of thalium in the obtained crystals of both compounds was determined by EDX-analysis (Fig. 4.62, 4.63).

The presence of Tl in the compound $TlIn_4S_5Cl$ is displayed from the Tl-Lα line (Fig. 4.62). The Tl-Mα-line overlaps with the S-K line. The EDX spectrum recorded from a crystal of $TlIn_4Se_5Cl$ (Fig. 4.63) displays distinctively the presence of thalium by means of the Tl-Mα.- line.

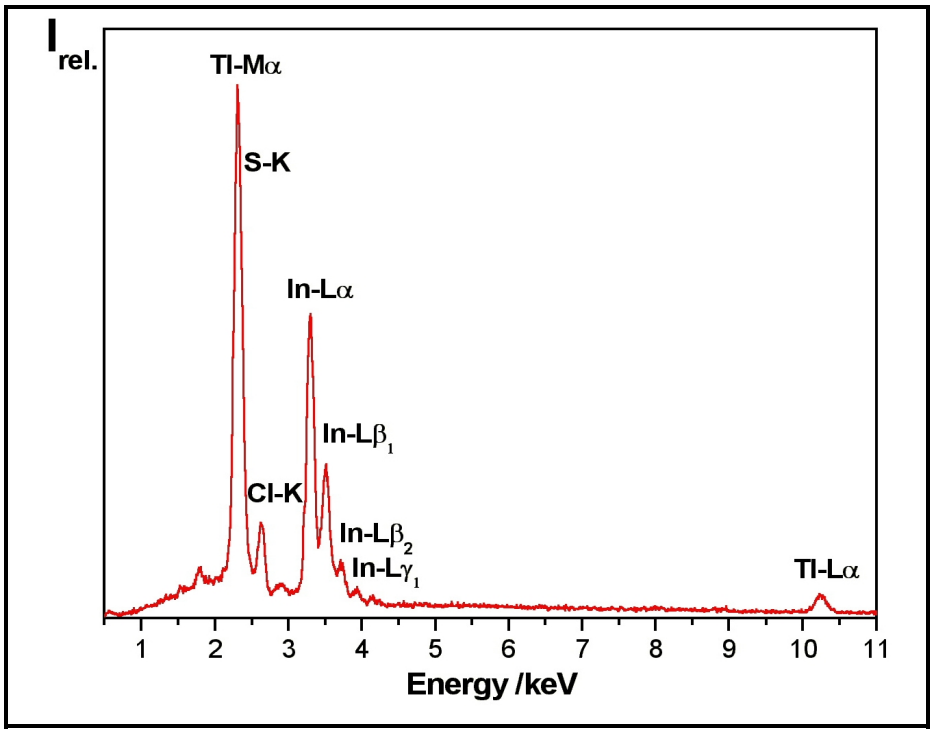

Fig. 4.62: EDX spectrum (20 kV) of a fine yellow-orange crystallite of $TlIn_4S_5Cl$.

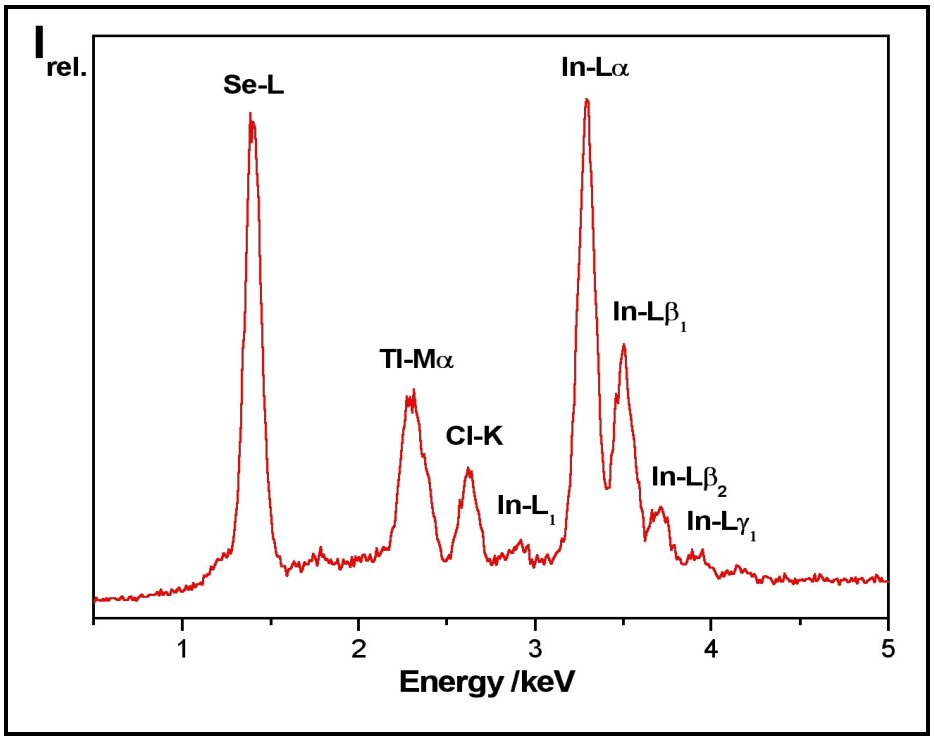

Fig. 4.63: EDX spectra (20 kV) of a grey crystal of $TlIn_4Se_5Cl$.

The samples in booth cases are nearly homogeneous (the presence of traces of by-products can not be excluded, see chapter 4). Part of the products has been ground and measured at the powder diffraction system SIEMENS D5000. Comparisons of the powder patterns of $TlIn_4In_5Cl$ with the powder patterns of In_5Ch_5X (Ch = S, Se) are presented in figures 4.64 and 4.65.

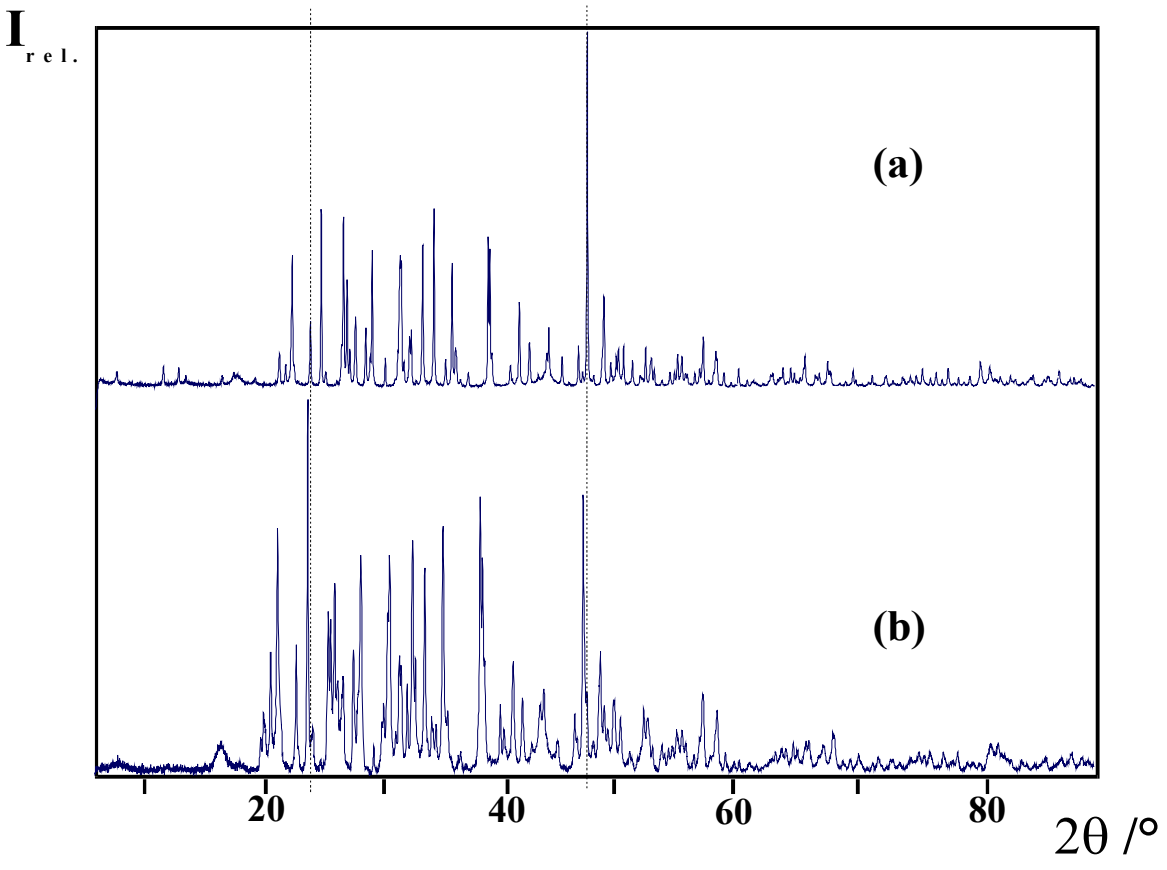

Fig. 4.64: Comparison of the measured powder patterns of a) In_5S_5Cl, b) $TlIn_4S_5Cl$. The dashed lines show the slight displacement to low 2θ angles of the reflections of $TlIn_4S_5Cl$.

Despite of the thalium content, the investigated samples show quite similar diffraction patterns, emphasising their isotypic character. As expected, the substitution of In^+ ion by a bigger Tl^+ ion leads in both cases to a slight displacement of the reflection positions to lower 2θ angles (see diffraction patterns in fig. 4.64, 4.65). This is evident from table 4.24 where a slight increase of the lattice parameters of the thalium containing compounds compared to the parameters of pure compounds can be seen.

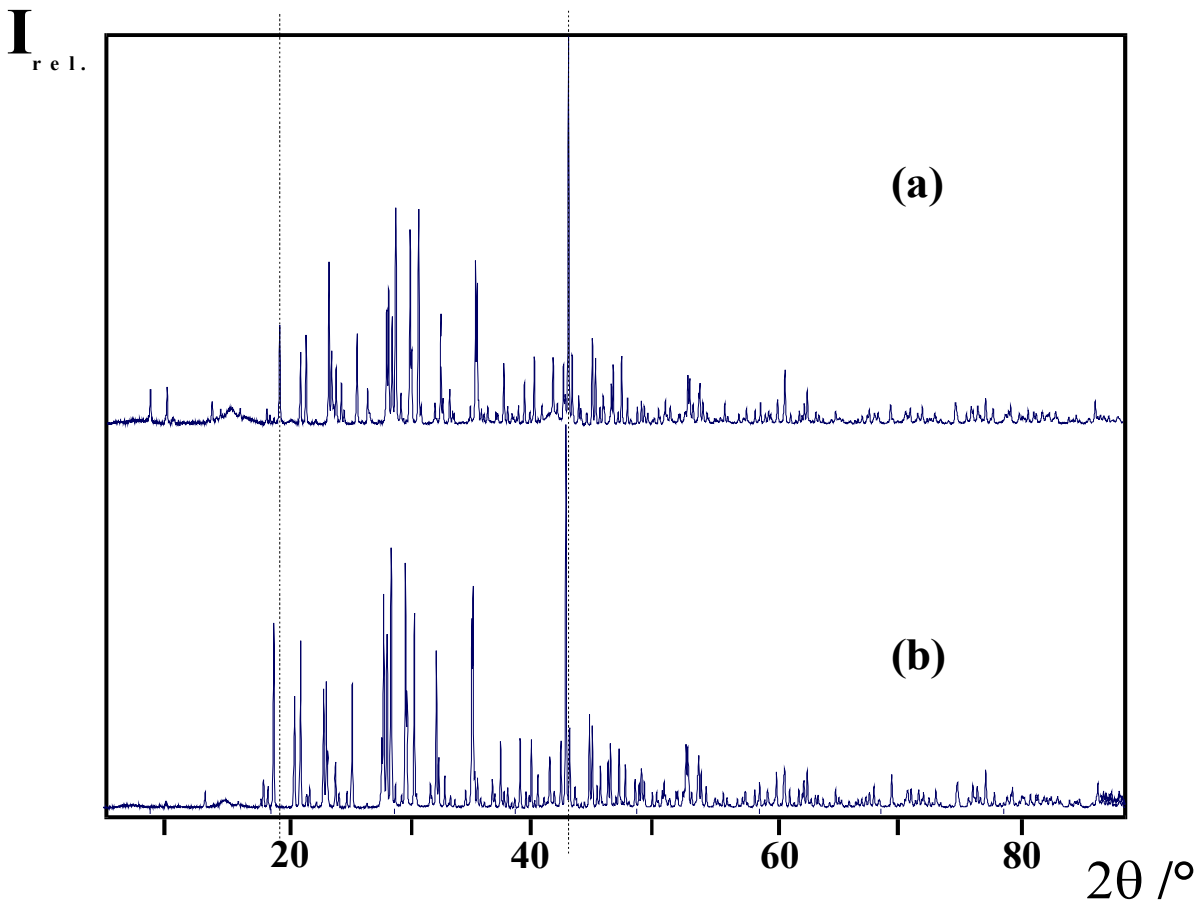

Fig. 4.65: Comparison of the measured powder patterns of a) In_5Se_5Cl , b) $TlIn_4Se_5Cl$. The Dashed lines show the slight displacement to low 2θ angles of the reflections of $TlIn_4Se_5Cl$.

The diffraction patterns of both compounds could be indexed based on monoclinic cells with the lattice constants listed in table 4.24.

Table 4.24: Comparison of the lattice parameters of In_5Ch_5Cl and $TlIn_4Ch_5Cl$ (Ch = S, Se) obtained from the indexation and the refinement of the measured powder patterns.

Compounds	**a /Å**	**b / Å**	**c / Å**	**β /°**	**V / Å^3**
In_5S_5Cl	8.949(1)	3.9165(5)	14.989(2)	93.67(1)	524.28(9)
In_5Se_5Cl	9.279(5)	4.090(1)	15.164(9)	92.97(4)	574.7(4)
$TlIn_4S_5Cl$	8.951(1)	3.9237(6)	15.059(4)	93.76(2)	527.7(1)
$TlIn_4Se_5Cl$	9.275(2)	4.102(1)	15.376(3)	92.77(2)	584.3(2)

4.8.3 Thermal analysis of $TlIn_4S_5Cl$ and $TlIn_4Se_5Cl$

The compounds $TlIn_4Ch_5Cl$ are relatively stable in air. Their thermal behaviour was investigated by means of differential thermal analysis (DTA). Sections from the DTA measurements are presented in figure 4.66. They exhibit incongruent melting behaviour similarly to the pure compounds In_5Ch_5Cl.

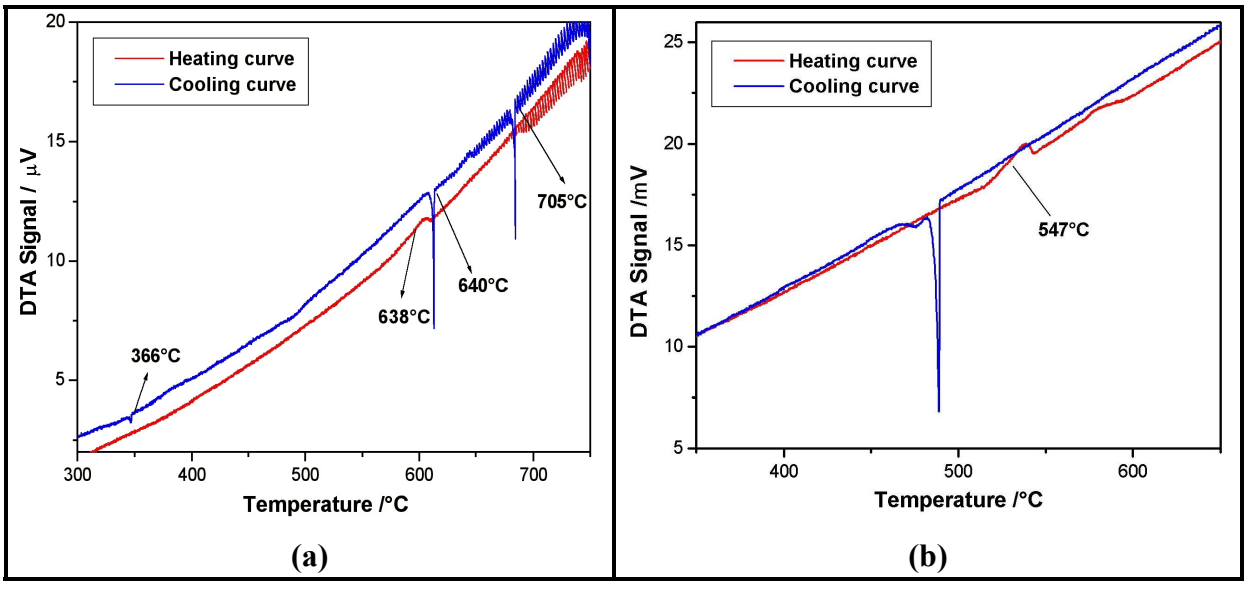

Fig. 4.66: Sections from the DTA measurements of the compounds: a) $TlIn_4S_5Cl$, b) $TlIn_4Se_5Cl$. The heating curve shows an endothermic effect (a) at 638°C for $TlIn_4S_5Cl$ and (b) at 547°C for $TlIn_4Se_5Cl$. The cooling curve shows three exothermic effects in case (a) and two exothermic effects in case (b).

In case of $TlIn_4S_5Cl$ a broad endothermic effect is observed in the heating curve (red curve, onset 638°C), this effect is accompanied by three exothermic effects in the cooling curve (blue curve). The exothermic effects belong to the solidification of the decomposition compounds: a) $Tl_xIn_{(5-x)}S_7$ onset (705°C), b) $TlIn_4S_5Cl$ (640°C), c) and $Tl_xIn_{(1-x)}Cl$ (366°C) respectively. Another decomposition product which is not displayed in the figure 4.66(a) is In_2S_3 (m.p. = 1080°C). The post-DTA sample investigated by powder diffraction analysis showed only the presence of the investigated compound ($TlIn_4S_5Cl$).

The compound $TlIn_4Se_5Cl$ shows a similar thermal behaviour as In_5Se_5Cl. A broad endothermic effect (onset 547°C) is observed in the heating curve associated with two effects (close peaks) in the cooling curve (Fig. 4.66(b)). The powder pattern of the post-DTA sample confirmed again only the presence of $TlIn_4Se_5Cl$.

4.8.4 Single crystal investigation of $TlIn_4Se_5Cl$

Due to the lack of measurable crystals of the compound $TlIn_4S_5Cl$ only single crystals of $TlIn_4Se_5Cl$ have been investigated. According to the isotypic character of these compounds the results obtained from the single crystal investigation of $TlIn_4Se_5Cl$ are generalised for both of them.

For the single crystal investigation, the crystal of $TlIn_4Se_5Cl$ already investigated by EDX was selected and fixed on the top of a glass capillary. The measurement and collection of data followed in IPDS (STOE).

The investigation of the reflections of the chosen crystal in the reciprocal space (RECIPE [P5]) displayed the presence of multiple twinning. The multiple twinning individuals appear to be shifted to very small angles from each-other (Fig. 4.67). Several measured crystals exhibited the presence of systematic multiple twinning individuals in all of them. The integration of data from such crystals was carried out in two different ways.

The first consisted of the data integration without taking into account the presence of twinning (due to the small angle between the individuals, many reflections of one domain belong at the same time to the others). In the second, the domains were separated based on the method described in chapter 4 and simultaneously integrated. During this process a huge number of reflections were suppressed.

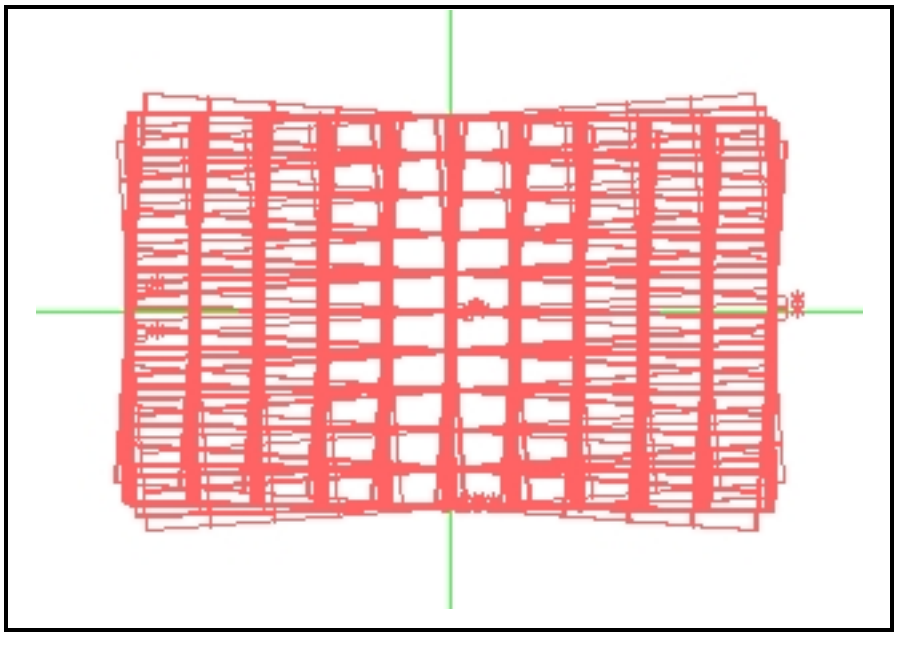

Fig. 4.67: The penetrating reciprocal lattices of the multiple twinning individuals of the measured crystal of $TlIn_4Se_5Cl$.

The obtained data sets, were corrected for Lorenz and polarisation effects. The crystal-face indexation was performed with a CCD-camera [P8] and optimised using the program X-SHAPE [P9]. The numerical absorption correction based on an adequate number of symmetrically equivalent reflections was done using the program X-RED [P10].

In both cases (in the second case the best individual was chosen) the structure solution (SHELXS [P11]) and refinement (SHELXL [P12]) was performed in the space group $P2_1/m$ (centrosymetric). The structure refinement occurred similar to In_5Se_5Cl where the In^+-position (In5), had been assigned to Tl^+. This refinement displayed an under occupancy of the Tl-position (sof = 0.960(2) and 0.939(5)) similarly to In^+ position in In_5Se_5Cl, giving an evidence of a partial occupation of this position whether by In^+ or by $(In_2)^{4+}$-species due to their similar coordination to In^+ (see chapter 4). All the other indium positions (In1, In2, In3, In4) resulted fully occupied within the three fold standard deviation.

Quite satisfactory values were obtained for the structure refinement using the whole data set instead of the incomplete data set of the best domain obtained from the second integration (see table 4.25).

Table 4.25: The R-values and the Fourier residuals for the structure of $TlIn_4Se_5Cl$.

Data set	R_1	wR_2	$\rho_{max.}$	$\rho_{min.}$
Whole	0.0592	0.1475	3.750	-3.624
The best domain	0.1355	0.3729	7.055	-6.798

For similarity to In_5Ch_5Cl compounds, the following discussion takes into account only the data obtained from the best individual (second case), regardless the quality of the R-values and high Fourier residuals.

Assuming that the M^+ position (In5) might be partially occupied by Tl^+ and In^+, a mixed occupancy of Tl5/In5 (standardised at one) has been tested in the last refinement cycle. The measuring parameters as well as the anisotropic displacement parameters are listed in table 4.26 and 8.16, 8.17 in appendix. This refinement yielded a composition with thalium content x = 0.86 ($Tl_{0.86}In_{0.14}Se_5Cl$ see table 4.26) which is comparable to the mixed occupancy described from Walter in the compound $TlIn_5Se_7$ (Tl/In: 0.74(2)/0.26(1)) [92].

Table 4.26: Position, isotropic displacement parameter U_{eq} and occupancy factors for $TlIn_4Se_5Cl$.

Atom	**Wyck.**	***x***	***y***	***z***	U_{eq}	***sof***
In1	2*e*	0.6600(2)	-1/4	0.4459(1)	0.0174(4)	1
In2	2*e*	0.1308(2)	-1/4	0.0630(1)	0.0255(5)	1
In3	2*e*	-0.0466(2)	1/4	0.3498(1)	0.0219(4)	1
In4	2*e*	0.2299(2)	1/4	0.2925(1)	0.0170(4)	1
Se1	2*e*	0.4674(2)	1/4	0.3968(2)	0.0144(5)	1
Se2	2*e*	0.8370(3)	-3/4	0.5028(2)	0.0160(5)	1
Se3	2*e*	0.3180(3)	-1/4	0.1975(2)	0.0147(5)	1
Se4	2*e*	-0.0409(3)	-3/4	0.1046(2)	0.0187(6)	1
Se5	2*e*	0.7897(3)	-1/4	0.2906(2)	0.0180(5)	1
Cl	2*e*	0.3244(8)	-3/4	0.0023(4)	0.025(2)	1
In5	**2*e***	**-0.3961(1)**	**-3/4**	**0.14762(9)**	**0.0319(4)**	**0.14(1)**
Tl	**2*e***	**-0.3961(1)**	**-3/4**	**0.14762(9)**	**0.0319(4)**	**0.86(1)**

The educts used for these reactions can yield both phases (In_6S_7/$TlIn_5S_5Cl$, In_6Se_7/$TlIn_5Se_5Cl$), therefore, it is assumed that local concentration differences or intergrowth processes might lead to composition deviations of the investigated crystals.

The single crystal data show that In_5Se_5Cl and $TlIn_4Se_5Cl$ are isotypic. The atomic positions as well as the temperature factors of all atoms agree quite well with each other within the three fold standard deviation and there are no evidences for deviations from the space group $P2_1/m$. This is also confirmed from the good agreement between the measured and the calculated powder pattern (from single crystal data, fig. 4.68).

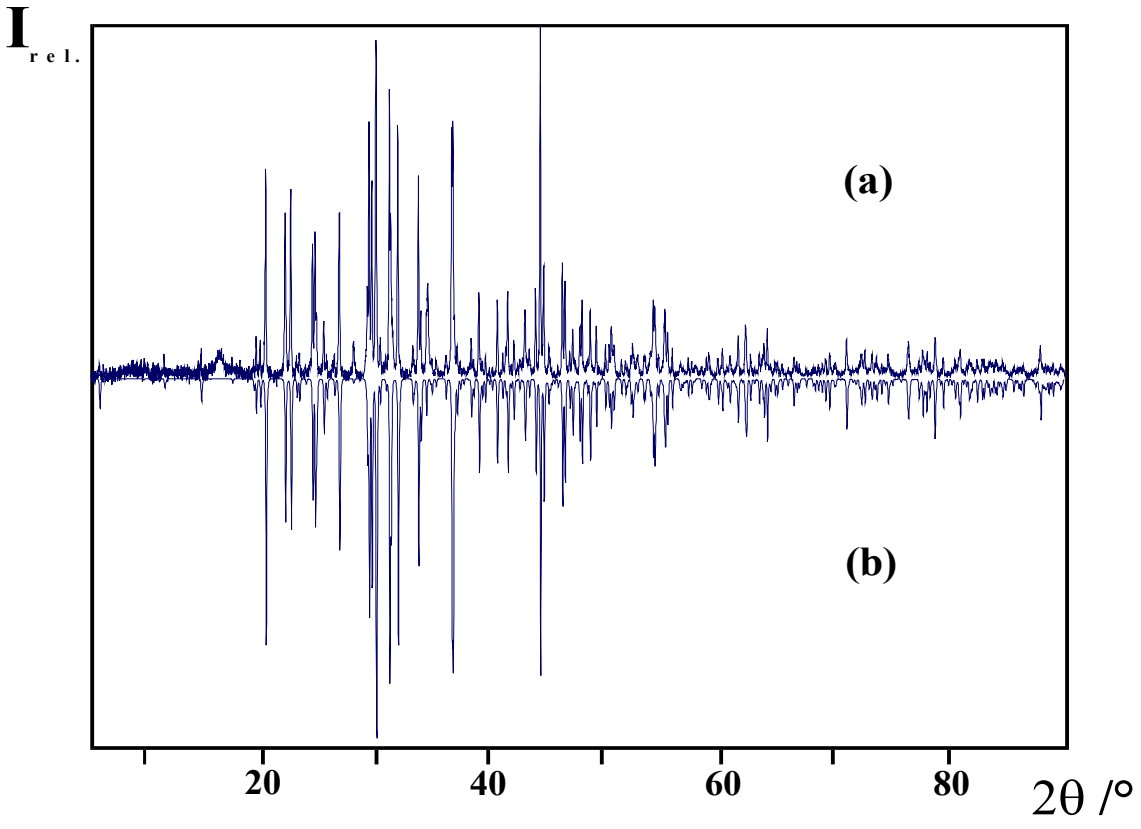

Fig. 4.68: Comparison of a measured powder diffraction pattern of $TlIn_5Se_5Cl$ (a) with the powder pattern of In_5S_5Cl calculated from single crystal data (b).

4.8.5 Structure description of $TlIn_4Se_5Cl$

The compound $TlIn_4Se_5Cl$ crystallises in the monoclinic crystal system ($P2_1/m$) with two formula units in the unit cell. The mixed valence character of this compound can be manifested by the following explicit formula:

$$\mathbf{TlIn_4Se_5Cl \rightarrow [Tl^+/In^+]\,[(In_2)^{4+}]\,2[In^{3+}]\,5[Se^{2-}]\,[Cl^-]}$$

The structure of $TlIn_4Se_5Cl$ is similar to the structure of In_5Se_5Cl (Fig. 4.33a) and for analogy the coordination of species is similar too. The only difference consists in the statistical mixed occupancy of the three capped trigonal prismatic holes by Tl^+ and In^+ (Fig. 4.69).

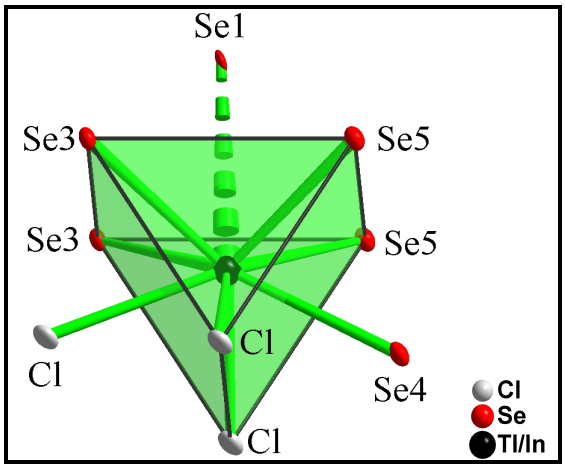

Fig. 4.69: A partial occupancy of the three capped prismatic hole by Tl^+ and In^+ in the compound $TlIn_4Se_5Cl$. The presented ellipsoids are shown with a probability of 90%.

4.8.6 Comparison of the interatomic distances of In_5Se_5Cl and $TlIn_4Ch_5Cl$

A comparison of the interatomic distances in both compounds (table 4.27), namely In_5Se_5Cl and $TlIn_4Ch_5Cl$ exhibits very small differences which are reflected in their lattice constants (table 4.24).

Table 4.27. The interatomic distances in the isotypic compounds In_5Se_5Cl, $TlIn_4Se_5Cl$.

Ionic specie	**In_5Se_5Cl**	**$TlIn_4Se_5Cl$**	**Ionic specie**	**In_5Se_5Cl**	**$TlIn_4Se_5Cl$**
$M = In^+, Tl^+$			**In^{3+}**		
M-Cl (2x)	3.136(6)	3.169(5)	In1-Se5	2.798(3)	2.702(3)
M-Se5 (2x)	3.410(3)	3.399(2)	In1-Se2 (2x)	2.743(2)	2.743(2)
M-Se4	3.350(4)	3.372(3)	In1-Se1	2.734(3)	2.719(3)
M-Cl	3.303(7)	3.312(7)	In1-Se1 (2x)	2.789(2)	2.799(2)
M-Se3 (2x)	3.447(3)	3.461(2)	In-Se*	2.766	2.751
M-Se1	4.098(4)	4.055(5)			
In_2^{4+}			In2-Se3	2.625(3)	2.611(3)
In3-In4	2.748(2)	2.736(3)	In2-Se4	2.678(2)	2.644(3)
In3-Se2	2.636(3)	2.612(3)	In2-Se4 (2x)	2.654(3)	2.694(2)
In3-Se5 (2x)	2.671(2)	2.684(2)	In-Se*	2.653	2.661
In4-Se3 (2x)	2.658(2)	2.669(2)			
In4-Se1	2.651(3)	2.640(3)	In2-Cl (2x)	2.907(5)	2.908(5)

Worth to mention here are the small differences observed especially for the distances of selenium and chlorine atoms from the central atom Tl. The other differences (taken as the average) are negligible within the three fold standard deviation.

5 High temperature X-ray investigations

5.1 Introduction

Powder diffractometry is widely used as a non destructive analytical method for characterization of crystalline materials. Fig. 5.1 shows the schematic of STOE transmission diffraction system (type STADI-P) based on the Debye-Scherrer method. Thin capillaries filled with powdered material are centred and rotated. The reflections which occur at different Bragg angles after the interaction of the X-rays with the sample material are captured from a movable Position Sensitive Detector (PSD) instead of the cylindrical film which is used at the Debye-Scherrer method.

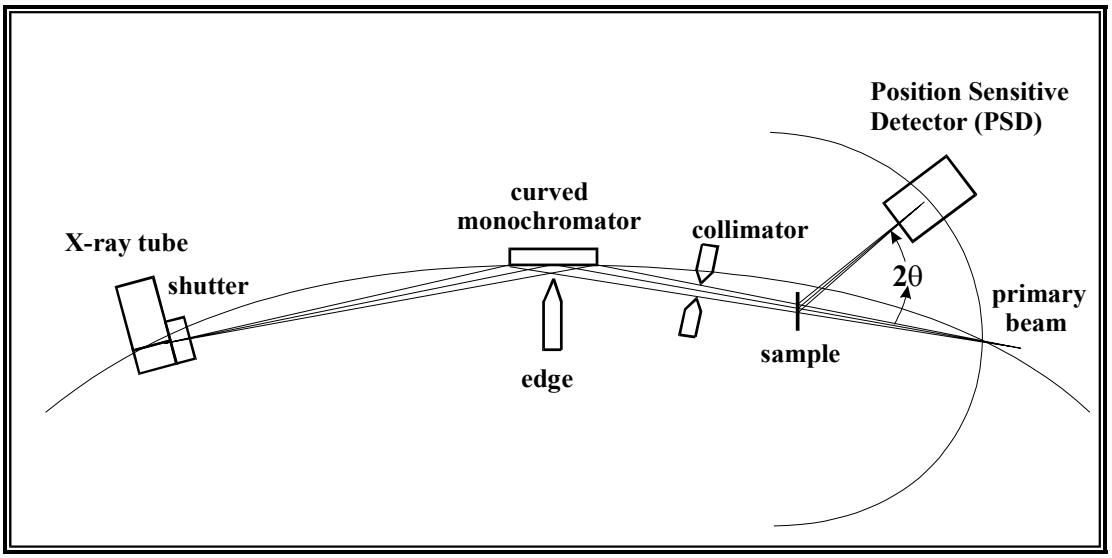

Fig. 5.1: Schematic of X-ray beam path in the STOE transmission diffraction system.

The basics of the method are described by Bragg's law

$$2d\sin\theta = n\lambda \qquad (5.1)$$

This equation (5.1) correlates the known Bragg angle θ, and the wavelength λ (Cu-radiation) with the unknown lattice spacing d.

Because of precise adjustment and randomly oriented powder particles in capillaries the Debye-Scherrer technique provides reliable intensities from only a small amount of substance. The sample must be randomly oriented because the sample might consist of needle shaped or flat crystallites therefore, it is possible that each orientation of them scatters the X-ray beam, obtaining in this way information even about the weak reflections. To perform the measurements of crystalline samples, capillaries of different outer diameters (varying from 0.1-1.0 mm) can be used.
The STOE transmission diffraction system can be also used for samples fixed in flat bed holders. The only drawback arising in this case, is the impossibility of measuring at high temperatures.

5.2 Thermal expansion of the lattice

The inner energy of a solid material can be imagined as a cooperation of three parts, respectively: vibration energy of lattice $E_{(L)}$, kinetic energy of free electrons $E_{(E)}$ and cooperative interactive energy between atom cores and electrons $E_{(I)}$.

$$\mathbf{E = E_{(L)} + E_{(E)} + E_{(I)}} \qquad \mathbf{(5.2)}$$

An increase of the temperature leads to an increase of the lattice vibration energy and the kinetic energy of free electrons. The lattice energy is more important to consider because:

1. It is found in all solid state materials
2. It is normally the highest energy

Considering the below presented model, where the forces between atoms (empty circles) are presented as springs, the thermal energy is “hidden” in the vibration of atoms along their equilibria and exactly in the kinetic energy of vibration masses and in the potential energy of the tense springs (Fig. 5.2).

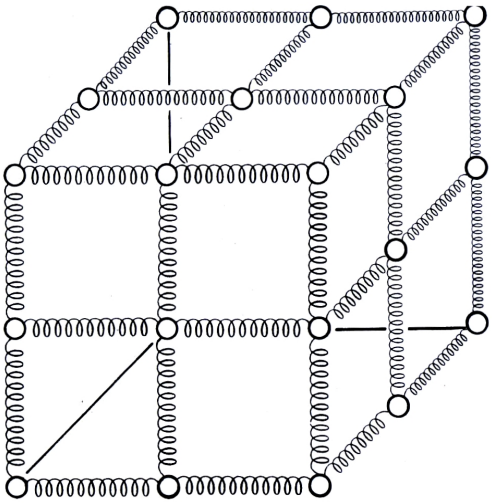

Fig. 5.2 : Spring-like model of a lattice [116].

Taking into account the easiest linear lattice model of two atoms A_1 and A_2 with a distance L_0 between them, where the atom A_1 is fixed and A_2 because of thermal energy vibrates forward and backward the potential minimum, one will find out that the middle point of vibration moves with increasing the temperature.

Lennard – Jones – Potential equation (5.3) can be used to calculate the distance (L) between both atoms.

$$U(L) = 4\varepsilon' \left[\left(\frac{\sigma}{L} \right)^{12} - \left(\frac{\sigma}{L} \right)^{6} \right] \qquad \textbf{(5.3)}$$

where U(L) is the Lennard – Jones – Potential, L the distance of atom 2 from atom 1, ε' and σ are the specific Lennard – Jones parameters. The distance (L) as a function of energy L(ε') could be easily calculated after some necessary simplifications (equation 5.4).

$$L = L_0\left[1 - \frac{7}{72\varepsilon'}(U_0 + kT)\right] \tag{5.4}$$

$U_0 = \varepsilon'$(bonding energy), k is the Boltzmann constant and T the absolute temperature.

The thermal expansion coefficient at constant pressure is $\alpha \equiv (1/L)(\partial L/\partial T)$, substituting here the value L obtained above, the thermal coefficient can be written in the following form.

$$\alpha = \frac{\partial}{\partial T}\left(\frac{L - L_0}{L_0}\right) = \frac{7k}{72\varepsilon'} \tag{5.5}$$

This equation (5.5) reveals the right values of thermal expansion (ex. for $\varepsilon' \approx 10^{-20}$ J, $\alpha = 10^{-4}$ K^{-1}) which normally for most of the substances lie between 10^{-6} and 10^{-4} K^{-1}. That is a good accordance for such a linear model which doesn't take into account the neighbouring atoms. The linear thermal expansion in most crystals is anisotropic because the potential U(L) is also anisotropic. The differences between several crystal directions can be up to two orders of magnitude.

5.3 The high temperature X-ray diffraction system

The high temperature powder diffraction measurements were performed with a STOE diffraction system designed for thin transmission samples and capillaries. The Stoe Diffractometer System (Fig. 5.3) constists of: A beam guiding tube (1) to the monochromator holder (2). On the exit port of the monochromator cage a long slit collimator (3) is fixed. The capillary sample holder is fixed on the top of a goniometer head (4). The goniometer head rotates around its perpendicular axes. The platform (5) is necessary for the rotation of flat bed holders. The diffracted X-rays are captured from the detector (6). The high temperature attachment (7) fixed above the capillary makes possible the achievement of high temperatures. The primary beam stopper (8) fixed on the monochromator cage stops the primary X-ray beam, and the microscope holder (9) is necessary to fix the

microscope during the capillary adjustments. The focusing and the monochromatisation are achieved through a bent Ge-monochromator (Johann-type) along [111].

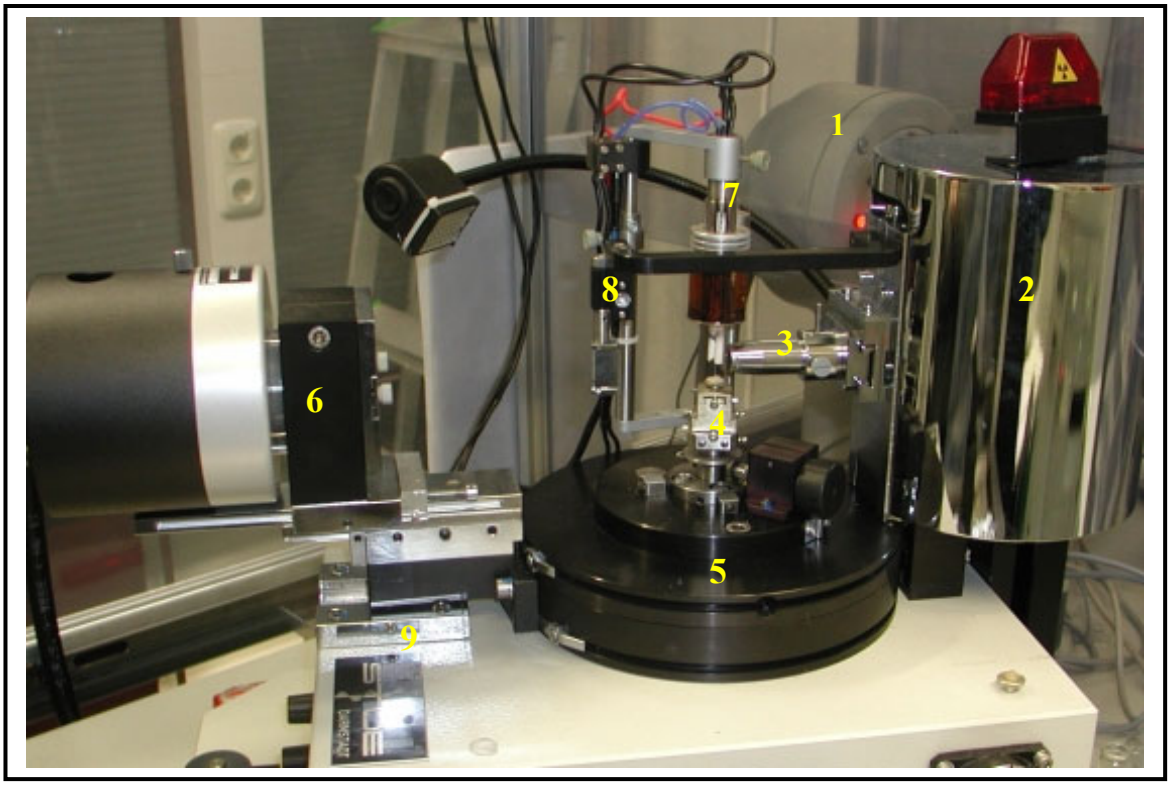

Fig. 5.3: Linear STOE Diffraction System.

After the monochromatisation, the X-ray beam is further collimated through short or long collimators according to the peak-background ratio. The collimator is precisely adjusted perpendicular to the beam.

The capillary filled with the sample is evacuated in order to remove the air inside it. The presence of air might lead to sample oxidation and/or capillary blast through pressure increase. The capillary is sealed according to the required length and fixed on the sample holder (Fig. 5.4) using cement as fixing material. The capillary together with the sample holder is mounted on a goniometer head which allows the necessary adjustments. Small deviations of capillary from the rotating position lead to a high background – peak ratio. The rotation of the sample is necessary to average over many crystallites in different positions. The device offers another rotation, the rotation of the platform (5), called **ω** rotation which is externally controlled. This rotation is intended for measurements of circular sample supports (sample spread on thin circular foils). For measurements

of capillary specimen at room or high temperature the rotation speed of **ω** rotation is set to fixed value.

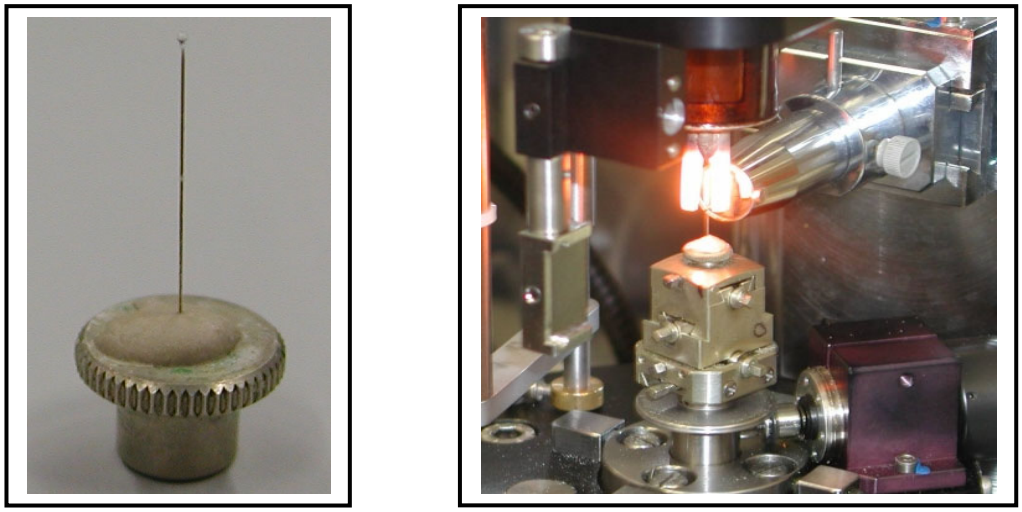

Fig. 5.4: Capillary fixed on a capillary holder (left), high temperature equipment in use.

On the 2θ arm of the diffractometer a small linear PSD (Position Sensitive Detector) is mounted, covering an angular range of Δ2θ = 7-11° depending on the distance between specimen and PSD. The PSD moves with respect to the selected 2θ range around the sample controlled externally from the software. The PSD measures in transmission mode, 5 – 90° (in 2θ region) for room temperature measurements (mainly air sensitive compounds) and 5 – 60° (in 2θ region) for high temperature measurements.

5.3.1 The high temperature attachment

The high temperature attachment consists of a high temperature ceramic cylinder designed for measurements of quartz capillaries (up to 1300 K) equipped with a U-shaped aperture which allows the capillary rotation within it and the data collection from PSD in a range of 5 - 60° (2θ). The thermocouple is mounted closest to the specimen, at the top of the aperture in a position which excludes the interaction with X-ray beam path. The temperature is controlled by an external unit connected to the thermocouple. The whole system is fixed with a screw on top of the **ω** rotating platform (5). The capillary is adjusted using a portable microscope.

5.3.2 Sample preparation

The crystalline sample is ground in an agate mortar in order to obtain small particle sizes ranging from 5 – 50 μm and filled into quartz capillaries with the help of a test tube. The choice of capillary diameter depends on the absorption coefficient of the material. For high absorbing materials capillaries of 0.1 - 0.2 mm outer diameter are used, whereas for medium and low absorbing materials diameters between 0.5 and 1.0 mm are suitable. Extremely high absorbing materials have to be diluted with suitable low absorbing materials (eg. SiO_2 – glass, BN).
For high temperature measurements quartz capillaries with outer diameters of 0.1 or 0.2 mm and wall thickness of 0.01 mm are used. To avoid the high background noise sometimes double capillaries are used, this means a 0.1 ∅ capillary is stacked into 0.2 ∅. The sample was filled in the region between these two capillaries.

The filled capillary was inserted tightly in the hole of rubber cork, the cork itself was inserted in an evacuating glass tap (Fig. 5.5) and the whole system was evacuated to a pressure of 0.1 mbar.

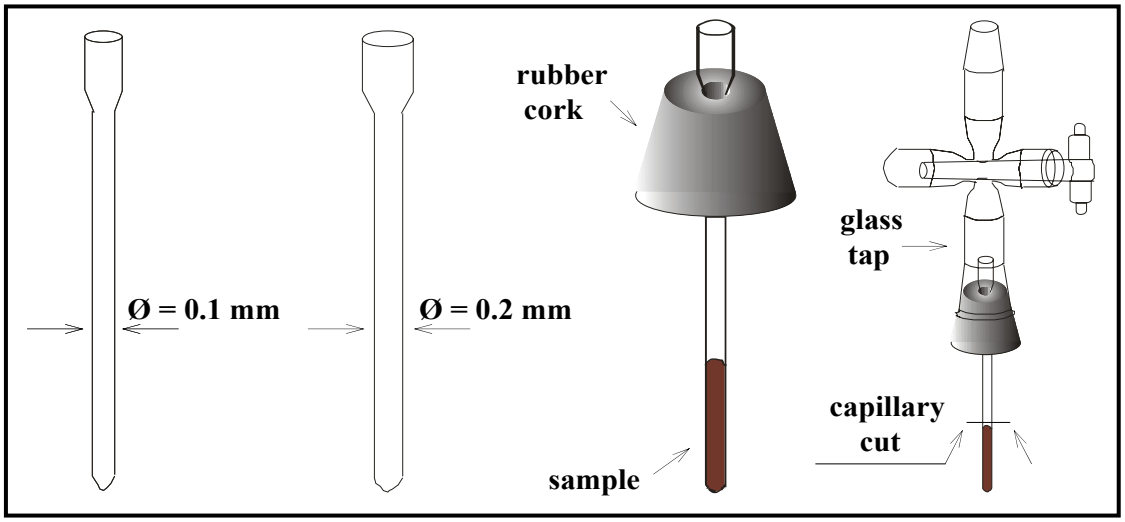

Fig. 5.5: Preparation of evacuated capillaries.

The evacuated quartz capillary was sealed by means of the hydrogen-oxygen flame to a length of 25 mm and was fixed on the holder using cement as fixing material (Fig. 5.4).

5.3.3 Device accuracy

The angular accuracy according the producer ranges 0.001°. For high temperature measurements, the temperature displayed by the control unit could be held constant within about ± 2 K by using a voltage stabilizer. A greater error arises due to the difficulty of measuring the temperature at the position of the sample.

5.3.4 Data evaluation

Using the program $WinX^{POW}$[P15] delivered from the company "STOE" and the command find peaks was possible to find all peaks. The edited peaks were saved under the "pks" format. The indexation of all peaks was done by Werner's algorithm in case of high symmetry cell and Louer's algorithm in case of low symmetry cell. The indexation started with the first 20 peaks and followed by a refinement of all reflections.

5.3.5 Calibration of the measuring device

According to the observed discrepancy between the set temperature and the real value of temperature obtained at thermocouple a calibration curve was required. To perform such calibration, a standard compound with a known thermal behaviour was used. For the purpose of this work iridium was used as standard. Its thermal behaviour has been widely investigated and reported by Schröder et al [117]. Prior the measurements, the fine crystalline iridium powder (99.9999% *Degussa*) was filled into 0.1 ∅ capillary evacuated and sealed. Its powder diffraction measurement at room temperature is presented in fig. 5.6. The strongest reflection of Ir 111 was measured in the range of 35 – 42° (in 2θ region) at different temperatures. The operating parameters were: ω rotation = 2.5°, scanning step 0.1° and time/step 60 sec.

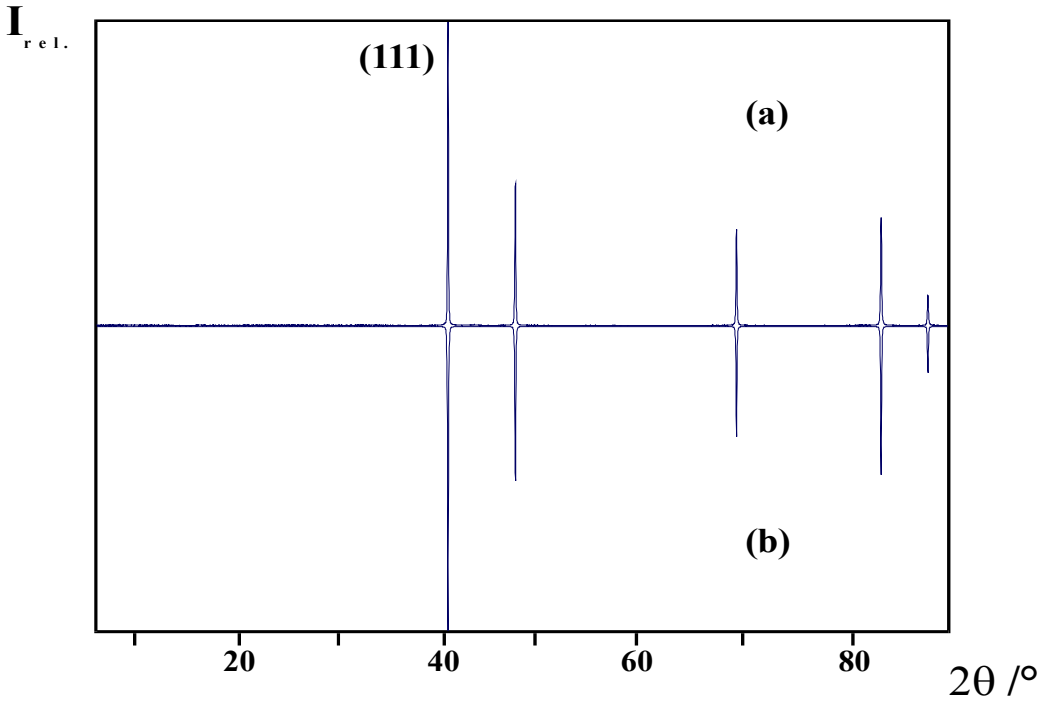

Fig. 5.6: Measured (a) and calculated (b) powder pattern of Ir.

The exact position of the 111 reflection was determined by the Lorentzian fitting. The results are listed in table 5.1 and presented graphically in fig. 5.7.

The temperature dependence of 2θ values can be presented by the equation (5.6):

$$2\theta = P1 + P2(t-t_0) + P3(t-t_0)^2 + P4(t-t_0)^3 \qquad (5.6)$$

The non-linear least square fitting based on Marquardt algorithm displays the following parameters for the equation (5.6):

Parameter	**P1**	**P2 x 10^{-4}**	**P3 x 10^{-7}**	**P4 x 10^{-10}**
Value	40.6567(7)	-2.9(1)	-1.8(4)	1.0(5)
t_0 = 24,		χ^2 = 0.93448	R^2 = 0.99972	

Table 5.1: The obtained 2θ values for the 111 reflection of iridium sample at different (uncorrected) temperatures.

Set t /°C	2θ /°
24	40.657 (1)
43	40.651 (1)
88	40.637 (1)
128	40.624 (1)
162	40.6126 (9)
194	40.602 (1)
226	40.593 (1)
258	40.579 (1)
290	40.567 (1)
325	40.556 (1)
361	40.542 (1)
396	40.527 (1)
432	40.515 (1)
468	40.500 (2)
505	40.488 (2)
546	40.471 (2)
588	40.452 (2)
632	40.433 (2)
678	40.420 (2)

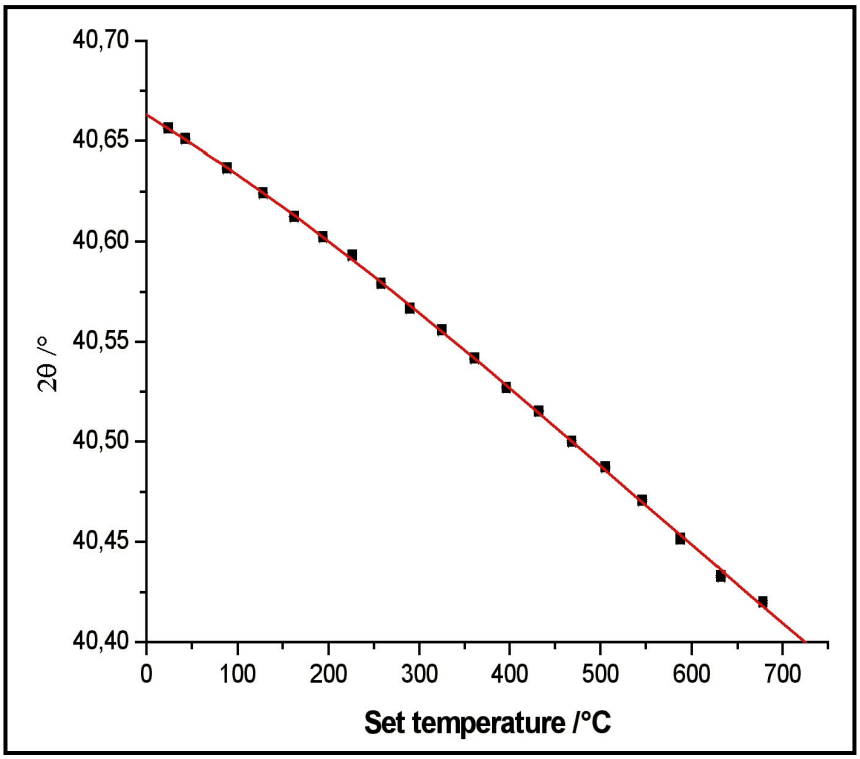

Fig. 5.7: The 2θ values for the 111 reflection of iridium sample at different temperatures plotted against the temperature.

The increasing of the temperature caused the expansion of the iridium lattice, and therefore an evident shift of the 111 reflection to smaller 2θ angles was observed. From the 2θ position of this reflection, the corresponding lattice constant was found.

The lattice constant ***a*** of the cubic system can be easily obtained as a function of θ from the Bragg-law as follows:

$$a^2 = \frac{\lambda^2}{4\sin^2\theta} \cdot (h^2 + k^2 + l^2) \qquad \textbf{(5.7)}$$

In the equation (5.7): *a* is the lattice constant, λ is the wavelength of the radiation used (1.540598 Å), θ the half of the 2θ angle, h, k, l are the indices of the reflection taken in consideration (111).

The standard deviations of the lattice constants can be obtained from the standard deviations of the 2θ angles (of the reflection 111) by the equation (5.8).

$$\Delta a = \sqrt{\left(\frac{da}{d\theta}\right)^2 \cdot (\Delta\theta)^2} \qquad \textbf{(5.8)}$$

In this equation: Δa represents the absolute error of the *a* value, da/dθ the first derivative of the function of *a* according to the variable θ, Δθ is the absolute error of the determined θ angle.
After the substitution of the equation (5.7) in the equation (5.8) the following equation (5.9) is obtained:

$$\Delta a = \left|\frac{1}{2} \cdot a \cdot \cot\theta \cdot \Delta(2\theta)\right| \qquad \textbf{(5.9)}$$

The obtained values for the lattice constants are given in table 5.2 and figure 5.8.

The temperature dependence of lattice constant ***a*** can be presented by the equation (5.10):

$$\mathbf{a(t_{set}) = P1 + P2(t\text{-}t_0) + P3(t\text{-}t_0)^2 + P4(t\text{-}t_0)^3} \qquad \textbf{(5.10)}$$

The non-linear least square fitting based on Marquardt algorithm displays the following parameters for equation (5.10):

Parameter	**P1**	**P2 x 10^{-4}**	**P3 x 10^{-7}**	**P4 x 10^{-10}**
Value	3.84054(8)	3.0(1)	1.7(5)	-9(5)
t_0 = 24		**χ^2** = 1.31559	**R^2** = 0.99972	

Table 5.2: The lattice parameters of iridium at different set (uncorrected) temperatures.

Set t /°C	a /Å
24	3.8405 (1)
43	3.8411 (1)
88	3.8423 (1)
128	3.8434 (1)
162	3.8445 (1)
194	3.8454 (1)
226	3.8463 (1)
258	3.8475 (1)
290	3.8487 (1)
325	3.8496 (1)
361	3.8509 (1)
396	3.8523 (1)
432	3.8534 (1)
468	3.8547 (1)
505	3.8559 (1)
546	3.8574 (1)
588	3.8592 (1)
632	3.8608 (1)
678	3.8620 (2)

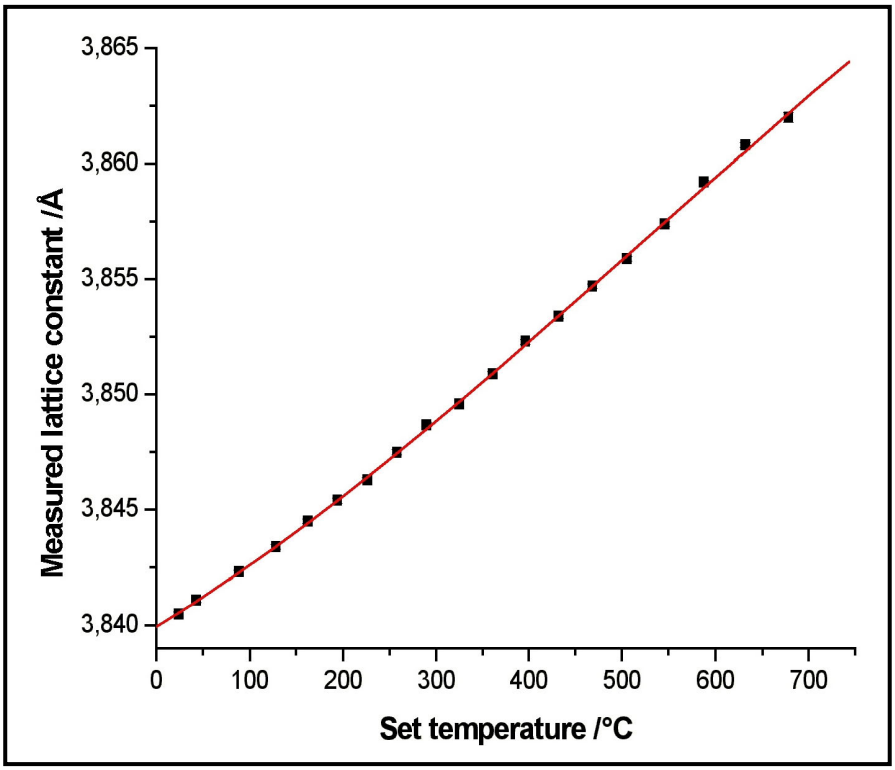

Fig. 5.8: The obtained lattice parameters of iridium plotted against set temperature.

The calibration of temperature is done according the equation (5.11) given from Schröder et al [117]:

$$\alpha(T) = \sum_{v=1}^{N} \alpha_v (T - 273)^{v-1} \qquad \textbf{(5.11)}$$

Where $\alpha(T)$ is the lattice constant dependent from the temperature, α_v : α_1, α_2, α_3, α_4 are the coefficients of the equation, T is the temperature in K.

Knowing the values of α_v in the segment v = 1 – 4, respectively: $\alpha_1 = 3.8380$, $\alpha_2 = 2.7815 \times 10^{-5}$, $\alpha_3 = 2.5390 \times 10^{-9}$ and $\alpha_4 = 1.9527 \times 10^{-13}$ (literature values), and for N = 3 the following equation is obtained:

$$\alpha(T) = \alpha_1 + \alpha_2 (T - 273) + \alpha_3 (T - 273)^2 + \alpha_4 (T - 273)^3 \qquad \textbf{(5.12)}$$

for t = T – 273 the equation (5.12) simplifies to the equation (5.13):

$$\alpha(t) = \alpha_1 + \alpha_2 t + \alpha_3 t^2 + \alpha_4 t^3 \qquad \textbf{(5.13)}$$

From this equation, knowing $\alpha(t) = a(t)$, where a(t) are the lattice constant obtained at different temperatures (see table 5.2) it is possible to find the temperature t in (°C) for each measurement.

The lattice constant obtained from the respective 2θ value at room temperature (24°C) a = 3.8404 Å compared with the value obtained from the calibration curve (see equation 5.13) 3.8388 Å at the same temperature reveals a difference of 1.8 x 10^{-3} Å. This difference was subtracted from the obtained lattice constants at different temperature in order to have comparable values, which reveal the calculated temperatures after their substitution at the calibration curve.

The value 3.8388 Å (24°C) obtained after subtraction is comparable to the predicted values a = 3.8385 Å, (Schröder et al [117], a = 3.8389 Å E. A. Owen and E. L. Yates [118] and a = 3.8390 Å H. P. Singh [119]).

5.4 The determination of temperatures

To solve this problem a numerical approaching is done. The inverse function of the equation (5.13) is found graphically in the form:

$$t(a) = \beta_1 + \beta_2\, a + \beta_3\, a^2 + \beta_4 a^3 + \ldots + \beta_n \qquad \textbf{(5.14)}$$

The inverse function (equation 5.14), which expresses the temperature as a function of lattice constant a can be presented in the form of equation (5.15).

$$\mathbf{t(a) = P1 + P2(a - a_0) + P3(a - a_0)^2} \qquad \textbf{(5.15)}$$

The parameters P1, P2 and P3 of the equation (5.15) obtained from the non-linear least square fitting based on Marquardt algorithm are:

Parameter	**P1**	**P2**	**P3**
Value	29.1(2)	35538(36)	-97609(1732)
$\mathbf{a_0}$ = 8.8388	χ^2 = 4.96 x 10^{-3}		$\mathbf{R^2}$ = 1

The standard deviation for each calculated temperature (Δt) arising from the standard deviation of the lattice constant (Δa) can be obtained from the equation (5.16).

$$\Delta t = \left| \frac{dt}{da} \cdot \Delta a \right| \qquad \textbf{(5.16)}$$

In this equation: dt/da represents the first derivative of the function (5.15).

The obtained values of the calculated temperatures and the respective standard deviations are listed in the table 5.3 together with the set temperature values. A graphical demonstration of them is given in figure 5.9.

The calculated standard deviations corresponding to the found values of temperature are in good agreement with the measured data. Three consequent measurements at room temperature show a deviation of approximately 6 °C, while at higher temperatures (600°C) the deviation can vary up to 8 °C from the corrected temperature.

Table 5.3: Set and calculated temperatures.

Set t /°C	Corr. t /°C
24	29 (4)
43	50 (4)
88	93 (4)
128	131 (4)
162	170 (3)
194	201 (4)
226	232 (4)
258	273 (4)
290	314 (4)
325	344 (4)
361	388 (4)
396	435 (4)
432	471 (4)
468	514 (5)
505	553 (4)
546	602 (4)
588	660 (4)
632	710 (4)
678	748 (6)

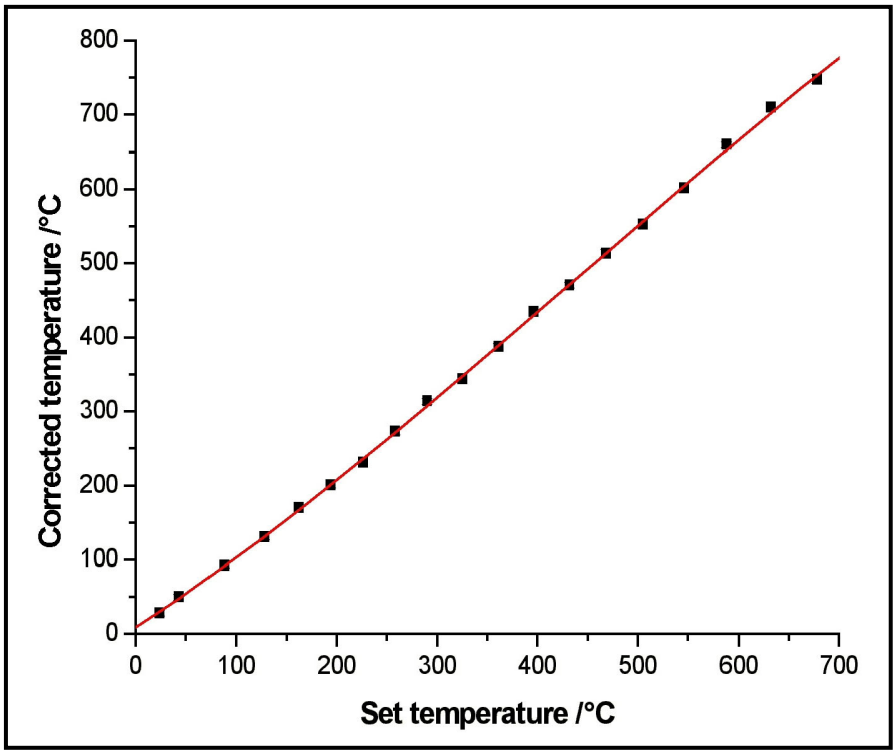

Fig. 5.9: Corrected temperature from the inverse function plotted against the set temperature.

The dependence shown in figure 5.9 (the corrected temperature against the set temperature) is given by the equation (5.17).

$$a(t_{corr.}) = P1 + P2(t_{set}-t_0) + P2(t_{set}-t_0)^2 + P3(t_{set}-t_0)^3 \qquad (5.17)$$

The fitting parameters for equation (5.17), obtained by the least square fitting based on Marquardt algorithm are:

Parameter	P1	P2	P3 x 10^{-4}	P4 x 10^{-7}
Value	31(3)	0.9(4)	5(2)	-4(2)
$t_0 = 24$		$\chi^2 = 1.02634$	$R^2 = 0.99971$	

After the calibration of the high temperature measuring device, the main purpose was to investigate the thermal behaviour of several compounds. Starting with the first two compounds, namely

$K_2In_{12}Se_{19}$, $K_2In_{12}Se_{12}Te_7$ and continuing with the mixed valence compounds In_5Ch_5X (Ch = S, Se; X = Cl, Br).

According to Schlosser et al [120-121], $K_2In_{12}Se_{19}$ shows a complicated structure due to a temperature dependent order-disorder transformation caused by a dynamic disorder of indium atoms. This order-disorder transition is accompanied by the formation of the superstructure which is revealed by diffuse X-Ray reflections in single crystal measurement at STOE IPDS. Temperature dependent X-ray diffraction on single crystals displayed a significant decrease in intensity of the diffuse scattering with temperature increasing. At 670 K the diffuse scattering disappears completely, while at low temperatures an ordering process for In2/In3 positions is observed [120-121]. This ordering process is accompanied by the gradual appearance of the ring-shaped diffuse reflections around Bragg positions in *hkl* with $l = 2n+1$ which leads to the doubling of the ***c*** axis. Diffuse rings were observed independent of cooling velocity of the investigated crystals. Anyway, in the measured powder pattern of this compound no superstructure reflections could be observed due to their diffuse character and weakness. Further investigations (e.g. substitution of some selenium positions with tellurium) in this compound, mainly based on the chemical influence on the real structure of this compound led to an array of mixed crystals e.g. $K_2In_{12}Se_{19-x}Te_x$. One of the most investigated species of this array was $K_2In_{12}Se_{12}Te_7$. Single crystal investigations of this compound did not present any anomalies (see Schlosser [120-121]). The depiction of the reciprocal space displayed in contrast to $K_2In_{12}Se_{19}$ no diffuse intensities, and instead of the ring-shaped diffuse intensities in the positions *hkl*: $l = 2n+1$ and $-h+k+l = 3n$ only sharp reflections were observed.

The optimisation of the high temperature system with double capillaries was performed using $K_2In_{12}Se_{12}Te_7$. Therefore in the following discussion this compound is considered at first.

5.5 High temperature X-ray investigations of $K_2In_{12}Se_{12}Te_7$

The compound $K_2In_{12}Se_{12}Te_7$ was synthesised by high temperature solid state reaction of the elements in stoichiometric proportions in evacuated and sealed quartz ampoules. The details of

synthesis are given elsewhere [122]. The powder diffraction of this compound (1 hour measurement D5000) is presented in figure 5.10.

This compound crystallizes in the hexagonal system in the space group $R\bar{3}$ with the lattice constants a = 14.175 (3) Å, c = 35.838 (9) Å.

The obtained data presented full agreement with those of the author, see fig. 5.10

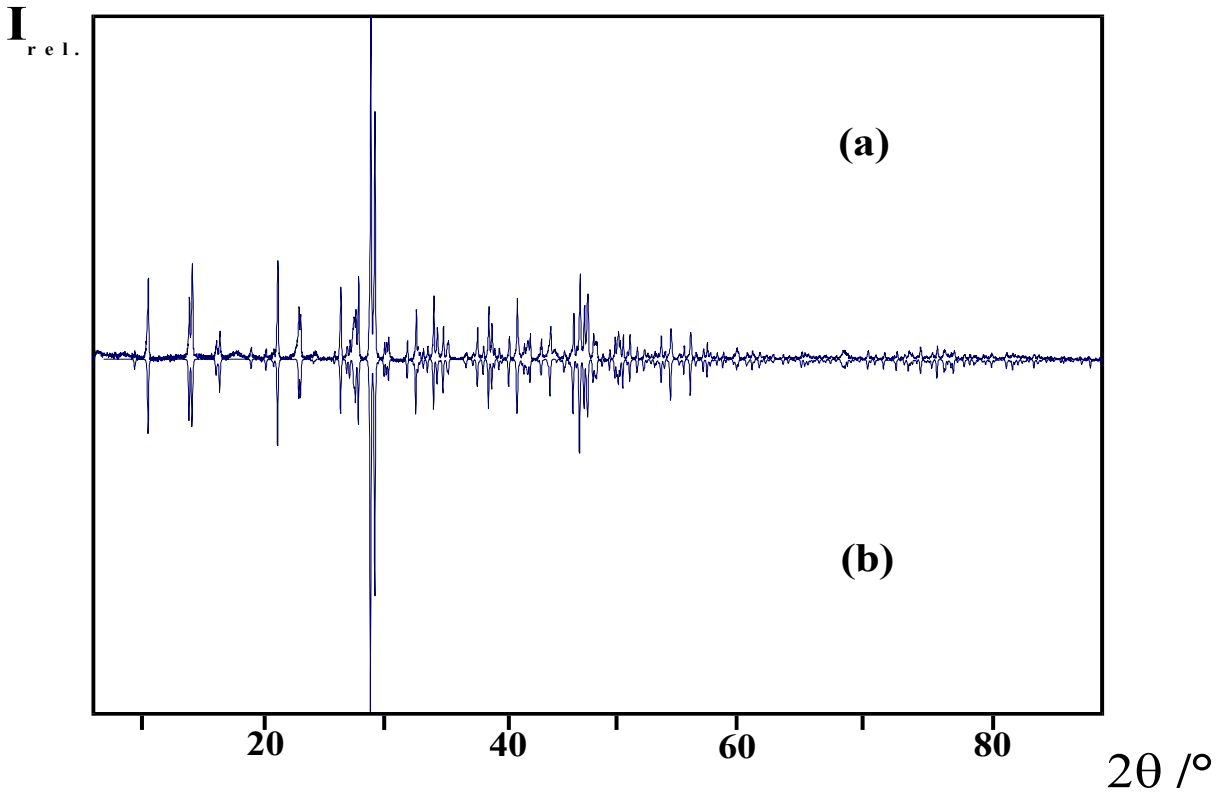

Fig. 5.10: Comparison of the measured (a) and the calculated (b) diffraction pattern of $K_2In_{12}Se_{12}Te_7$.

5.5.1 Sample preparation

The specimen for this study was firstly prepared by filling the ground crystals of $K_2In_{12}Se_{12}Te_7$ in a quartz capillary tube of 0.1 mm outer diameter and 0.01 mm wall thickness. The X-ray diffraction patterns were recorded first at room temperature, in order to observe the quality of the measurement.

Two different capillaries (similar diameters) were prepared and measured. The patterns are presented in fig. 5.11.

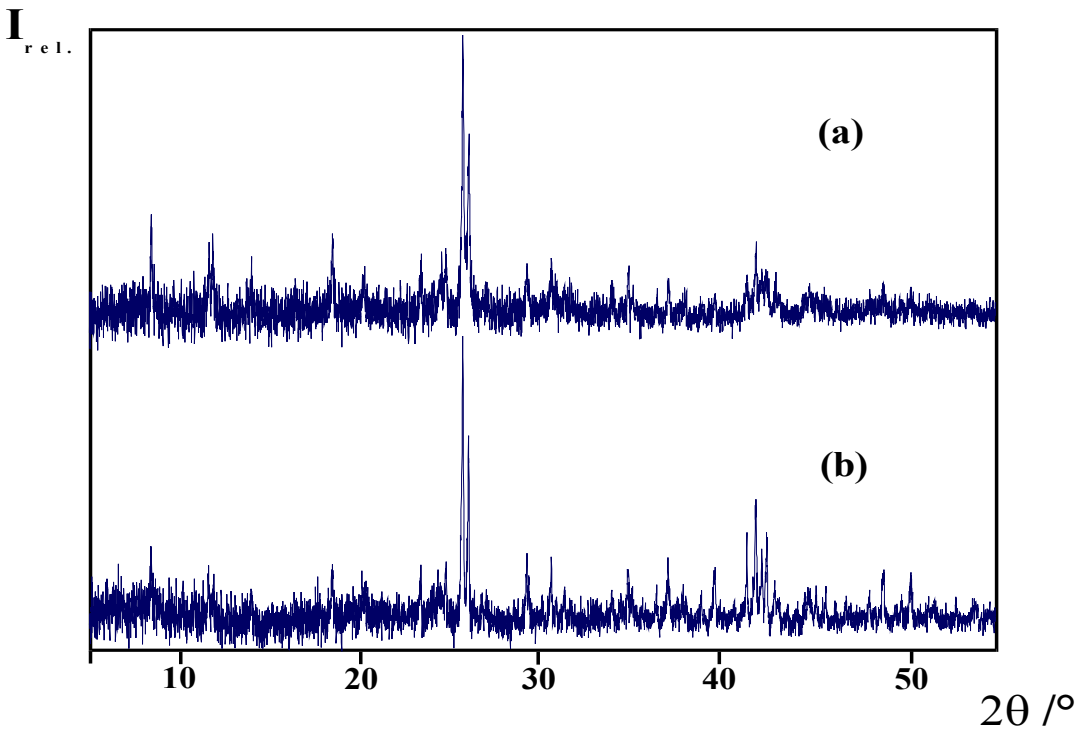

Fig. 5.11: Powder patterns of $K_2In_{12}Se_{12}Te_7$ measured in capillaries with 0.1 mm outer diameter and 0.01 mm wall thickness at room temperature respectively.

It is obvious that the quality of the measurements is not good because of the high background proceeding from the high absorption coefficient.

To overcome this problem, a quartz capillary with 0.1 mm outer diameter and 0.01 mm wall thickness was covered from outside with a thin film of grease and rotated carefully over the spread powdered sample ($K_2In_{12}Se_{12}Te_7$). A cylindrical thin film of crystallites around the capillary was formed. The obtained diffraction pattern is presented in fig. 5.12 (step width 0.1°, time/step 60 sec).

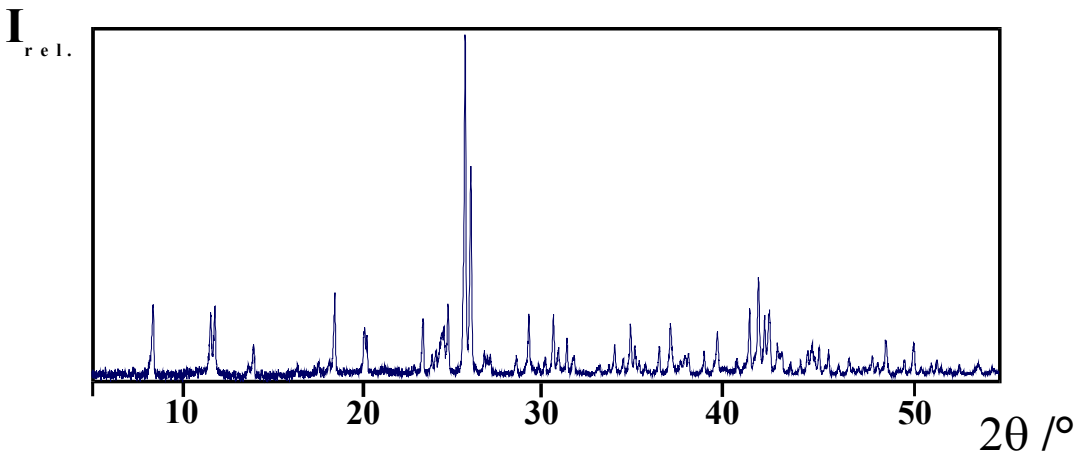

Fig. 5.12: Powder pattern of $K_2In_{12}Se_{12}Te_7$ using a 0.1 mm capillary covered from the outside with crystallites.

The obtained diffraction pattern demonstrates a much better quality, the peak/background ratio is high. Unfortunately this method is limited to measurements at room temperature and to compounds which are stable in contact with grease. For high temperature measurements the described method must be improved.

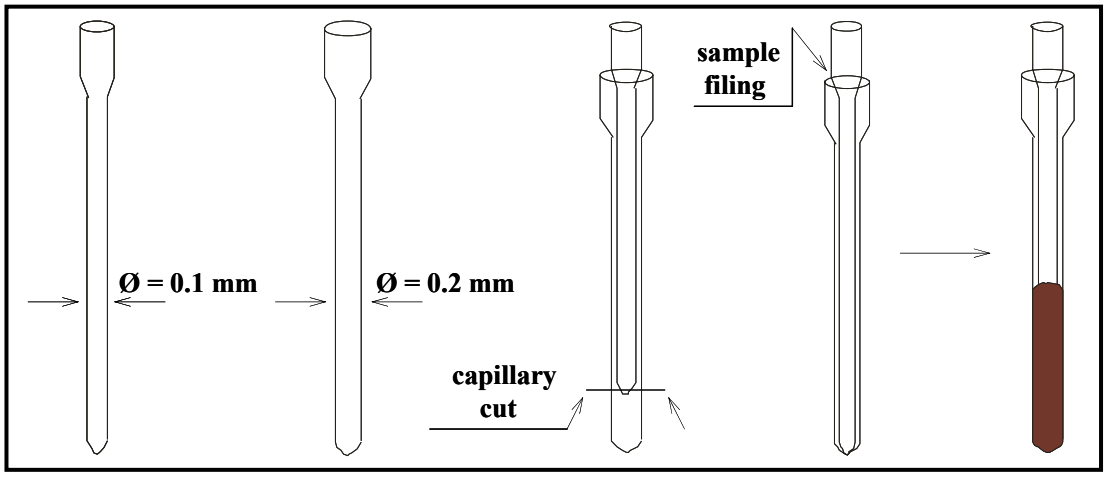

Fig. 5.13: Preparation of a double capillary using a combination of 0.1mm ∅ and 0.2 mm ∅ capillaries.

This improvement consisted on measurements using a combination of double capillaries. The preparation of the double capillaries is presented in figure 5.13.

Characteristic for $K_2In_{12}Se_{12}Te_7$ are the superstructure reflections (not found in $K_2In_{12}Se_{19}$ [122]). The following powder patterns give an overview of these reflections ($\bar{2}$ 4 9, 2 3 5 and $\bar{4}$ 5 3; Fig. 5.14).

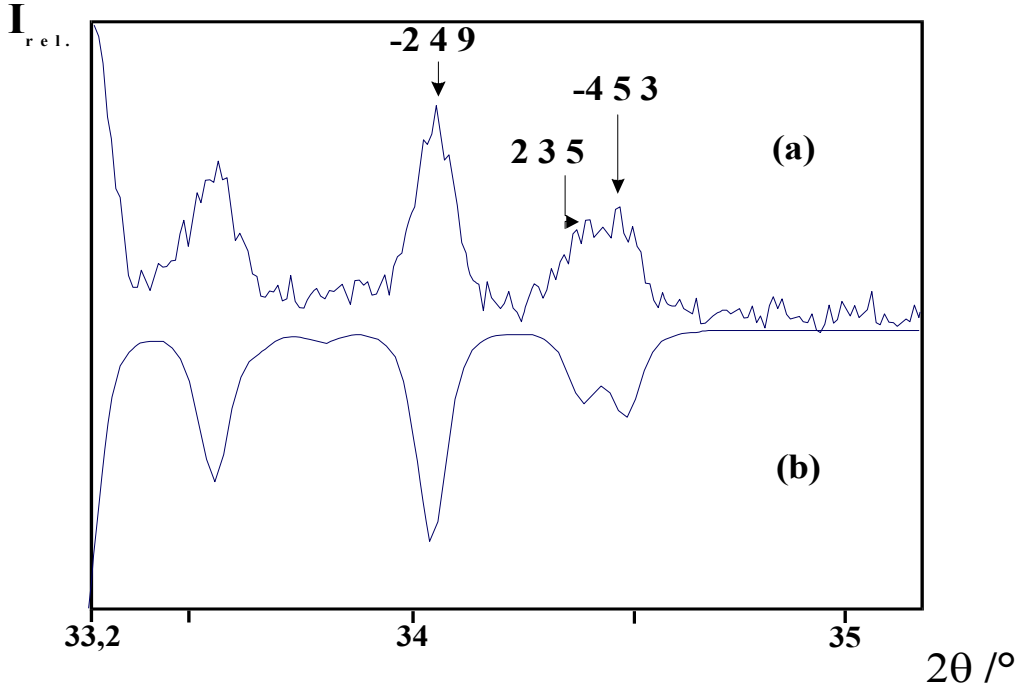

Fig. 5.14: Section of a measured pattern of $K_2In_{12}Se_{12}Te_7$ (a) in comparison to a calculated one (b), showing the important superstructure reflections.

5.5.2 Room temperature measurements with double capillaries

The achieved results of typical experiments performed with double capillaries are presented in fig. 5.15.

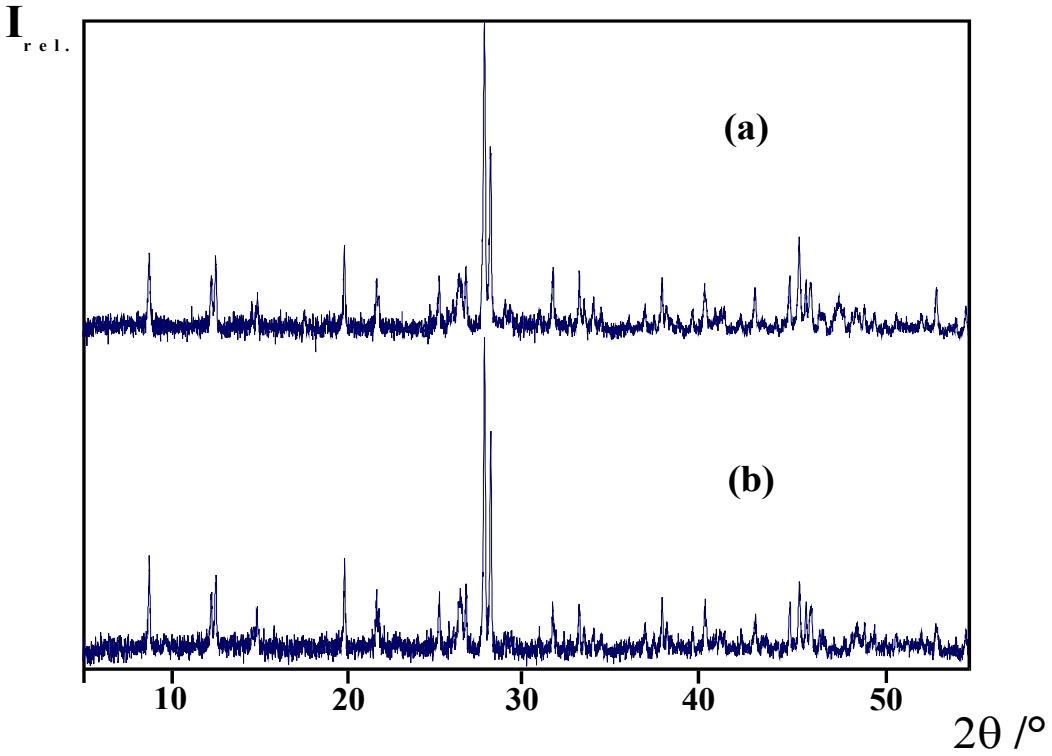

Fig. 5.15: Two powder patterns (a), (b) of $K_2In_{12}Se_{12}Te_7$ measured in two different double capillaries at room temperature.

The obtained powder patterns are reproducible (Fig. 5.15), have a higher quality than those measured in ∅ 0.1 mm capillaries and are comparable with the measurement done with the thin film technique.

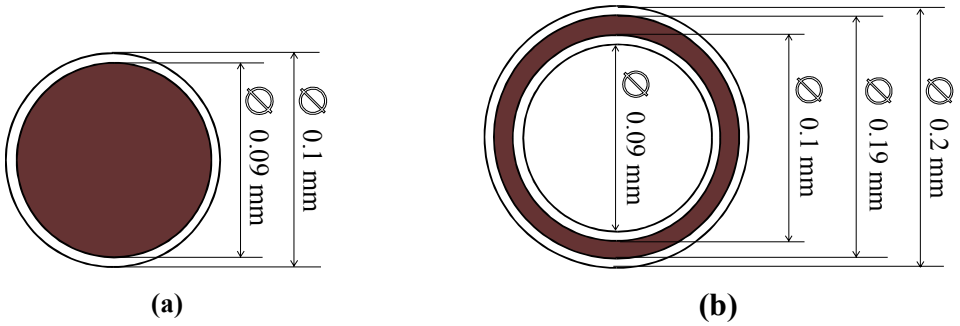

Fig. 5.16: Cross-section of a) ∅ 0.1 mm capillary, b) ∅ 0.1 + 0.2 mm capillary. The brown colour inside the capillaries represents the filling substance.

The investigated volume of sample inserted in double capillaries is almost 1/3 of the volume contained in 0.1 mm capillary (Fig. 5.16).

To determine the thermal expansion coefficients and/or a possible phase transition, high temperature measurements of $K_2In_{12}Se_{12}Te_7$ are performed using double capillaries and these measuring parameters: ω = 2.5, 2θ: 5 – 60°, step width 0.1°. The obtained data from these measurements are given in table 5.4 and figure. 5.17.

Table 5.4: Lattice parameters and volume of $K_2In_{12}Se_{12}Te_7$ obtained at different temperatures.

T /K	a /Å	c /Å	V /Å^3
297(4)	14.178(3)	35.820(5)	6235(1)
328(4)	14.182(6)	35.82(2)	6240(3)
381(4)	14.193(3)	35.86(1)	6258(2)
436(4)	14.206(6)	35.88(1)	6271(3)
492(4)	14.218(3)	35.906(7)	6286(2)
550(4)	14.228(4)	35.965(8)	6305(2)
609(4)	14.248(3)	36.04(1)	6337(2)
733(4)	14.267(3)	36.218(9)	6384(2)

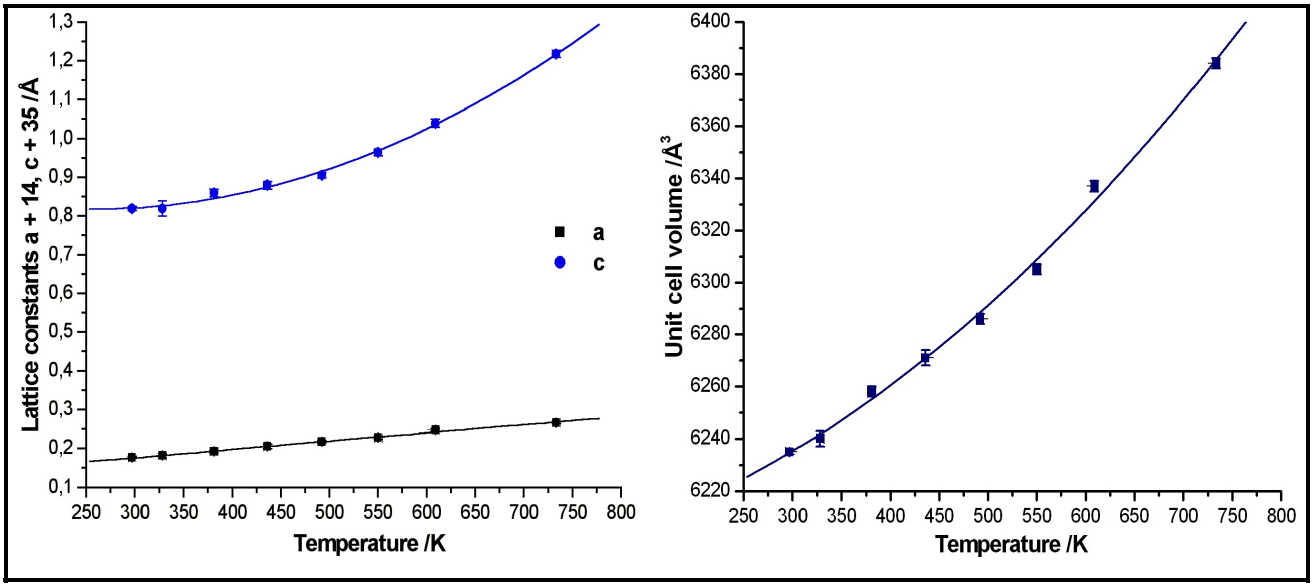

Fig. 5.17: The temperature dependence of the lattice constants (left) and volume (right) of $K_2In_{12}Se_{12}Te_7$ measured in double capillaries.

The dependence of lattice constants and volume from the temperature /K can be presented by the equation (5.18) and (5.19).

$$\mathbf{a(T),\ b(T) = P1 + P2(T - T_0)} \qquad \mathbf{(5.18)}$$

$$\mathbf{c(T),\ V(T) = P1 + P2(T-T_0) + P3(T-T_0)^2} \qquad \mathbf{(5.19)}$$

The fitting parameters for the equations (5.18) and (5.19) obtained by the least square fitting based on Marquardt algorithm are listed in table 5.5.

Table 5.5: The fitting parameters of the equations (5.18) and (5.19).

Parameter	P1	P2	P3	χ^2	R^2
a	14.177(2)	2.10(7) x 10^{-4}	-	0.71059	0.99353
b	14.177(2)	2.10(7) x 10^{-4}	-	0.71059	0.99353
c	35.822(5)	1.2(6) x 10^{-4}	1.8(1) x 10^{-6}	0.92673	0.99736
V	6235(2)	0.22(2)	2.9(5) x 10^{-4}	3.17801	0.99735

The lattice constant **a** changes linearly with temperature, the change of the lattice constant **c** and the **volume** correspond to a second order function. A phase transition or other special physical effects could not be observed at the studied temperature range. Further attempts were done to measure this substance at higher temperatures, but the diffraction patterns obtained could not be indexed because of their low peak/background relation.

5.5.3 The superstructure reflections

To investigate the thermal behaviour of the superstructure reflections, accurate measurements of the narrow 2θ region (6°) were performed. The measuring time of almost 3 hours and the step width was 0.1°. The recorded patterns are aligned in fig. 5.18.

By comparing the obtained patterns at different temperatures with the calculated pattern, the shifting to smaller 2θ angles is obvious. According to the measured patterns, the superstructure reflections $\bar{2}$ 4 9, 2 3 5 and $\bar{4}$ 5 3 are observable up to 492 K, at higher temperatures only the

strongest representative of them $\bar{2}$ 4 9 could be observed, while the other cannot be observed due to the low peak/background ratio.

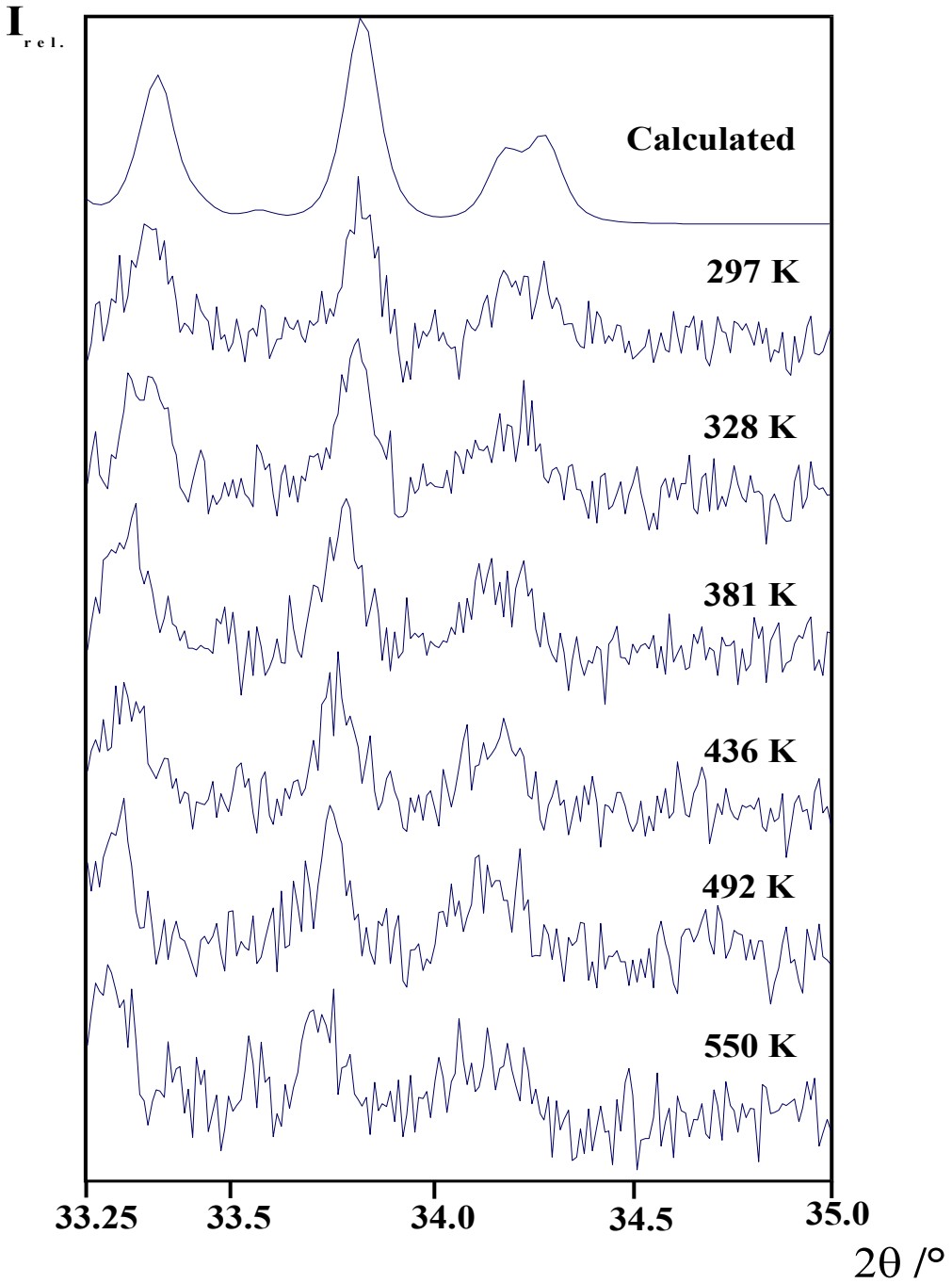

Fig. 5.18: Patterns of the measured superstructure reflections of $K_2In_{12}Se_{12}Te_7$ at different temperatures and compared with the calculated one.

5.5.4 Determination of the expansion coefficients

From the thermal behaviour of the lattice parameters, it is possible to determine the corresponding expansion coefficients at different temperatures. The calculation of the expansion coefficient from lattice parameters and temperature can be determined by the relation (5.20):

$$\alpha = \frac{1}{L_0}\frac{dL}{dT} \qquad \textbf{(5.20)}$$

Where: α represents the coefficient of thermal expansion, L_0 the lattice constant parameter at room temperature (297 K), dL and dT the respective differentials of lattice constants parameters and temperature. The calculation of the standard deviation (error of single measurement) for each value of the thermal expansion coefficient is done according to the equation (5.21):

$$\Delta\alpha = \left|\frac{1}{L_0}\cdot\frac{d^2L}{dT^2}\cdot\Delta T\right| \qquad \textbf{(5.21)}$$

Where: $\Delta\alpha$ represents the absolute error of the expansion coefficient, d^2L/dT^2 the second derivative of the lattice parameters as a functions of absolute temperature, ΔT is the absolute error (standard deviation) of the absolute temperature.

The coefficients of thermal expansion for $K_2In_{12}Se_{12}Te_7$ with the respective standard deviations for ***c*** axis and ***volume*** are listed in table 5.6. The coefficients of the thermal expansion in ***a*** and ***b*** directions are equal and show a linear behaviour (see figure 5.17) while the coefficients of the ***c*** direction and ***volume*** show a non linear behaviour.

Table 5.6: Coefficients of thermal expansion of $K_2In_{12}Se_{12}Te_7$ for c axis and volume calculated at different temperatures.

T /K	α_c x 10^{-5} /K^{-1}	α_V x 10^{-5} /K^{-1}
297(4)	0.34(4)	3.49(4)
328(4)	0.65(4)	3.78(4)
381(4)	1.18(4)	4.27(4)
436(4)	1.74(4)	4.78(4)
492(4)	2.31(4)	5.31(4)
550(4)	2.89(4)	5.84(4)
609(4)	3.49(4)	6.39(4)
733(5)	4.74(4)	7.55(4)

The linear coefficients of the thermal expansion in ***a*** and ***b*** directions are equal: $\alpha_a = \alpha_b = 1.5\ (2) \times 10^{-5}\ K^{-1}$, the mean coefficients of thermal expansion in ***c*** direction and ***volume*** are respectively $\overline{\alpha_c} = 2.17\ (4) \times 10^{-5}\ K^{-1}$ and $\overline{\alpha_V} = 5.18\ (4) \times 10^{-5}\ K^{-1}$.

The powder patterns measured at different temperatures are presented in appendix (Fig. 8.7).

5.6 High temperature X-ray investigations of $K_2In_{12}Se_{19}$

The compound $K_2In_{12}Se_{19}$ was synthesised by high temperature solid state reaction of the elements in stoichiometric proportions in evacuated and sealed quartz ampoules. The synthesis is described in details in [122]. A powder diffraction of the measured compound is presented in figure 5.19 (1 hour measurement D5000 flat bed). No reflections of a by-product could be detected. All lines could be indexed in the trigonal system with the hexagonal constants a = 13.847(3) Å , c = 17.587(3) Å.

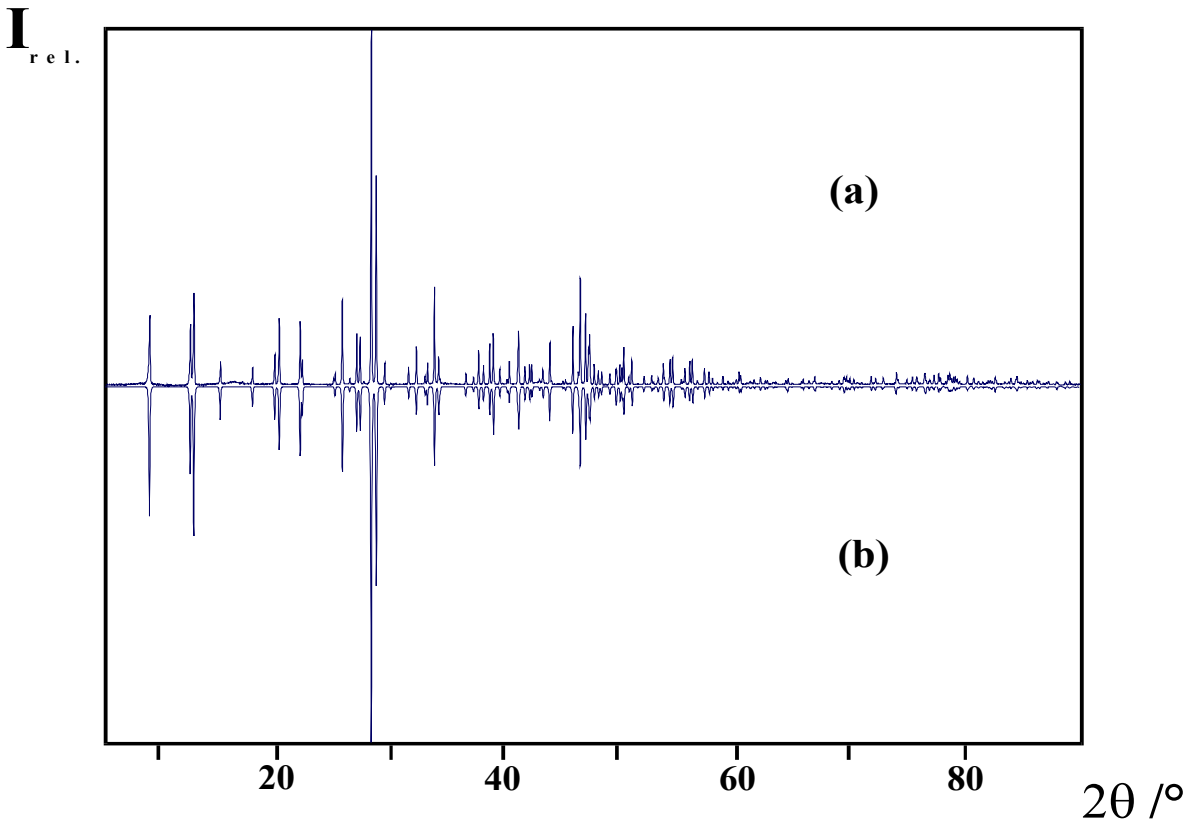

Fig. 5.19: Comparison of a measured (a) and calculated (b) diffraction pattern of $K_2In_{12}Se_{19}$.

5.6.1 Sample preparation and measurement

The powdered sample was measured using the double capillaries technique (2θ-range: 5-60°; step width 0.1°, time/step 60 sec). The obtained data from these measurements are presented in table 5.7, figure 5.20.

Table 5.7: Lattice parameters and volume of $K_2In_{12}Se_{19}$ obtained at different temperatures.

T /K	a /Å	c /Å	V /Å^3
297 (4)	13.847 (3)	17.587 (3)	2920 (1)
320 (4)	13.848 (4)	17.592 (3)	2922 (1)
368 (4)	13.855 (4)	17.609 (4)	2927 (2)
412 (4)	13.859 (3)	17.612 (3)	2930 (1)
449 (4)	13.860 (3)	17.629 (3)	2933 (1)
485 (4)	13.870 (4)	17.638 (3)	2938 (1)
522 (4)	13.876 (3)	17.654 (3)	2944 (1)
559 (4)	13.884 (3)	17.665 (3)	2949 (1)
597 (4)	13.899 (4)	17.682 (4)	2958 (2)
640 (4)	13.911 (4)	17.698 (4)	2966 (2)
684 (4)	13.921 (3)	17.711 (3)	2972 (1)
728 (5)	13.929 (3)	17.723 (3)	2978 (1)
773 (5)	13.935 (2)	17.741 (2)	2983.6 (8)
829 (5)	13.943 (3)	17.755 (3)	2989 (1)
859 (5)	13.950 (3)	17.758 (3)	2993 (1)
880 (6)	13.951 (3)	17.761 (3)	2994 (1)
903 (6)	13.955 (2)	17.768 (2)	2996.7 (8)

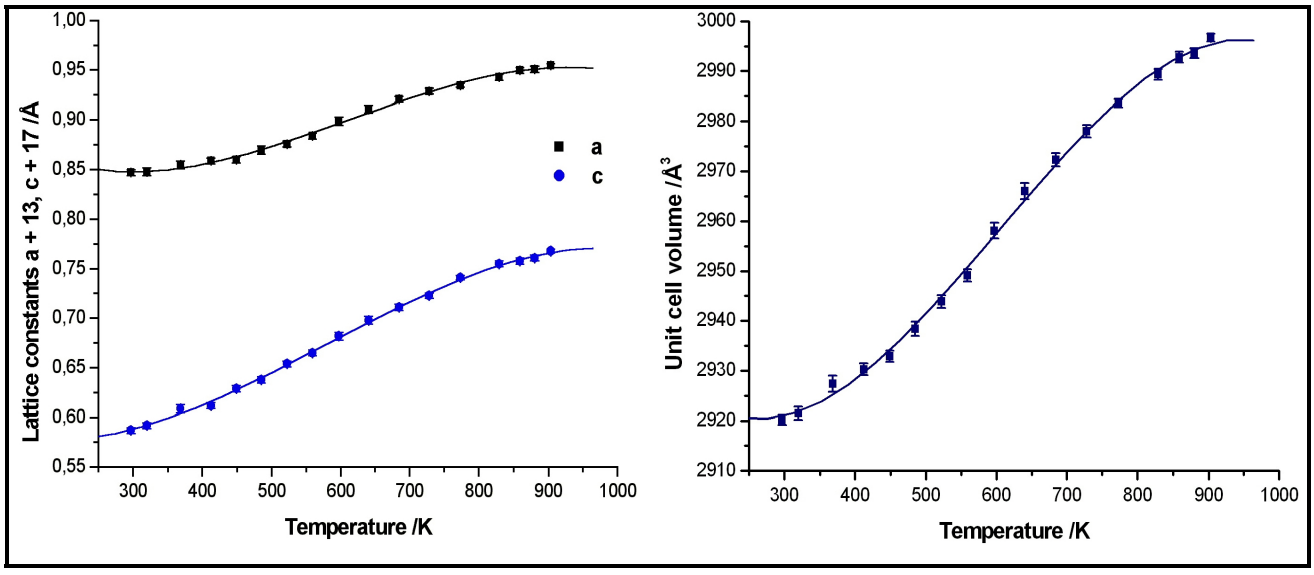

Fig. 5.20: The temperature dependence of the lattice constants (left) and the volume (right) of $K_2In_{12}Se_{19}$.

The dependence of lattice constants and volume from the temperature (K) can be presented by the equation (5.22).

$$\mathbf{Y(T) = P1 + P2(T-T_0) + P3(T-T_0)^2 + P4(T-T_0)^3 \quad Y = a, b, c, V} \qquad \mathbf{(5.22)}$$

The fitting parameters obtained by the least square fitting based on Marquardt algorithm for the lattice parameters ***a***, ***b*** and ***c*** are listed in table 5.8:

Table 5.8: The fitting parameters of the equation (5.22).

Parameter	P1	P2	P3	P4	χ^2	R^2
a	13.848(2)	1(3) x 10^{-5}	8(1) x 10^{-7}	-8(1) x 10^{-10}	0.73216	0.99677
b	13.848(2)	1(3) x 10^{-5}	8(1) x 10^{-7}	-8(1) x 10^{-10}	0.73216	0.99677
c	17.588(2)	1.8(3) x 10^{-4}	7(1) x 10^{-7}	-8(1) x 10^{-10}	0.63214	0.99899
V	2949(7)	-0.28(4)	7.9(7) x 10^{-4}	-4.6(4) x 10^{-7}	0.89783	0.99905

The lattice constants ***a***, ***c*** and the lattice ***volume*** vary according to a third order function (s-shaped) from temperature. No phase transition or other special physical effects could be observed in the studied temperature range. These observations are in a good agreement with those discussed from Schlosser in his PhD - thesis [122].
The obtained values of the thermal expansion coefficients and the respective standard deviations according the equations (5.20), (5.21) are listed in table 8.18 (appendix).

The mean coefficients of thermal expansion in ***a*** and ***b*** directions are equal $\overline{\alpha_a} = \overline{\alpha_b}$ = 1.14 (2) x 10^{-5} K^{-1}, the mean coefficients of thermal expansion in ***c*** direction and ***volume*** are respectively $\overline{\alpha_c}$ = 1.59(2) x 10^{-5} K^{-1} and $\overline{\alpha_V}$ = 4.02 (6) x 10^{-5} K^{-1}.

The powder patterns measured at different temperatures are presented in figure 8.8 (appendix).

5.7 Comparison of the thermal expansion of $K_2In_{12}Se_{12}Te_7$ and $K_2In_{12}Se_{19}$

To compare the thermal expansion for both analysed compounds it is necessary that the highest considered temperature should be the same for both compounds. Actually $K_2In_{12}Se_{12}Te_7$ was measured and indexed up to 733 K, while $K_2In_{12}Se_{19}$ up to 903 K. Hence the upper temperature limit for comparison is 733 K. The temperature difference of 5 K is within the measuring error.

The behaviour of the lattice constants with the temperature is not the same for both compounds. Based on the Marquardt least square fitting, the lattice constants **a** and **c** of $K_2In_{12}Se_{19}$ obey a third order while the lattice constants **a** and **c** of $K_2In_{12}Se_{12}Te_7$, obey linearly and according to a second order function respectively.
The thermal expansion coefficients within the respective temperature comparing range are summarised in table 5.9.

Table 5.9: Thermal expansion coefficients of $K_2In_{12}Se_{19}$ and $K_2In_{12}Se_{12}Te_7$ (* represents the mean value).

Compound \ Coefficient	α_a	α_b	α_c	α_V
	10^{-5} /K^{-1}	**10^{-5} /K^{-1}**	**10^{-5} /K^{-1}**	**10^{-5} /K^{-1}**
$K_2In_{12}Se_{19}$	1.26 (2)*	1.26 (2)*	1.78 (1)*	4.41 (5)*
$K_2In_{12}Se_{12}Te_7$	1.5 (2)	1.5 (2)	2.17 (4)*	5.18 (4)*

Referring to the thermal expansion coefficients, the thermal expansion for both compounds along ***a*** and ***b*** are similar (within the calculated standard deviation) and differ somehow along ***c*** direction.
The mixed crystal ($K_2In_{12}Se_{12}Te_7$) represents a larger elongation along ***c*** axis compared to $K_2In_{12}Se_{19}$, this phenomenon occurs due to the larger expansion caused from the presence of the tellurium atoms.
A similar behaviour is observed in the investigation of the thermal behaviour of ZnSe (692 K) and ZnTe (718 K) both belonging to the sphalerite type structure. Singh and Dayal [123-124] reported a higher thermal expansion ability of zinc telluride expressed from its mean expansion coefficient 9.67 x 10^{-6} compared to the mean value displayed from zinc selenide 9.11 x 10^{-6}.

5.8 Investigation of the thermal behaviour of In_5S_5Cl, In_5Se_5Cl, In_5S_5Br and In_5Se_5Br

5.8.1 Discussion

An interesting aspect of the high temperature X-ray investigations of In_5Ch_5X (Ch = S, Se; X = Cl, Br) would be their thermal behaviour and especially the behaviour of the polysynthetic nanolayers of the chloride type compounds with the temperature. Anyway, in these investigations no distinguishable movements or replacement of In^+ and $(In_2)^{4+}$-species within the same structure are expected.

5.9 Lattice thermal expansion behaviour of In_5Ch_5Cl (Ch = S, Se)

5.9.1 The Sample preparation and measurement

The samples of In_5S_5Cl and In_5Se_5Cl for this investigations were prepared by the syntheses of binary educts In_2Ch_3, InCh (Ch = S, Se) and InCl in pressed pellets (see chapter 4). The crystalline powders obtained from the crushed crystallites were transferred into ∅ 0.1 mm quartz capillaries and measured.

The room temperature and high temperature measurements proceeded measuring in region 5-65 ° (2θ), measuring step 0.1° and a ratio time/step 120 sec, ω-rotation = 2.5. The temperature range in this study was in the interval 296 – 873 K. For both compounds, the last powder pattern whose reflections could be indexed was recorded at 723 K, at higher temperatures the indexation of the reflections of the diffraction patters led to erroneous determinations.

At room temperature all lines of measured powder patterns of both compounds could be indexed under the monoclinic primitive cell with the space group $P2_1/m$. The thermal variation of the lattice parameters at different measured temperatures is listed in table 5.10 (In_5S_5Cl) and 5.11 (In_5Se_5Cl). The dependence of lattice parameters as a function of temperature is presented graphically in figures 5.21 and 5.22.

Table 5.10: Lattice parameters of In_5S_5Cl obtained at different temperatures.

T /K	a /Å	b /Å	c /Å	β /°	V Å^3
296(4)	8.939(1)	3.9163(8)	14.986(2)	93.69(2)	523.6(1)
373(4)	8.951(1)	3.9206(6)	14.999(2)	93.73(2)	525.3(1)
473(4)	8.970(2)	3.9270(8)	15.027(4)	93.74(2)	528.0(2)
573(4)	8.991(1)	3.9343(9)	15.039(2)	93.79(2)	530.8(1)
623(4)	9.002(2)	3.938(1)	15.056(3)	93.82(2)	532.6(2)
673(4)	9.006(3)	3.940(2)	15.067(3)	93.87(3)	533.4(3)
723(4)	9.010(3)	3.941(2)	15.081(4)	93.87(3)	534.3(2)

Table 5.11: Lattice parameters of In_5Se_5Cl obtained at different temperatures.

T /K	a /Å	b /Å	c /Å	β /°	V Å^3
296(4)	9.233(1)	4.0921(6)	15.278(2)	92.73(1)	576.6(1)
373(4)	9.242(2)	4.0964(7)	15.280(2)	92.76(1)	577.8(1)
423(4)	9.246(1)	4.0985(7)	15.284(2)	92.75(1)	578.5(1)
473(4)	9.254(2)	4.1024(9)	15.290(3)	92.75(2)	579.9(2)
523(4)	9.262(2)	4.103(1)	15.302(3)	92.76(2)	580.9(2)
573(4)	9.269(2)	4.106(1)	15.308(4)	92.70(2)	581.9(2)
623(4)	9.279(2)	4.109(1)	15.313(3)	92.79(2)	583.1(2)
673(4)	9.288(4)	4.113(2)	15.314(4)	92.81(3)	584.3(3)
723(4)	9.290(3)	4.113(1)	15.314(4)	92.83(2)	584.5(2)

The powder patterns of In_5S_5Cl and In_5Se_5Cl measured at different temperatures are aligned in appendix (Fig.8.9-8.12). The dependence of lattice parameters of In_5S_5Cl from the temperature (K) is presented by the equation (5.23) and (5.24):

$$\mathbf{a(T), b(T) = P1 + P2(T-T_0) + P3(T-T_0)^2 + P4(T-T_0)^3} \quad \textbf{(5.23)}$$

$$\mathbf{c(T), V(T) = P1 + P2(T-T_0)} \quad \textbf{(5.24)}$$

The fitting parameters of the above equations are obtained by the least-squares fittings using Marquardt algorithm and are listed in appendix (table 8.18).

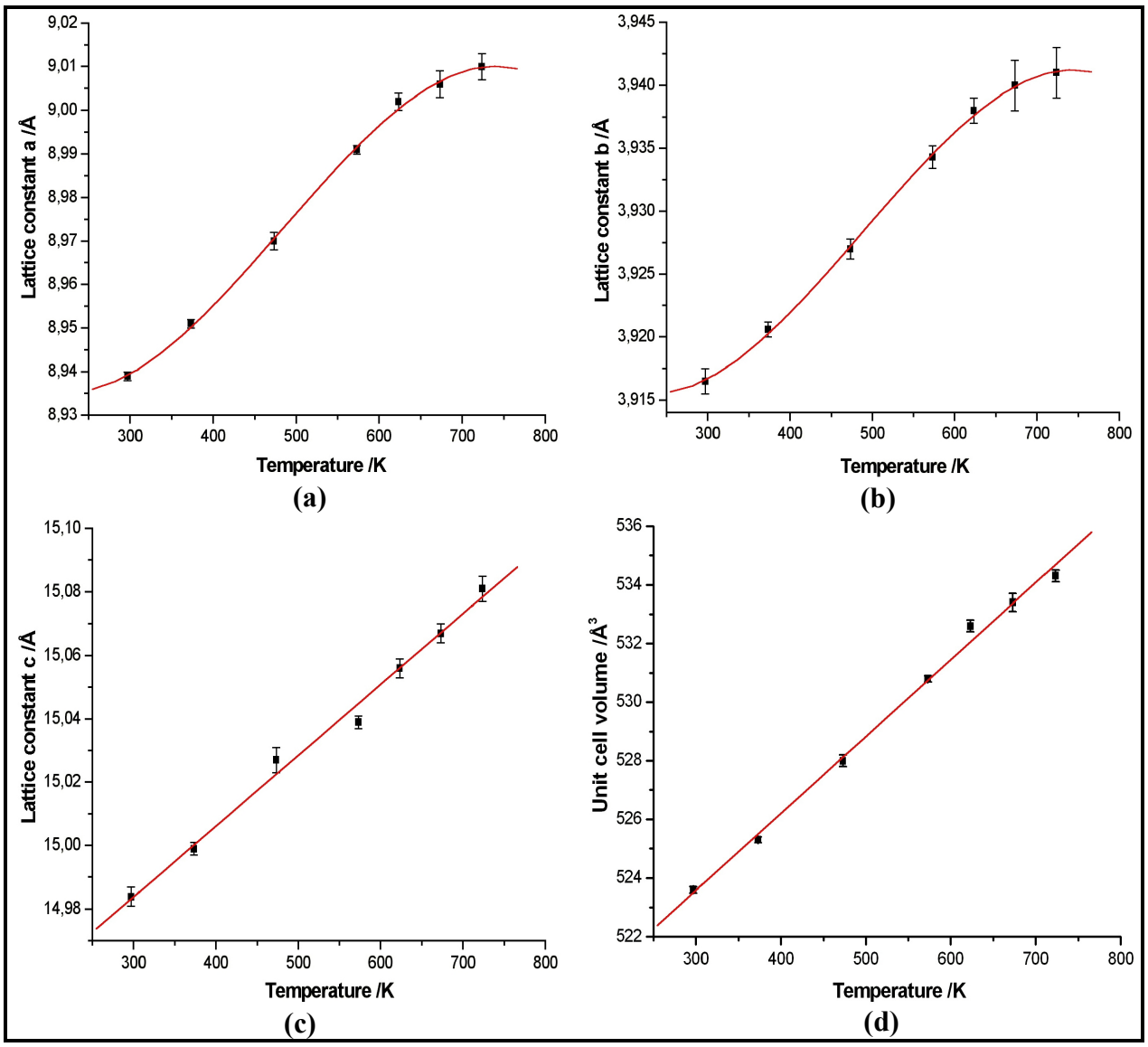

Fig. 5.21: The temperature dependence of the lattice parameters: (a) ***a***, (b) ***b***, (c) ***c*** and (d) ***volume*** of In_5S_5Cl.

The lattice constants ***a*** and ***b*** vary according to a third order function from temperature, differently from lattice constant ***c*** and the unit cell ***volume*** which vary linearly. No phase transition or other special physical effects could be observed for In_5S_5Cl in the studied temperature range.

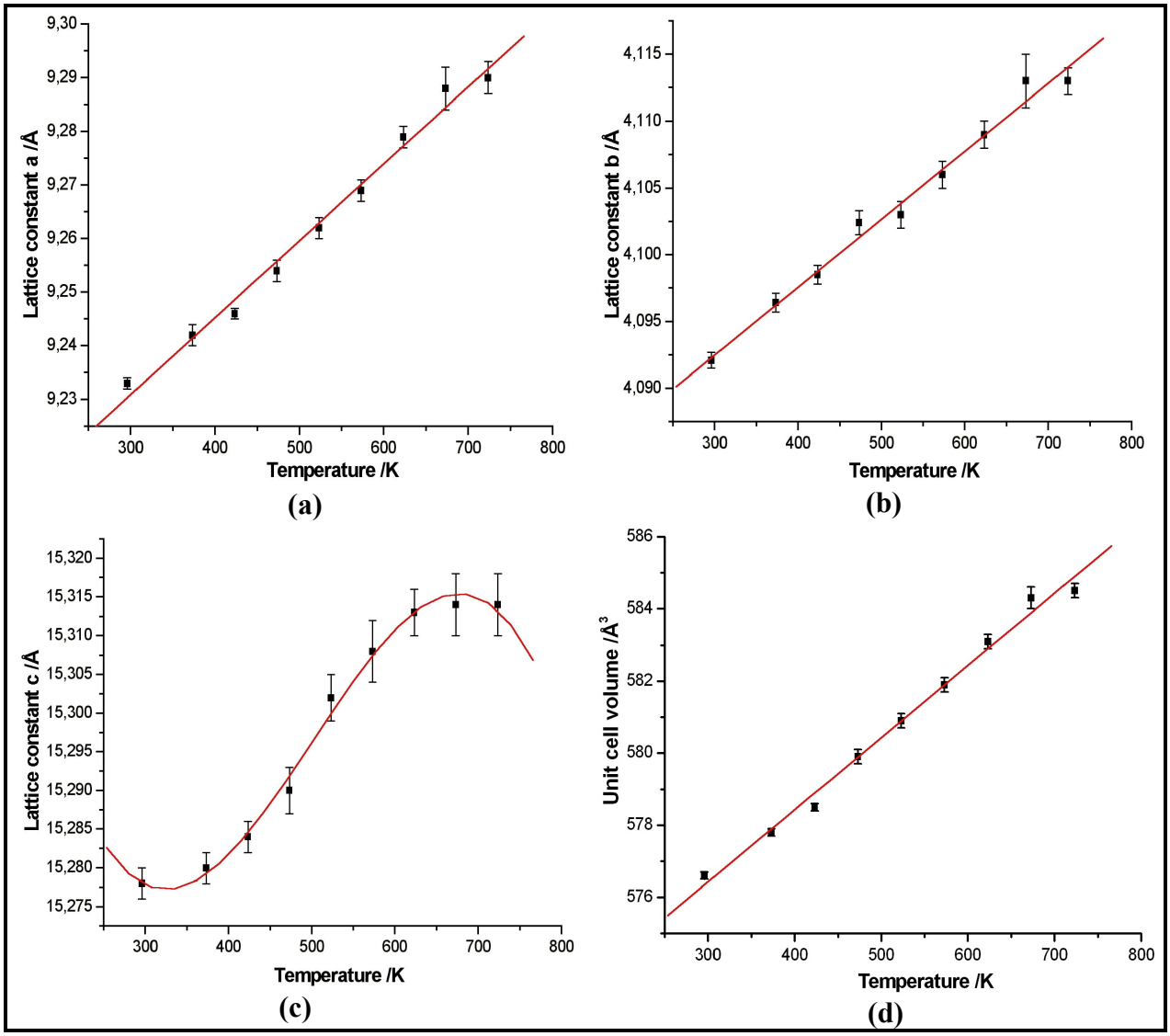

Fig. 5.22: The temperature dependence of the lattice parameters: (a) ***a***, (b) ***b***, (c) ***c*** and (d) ***volume*** of In_5Se_5Cl.

The dependence of lattice parameters from the temperature (K) can be presented according to the equations (5.25) and (5.26).

$$a(T), b(T), V(T) = P1 + P2(T-T_0) \quad (5.25)$$

$$c(T) = P1 + P2(T-T_0) + P3(T-T_0)^2 + P4(T-T_0)^3 \quad (5.26)$$

The fitting parameters of the above equations are obtained by the least-squares fittings using Marquardt algorithm and are listed in appendix (table 8.18).

The lattice constants ***a***, ***b*** and the lattice ***volume*** vary linearly from temperature. The lattice constant ***c*** varies according to a third order function (s-shaped) from temperature. The thermal behaviour of this compound shows no phase transition within the studied temperature range.

5.9.2 Thermal expansion coefficients of In_5S_5Cl and In_5Se_5Cl

The calculation of the thermal expansion coefficients is done according to the equations (5.20) and (5.21). The calculated values for the lattice constants ***a*** and ***b*** of In_5S_5Cl and for the lattice constant ***c*** of In_5Se_5Cl which do not show a linear behaviour are listed in tables 5.12 and 5.13.

Table 5.12: The coefficients of the thermal expansion α_a and α_b of In_5S_5Cl calculated at different temperatures.

T /K	α_a x 10^{-5} /K^{-1}	α_b x 10^{-5} /K^{-1}
296(4)	1.34(5)	1.02(4)
373(4)	2.06(3)	1.58(2)
473(4)	2.423(2)	1.88(2)
573(4)	2.16(2)	1.70(2)
623(4)	1.79(4)	1.43(3)
673(4)	1.26(5)	1.04(4)
723(4)	0.57(6)	0.53(5)

The mean coefficients of the thermal expansion (In_5S_5Cl) in ***a*** and ***b*** directions are: $\overline{\alpha_a}$ = 1.66(4) x 10^{-5} K^{-1}, $\overline{\alpha_b}$ = 1.31(3) x 10^{-5} K^{-1}, while the linear expansion coefficients for the ***c*** direction and the unit cell ***volume*** are: α_c = 1.4(3) x 10^{-5} $K^{-1}$and α_V = 5.0(5) x 10^{-5} K^{-1} respectively.

Table 5.13: The coefficient of thermal expansion (α_c) of In_5Se_5Cl calculated at different temperatures.

T /K	296(4)	373(4)	423(4)	473(4)	523(4)	573(4)	623(4)	673(4)	723(4)
α_c x 10^{-5} /K^{-1}	0.01(6)	0.49(4)	0.85(2)	1.030(8)	1.040(6)	0.88(2)	0.54(3)	0.03(5)	0.01(6)

The coefficients of the thermal expansion (In_5Se_5Cl) in ***a*** and ***b*** directions are: $\alpha_a = 1.5(3) \times 10^{-5}\ K^{-1}$, $\alpha_b = 1.2(2) \times 10^{-5}\ K^{-1}$, the mean coefficient in ***c*** direction is $\overline{\alpha_c} = 5.4(3) \times 10^{-6}\ K^{-1}$ and coefficient of thermal expansion for the unit cell ***volume*** is $\alpha_V = 3.4(5) \times 10^{-5}\ K^{-1}$.

5.9.3 Discussion of the results

The compound In_5S_5Cl reveals comparable expansion coefficients in the three directions, while In_5Se_5Cl displays a higher elongation in ***a*** and ***b*** direction compared to ***c*** direction.

At 873 K, the powder patterns of both compounds exhibit the presence of In_2S_3 and In_2Se_3 in case of In_5S_5Cl (Fig. 8.10 appendix) and In_5Se_5Cl (8.12 appendix) respectively. A detailed investigation of their powder patterns revealed a decomposition temperature ranging in the interval of 673 K - 723 K. The decomposition process in the case of In_5S_5Cl is displayed in figure 5.23. Its occurrence takes place according to the reaction (5.27):

$$\mathbf{In_5Ch_5Cl \rightarrow 2InCh + In_2Ch_3 + InCl \quad (Ch = S, Se)} \qquad \mathbf{(5.27)}$$

A proof of this mechanism is the presence of InS and InSe together with In_2S_3 (m.p. = 1323 K) and In_2Se_3 (m.p. 933 K) observed at 723 K. At this temperature the presence of InCl was not identifiable (m.p. = 489 K). At temperatures around 873 K the binary compounds InS and InSe obtained as a consequence of the decomposition are hardly identifiable due to a possible phase transition (crystalline – amorphous) or a further decomposition to In_2Ch_3 (Ch = S, Se) and elemental In.

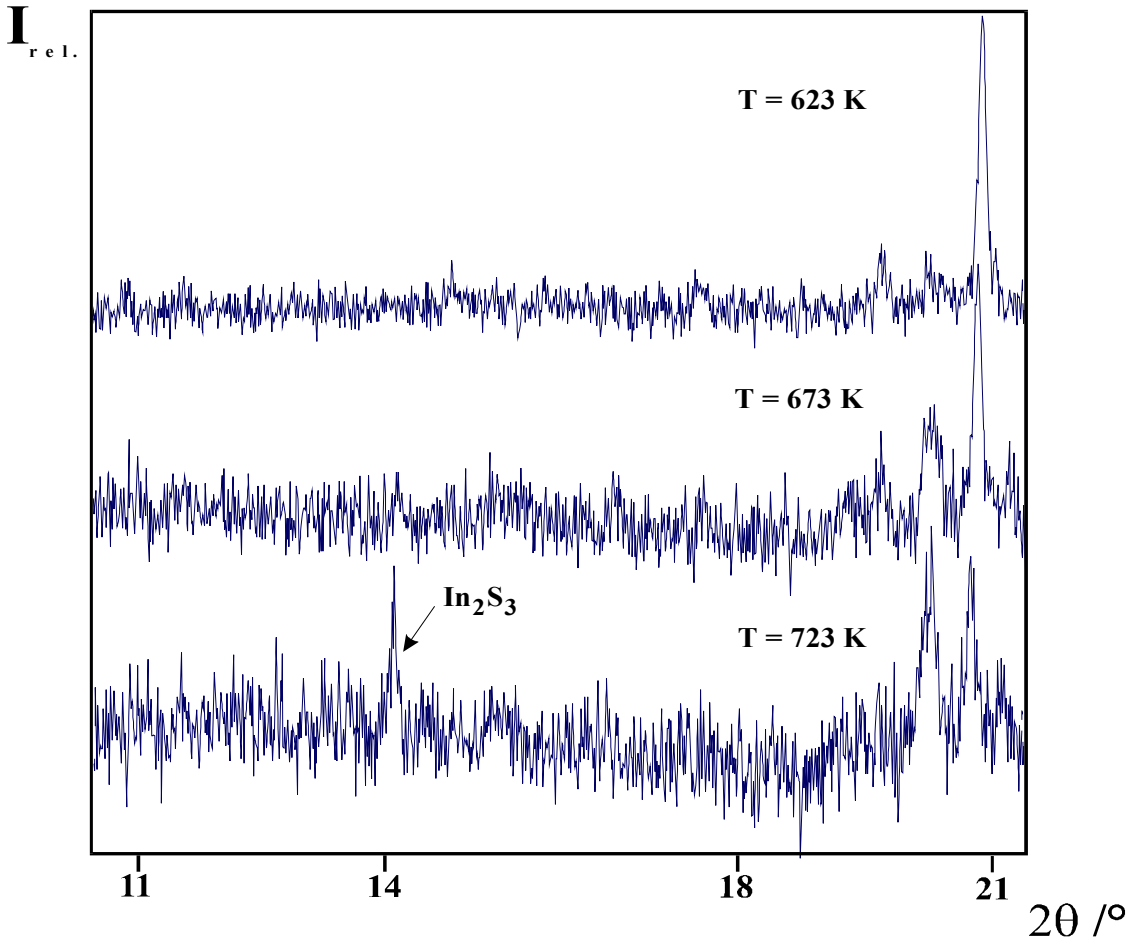

Fig. 5.23: Section of the powder diffraction patterns of In_5S_5Cl measured at three different temperatures. A evident sign for the gradual decomposition of In_5S_5Cl is the appearance of the reflection (111) of In_2S_3 between 673 and 723 K.

5.10 Investigation of the thermal expansion of In_5S_5Br and In_5Se_5Br

5.10.1 Sample preparation and measurement

In_5S_5Br and In_5Se_5Br are synthesised from elements and $InBr_3$ in dried and evacuated ampoules (See paragraph 4.3). The crystalline powders obtained from the ground crystals were transferred into quartz capillaries of 0.1 mm outer diameter and measured. The measuring procedure and the measuring parameters were similar to In_5S_5Cl and In_5Se_5Cl.

The investigated temperature ranged from room temperature up to 823 K. The quality of diffractions patterns of both compounds was acceptable (Fig. 8.13-8.16 in appendix). The indexation of the reflections, the refinement and the lattice parameters succeeded until 723 K. The powder patterns measured at higher temperatures show difficulties in the indexing of the reflections, due to the presence of the decomposition products and the decrease of the intensities of many reflections.

At room temperature all reflections of the measured powder patterns of In_5S_5Br and In_5Se_5Br, could be indexed under the orthorhombic primitive cell with the space group $Pmn2_1$. The thermal expansion of the lattice constants at different measuring temperatures is listed in tables 5.14 and 5.15. Their dependence as a function of temperature is presented graphically in figures 5.24 and 5.25.

Table 5.14: Lattice parameters of In_5S_5Br obtained at different temperatures.

T /K	a /Å	b /Å	c /Å	V Å^3
296(4)	3.931(1)	9.077(2)	14.831(3)	529.1(1)
323(4)	3.931(1)	9.078(2)	14.830(3)	529.2(2)
373(4)	3.934(1)	9.085(2)	14.835(3)	530.3(2)
423(4)	3.936(1)	9.093(2)	14.837(4)	531.0(2)
473(4)	3.938(1)	9.101(2)	14.843(3)	532.0(2)
523(4)	3.9402(9)	9.108(1)	14.843(3)	532.7(1)
573(4)	3.9431(9)	9.116(1)	14.846(3)	533.7(1)
623(4)	3.946(1)	9.125(2)	14.854(3)	534.9(2)
673(4)	3.947(1)	9.137(1)	14.863(2)	536.0(2)
723(4)	3.946(1)	9.141(2)	14.866(4)	536.2(2)

Table 5.15: Lattice parameters of In_5Se_5Br obtained at different temperatures.

T /K	a /Å	b /Å	c /Å	V /Å^3
296(4)	4.099(1)	9.336(2)	15.250(4)	583.6(2)
373(4)	4.1037(7)	9.3569(9)	15.251(2)	585.6(1)
423(4)	4.1056(8)	9.3607(9)	15.255(2)	586.3(1)
473(4)	4.1089(7)	9.375(1)	15.257(2)	587.7(1)
523(4)	4.115(1)	9.386(1)	15.255(4)	589.1(2)
623(4)	4.120(1)	9.403(1)	15.262(3)	591.3(2)
723(4)	4.1232(8)	9.431(2)	15.275(2)	594.0(1)

The powder patterns of In_5S_5Br and In_5Se_5Br measured at different temperatures are aligned in appendix (Fig. 8.13-8.16).

The dependence of lattice constants and volume of In_5S_5Br from the temperature (K) can be presented according to the equations (5.28), (5.29) and (5.30).

$$a(T) = P1 + P2(T-T_0) + P3(T-T_0)^2 + P4(T-T_0)^3 \quad (5.28)$$

$$b(T), V(T) = P1 + P2(T-T_0) \quad (5.29)$$

$$c(T) = P1 + P2(T-T_0) + P3(T-T_0)^2 \quad (5.30)$$

The fitting parameters of the above equations are obtained by the least-squares fittings using Marquardt algorithm and are listed in appendix (table 8.18).

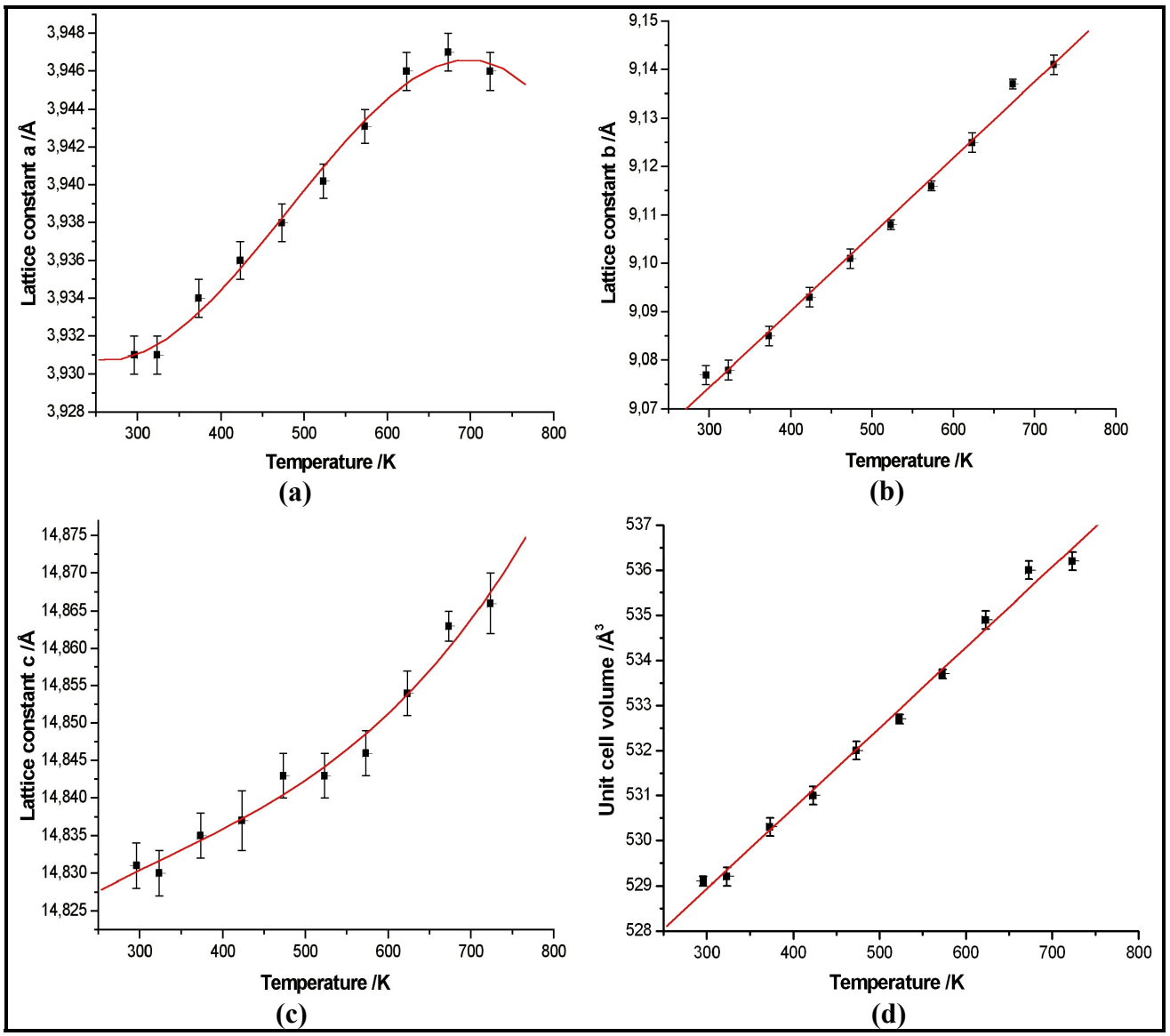

Fig. 5.24: The temperature dependence of the lattice parameters: (a) ***a***, (b) ***b***, (c) ***c*** and (d) ***volume*** of In_5S_5Br.

The lattice constant ***a*** varies according to a third order function (s-shaped) from the temperature, the lattice constant ***b*** and ***volume*** vary linearly from temperature, while the lattice constant ***c*** varies according to a second order function from temperature. The thermal behaviour of this compound shows no phase transition within the investigated temperature range.

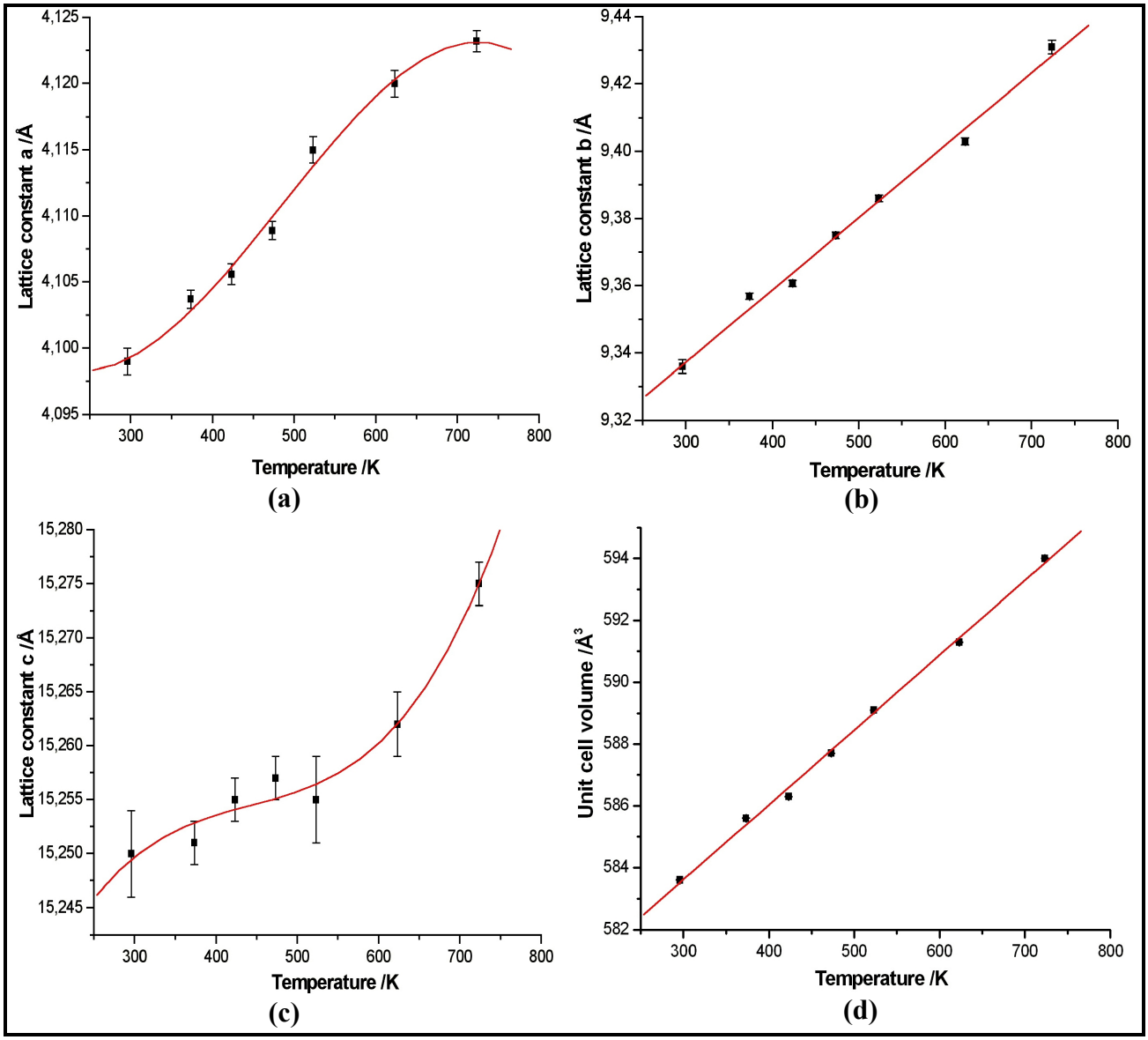

Fig. 5.25: The temperature dependence of the lattice parameters (a) ***a***, (b) ***b***, (c) ***c*** and (d) ***volume*** of In_5Se_5Br.

The dependence of lattice constants and volume of In_5Se_5Br from the temperature (K) can be presented according to the equations (5.31) and (5.32).

$$\mathbf{a(T),\ c(T)\ = P1 + P2(T-T_0) + P3(T-T_0)^2 + P4(T-T_0)^3} \qquad \mathbf{(5.31)}$$

$$\mathbf{b(T),\ V(T) = P1 + P2(T-T_0)} \qquad \mathbf{(5.32)}$$

The fitting parameters of the above equations are obtained by the least-squares fittings using Marquardt algorithm and are listed in appendix (table 8.18).

The lattice constants ***a***, ***c*** and lattice ***volume*** of In_5Se_5Br vary according to a third order function (s-shaped) from temperature while the lattice constant ***b*** varies linearly. Again no phase transition or other special physical effects could be observed in the studied temperature range.

The values of the thermal expansion coefficients for lattice constants ***a*** and ***c*** (which do not vary linearly with temperature) are listed in table 5.16 (In_5S_5Br) and 5.17 (In_5Se_5Br).

Table 5.16: The coefficients of thermal expansion α_a and α_c (In_5S_5Br) calculated at different temperatures.

T /K	α_a x 10^{-5} /K^{-1}	α_c x 10^{-6} /K^{-1}
296(4)	0.51(4)	2.02(8)
323(4)	0.78(4)	2.54(8)
373(4)	1.17(3)	3.49(8)
423(4)	1.41(1)	4.44(8)
473(4)	1.509(2)	5.39(8)
523(4)	1.46(1)	6.35(8)
573(4)	1.27(2)	7.30(8)
623(4)	0.93(3)	8.25(8)
673(4)	0.44(4)	9.21(8)
723(4)	0.1(6)	10.16(8)

The mean coefficients of thermal expansion in ***a*** and ***c*** direction are $\overline{\alpha_a}$ = 9.5(3) x 10^{-6} K^{-1}, $\overline{\alpha_c}$ = 5.92(8) x 10^{-6} K^{-1}. The coefficient of thermal expansion in ***b*** direction and the coefficient of the volume expansion are α_b = 1.8(3) x 10^{-5} K^{-1}, α_V = 3.3(4) x 10^{-5} K^{-1}.

Table 5.17: The coefficients of the thermal expansion α_a and α_c (In_5Se_5Br) calculated at different temperatures.

T /K	α_a x 10^{-5} /K^{-1}	α_c x 10^{-6} /K^{-1}
296(4)	0.7(1)	5.2(5)
373(4)	1.5(1)	2.8(5)
423(4)	1.7(1)	2.0(5)
473(4)	1.9(1)	1.9(5)
523(4)	1.8(1)	2.4(5)
623(4)	1.3(1)	5.4(5)
723(4)	0.2(1)	11.0(5)

The coefficient of thermal expansion in ***b*** direction is α_b = 2.3(4) x 10^{-5} K^{-1} (until 723 K). The mean coefficients of thermal expansion in ***a*** and ***c*** directions are: $\overline{\alpha_a}$ = 1.3(1) x 10^{-5} K^{-1}, $\overline{\alpha_c}$ = 4.4(5) x 10^{-6} K^{-1}, the coefficient of the volume expansion is α_V = 4.2(4) x 10^{-5} K^{-1}.

The decomposition mechanism of this compound is similar to that of In_5S_5Cl and In_5Se_5Cl. At 873 K, again only the reflections belonging to In_2S_3 and In_2Se_3 could be observed (Fig. 8.14-8.16 in appendix).

5.11 Comparison of the results

The aim of the present investigation was the thermal behaviour under ambient pressure of In_5Ch_5X (Ch = S, Se; X = Cl, Br). All the investigated compounds displayed no phase transitions or other effects (except a non linear thermal behaviour in some cases). At elevated temperatures, they decompose gradually to In_2Ch_3, InCh (Ch = S, Se) and InX (X = Cl, Br). Clear evidence for this

assumption comes from the measured powder patterns of these compounds at temperatures over 800 K.

In the course of this study, the thermal expansion coefficients of the nominated compounds have been determined and are listed in table 5.18.

Table 5.18: Comparison of the thermal expansion coefficients of four compounds In_5Ch_5X (Ch = S, Se, X = Cl, Br). The mean value is represented by the (*) symbol.

Coefficient	In_5S_5Cl	In_5Se_5Cl	In_5S_5Br	In_5Se_5Br
α_a x 10^{-5} /K^{-1}	1.66(4)*	1.5(3)	0.95(3)*	1.3(1)*
α_b x 10^{-5} /K^{-1}	1.31(3)*	1.2(2)	1.8(3)	2.3(4)
α_c x 10^{-6} /K^{-1}	14(3)	5.4(3)*	5.92(8)*	4.4(5)*
α_V x 10^{-5} /K^{-1}	5.0(5)	3.4(5)	3.3(4)	4.2(4)

In the chloride-type compounds: In_5S_5Cl, In_5Se_5Cl the elongation in ***a*** direction is higher compared to the expansion coefficients in ***b*** and ***c*** directions (this is confirmed from the calculated expansion coefficients). A similar analogy can be concluded for the bromide type, where the elongation in ***b*** direction is higher compared to ***a*** and ***c***. Generally low is the elongation in the ***c*** direction for the compounds In_5S_5Br, In_5Se_5Cl and In_5Se_5Br. All the investigated compounds exhibit linear thermal expansion of the lattice volume.

The differences of the expansion coefficients within one structure type can be explained based on the differences of the bond strength between the atoms e.g. In-S, In-Se, while the differences of the expansion coefficients between the compounds of both structure types arise due to the difference of the proper structures. Therefore, one should not expect similar coefficients thinking that a change of chloride with bromide makes only 9.1% difference in the structure, but should take in account the structural differences as well.

6 Summary

This thesis summarises three different research aspects concerning:

1. The attempts for inorganic syntheses in supercritical CO_2
2. The syntheses, the structure determination and the characterisation by several methods of the mixed valence indium chalcogen halides In_5Ch_5X (Ch = S, Se; X = Cl, Br) and their derivative compounds.
3. High temperature X-ray investigations of powdered samples of $K_2In_{12}Se_{12}Te_7$ and $K_2In_{12}Se_{19}$ ensued by the mixed valence compounds In_5S_5Cl, In_5Se_5Cl, In_5S_5Br, In_5Se_5Br.

The attempts for inorganic syntheses in supercritical CO_2

The purpose of this research topic consisted in testing the ability of $scCO_2$ or tuned $scCO_2$ to dissolve and mediate in several reactions of inorganic compounds. The employment of $scCO_2$ as a reaction medium required the projection and construction of several devices concerning: a) its manipulation to dry ice (purifying, metering and condensing subsystems), b) the reaction environment (ampoule, autoclaves), c) the measuring and safety devices. The reactions were performed at temperatures varying from 100°C until 240°C. The latter was the maximum working temperature due to the limitations occurring of the O-ring material (Viton). The reaction pressures varied from 140 up to 260 bar. In order to distinguish whether a reaction depended on the presence of $scCO_2$, parallel reactions involving the same educts without CO_2 (solid state or hydrothermal reactions) were performed. The investigation of the reaction products was done by X-ray powder diffractometry and/or IR and Raman spectroscopy

Within the mentioned conditions the solubility and the reactions of several inorganic compounds were tested. The nature of the involved compounds ranged from fairly non polar molecular compounds (e.g. SnI_4) up to polar or ionic crystalline compounds (e.g. $CsCO_3$, NaCl etc). Beside these, reactions which for different reasons failed in usual solid state methods as well as searches for new modifications of chalcogenides (i.e. Se, Te) were carried out.

All the attempted syntheses did not exhibit the presence of new compounds or new modifications occurring from the presence of $scCO_2$. The synthesised compounds were merely a product of solid state or hydrothermal synthesis, where the temperature played the decisive role and not the pressure. Hence, indicating a low or no solubility of the employed species in the $scCO_2$. According to this experience, $scCO_2$ can be regarded an improper solvent (for the above conditions) for inorganic syntheses.

The syntheses, the structure determination and the characterisation by several methods of the mixed valence indium chalcogen halides In_5Ch_5X (Ch = S, Se; X = Cl, Br) and their derivative compounds

In the course of the investigation of the systems In-Ch-X (Ch = S, Se; X = Cl, Br) four new compounds were synthesised, namely: In_5S_5Cl, In_5Se_5Cl, In_5S_5Br and In_5Se_5Br. These compounds are not isotypic, they crystallise in two different crystal systems: monoclinic (SG $P2_1/m$) in the case of In_5Ch_5Cl and orthorhombic (SG $Pmn2_1$) for In_5Ch_5Br. In all these compounds, the indium atoms occurs in three different oxidation states: In^+, $(In_2)^{4+}$ and In^{3+}. In^+ shows a three capped trigonal prismatic coordination, the formal In^{2+}-ions build ethane analogue In_2Ch_6 units with covalently bonded indium atoms and In^{3+} is octahedrally coordinated.

Similarly to the already known mixed valence compounds MIn_5Ch_6, MIn_5Ch_7 and MIn_7Ch_9, the newly synthesised compounds can be discussed based on two dimensional building units. The chloride-type compounds consist of a characteristic and common building unit, while the bromide-type compounds In_5Ch_5Br consist of one building unit which can be regarded as a hybrid of both layers observed in the chloride-type compounds.

A good agreement consists between the environment of In^+ and $(In_2)^{4+}$ species in both structures. The difference between both structure types consists in the exchange of In^+ and $(In_2)^{4+}$ -species in some positions building a mosaic of six triangular prisms around two edge-sharing octahedra. Topologically both structures are built from layers, where the chloride-type structure contains layers with 4:2 and 2:4 arrangements in contrast to In_5Ch_5Br which contains only layers with 3:3 arrangements.

Regardless to the close similarities of these compounds evidenced from their lattice constants and the formula sum, the X-ray investigations presented numerous differences. All crystals of In_5S_5Cl and In_5Se_5Cl are twinned by reticular pseudomerohedry. The refinements performed by neglecting

the overlapping reflections revealed bad figures of merit accompanied by high residual electron densities. In_5S_5Br and In_5Se_5Br in contrast to the chloride type compounds presented no structural anomalies. Their refinements show good figures of merit and lower Fourier residuals.

Starting from the similarities and at the same time the differences of these structure-types observed from the X-ray measurements, further detailed investigations were carried out using HRTEM accompanied by SAED and EDX measurements.

The HRTEM investigations of the bromide-type structure (In_5S_5Br) displayed only layers with 3:3 arrangements presented in micrographs as oval contrasts. The SAED patterns recorded from several crystallites displayed only sharp reflections.

The HRTEM investigations of the chloride-type structure (In_5S_5Cl) exhibited several anomalies of the real structure. Differently from the observations of the X-ray investigations, these measurements displayed the existence of orthorhombic polymorph layers with 3:3 arrangements perturbing frequently the monoclinic layers with 4:2 and 2:4 arrangements. At the same time, a good compatibility between layers with different arrangements is observed.

Secondly the existence of polysynthetic twinning of lamellas with different orientations was observed. The HRTEM images presented a layer with 3:3 arrangements exactly at the twin boundary (between layers with 4:2 and 2:4 arrangements) causing the necessary shift for a perfect fitting of both domains. This fact confirmed again the good compatibility between layers with different arrangements. A good compatibility exists not only between layers with different arrangement of In_5S_5Cl but between the layers with different arrangements of In_5S_5Cl and layers with 2:4 arrangements of In_6S_7 too. An intergrowth of orthorhombic domains of In_5S_5Cl and monoclinic domains of In_6S_7 is observed due to the similarities (morphological and structural) that exists between them.

The mixed valence character of indium in these compounds allows three well defined substitution possibilities of indium species, namely: a) In^+, $(In_2)^{4+}$ and In^{3+}. The series of substitution experiments revealed the compounds $TlIn_4S_5Cl$ and $TlIn_4Se_5Cl$ in case of substitution of In^+, and $In_{(5-x)}Cr_xSe_5Cl$ in case of substitution In^{3+}. In addition to these substitutions further substitutions of chalcogen and halogen atoms yielded several mixed crystals ($In_5S_{(5-x)}Se_xCl$, $In_5S_{(5-x)}Se_xBr$, $In_5S_5Cl_{(1-x)}Br$ and $In_5Se_5Cl_{(1-x)}Br$), where $In_5Se_{(5-x)}Te_xBr$ displayed some interest. In fact a complete

substitution of Se atoms by Te atoms could not be obtained, while in case of Br atoms by I atoms nor partial, neither complete substitution is possible. The X-ray single crystal investigations of the mixed crystals ($In_5S_{(5-x)}Se_xCl$, $In_5S_{(5-x)}Se_xBr$, $In_5S_5Cl_{(1-x)}Br$, $In_5Se_5Cl_{(1-x)}Br$ and $TlIn_4Se_5Cl$) displayed the presence of multiple twinning individuals in all of them. The structure solution and refinement of the latter ($TlIn_4Se_5Cl$) was performed in the space group $P2_1/m$ based on the structure model of In_5Se_5Cl. The refinement showed a significant reduced occupancy of Tl^+ -position, which evidences a partial occupancy of it by Tl^+ and In^+.

High temperature X-ray investigations of powdered samples of $K_2In_{12}Se_{12}Te_7$ and $K_2In_{12}Se_{19}$ ensued by the mixed valence compounds In_5S_5Cl, In_5Se_5Cl, In_5S_5Br, In_5Se_5Br

The third topic of this work considers mainly the X-ray high temperature investigations of the compounds $K_2In_{12}Se_{12}Te_7$ and $K_2In_{12}Se_{19}$ followed by the mixed valence compounds In_5Ch_5X (Ch = S, Se; X = Cl, Br). The measurements were performed in a high temperature X-ray diffraction system equipped with a PSD by using quartz capillaries. Prior to these measurements, the calibration of the device using an external standard (Iridium powder) was done. The temperature calibration was followed by the optimisation measurements using powdered sample of $K_2In_{12}Se_{12}Te_7$ and ∅ 0.1 and ∅ 0.2 mm capillaries. These measurements displayed a better quality of diffraction patterns (low background) in case of using a double capillary (∅ 0.1 and ∅ 0.2 mm) capillaries instead of separated ∅ 0.1 or ∅ 0.2 capillaries.

The thermal behaviour of both compounds was investigated up to 733 K for $K_2In_{12}Se_{12}Te_7$ and 903 K for $K_2In_{12}Se_{19}$ and displayed no phase transitions. In some cases a significant deviation from the expected linear behaviour was observed. The lattice constants *a* and *c* of $K_2In_{12}Se_{12}Te_7$ show respectively linear and parabolic behaviour with the temperature, while the lattice constants *a* and *c* of $K_2In_{12}Se_{19}$ behave like a third ordered function (s-shaped). The latter observation is in full agreement with the temperature dependent single crystal investigations performed by Schlosser [120]. The behaviour of the superstructure reflections shown by $K_2In_{12}Se_{12}Te_7$ is investigated up to 733 K. In contrast to $K_2In_{12}Se_{12}Te_7$, no superstructure reflections could be observed for the compound $K_2In_{12}Se_{19}$ at temperatures higher than 673 due to their weakness.

The coefficients of the thermal expansion are similar in the [100] and [010] directions and differ slightly in case of [001] direction.

In the course of the X-ray high temperature investigations, the thermal behaviour of the new solids (In_5Ch_5X) was studied. The investigation temperature varied from room temperature up to 823 K. Within this range, no phase transition was observed. The compounds start to decompose gradually at high temperatures and the decomposition compounds that can barely observed are In_2S_3 (in case of In_5S_5X) and In_2Se_3 (in case of In_5Se_5X). The thermal behaviour of the lattice constants of these compounds differed from each other, while the unit cell volume in all cases behaved linearly.

7 References

[1] M. Poliakoff, P. King: Phenomenal fluids. *Nature* **2001**, *412*, 125.

[2] M. Poliakoff, P. Anastas: A principled stance. *Nature* **2001**, *413*, 257.

[3] O. J. Catchpole, J. B. Grey, K. A. Noermark: Fractionation of fish oils using supercritical CO_2 and CO_2 + ethanol mixtures. *J. Supercrtitical fluids* **2000**, *19(1)*, 25-37.

[4] M. Markom, H. Singh, M. Hasan: Supercritical CO_2 fractionation of crude palm oil. *J. Supercritical fluids* **2001**, *20(1)*, 45-53.

[5] D. P. Ndiomu, C. F. Simpson: Some applications of supercritical fluid extraction. Analytica Chimica Acta **1988**, *213(1-2)*, 237-243.

[6] G. Vesapollo, L. Longo, L. Rescio, L. Ciurlia: Innovative supercrtical CO_2 extraction of lycopene from tomato in the presence of vegetable oil as co-solvent. *J. Supercritical fluids* **2004**, *29(1-2)*, 87- 96.

[7] S. Spilimbergo, N. Elvassore, A. Bertucco: Microbial inactivation by high-pressure. *J. Supercrtical fluids* **2002**, *22(1)*, 55-63.

[8] A. Vatanara, A. R. Najafabadi, M. Khajeh, Y. Yamini: Solubility of some inhaled glucocorticoids in supercritical carbon dioxide *J. Supercritical fluids* **2005**, *33(1)*, 21-25.

[9] B. R. Simmons, J. T. Stewart: Supercritical fluid extraction of selected phamaceuticals from water and serum. *J. Chromatography B* **1997**, *688(2)*, 291-302.

[10] C. M. Wai, Y. Kulyako, H.-K. Yak, X, Chen, S.-J. Lee: Selective extraction of strontium with supercritical fluid carbon dioxide. *Chem. Commun*. **1999**, *24*, 2533 - 2534.

[11] C. M. Wai, S. Wang, Y. Liu, V. L.-Avila, W. F. Beckert: Evaluation of dithiocarbamates and β-diketones as chelating agents in supercritical fluid extraction of Cd, Pb, and Hg from solid samples. *Talanta* **1996**, *43*, 2083-2091.

[12] C. M. Wai: Supercritical fluid extraction of trace metals from solid and liquid materials for analytical publications. *Analytical Sciences* **1995**, *11(1)*, 165-167.

[13] Y. Lin, R. D. Brauer, K. E. Laintz, C. M. Wai: Supercritical fluid extraction of lanthanides and actinides from solid materials with a fluorinated β-Diketone. *Analytical Chemistry* **1993**, *65(18)*, 2549-2551.

[14] Y. Lin, C. M. Wai: Supercritical fluid extraction of Lanthanides with fluorinated β-Diketones and Tributyl Phosphate *Analytical Chemistry* 1994, *66(13)*, 1971-1975.

[15] S.N. Joung, S. J. Yoon, S. Y. Kim, K.-P. Yoo: Extraction of lanthanide ions from aqueous solution by modified supercritical CO_2. *J. Supercritical fluids* 2000, *18(2)*,157-166.

[16] M. D. Samsonov, C. M. Wai, S.-C. Lee, Y. Kulyako, N. G. Smart: Dissolution of uranium dioxide in supercritical fluid carbon dioxide. *Chem. Commun.* **2001**, *18*, 1868-1869.

[17] U. Fehrenbacher, M. Ballauff, O. Muth, T. Hirth: Investigation of heterogeneous radical polymerization of methyl methacrylate with polydimethysiloxane as stabilizing agent in supercrtitical CO_2 by turbidimetry. *Appl. Org. Chem.* **2001**, *15(7)*, 613-616.

[18] J. Liu, R. Zhang, H. Li, B. Han, Z. Liu, T. Jiang, J. He, X. Zhang, G. Yang: How does magnetic field affect polymerisation in supercrtitical fluids? Study of radical polymerization in supercritical CO_2. *N. J. Chem.* **2002**, *26(7)*, 958-961.

[19] P. Lozano, T. De Diego, D. Carrie, M. Vaultier, J. L. Iborra: Synthesis of glycidyl esters catalyzed by lipases in ionic liquids and supercritical carbon dioxide *Journal of Molecular Catalysis A* **2004**, *214(1)*, 113-119.

[20] P. B. Webb, D. J. Cole-Hamilton: Continuous flow homogeneous catalysis using supercritical fluids. *Chem. Commun.* 2004, *5*, 612-613.

[21] O. Kroecher, R. A. Koeppel, A. Baiker: Sol-gel derived hybrid materials as heterogeneous catalysis for the synthesis of N,N-dimethylformaminde from supercritical carbon dioxide. *Chem. Commun.* **1996**, *13*, 1497-1498.

[22] T. Matsuda; T. Harada, K. Nakamura: Organic synthesis using enzymes in supercritical carbon dioxide. Green Chemistry **2004**, *6(9)*, 440-444.

[23] Th. Hartman, E. Schwabe, Th. Scheper, D. Combes: Enzymatic reactions in supercritical carbon dioxide. *Stereoselective Biocatalysis* **2000**, 799-838.

[24] E. Castillo, A. Marty, D. Combes, J. S. Condoret: Polar substrates for enzymic reactions in supercritical CO_2: how to overcome the solubility limitation. *Biotechnology Letters* **1994**, *16(2)*, 169-74.

[25] J. Zhang, B. Han, J. Liu, X. Zhang, Z. Liu, J. He: A new method to recover the nanoparticles from reverse micelles: recovery of ZnS nanoparticles synthesized in reverse micelles by compressed CO_2. *Chem. Commun.* **2001**, *24*, 2724-2725.

[26] K. T. Lim, H. S. Hwang, M. S. Lee, G. D. Lee, S.-S. Hong, K. P. Johnston: Formation of TiO_2 nanoparticles in water-in-CO_2 microemulsions. *Chem. Commun.* **2002**, *14*, 1528-1529.

[27] K. Chhor, J.F. Bocquet, C. Pommier: Syntheses of submicron magnesium oxide powders. *Materials Chemistry and Physics* **1995**, *40*, 63-68.

[28] Z. Lou, Q. Chen, W. Wang, Y. Qian, Y. Zhang: Growth of Large Diamond Crystals by Reduction of Magnesium Carbonate with Metallic Sodium. *Angew. Chem. Int. Ed.* **2003**, *42*, 4501-4503.

[29] Z. Lou, Q. Chen, Y. Zhang, W. Wang, Y. Qian: Diamond Formation by Reduction of Carbon Dioxide at Low Temperatures. *J. Am. Chem. Soc.* **2003**, *125*, 9302-9303.

[30] M. Motiei, Y. R. Hacohen, J. C.-Moreno, A. Gedanken: Preparing Carbon Nanotubes and Nested Fullerenes from Supercritical CO_2 by a Chemical Reaction. *J. Am. Chem. Soc.* **2001**, *123*, 8624-8625.

[31] J. L. Roberts Jr., D. T. Sawyer: Electrochemical oxidation of carbon monoxide at gold electrodes. *J. Electroanal. Chem.* **1965**, *10*, 989-1000.

[32] P. G. Russel, N. Kovac, S. Srinivasan, M. Sterrinberg: The electrochemical reduction of carbon dioxide, formic acid, and formaldehyde. *J. Electrochem. Soc.* **1977**, *124(9)*, 1329-38.

[33] J. L. Grant, K. Goswami, L. O. Spreer, J. W. Otvos, M. J. Calvin: Photochemical reduction of carbon dioxide to carbon monoxide in water using a nickel(II) tetraazamacrocycle complex as catalyst. *Chem. Soc., Dalton Trans.* **1987**, 2105.

[34] C. A. Craig, L. O. Spreer, J. W. Otvos, M. Calvin: Photochemical reduction of carbon dioxide using nickel tetraazamacrocycles. *J. Phys. Chem.* **1990**, *94(20)*, 7957-60.

[35] D. C. Dahlin, W. K. O'Connor, D. N. Nilsen, G. E. Rush, R. P. Walters, P.C. Turner: A method for permanent CO_2 sequestration: supercritical CO_2 mineral carbonation. *An. Int. Pittsburgh Coal Conf.* **2000**, *17*, 1174-1190.

[36] N. Yanagihara, K. Vemulapalli, Q. Fernando: Synthesis of lanthanide carbonates using supercritical carbon dioxide. *Kidorui* **1991**, *18*, 136-137.

[37] N. Yanagihara, K. Vemulapalli, Q. Fernando, D. Quintus, T. James. Synthesis of lanthanide carbonates. *J. Less-Com. Met.* **1991**, *167(2)*, 223-232.

[38] S. Angus, B. Armstrong, K. M de Reuck (Eds.), International Thermodynamic Tables of the Fluid State-3: Carbon Dioxide, IUPAC, Pergamon Press, Oxford, 1976.

[39] J. F. Mathews: The Critical Constants of Inorganic Substances. *Chem. Rev.* **1972**, *72*, 71-100.

[40] A. L. Horvath: Physical properties of hydrogen chloride in SI units. *Process Technol. Int.* **1973**, *18(1-2)*, 67-69.

[40] N. B. Vargaftik, Y. R. Vinogradov, V. S. Yargin: *Handbook of Physical Properties of Liquids and Gases*, New Augmented and Revised Edition of a Bestseller. USA **1996**, 1370 pp.

[41] A. Harlow, G. Wiegand, E. U. Franck: The Density of Ammonia at High Pressures to 723 K and 950 Mpa. *Ber. Bunsenges. Phys. Chem.* **1997**, *101*, 1461-1465.

[42] J. M. H. Levelt Sengers, B. Kamgar-Parsi, F. W. Balfour, J. V. Sengers: Thermodynamic properties of steam in the critical region. *J Phys. Chem. Ref. Data* **1983**, *12(1)*, 1-28.

[43] Joseph H. Keenan ET AL: Steam Tables: Thermodynamic Properties of Water, including Vapor, Liquid and Solid Phases. *WILEY* **1978**.

[44] W. Wagner, K. M. de Reuck (Eds.) *International Thermodynamic Tables of the Fluid State-13 : Methane*, IUPAC, Pergamon Press, Oxford, **1996**.

[45] D. Ambrose, C. Tsonopoulos: Vapor-Liquid Critical Properties of Elements and Compounds. 2. Normal Alkanes. *J. Chem. Eng. Data* **1995**, *40(3)*, 531-546.

[46] O. Maass, D. Mcintosh: Some physical properties of ethane, ethylene and acetylene. *J. Am. Chem. Soc.* **1914**, *36*, 737-742.

[47] K. M de Reuck, R. J. B. Craven (Eds.), International Thermodynamic Tables of the Fluid State-12: Methanol, IUPAC, Pergamon Press, Oxford **1993**.

[48] G. Narsimham: $C_2H_8N_2$ Some physical properties of ethylene amines. *Chem. Process Eng.* **1965**, *46(9)*, 498-500.

[49] T. Moriyoshi, T. Kita, Y. Yosaki: Static Relative Permetivity of Carbon Dioxide and Nitrous Oxide up to 30 MPa. *Ber. Bunsenges. Phys. Chem.* **1993**, *97(4)*, 589-596.

[50] D. A. Skoog, J. J. Leary: Instrumentelle Analytik, *Springer Verlag Berlin*. **1996**, 723.

[51] J. C. Giddings, M. N. Myers, L. McLaren, R. A. Keller: High Pressure Gas Chromatography of Nonvolatile Species. *Science* **1968**, *4*, 67-73.

[52] R. F. Fedors: A Relationship between Chemical Structure and the Critical Temperature. *Chem. Eng. Commun.* **1982**, *16*, 149.

[53] K. M. Klincewicz; R. C. Reid: Estimation of Critical Properties with Group Contribution Methods. *AIChE J.* **1984**, *30(1)*, 137.

[54] J. H. Hildebrand: A History of Solution Theory. *An. Rev. Phys. Chem.* **1981**, *32*, 1-23.

[55] P. G. Jessop, W. Leitner: Chemical Synthesis Using Supercritical Fluids. *(Eds.)*, *Whiley-VCH* **1999**.

[56] A. Rabenau: Die Rolle der Hydrothermalsynthese in der präparativen Chemie. *Angew. Chem.* **1985**, *97*, 1017-1032.

[57] J. Ke, B. Han, M. W. George, H. Yan, M. Poliakoff: How Does the Critical Point Change during a Chemical Reaction in Supercritical Fluids? A Study of the Hydroformulation of Propene in Supercritical CO_2. *J. Am. Chem. Soc*. **2001**, *123*, 3661-3670.

[58] A. Rabenau, H. Rau: Chalcogenide Halides Of Copper, Gold, Mercury, Antimony, and Bismuth. *Inorganic Syntheses* **1973**, *14*, 160-173.

[59] H. Rau, A. Rabenau: Hydrothermalsynthese von CuS UND CuSe in 48%iger HBr. *Mat. Res. Bull.* **1967**, *2*, 609-614.

[60] R. G. Dickinson: The Crystal Structure of Tin Tetra-Iodide. *J. Am. Chem. Soc.* **1923**, *45*, 958-62.

[61] G. Meyer, T. Staffel: Notiz zur kenntnis der roten Monohalogenide des Indiums, InX (X = Cl, Br, I). *Z. Anorg. Allg. Chem.* **1989**, *574*, 114-118.

[62] R. E. Jones, D. H. Templeton: The crystal structure of indium (I) iodide. *Acta Cryst.* **1955**, *8*, 847.

[63] K. Stöwe, H. P. Beck: Low temperature polymorphs of the compound In_3SnI_5. *Z. für Kristallographie* **1994**, *209*, 36-42.

[64] H. P. Beck: Refinement of the structures of $InSn_2Br_5$ and $InSn_2I_5$. *Z. Anorg. Allg. Chem.* **1986**, *536*, 45-52.

[65] K. F. Tebbe, U. Georgy: Die Kristallstrukturen von Rubidiumtriiodid und Thalliumtriiodid (RbI_3). *Acta Cryst.*, **1986**, *C42*, 1675-1678.

[66] J. Runsink, S, S-Walstra, T, Migchelsen: Refinement of the Crystal Structures of $(C_6H_5)_4AsI_3$ and CsI_3 at 20°C and at –160°C (CsI_3). *Acta Cryst.* **1972**, *B 28*, 1331.

[67] M. Wagener, Dissertation: Synthese, Charakterisierung und struktur- chemische Aspekte von Kupfer- und Silberchalkogenohalogeniden sowie von Halogeno- und Oxochalkogenaten(IV). Siegen **2005**.

[68] B. Reuter, K. Hardel: Darstellung, Eigenschaften und Phasenverhältnisse von Ag_3SBr und Ag_3SI. *Z. Anorg. Allg. Chem.* **1965**, *B340*, 158-167.

[69] R. Walther, H. J. Deiseroth: Redetermination of the crystal structure of indium monosulfide, InS. *Z. für Kristallographie* **1995**, *210*, 360.

[70] W. Klemm, H. U. von Vogel: Über die Chalkogenide von Gallium und Indium. *Z. Anorg. Allg. Chem.* **1934**, *219*, 53.

[71] T. Irifune, A. Kurio, S. Sakamoto, T. Inoue, H. Sumiya: Synthesis of pure polycrystalline diamond by direct conversion of graphite at high pressure. *Goldschmidt Conference Abstracts* **2003**, A174.

[72] M. Geshi, T. Oda, Y. Hiwatari: Electronic structures and the space group of orthorhombic selenium under high pressure. *J. Phys.: Condens. Matter* **2002**, *14*, 10885-10890.

[73] I. Yamamoto, Y. Ohmasa, H. Ikeda, H. Endo: The optical properties of tellurium under high pressure. *J. Phys.: Condens. Matter* **1995**, *7*, 4299-4312.

[74] R. H. Williams, J. I. Polanco: The electronic structure of chalcogenide solids: a photoemission study of ordered and disordered selenium and tellurium. *J. Phys. C: Solid State Phys.* **1974**, *7*, 2745-2759.

[75] R. C. Weast *Handbook of Chem. and Phys.* **51**ed. 1970-1971.

[76] J. F. Coetzee, J. J. Campion, D. R. Liberman: Reaction of Silver(I), Mercury(I), and Mercury(II) with Halide Ions in Acetonitrile as Solvent. *Anal. Chem.* **1973**, *45*, 343-347.

[77] W. Bottger: Bestimmung kleiner Mengen Quecksilbersalz in starker Verdünnung. *Chem. Zeit.* **1915**, *39*, 817.

[78] Y. F. Markov, E. M. Roginskii: Low-Temperature Raman Spectra of $Hg_2(Br,I)_2$ Mixed Crystals. *Phys. Solid State* **2003**, *45(6)*, 1131-1136.

[79] L. Vegard, Th. Hauge: Mixed crystals and their formation by contact in the solid phase and by precipitation from solutions. *Z. Physik* **1927**, *42*, 1-14.

[80] H. Mikler, E. Hayer, K. L. Komarek: Mercury-halogen systems, III. System dimercury diiodide-dimercury dichloride [Hg_2I_2-Hg_2Cl_2].*Monatsh. Chem*. **1973**, *104(5)*, 1251-1258.

[81] N. V. Pervukhina, G. V.Romanenko, S. V.Borisov, S. A. Magarill, N. A. Palchik: Crystal chemistry of mercury(I) and mercury(I, II) minerals *J. Struct. Chem.* **1999**, *40(3)*, 461-476.

[82] H. Ehrhardt, H. Schweer, H. Seidel: Hochdrucksynthesen einiger Carbonate mit überkritischem CO_2. *Z. Anorg. Allg. Chem.* **1980**, *462*, 185-198.

[83] A. Doiwa, A. Tomanek: Die Bildung von Cadmiumcarbonat und Cadmiumsulfit aus Cadmiumoxid. *Z. Anorg. Allg. Chem.* **1964**, *334*, 12-14.

[84] H. Bilinski, M. Markovic, M. Gessner: Solubility and Equilibrium Constants of Mercury (II) in Carbonate Solutions (25°C, I = 0.5 mol dm^{-3}). *Inorg. Chem.* **1980**, *19*, 3440-3443.

[85] D. S. Shlyapnikov, E. K. Shtern: Solubility of cadmium and mercury oxides in sodium chloride solutions at elevated carbon dioxide pressures. *Doklady Akademii Nauk SSSR* **1979**, *249(2)*, 457-6.

[86] K. Brodersen, G. Göbel, G. Liehr: Terlinguait $Hg_4O_2Cl_2$ - ein Mineral mit ungewöhnlichen Hg_3-Baueinheiten. *Z. Anorg. Allg. Chem.* **1989**, *575*, 145-153.

[87] K. Aurivillius, L. Folkmarson: The crystal structure of terlinguaite $Hg_4O_2Cl_2$ *Acta Chemica Scandinavic*a **1968**, *22*, 2529-2540.

[88] J. H. C. Hogg, W. J. Duffin: The Crystal Structure of In_6S_7. *Acta Cryst.* **1973**, *A 23*, 111.

[89] H. J. Deiseroth, H. Pfeifer, A. Stupperich: Structural chemistry and valence of In_6S_7. New determination of crystal structure. Z. Kristallogr. **1993**, *207(1)*, 45-52.

[90] J. H. C. Hogg: The Crystal Structure of In_6Se_7. *Acta Cryst.* **1971**, *B27*, 1630.

[91] R. Walther, H. J. Deiseroth: Redetermination of the crystal structure of hexaindium heptaselenide, In_6Se_7. *Z. Kristallogr.* **1995**, *210*, 359.

[92] R. Walther, Disertation: Beiträge zur Strukturchemie gemischtwalenter Chalkogenide mit Elementen der 3. Hauptgruppe. Siegen **1995**.

[93] H. J. Deiseroth, C. Reiner: KIn_5S_6 and MIn_5S_7 (M: Na, K). Three new mixed valent thioindates of alkali metals and their crystal chemical relations.*Z. Anorg. Allg. Chem.* **1998**, *624(11)*, 1839-1845.

[94] R. Walther, H. J. Deiseroth: Crystal structures of thallium pentaindium heptasulfide, $TlIn_5S_7$ and thallium pentaindium heptaselenide, $TlIn_5Se_7$. *Z. Kristallogr*. **1996**, *211*, 51-52.

[95] H. J. Deiseroth, R. Walther: $TlIn_5S_6$: ein neues, gemischtvalentes ternäres Chalkogenid und sein kristallchemisches Umfeld. *Z. Kristallogr.* **1995**, *210*, 88-92.

[96] C. Reiner, H. J. Deiseroth, M. Schlosser, L. Kienle: Die neuen gemischtvalenten Chalkogenoindate MIn_7X_9 (M = Rb, Cs; X = S, Se); Strukturchemie, Röntgen- und HRTEM-Untersuchungen. *Z. Anorg. Allg. Chem.* **2002**, *628*, 1641-1647.

[97] C. Reiner, H. J. Deiseroth: Crystal structure of cesium heptaindium nonasulfide, $CsIn_7S_9$. *Z. Kristallogr.* **1999**, *214*, 13.

[98] S. Paashaus, R. Kniep: Gemischvalente Telluridhalogenide des Aluminiums, Galliums und Indiums: Verbindungen E_3Te_3Hal auf Gehaltschnitten ETe – ETeHal. *Z. Naturforsch.* **1990**, *B45,* 667.

[99] D.H. Templeton, G. F. Carter: The crystal structure of yttrium chloride and similar compounds. *J. Phys. Chem.* **1954**, *58*, 940-944.

[100] R. Walther, H. J. Deiseroth: Redetermination of the crystal strucuture of indium monosulfide, InS. *Z.Kristallogr.* **1995**, *210*, 360.

[101] A. Likforman, D. Carre, J. E. Bachet, B. Bachet: Structure cristalline du monoselenieure d'indium InSe. *Acta Cryst.* **1975**, *B31*, 1252.

[102] R. Kniep, W. Welzel: Phasenbeziehungen und intermediäre Verbingungen in Systemen GaX_3-Ga_2S_3 und InX_3-In_2S_3 (X = Cl, Br, I). *Z. Naturforsch.* **1985**, *40b*, 26-31.

[103] K. Osamura, Y. Murakami, Y. Tomiie: Crystal structures of alpha and beta-Indium Selenide = In_2Se_3. *J. Phys. Soc. Jap.* **1966**, *21*, 1848.

[104] K. C. Nagpal, S. Z. Ali: X-ray crystallographic study of indium monoselenide. *Indian Journal for Pure and Applied Physics.* **1976**, *14*, 434-440.

[105] M. B. Robin, P. Day: Mixed valence chemistry. A survey and classification. *Adv. Inorg. Chem. Radiochem.* **1967**, *10*, 247-422.

[106] R. Hoppe:Über eine neue einfache Methode zur Berechnung von MADELUNG-Faktoren. *Z. Anorg. Allg. Chem.* **1956**, *283*, 196-206.

[107] R. Hoppe: Über Madelungfaktoren. *Angw. Chem.* **1966**, *78*, 52.

[108] R. Hoppe: The Madelung Part of the Lattice Energy, MAPLE, as a Guide in Crystal Chemistry: *Proceedings of an International Symposium, Wageningen, 21-22 February 1974*, The Netherlands, Edited by C.J.M. Rooymans, A. Rabenau. Amsterdam, Oxford, North-Holland Publishing CO. ETC. **1975**, S. 127.

[109] H. Haas, M. Jansen: Kristallstruktur von Natriumoxidsulfat. *Z. Anorg. Allg. Chem.* **2001**, *627*, 1949-1951.

[110] G. A. Steigmann, H. H Sutherland, J. Goodyear: The Crystal Structure of beta-In_2S_3. *Acta Cryst.* **1965**, *19*, 967-971.

[111] C. P. J. M van der Vorst, W. J. A. Maaskant: Indium (I) Chloride – Alpha. *Acta Cryst.* **1978**, *B 34*, 3333-3335.

[112] T. Staffel, G. Meyer: The mono-, sesqui-, and dibromides of indium: InBr, In_2Br_3, and $InBr_2$. *Z. Anorg. Allg. Chem.* **1987**, *552*, 113-122.

[113] K. Cenzual, L. M. Gelato, M. Penzo, E. Parthe: Inorganic structure types with revised space groups I. *Acta Cryst.* **1991**, *B47*, 433-439.

[114] A. Likforman, D. Carre, R. Hillel: Structure cristalline du selenieure d'indium In_2Se_3. *Acta Cryst.* **1978**, *B34*, 1-5.

[115] R. D. Shannon: Revised Effective Ionic Radii and Systematic Studies of Interatomic Distances in Halides and Chalcogenides. *Acta Cryst.* **1976**, *A32*, 751-767.

[116] K. Stierstadt: Physik der Materie. *VCH Verlags GmbH* **1989**.

[117] R. H. Schröder, N. S.-Pranghe, R. Kohlhaas: Experimentelle Bestimmung der Gitterparameter der Platinmetalle im Temperaturbereich von –190 bis 1709°C. *Z. Metallkde.* **1972,** *63*, 12-16.

[118] E. A. Owen, E. L. Yates: Precision measurements of crystal parameters. *Phil. Mag.* **1933**, *15*, 472-488.

[119] H. P. Singh: Determination of thermal expansion of germanium, rhodium, and iridium by x-rays. *Acta cryst.* **1968**, *A24*, 469-471**.**

[120] M. Schlosser, C. Reiner, H.-J. Deiseroth, L. Kienle: $K_2In_{12}Se_{19}$, a Complex New Structure Type Based on Icosahedral Units of Se^{2-}. *Eur. J. Inorg. Chem.* **2001**, 2241-2247.

[121] L. Kienle, A. Simon: Microdomains and Diffuse Scattering in $K_2In_{12}Se_{19}$. *J. Solid State Chem.* **2001**, *161*, 385-395.

[122] M. Schlosser, Dissertation: Zur Micro- und Nanostruktur der neuen ternären Chalkogenide $RbIn_3S_5$, und $K_2In_{12}Se_{19}$. Siegen **2005**.

[123] H. P. Singh, B. Dayal. X-Ray Determination of the Thermal Expansion of Zinc Selenide. *Phys. Stat. Sol.* **1967**, *23*, K93.

[124] H. P. Singh, B. Dayal. Lattice Parameters and Thermal Expansion of Zinc Telluride and Mercury Selenide. Acta Cryst**. 1970,** *A26***,** 363.

Used programs

[P1] P. A. Stadelmann: EMS - a Software Package for Electron Diffraction Analysis and HREM Simuations in Materials Science. *Ultramicroscopy* **1987**, *21*, 131.

[P2] STOE & CIE: EXPOSE – *Diffractometer Control*, Darmstadt, **1999**.

[P3] STOE & CIE: INDEX – *Assignment of Indices*, Darmstadt, **1999**.

[P4] STOE & CIE: CELL – *Orientation Matrix Operations*, Darmstadt, **1999**.

[P5] STOE & CIE: RECIPE – *Examination of Reciprocal Space*, Darmstadt, **1999**.

[P6] STOE & CIE: SPACE – *Sections of Reciprocal Space,* Darmstadt, **1999**.

[P7] STOE & CIE: IPDS – Software, Version 2.93, Darmstadt, **1999**.

[P8] STOE & CIE: FaceIt Video, Version 1 35b p3i, Copyright © **2000**.

[P9] STOE & CIE: X-SHAPE 1.06 – *Crystal Optimisation for Numerical Absorption Correction*, Darmstadt, **1999**.

[P10] STOE & CIE: X-RED 1.19 – *Data Reduction Program*, Darmstadt, **1999**.

[P11] G. M. Sheldrick: SHELXS-97 – *Program for the Solution of Crystal Structures*, University of Göttingen, 1997.

[P12] G. M. Sheldrick: SHELXL-97 - *Program for Structures Refinement*, University of Göttingen **1997**.

[P13] Crystal Impact GbR: DIAMOND, Version 2.1e/3.0a, Bonn, **2001/2004**.

[P14] STOE & CIE: VISUAL X^{POW} – *Powder Diffraction Software*, Version 2.2, Darmstadt, **1994**.

[P15] STOE & CIE: $WinX^{POW}$ – *Powder Diffraction Software*, Version 1.08, Darmstadt, **2000**.

[P16] LINSEIS GmbH: *TAWin*-Datenauswertung für Windows, Version 2.18, Selb, **1993**.

[P17] OPUS 2.2, Bruker, Karlsruhe, **1997**.

[P18] B. Toby, CMPR, NIST Center for Neutron Research, USA, **2000**.

[P19] R. Hoppe, R. Hübenthal: *MAPLE 4 – Program for the Calculation of the MAPLE values*, University of Gießen, **1993**.

8 Appendix

8.1 Abbreviations

EDX = **E**nergy **D**ispersive **X**-ray Spectroscopy

HRTEM = **H**igh **R**esolution **T**ransmission **E**lectron **M**icroscopy

HT = **H**igh **T**emperature

IPDS = **I**mage **P**late **D**iffraction **S**ystem

IR = Infra **R**ed Spectroscopy

MAPLE = **M**adelung **P**art of **L**attice **E**nergy

PDS = Position **S**ensitive **D**etector

RT = **R**oom **T**emperature

SAED = **S**elected **A**rea **E**lectron **D**iffraction

sc = supercritical

SEM = **S**canning **E**lectron **M**icroscope

sof = **s**ite **o**ccupation **f**actor

WDX = **W**avelength **D**ispersive **X**-Ray Spectroscopy

WPOA = Weak Phase Object Approximation

XRD = **X**-**R**ay **D**iffraction

8.2 Definitions

Van der Waals' equation of state for real gases

$$\left(P - a\frac{n^2}{V^2}\right)(V - nb) = nRT$$

a is the mass of the attractive force between the molecules of the gas and *b* is the effective volume of the molecules in one mole of gas (for CO_2 : a = 3.592 atm l^2 mol^{-2} (3.64 bar l^2 mol^2, b = 0.04267 l mol^{-1})

R-Values

$$R_{\text{int}} = \frac{\sum\left||F_o|^2 - |\overline{F_o}|^2\right|}{\sum|F_o|^2}$$

$$R = \frac{\sum\left||F_o| - |F_c|\right|}{\sum|F_o|}$$

$$wR = \sqrt{\frac{\sum\left[w\left(F_o^2 - F_o^2\right)^2\right]}{\sum\left[w\left(F_o^2\right)\right]^2}}$$

$$Goof = \sqrt{\frac{\sum\left[w\left(F_o^2 - F_o^2\right)^2\right]}{n - p}}$$

n = number of reflections, p = number of parameters

Weighting scheme

$$w = 1/\left(\sigma^2\left(F_o^2\right) + (aP)^2 + bP\right) \qquad P = \frac{1}{3}\left(\max(F_0^2, 0) + 2F_c^2\right)$$

Atom displacement factors

U_{eq} = is defined as one third of the ortogonalised U^{ij} tensor

Uij = the anisotropic temperature exponent factor is expressed:

$$-2\pi \cdot \left(h^2 \cdot a^{*2} \cdot U_{11} + ... + 2 \cdot h \cdot k \cdot a^* \cdot b^* \cdot U_{12} + ...\right)$$

Lorentzian fitting function

$$L(2\theta) = \frac{1}{\pi} \frac{\frac{1}{2}\Gamma}{(2\theta - 2\theta_0)^2 + (\frac{1}{2}\Gamma)^2}$$

2θ = diffraction angle; Γ= full width at half maximum

8.3 Data for the reactions of some inorganic compounds in supercritical CO_2

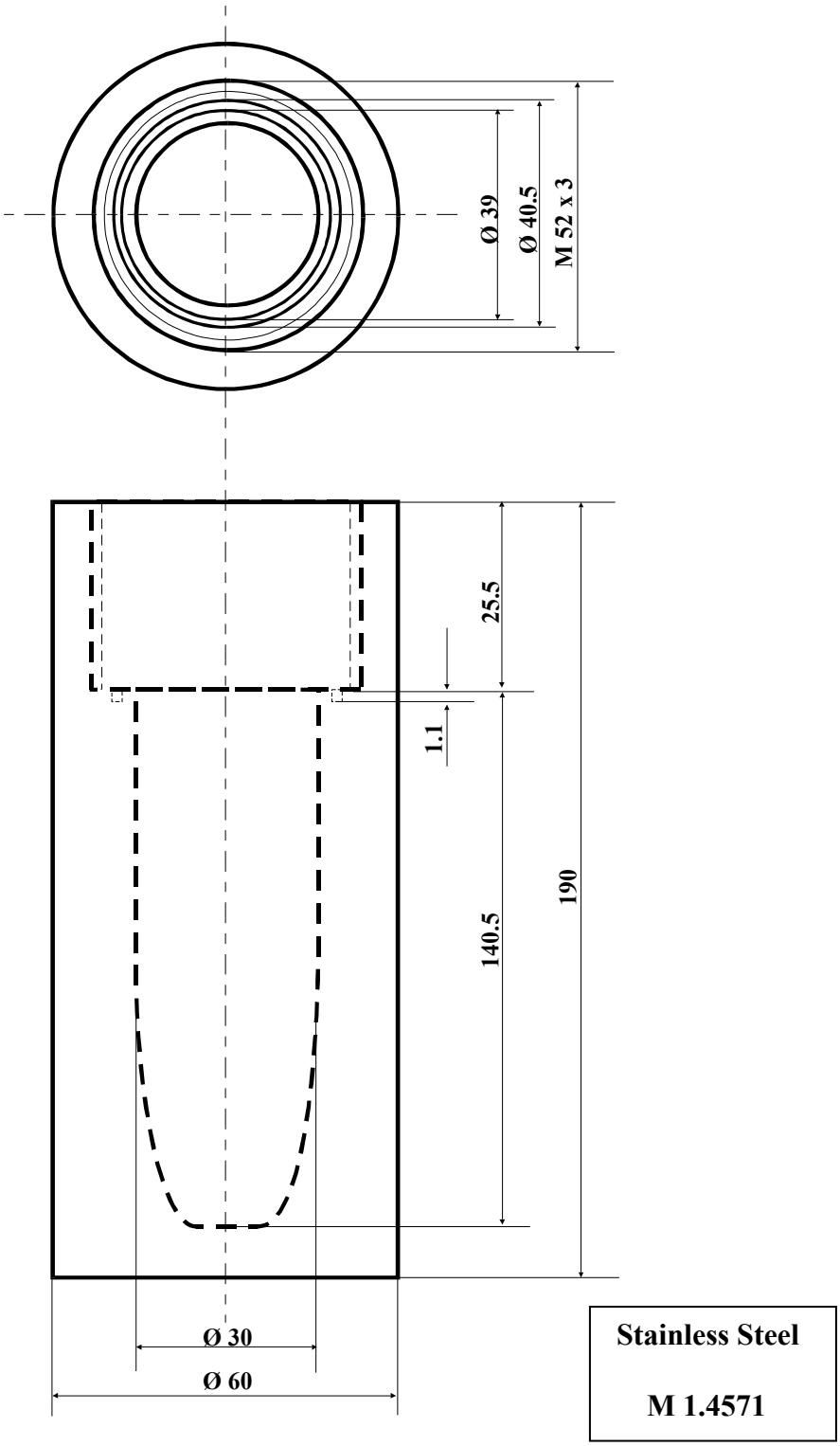

Fig. 8.1: Schematic of the autoclave 1 (body).

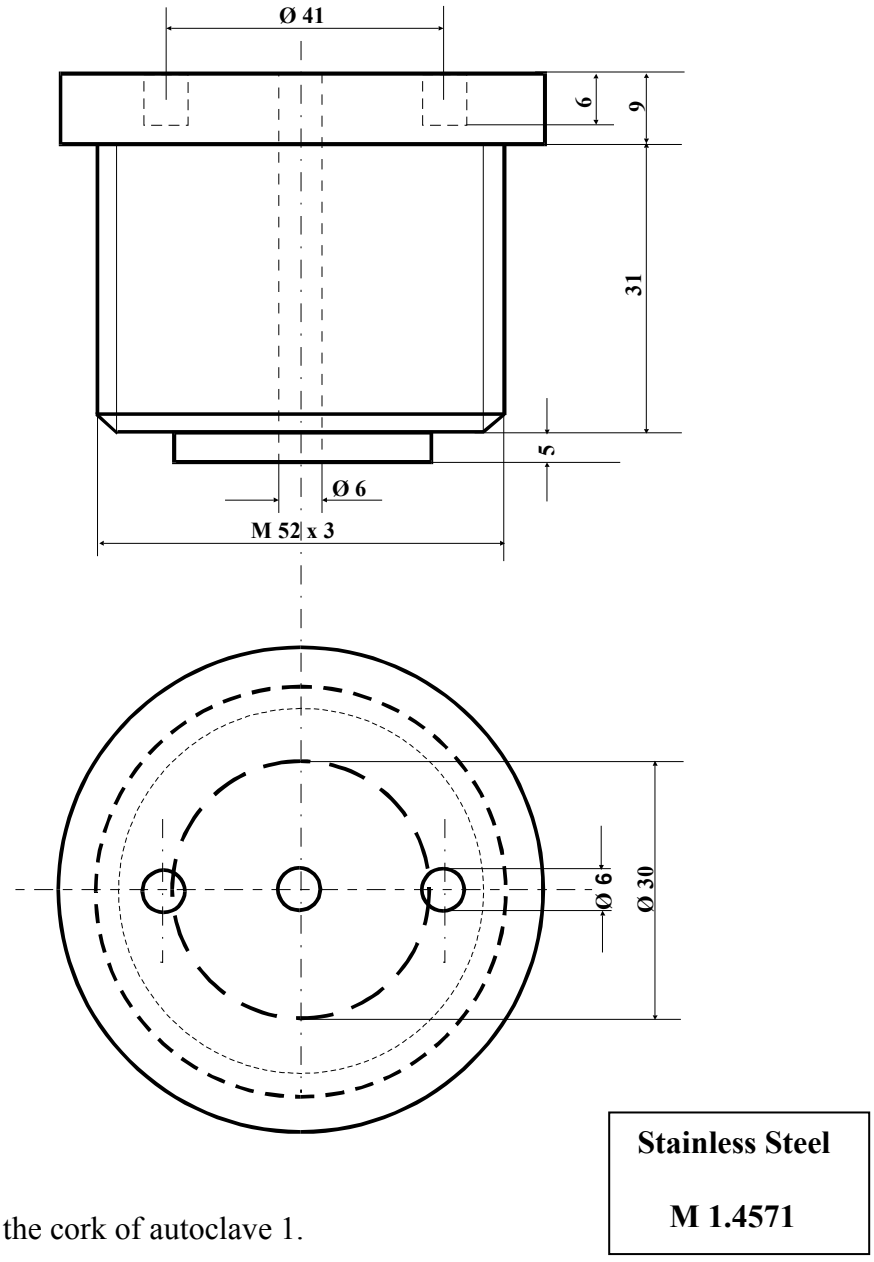

Fig. 8.2: Schematic of the cork of autoclave 1.

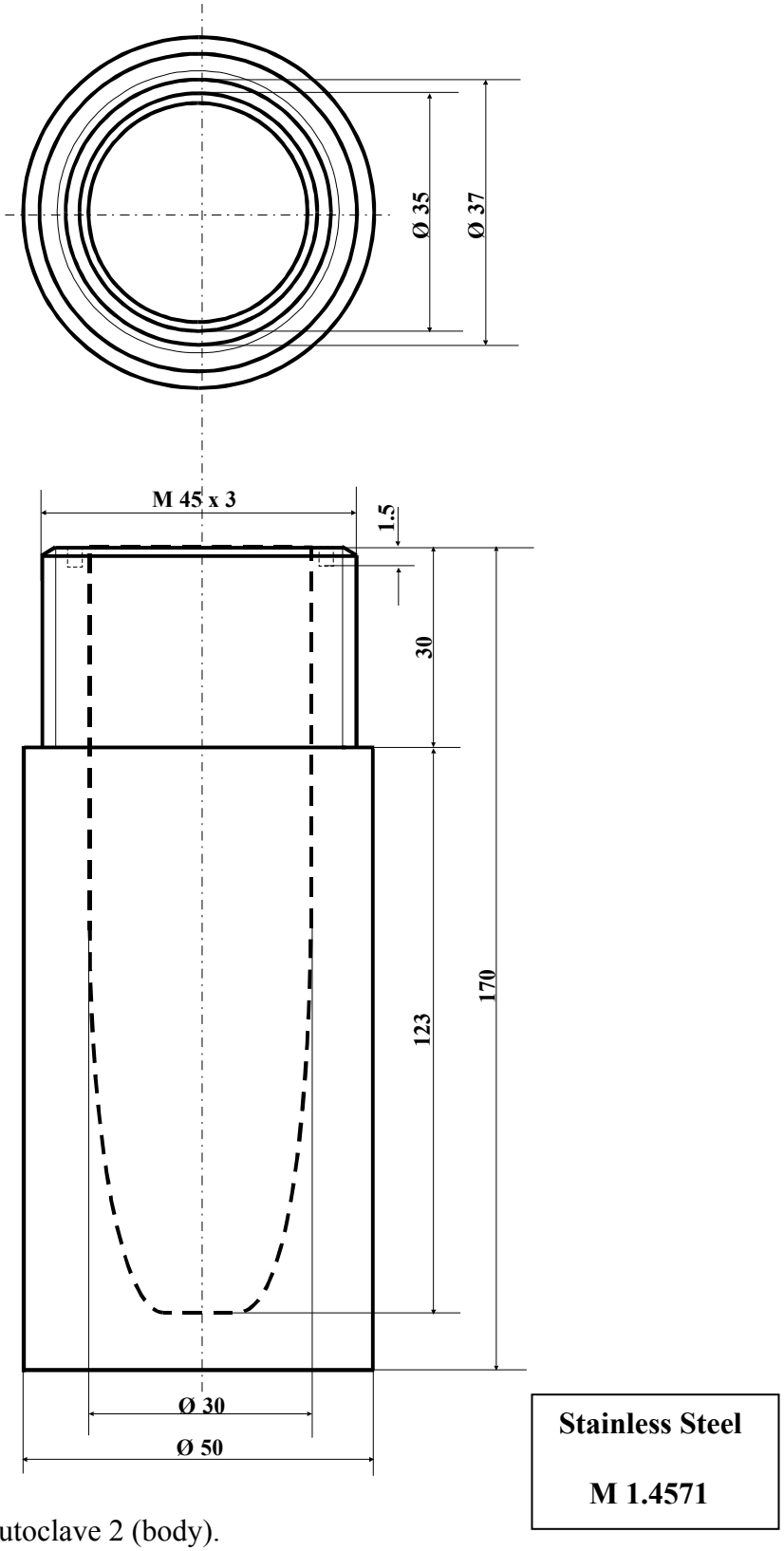

Fig. 8.3: Schematic of the autoclave 2 (body).

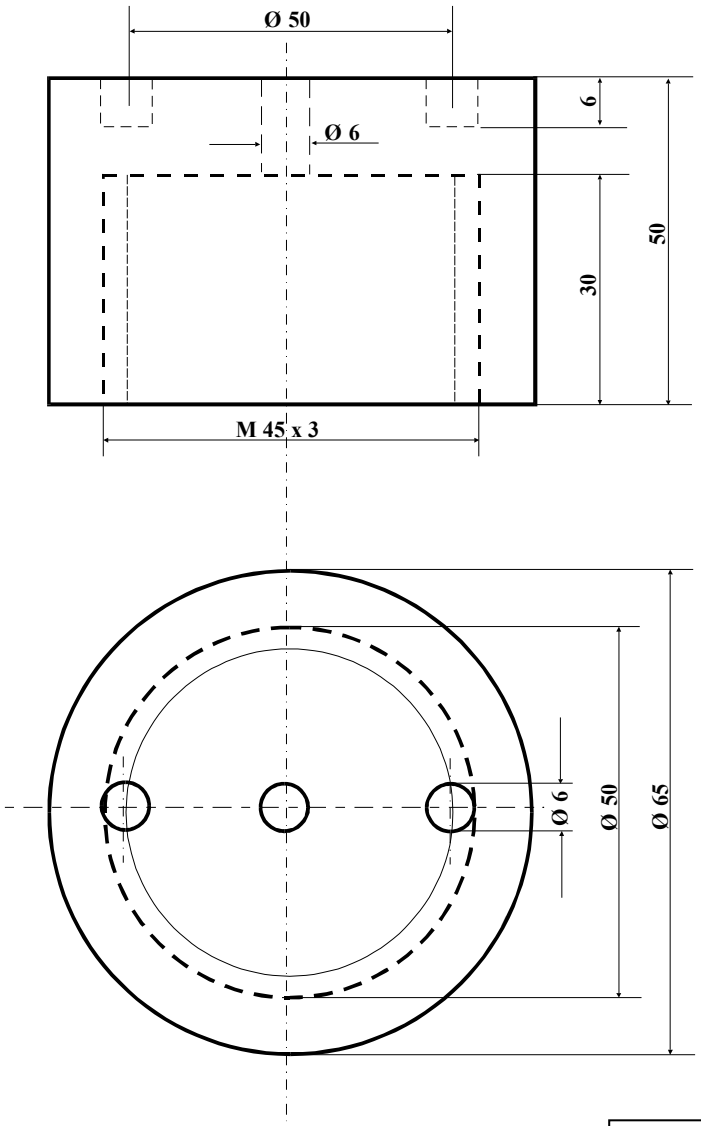

Fig. 8.4: Schematic of the cork of autoclave 2.

Note: The construction of both autoclaves was performed in cooperation with the research group of Prof. Dr. rer. nat. Bernd Wenclawiak by Ms. Sylvia Wilnewski.

The procedure of condensation of CO_2 in the ampoule

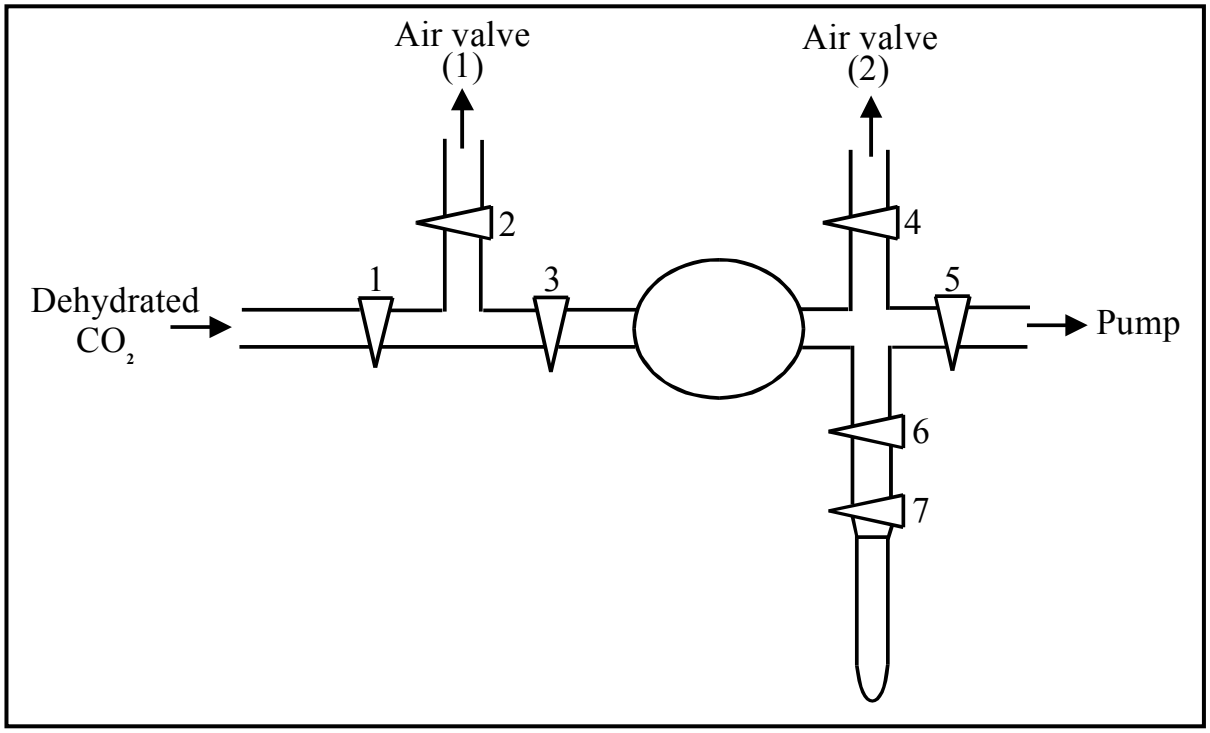

Fig. 8.5: Sketch the system for the production of the defined amounts of dry ice.

Steps of usage (filling procedure)

1. All valves are closed
2. The pump is set on
3. Open the valves 1 and 2
4. Disconnect the CO_2 – tube
5. Open the main CO_2 – bottle valve
6. Gradually open the small CO_2 – bottle valve
7. Check at the end of disconnected tube the flow pressure
8. Reconnect the tube to the system
9. Regulate the CO2 flow (optimal flow c.a. 2 bubbles / sec)
10. Open valves 3, 4
11. Close valve 2 (wait until the pressure regulator connected at valve 4 bubbles)
12. Close valve 3
13. Open valves 6, 7
14. Close valve 4
15. Open valve 5 (evacuation lasts at least 2 min)
16. Heat the ampoule with the gas burner
17. Close valve 5

Second step (purging)

18. Open valve 3 (wait until CO_2 bubbles out through the valve 2)
19. Open valve 4
20. Close valve 2 (wait until CO_2 bubbles out through the valve 4)
21. Purge out for 2 min
22. Open valve 2
23. Close valves 3, 4
24. Open valve 5 (evacuate for at least 2 min)
25. Close valve 5
26. Open valve 3 (wait until CO_2 bubbles out through the valve 2)
27. Open valve 4
28. Close valve 2 (wait until CO_2 bubbles out through the valve 4)
29. Purge out for 2 min
30. Open valve 2
31. Close valves 3, 4
32. Open valve 5 (evacuate for at least 2 min)
33. Close valves 5, 6, 7

System filling and condensing

34. Open valve 3 (wait until CO_2 bubbles out through the valve 2)
35. Open valve 4
36. Close valve 2
37. Open valve 2
38. Close valves 3, 4
39. Approach gradually the thermos with liquid N_2 to the bottom of the ampoule
40. Open valves 6, 7
41. Wait until CO_2 condenses in the lower part of the ampoule
42. Check the quantity of the CO_2 in the ampoule

    not enough proceed further $\leftarrow$ if $\rightarrow$ enough go to step 54

43. Close valves 7, 6
44. Move upwards the N_2 thermos (1 cm)
45. Open valve 3 (wait until CO_2 bubbles through valve 2)
46. Open valve 4
47. Close valve 2 (wait until CO_2 bubbles out through the valve 4)
48. Open valve 2
49. Close valve 3
50. Close valve 4
51. Open valves 6, 7
52. Wait until CO_2 condenses in the lower part of the ampoule

53. Move upwards the N_2 thermos (1 cm)
54. Close valves 7, 6
55. Disconnect the ampoule and the valve 7 from the glass apparatus
56. Open valve 3, 4
57. Close valve 2
58. Switch off the pump and immediately open valve 5
59. Wait until CO_2 bubbles through valve 4 and then close valve 5
60. Turn off the CO_2 bottle valves

Table 8.1: The pressure dependence of the absolute temperature for constant values of the density of CO_2 [38].

	$\rho = 3.50 \times 10^{-3}$ mol cm^{-3}	$\rho = 6.75 \times 10^{-3}$ mol cm^{-3}	$\rho = 7.00 \times 10^{-3}$ mol cm^{-3}	$\rho = 7.25 \times 10^{-3}$ mol cm^{-3}
Temperature / K	**Pressure /bar**	**Pressure /bar**	**Pressure /bar**	**Pressure /bar**
370	84.322	135.66	139.09	142.48
380	88.251	144.81	148.71	152.57
390	92.154	153.91	158.27	162.61
400	96.032	162.96	167.78	172.59
410	99.888	171.97	177.25	182.53
420	103.73	180.93	186.67	192.43
430	107.54	189.86	196.06	202.29
440	111.35	198.76	205.42	212.12
450	115.14	207.62	214.74	221.91
460	118.91	216.45	224.03	231.68
470	122.67	225.26	233.30	241.41
480	126.42	234.03	242.53	251.10
490	130.15	242.78	251.73	260.77
500	133.88	251.50	260.90	270.41
510	137.59	260.19	270.05	280.02
520	141.30	268.86	279.17	289.60
530	144.99	277.50	288.26	299.15
540	148.68	286.12	297.33	308.68
550	152.35	294.71	306.37	318.18

Table 8.2: The dependence of the quantity of CO_2 transferred in both autoclaves from the quantity of CO_2 contained in the ampoule and the temperature (in case of an empty ampoule).

Temp t /°C	**Temp T /K**	**m CO_2 amp /g**	**m CO_2 aut.1 /g**	**m CO_2 aut. 2 /g**
		two fillings		
10	283	2.266	31	35
11	284	2.258	31	35
12	285	2.251	31	35
13	286	2.243	31	35
14	287	2.235	31	34
15	288	2.228	31	34
16	289	2.220	31	34
17	290	2.212	31	34
18	291	2.205	31	34
19	292	2.197	30	34
20	293	2.190	30	34
21	294	2.183	30	34
22	295	2.175	30	34
23	296	2.168	30	33
24	297	2.161	30	33
25	298	2.154	30	33
26	299	2.147	30	33
27	300	2.140	30	33
28	301	2.133	30	33
29	302	2.126	29	33
30	303	2.119	29	33

The entire volumes of the first autoclave and the second systems are 99.7 and 111 ml respectively. An empty ampoule with the inner volume 7.2 ml filled two times with CO_2 (see procedure) represents a molar density of CO_2 6.912 x 10^{-3} mol/ml.

Table 8.3: The dependence of the quantity of CO_2 transferred in both autoclaves from the quantity of CO_2 contained in the ampoule and temperature (in general case of ampoule filled with educts).

Temp t /°C	**Temp T /K**	**m CO_2 amp /g**	**m CO_2 aut.1 /g**	**m CO_2 aut.2 /g**
two fillings				
10	283	2.266	32	35
11	284	2.258	32	35
12	285	2.251	32	35
13	286	2.243	31	35
14	287	2.235	31	35
15	288	2.228	31	35
16	289	2.220	31	35
17	290	2.212	31	35
18	291	2.205	31	34
19	292	2.197	31	34
20	293	2.190	31	34
21	294	2.183	31	34
22	295	2.175	31	34
23	296	2.168	30	34
24	297	2.161	30	34
25	298	2.154	30	34
26	299	2.147	30	34
27	300	2.140	30	33
28	301	2.133	30	33
29	302	2.126	30	33
30	303	2.119	30	33

The volume of the 0.5 g substance filled into the ampoule is approx. 0.1-0.2 ml. A filled ampoule with the inner volume 7 - 7.1 ml filled two times with CO_2 (see procedure) represents a density of CO_2 varying from 7.00×10^{-3}– 7.10×10^{-3} mol/ml.

8.4 Data for the compounds In_5Ch_5Cl, In_5Ch_5Br (Ch = S, Se)

Table 8.4: Refined cell parameters and the parameters of the indexed lines of In_5Se_5Cl.

```
Diffractometer : Siemens D5000           Symmetry   : Monoclinic_B P
Monochromator  : Curved Germanium (111)  Cell_A     : 9.2391(3)
Wavelength     : 1.540598  Cu            Cell_B     : 4.09507(13)
Detector       : Scintillation Counter   Cell_C     : 15.2920(6)
Scan Mode      : Reflection              Cell_Beta  : 92.743(3)
Scan Type      : 2Theta                  Cell_Volume: 577.907(24
Expected halfwidth : 0.050               Cell_A     : 9.2391(3)
Significance level : 2.5
Peak height level  : 300
Peaklist [ Range 1 : 2Theta =   5.000  90.001 0.015  Imax = 27807]
```

D	2Theta	I(rel)	I(abs)	I(int)	FWHM	H	K	L
15.294569	5.7738	13.11	3623	0.00	0.0924	0	0	1
9.232869	9.5715	11.48	3173	0.00	0.0616	1	0	0
8.075778	10.9468	13.05	3606	0.00	0.0924	-1	0	1
5.751944	15.3923	4.11	1135	0.00	0.0924	1	0	2
4.615551	19.2143	5.02	1388	0.00	0.0616	2	0	0
4.552091	19.4848	3.79	1047	0.00	0.0616	-1	0	3
4.477264	19.8137	2.35	650	0.00	0.0308	-2	0	1
4.371012	20.3004	47.48	13123	0.00	0.0616	1	0	3
4.036337	22.0037	27.20	7517	0.00	0.0616	-2	0	2
3.955566	22.4588	31.54	8717	0.00	0.0616	0	1	1
3.818378	23.2768	2.32	641	0.00	0.0462	0	0	4
3.652063	24.3527	51.68	14284	0.00	0.0616	-1	1	1
3.619327	24.5764	27.25	7533	0.00	0.0616	1	1	1
3.590647	24.7758	8.64	2388	0.00	0.0462	-1	0	4
3.503697	25.4008	16.62	4594	0.00	0.0616	-2	0	3
3.471000	25.6442	7.14	1972	0.00	0.0616	1	0	4
3.336732	26.6947	39.23	10843	0.00	0.0924	1	1	2
3.062088	29.1397	33.64	9299	0.00	0.0616	2	1	0
3.044325	29.3135	56.23	15542	0.00	0.0616	-1	1	3
3.013653	29.6186	44.74	12365	0.00	0.0616	-2	0	4
2.986518	29.8940	91.63	25328	0.00	0.0924	3	0	1
2.942938	30.3472	9.85	2722	0.00	0.0924	-1	0	5
2.874789	31.0846	84.29	23298	0.00	0.0616	2	0	4
2.860095	31.2484	31.75	8777	0.00	0.0462	1	0	5
2.812365	31.7926	81.90	22638	0.00	0.0616	2	1	2
2.793537	32.0126	7.54	2083	0.00	0.0308	0	1	4
2.699472	33.1598	8.35	2307	0.00	0.0924	-1	1	4
2.662205	33.6376	39.77	10992	0.00	0.0616	-2	1	3
2.647957	33.8241	10.78	2979	0.00	0.0616	1	1	4
2.605428	34.3932	13.59	3755	0.00	0.0616	-2	0	5
2.588218	34.6291	5.10	1410	0.00	0.0154	2	1	3
2.579409	34.7511	4.59	1268	0.00	0.0462	3	0	3

2.484739	36.1199	6.30	1743	0.00	0.0616	-1	0	6
2.459530	36.5031	55.48	15335	0.00	0.0616	3	1	0
2.448640	36.6712	62.71	17333	0.00	0.0616	0	1	5
2.425027	37.0412	6.07	1677	0.00	0.0616	1	0	6
2.414312	37.2116	3.22	889	0.00	0.0308	3	1	1
2.353083	38.2169	5.64	1558	0.00	0.0308	2	1	4
2.343654	38.3767	5.11	1412	0.00	0.0924	1	1	5
2.315582	38.8605	20.88	5772	0.00	0.0616	3	1	2
2.297719	39.1749	5.49	1517	0.00	0.0616	-4	0	1
2.275873	39.5665	3.89	1076	0.00	0.0924	-2	0	6
2.248484	40.0690	5.18	1431	0.00	0.0924	-3	1	3
2.221372	40.5794	15.49	4283	0.00	0.0924	-3	0	5
2.198051	41.0292	3.67	1015	0.00	0.0616	-2	1	5
2.180083	41.3828	23.79	6575	0.00	0.0924	4	0	2
2.146397	42.0629	5.16	1427	0.00	0.0616	-1	0	7
2.103946	42.9532	18.24	5043	0.00	0.0924	-3	1	4
2.086413	43.3323	6.32	1747	0.00	0.0616	1	1	6
2.064739	43.8106	20.92	5781	0.00	0.0616	4	0	3
2.047485	44.1991	100.00	27640	0.00	0.0616	0	2	0
2.032733	44.5370	27.51	7604	0.00	0.0616	3	1	4
2.009791	45.0732	8.31	2298	0.00	0.0308	4	1	0
1.982679	45.7242	2.93	810	0.00	0.0616	4	1	1
1.964121	46.1811	29.90	8266	0.00	0.0616	-4	1	2
1.952673	46.4676	25.14	6950	0.00	0.0616	-3	1	5
1.937352	46.8570	7.18	1986	0.00	0.0616	2	0	7
1.926092	47.1474	13.37	3697	0.00	0.0924	0	1	7
1.900887	47.8112	17.19	4751	0.00	0.0616	-1	1	7
1.897243	47.9088	22.61	6249	0.00	0.0616	-4	1	3
1.880851	48.3529	5.21	1439	0.00	0.0616	3	1	5
1.869485	48.6659	26.84	7420	0.00	0.0924	1	1	7
1.854145	49.0949	10.10	2791	0.00	0.0616	1	2	3
1.825894	49.9060	5.98	1654	0.00	0.0616	-2	2	2
1.814018	50.2554	7.31	2021	0.00	0.0616	-5	0	2
1.804310	50.5447	7.49	2071	0.00	0.0924	-2	1	7
1.794793	50.8318	3.65	1010	0.00	0.0924	-2	0	8
1.778459	51.3324	1.81	500	0.00	0.0616	-1	2	4
1.767564	51.6720	4.48	1239	0.00	0.0616	-2	2	3
1.749158	52.2566	9.60	2654	0.00	0.0924	4	1	4
1.713216	53.4388	4.42	1222	0.00	0.0924	-4	1	5
1.700011	53.8873	4.84	1338	0.00	0.0924	0	2	5
1.693535	54.1102	18.30	5058	0.00	0.0616	-2	2	4
1.688002	54.3021	15.91	4399	0.00	0.0616	1	1	8
1.680752	54.5557	6.50	1796	0.00	0.0616	-1	2	5
1.667542	55.0243	11.82	3268	0.00	0.0674	2	2	4
1.664919	55.1184	16.23	4487	0.00	0.0924	1	2	5
1.658602	55.3462	6.94	1918	0.00	0.0616	-5	1	2
1.648046	55.7315	3.85	1064	0.00	0.0616	4	1	5
1.630979	56.3664	1.81	500	0.00	0.0924	5	0	4
1.618513	56.8398	1.95	538	0.00	0.0616	-5	1	3
1.609840	57.1742	7.06	1951	0.00	0.0616	-2	2	5
1.603248	57.4311	2.30	636	0.00	0.0924	3	2	3

1.580049	58.3549	3.11	859	0.00	0.0616	-1	2	6
1.564918	58.9745	4.87	1345	0.00	0.0616	-5	1	4
1.547286	59.7142	4.75	1312	0.00	0.0616	5	0	5
1.537727	60.1236	6.27	1734	0.00	0.0616	-6	0	1
1.528535	60.5228	2.83	782	0.00	0.0924	-4	2	1
1.522112	60.8051	4.54	1254	0.00	0.0616	-2	2	6
1.516797	61.0409	3.27	903	0.00	0.0924	-3	0	9
1.505532	61.5470	9.66	2669	0.00	0.0924	-3	2	5
1.492463	62.1455	17.43	4819	0.00	0.0924	4	2	2
1.481560	62.6543	3.41	941	0.00	0.0924	-1	2	7
1.466330	63.3802	4.96	1370	0.00	0.0616	1	2	7
1.461366	63.6206	3.46	956	0.00	0.0308	5	0	6
1.456413	63.8625	7.70	2129	0.00	0.0616	3	0	9
1.453962	63.9829	12.25	3385	0.00	0.0616	4	2	3
1.439638	64.6965	3.44	951	0.00	0.0924	-6	1	1
1.433989	64.9827	2.69	743	0.00	0.0308	-3	2	6
1.427674	65.3058	1.50	414	0.00	0.0616	6	1	1
1.407190	66.3780	4.64	1283	0.00	0.0616	2	2	7
1.367692	68.5563	2.32	641	0.00	0.0616	-6	1	4
1.358144	69.1063	4.64	1284	0.00	0.0924	-5	2	2
1.349585	69.6075	3.53	977	0.00	0.0924	-2	2	8
1.345817	69.8307	3.00	829	0.00	0.0674	-1	3	1
1.327857	70.9161	6.65	1838	0.00	0.0924	6	1	4
1.308357	72.1371	4.24	1172	0.00	0.0924	7	0	1
1.302738	72.4975	5.09	1406	0.00	0.0616	2	3	1
1.293057	73.1278	3.82	1057	0.00	0.0924	-2	3	2
1.287208	73.5146	6.48	1792	0.00	0.0924	2	3	2
1.277942	74.1364	2.01	556	0.00	0.0674	-6	1	6
1.276013	74.2673	2.23	616	0.00	0.0674	5	2	4
1.271884	74.5493	3.09	855	0.00	0.0616	-2	3	3
1.264828	75.0366	1.34	369	0.00	0.0674	-7	0	4
1.246646	76.3255	7.05	1948	0.00	0.0924	4	0	10
1.234443	77.2185	3.28	907	0.00	0.0924	5	2	5
1.229526	77.5848	5.83	1612	0.00	0.0616	-3	1	11
1.227934	77.7043	4.79	1325	0.00	0.0674	7	0	4
1.221735	78.1734	6.24	1725	0.00	0.0924	-5	1	9
1.219093	78.3753	3.45	954	0.00	0.0674	-3	2	9
1.212382	78.8933	7.55	2087	0.00	0.0924	-1	1	12
1.206225	79.3755	4.69	1297	0.00	0.0924	3	3	3
1.192574	80.4683	3.66	1010	0.00	0.0924	4	1	10
1.189461	80.7223	4.79	1323	0.00	0.0616	1	3	6
1.187066	80.9189	6.28	1737	0.00	0.0924	3	2	9
1.179271	81.5666	3.73	1031	0.00	0.0924	3	3	4
1.175080	81.9196	2.83	782	0.00	0.0924	0	0	13
1.169695	82.3783	4.96	1370	0.00	0.0924	5	1	9
1.165320	82.7553	3.79	1046	0.00	0.0616	4	0	11
1.162970	82.9595	3.56	984	0.00	0.0616	-3	3	5
1.156869	83.4948	4.23	1169	0.00	0.0924	4	3	2
1.151668	83.9575	4.94	1365	0.00	0.0924	-1	3	7
1.144702	84.5865	4.70	1299	0.00	0.0924	1	3	7
1.132628	85.7027	2.32	642	0.00	0.0616	8	0	2

1.129146	86.0310	1.91	527	0.00	0.0616	-3	3	6
1.125682	86.3605	3.07	849	0.00	0.0616	-2	2	11
1.115234	87.3721	1.80	499	0.00	0.0924	4	3	4
1.110215	87.8679	6.57	1817	0.00	0.0924	8	1	0
1.105682	88.3214	2.68	742	0.00	0.0924	-4	3	5
1.103529	88.5387	2.21	611	0.00	0.0924	-7	2	2
1.098810	89.0195	2.25	622	0.00	0.0924	1	3	8
1.090800	89.8496	1.24	343	0.00	0.0924	-3	2	11

Table 8.5: Anisotropic displacement parameters (U_{ij} /Å ^{2}) for In_5S_5Cl.

Atom	U_{11}	U_{22}	U_{33}	U_{23}	U_{13}	U_{12}
In1	0.010(1)	0.006(1)	0.013(1)	0	0.001(1)	0
In2	0.016(1)	0.008(1)	0.016(1)	0	-0.005(1)	0
In3	0.012(1)	0.012(1)	0.026(2)	0	0.010(1)	0
In4	0.008(1)	0.009(1)	0.016(1)	0	0.002(1)	0
In5	0.032(2)	0.028(2)	0.032(3)	0	0.006(2)	0
Cl	0.013(4)	0.014(4)	0.015(5)	0	0.005(4)	0
S1	0.005(4)	0.006(4)	0.013(4)	0	0.002(3)	0
S2	0.008(4)	0.004(4)	0.015(4)	0	0.000(4)	0
S3	0.009(4)	0.005(3)	0.009(4)	0	-0.004(3)	0
S4	0.013(4)	0.010(4)	0.006(4)	0	0.000(3)	0
S5	0.019(5)	0.007(4)	0.007(4)	0	0.002(4)	0

Table 8.6: Anisotropic displacement parameters (U_{ij} /Å ^{2}) for In_5Se_5Cl.

Atom	U_{11}	U_{22}	U_{33}	U_{23}	U_{13}	U_{12}
In1	0.0120(7)	0.0104(9)	0.0202(8)	0	0.0065(5)	0
In2	0.0276(9)	0.012(1)	0.0219(9)	0	-0.0118(7)	0
In3	0.0119(7)	0.011(1)	0.0297(9)	0	0.0107(6)	0
In4	0.0082(7)	0.0127(9)	0.0159(7)	0	0.0019(5)	0
In5	0.031(1)	0.035(2)	0.045(2)	0	0.010(1)	0
Cl	0.0061(8)	0.008(1)	0.0180(1)	0	0.0002(7)	0
Se1	0.0094(9)	0.010(2)	0.019(1)	0	0.0026(7)	0
Se2	0.0093(9)	0.008(1)	0.016(1)	0	0.0003(7)	0
Se3	0.013(1)	0.013(1)	0.020(1)	0	0.0018(8)	0
Se4	0.013(1)	0.010(1)	0.017(1)	0	0.0030(7)	0
Se5	0.015(2)	0.029(4)	0.025(3)	0	-0.003(2)	0

Table 8.7: Anisotropic displacement parameters (U_{ij} /Å ^{2}) for In_5S_5Br.

Atom	U_{11}	U_{22}	U_{33}	U_{23}	U_{13}	U_{12}
In1	0.0082(3)	0.0109(2)	0.0140(2)	0.0035(2)	0	0
In2	0.0081(3)	0.0142(2)	0.0119(2)	0.0038(2)	0	0
In3	0.0099(3)	0.0101(2)	0.0245(3)	0.0045(2)	0	0
In4	0.0098(2)	0.0088(2)	0.0126(2)	0.0003(2)	0	0
In5	0.0299(5)	0.0292(4)	0.0249(4)	0.0002(3)	0	0
Br	0.0106(4)	0.0119(3)	0.0156(3)	-0.0016(3)	0	0
S1	0.0082(9)	0.0070(7)	0.0088(8)	-0.0026(6)	0	0
S2	0.0073(8)	0.0105(7)	0.0099(7)	0.0009(6)	0	0
S3	0.0076(9)	0.0096(8)	0.0091(7)	0.0007(6)	0	0
S4	0.0063(8)	0.0088(7)	0.0115(7)	0.0006(6)	0	0
S5	0.0080(8)	0.0125(7)	0.0109(7)	0.0010(7)	0	0

Table 8.8: Anisotropic displacement parameters (U_{ij} /Å ^{2}) for In_5Se_5Br.

Atom	**U_{11}**	**U_{22}**	**U_{33}**	**U_{23}**	**U_{13}**	**U_{12}**
In1	0.0130(5)	0.0164(5)	0.0179(4)	0.0041(3)	0	0
In2	0.0135(5)	0.0203(5)	0.0174(4)	0.0065(4)	0	0
In3	0.0143(5)	0.0146(5)	0.0294(5)	0.0065(4)	0	0
In4	0.0154(4)	0.0124(4)	0.0178(4)	0.0008(4)	0	0
In5	0.0285(7)	0.0369(8)	0.0318(7)	0.0052(6)	0	0
Br	0.0168(7)	0.0144(7)	0.0212(6)	-0.0024(5)	0	0
Se1	0.0095(6)	0.0113(6)	0.0131(5)	-0.0019(5)	0	0
Se2	0.0098(6)	0.0109(6)	0.0140(5)	0.0014(5)	0	0
Se3	0.0112(7)	0.0135(7)	0.0127(6)	-0.0006(5)	0	0
Se4	0.0122(7)	0.0132(7)	0.0154(5)	-0.0004(5)	0	0
Se5	0.0116(6)	0.0152(6)	0.0147(5)	0.0022(5)	0	0

Interatomic angles for the mixed valence compounds In_5S_5Cl, In_5Se_5Cl, In_5S_5Br and In_5Se_5Br

Table 8.9: The selected interatomic angles for In_5Ch_5Cl.

Angle		In_5S_5Cl	In_5Se_5Cl	Angle		In_5S_5Cl	In_5Se_5Cl
Ch5 In1 Ch2	(2x)	88.6(3)	90.18(7)	Ch1 In4 Ch3	(2x)	95.3(3)	93.84(7)
Ch2 In1 Ch2		96.4 (3)	96.31(9)	Ch3 In4 Ch3		101.8(4)	100.46(9)
Ch5 In1 Ch1		177.2(3)	179.13(9)	Ch1 In4 In3		119.7(3)	124.23(9)
Ch2 In1 Ch1	(2x)	89.6(3)	84.59(5)	Ch3 In4 In3	(2x)	119.7(2)	119.23(6)
Ch5 In1 Ch1	(2x)	95.9(3)	93.91(7)				
Ch2 In1 Ch1	(2x)	175.6(3)	175.81(9)	Cl In5 Cl		75.6(3)	81.3(2)
Ch2 In1 Ch1	(2x)	84.2(2)	84.59(5)	Cl In5 Ch5	(2x)	141.5(3)	141.36(6)
Ch1 In1 Ch1	(2x)	86.0(3)	86.68(7)	Cl In5 Ch5	(2x)	92.1(2)	88.2(1)
Ch1 In1 Ch1		94.8(3)	94.23(8)	Ch5 In5 Ch5		75.1(2)	73.64(8)
				Cl In5 Ch4	(2x)	67.1(2)	68.6(1)
Ch3 In2 Ch4	(2x)	100.1(3)	101.63(8)	Ch5 In5 Ch4	(2x)	74.5(2)	70.22(7)
Ch4 In2 Ch4		100.3(4)	99.4(1)	Cl In5 Cl	(2x)	68.3(3)	72.3(2)
Ch3 In2 Ch4		160.3(4)	156.4(1)	Ch5 In5 Cl	(2x)	140.6(2)	141.36(6)
Ch4 In2 Ch4	(2x)	92.4(3)	93.50(8)	Ch4 In5 Cl		122.7(3)	127.7(2)
Ch3 In2 Cl	(2x)	82.5(3)	81.1(1)	Cl In5 Ch3	(2x)	87.3(2)	87.5(1)
Ch4 In2 Cl	(2x)	173.4(3)	173.7(1)	Cl In5 Ch3	(2x)	131.1(3)	136.7(2)
Ch4 In2 Cl	(2x)	85.0(2)	85.5(1)	Ch5 In5 Ch3	(2x)	125.7(3)	124.9(1)
Ch4 In2 Cl	(2x)	83.5(3)	82.2(1)	Ch5 In5 Ch3	(2x)	83.3(2)	82.08(6)
Cl In2 Cl		89.4(3)	89.4(2)	Ch4 In5 Ch3	(2x)	144.9(1)	143.32(4)
				Cl In5 Ch3	(2x)	62.8(2)	64.5(1)
Ch2 In3 Ch5	(2x)	91.1(3)	93.14(7)	Ch3 In5 Ch3		70.2(2)	72.71(7)
Ch5 In3 Ch5		98.9(4)	99.8(1)	Cl In5 Ch1	(2x)	141.4(1)	139.26(9)
Ch2 In3 In4		140.5(3)	134.7(2)	Ch5 In5 Ch1	(2x)	64.9(2)	63.80(7)
Ch5 In3 In4	(2x)	113.5(2)	114.66(6)	Ch4 In5 Ch1		127.9(3)	121.5(1)
				Cl In5 Ch1		109.4(3)	110.8(1)
				Ch3 In5 Ch1	(2x)	60.8(2)	61.14(6)

Table 8.10: The selected interatomic angles for In_5Ch_5Br.

Angle	In_5S_5Br	In_5Se_5Br	Angle	In_5S_5Br	In_5Se_5Br
Ch5 In1 Ch4 (2x)	87.52(5)	88.80(4)	Ch2 In4 Ch2	101.59(7)	100.61(5)
Ch4 In1 Ch4	96.47(6)	95.80(6)	Ch2 In4 Ch1 (2x)	94.98(5)	93.23(4)
Ch5 In1 Ch3	173.76(6)	175.22(6)	Ch2 In4 In3 (2x)	116.05(4)	118.08(4)
Ch4 In1 Ch3 (2x)	88.32(5)	88.00(4)	Ch1 In4 In3	128.09(5)	127.48(5)
Ch5 In1 Ch1 (2x)	96.52(5)	94.79(4)			
Ch4 In1 Ch1 (2x)	175.94(6)	176.38(6)	Ch4 In5 Ch4	77.46(5)	79.86(5)
Ch4 In1 Ch1 (2x)	84.05(4)	84.77(3)	Ch4 In5 Ch5 (2x)	137.85(5)	137.12(6)
Ch3 In1 Ch1 (2x)	87.67(5)	88.45(4)	Ch4 In5 Ch5 (2x)	88.99(4)	87.20(3)
Ch1 In1 Ch1	95.15(6)	94.43(5)	Ch5 In5 Ch5	74.69(5)	75.00(4)
			Ch4 In5 Br (2x)	69.42(4)	68.92(4)
Ch3 In2 Ch3	101.47(7)	99.92(6)	Ch5 In5 Br (2x)	141.76(2)	142.06(2)
Ch3 In2 Ch2 (2x)	100.52(5)	99.76(4)	Ch4 In5 Ch2 (2x)	89.08(4)	86.38(4)
Ch3 In2 Ch1 (2x)	91.02(5)	92.02(4)	Ch4 In5 Ch2 (2x)	135.14(5)	135.02(6)
Ch2 In2 Ch1	161.61(6)	161.58(6)	Ch5 In5 Ch2 (2x)	125.92(5)	128.66(5)
Ch3 In2 Br (2x)	170.36(4)	172.67(5)	Ch5 In5 Ch2 (2x)	83.34(4)	83.91(3)
Ch3 In2 Br (2x)	86.13(4)	86.03(3)	Br In5 Ch2 (2x)	65.79(4)	66.16(4)
Ch2 In2 Br (2x)	83.70(4)	83.32(4)	Ch2 In5 Ch2	70.80(4)	73.76(4)
Ch1 In2 Br (2x)	82.85(4)	83.43(4)	Ch4 In5 Ch3 (2x)	67.85(4)	69.12(4)
Br In2 Br	85.72(3)	87.74(5)	Ch5 In5 Ch3 (2x)	70.06(4)	68.06(4)
			Br In5 Ch3	124.31(4)	124.33(5)
Ch4 In3 Ch5 (2x)	90.98(5)	92.22(4)	Ch2 In5 Ch3 (2x)	144.39(2)	142.93(2)
Ch5 In3 Ch5	101.05(7)	100.10(6)	Ch4 In5 Ch1 (2x)	141.11(2)	139.94(2)
Ch4 In3 In4	131.12(5)	131.81(6)	Ch5 In5 Ch1 (2x)	65.18(4)	66.16(4)
Ch5 In3 In4 (2x)	117.87(4)	116.86(4)	Br In5 Ch1	112.97(4)	114.39(5)
			Ch2 In5 Ch1 (2x)	60.75(4)	62.50(3)
			Ch3 In5 Ch1	122.72(5)	121.28(5)

MAPLE calculations for the compounds In_5Se_5Cl, In_5S_5Br and In_5Se_5Br

Table 8.11: MAPLE values in kcal mol^{-1} of In_5Se_5Cl compared with InSe [113], In_2Se_3 [114] and InCl [111].

Atom	n	binary	ternary	n x Δ
In1	1	807.2781[a)]	832.0049	24.7268
In2	1	808.0565[b)]	789.7873	-18.2692
In3	1	352.7925[d)]	312.8991	-39.8934
In4	1	352.7925[d)]	320.1959	-32.5966
In5	1	86.7901[e)]	149.7686	62.9785
Se1	1	408.6874[c)]	420.3231	11.6357
Se2	1	408.6874[c)]	363.3731	-45.3143
Se3	1	408.6874[c)]	452.0036	43.3162
Se4	1	359.2128[d)]	379.948	20.7352
Se5	1	359.2128[d)]	444.6537	85.4409
Cl	1	86.3743[e)]	76.2919	-10.0824
		∑ = 4438.5718	∑ = 4541.2492	∑ = 102.6774
				→ **2.26%**

[a)] from In_2Se_3 (CN 6), [b)] from In_2Se_3 (CN 4), [c)] from In_2Se_3 (mean value), [d)] from InSe, [e)] from InCl.

Table 8.12: MAPLE values in kcal mol^{-1} of In_5S_5Br compared with InS [100] β-In_2S_3 [110], and InBr [112].

Atom	n	binary	ternary	n x Δ
In1	1	885.9332[a)]	913.3084	27.3752
In2	1	877.4353[b)]	800.9016	-76.5337
In3	1	385.0382[d)]	338.3128	-46.7254
In4	1	385.0382[d)]	318.4453	-66.5929
In5	1	93.0800[e)]	158.5410	65.4610
S1	1	446.6314[c)]	461.9750	15.3436
S2	1	446.6314[c)]	415.9594	-30.6720
S3	1	446.6314[c)]	448.0881	1.4567
S4	1	384.9244[d)]	374.4680	-10.4564
S5	1	384.9244[d)]	369.6098	-15.3146
Br	1	94.9990[e)]	117.9049	22.9059
		∑ = 4831.2669	∑ = 4717.5143	∑ = -113.7526
				→ **2.41%**

[a)] from In_2S_3 [(CN 6) + (CN 4)], [b)] from In_2S_3 (CN 6), [c)] from In_2S_3 (mean value), [d)] from InS, [e)] from InBr.

Table 8.13: MAPLE values in kcal mol^{-1} of In_5Se_5Br compared with InSe [113], In_2Se_3 [114] and InBr [112].

Atom	n	binary	ternary	n x Δ
In1	1	807.2781[a)]	866.1210	58.8429
In2	1	808.0565[b)]	761.9919	-46.0646
In3	1	352.7925[d)]	316.3532	-36.4393
In4	1	352.7925[d)]	297.6192	-55.1733
In5	1	93.0800[e)]	158.9142	65.8342
Se1	1	408.6874[c)]	443.1517	34.4643
Se2	1	408.6874[c)]	393.1807	-15.5067
Se3	1	408.6874[c)]	424.1894	15.502
Se4	1	359.2128[d)]	358.5328	-0.68
Se5	1	359.2128[d)]	347.5843	-11.6285
Br	1	94.9997[e)]	118.2350	23.2353
		∑ =4453.4871	∑ =4485.8734	∑ = 32.3863
				→ **0.72%**

[a)] from In_2Se_3 (CN 6), [b)] from In_2Se_3 (CN 4), [c)] from In_2Se_3 (mean value), [d)] from InSe, [e)] from InBr

8.5 Data for the substitution experiments

Table 8.14: Educts, expected products, conditions and the achieved products.

No.	Educts	expected products	Conditions	Products
	Experiments for the substitution of In^+			
1	NaCl, In, S	$NaIn_4S_5Cl$	500°C, 6d Q, 500°C (A), 2w	NaCl, In_6S_7
2	KCl, In, S	KIn_4S_5Cl	500°C, 6d Q, 500°C (A), 2w	KCl, In_6S_7
3	K, In, S,$InBr_3$	KIn_4S_5Br	500°C, 1w Tp(2°C/h) 500°C, 5d	KBr, In_2S_3
4	RbCl, In, S $RbIn_3S_5$, InCl	$RbIn_4S_5Cl$	500°C, 6d Q, 500°C (A), 2w 450°C, 9d	RbCl, In_6S_7
5	BaS, In_2S_3, S, InCl	$Ba_{0.5}In_4S_5Cl$	500°C, 3w	$BaIn_2S_4$, $BaCl_2$

6	SrS, In_2S_3, S, InCl	$Sr_{0.5}In_4S_5Cl$	500°C, 3w	In_2S_3, $SrIn_2S_4$, $SrCl_2$,
7	Tl, In, S, $InCl_3$ TlCl, In, S TlCl, InS, In_2S_3 (pell)	$TlIn_4S_5Cl$	820°C, 2d	$Tl_xIn_{(5-x)}S_5Cl$, In_6S_7 $TlIn_4S_5Cl$
8	Tl, In, S, $InBr_3$ TlBr, In, S TlBr, InS, In_2S_3 (pell)	$TlIn_4S_5Br$	500°C 28d Tp(2°C/h) 500°C, 2d 400°C, 2d 450°C, 2d	InS, In_2S_3, TlBr
9	TlCl, In, Se TlCl, InSe, In_2Se_3 (pell)	$TlIn_4Se_5Cl$	400°C, 2d 500°C, 2w	$Tl_xIn_{(5-x)}Se_5Cl$
10	TlBr, In, Se TlBr, InSe, In_2Se_3 (pell)	$TlIn_4Se_5Br$	Tp(2°C/h) 500°C, 2d 450°C, 2d	-
	Experiments for the substitution of $(In_2)^{4+}$ and In^{3+}			
11	Al, In, S, $InCl_3$	$AlIn_4S_5Cl$	600°C, 2w	In_2S_3, In_6S_7, $Al_xIn_{(6-x)}S_7$
12	Al, In, S, $InBr_3$	$Al_2In_3S_5Br$	500°C, 4w	$Al_2In_4S_9$, InBr
13	In, Ga, S, $InCl_3$ GaS, In_2S_3, InCl	$GaIn_4S_5Cl$ $Ga_2In_3S_4Cl$	Q, 450°C, 11d 400°C, 5d	Ga_2S_3, $Ga_xIn_{(2-x)}S_3$
14	In, Ga, Se, $InCl_3$ In, Ga, Se, $InCl_3$	$GaIn_4Se_5Cl$ $InGa_4Se_5Cl$	450°C, 11d 400°C, 5d	$In_xGa_{(1-x)}Se$ GaSe
15	In, Ga, S, $InBr_3$ GaS, In_2S_3, InBr In, Ga, S, $GaBr_3$	$GaIn_4S_5Br$ $Ga_3In_2S_5Br$ $Ga_2In_3S_5Br$ $InGa_4S_5Br$	500°C, 5d 550°C, 5d 400°C, 5d 480°C, 5d	Ga_2S_3 In_2S_3, Ga_2S_3 GaS, Ga_2S_3
16	In, Ga, Se, $GaBr_3$	$Ga_3In_2Se_5Br$ $InGa_4Se_5Br$	650°C, 5d 480°C, 1w	 Ga_2Se_3
17	In, Cr, S, $InCl_3$	In_4CrS_5Cl	450°C, 5d	$In_{(2-x)}Cr_xS_3$
18	In, Cr, Se, $InCl_3$	In_4CrSe_5Cl	450°C, 5d	$In_{(5-x)}Cr_xSe_5Cl$
	Experiments for partly and fully substitution of S^{2-} and Se^{2-}			
19	In, S, Se, $InCl_3$,	$In_5S_{2.5}Se_{2.5}Cl$	400°C, 10d 500°C, 10d	$In_5S_{2.5}Se_{2.5}Cl$
20	In, S, Se, InBr	$In_5S_{2.5}Se_{2.5}Br$	400°C, 10d 500°C, 10d	$In_5S_{2.5}Se_{2.5}Br$
21	In, Se, Te, $InBr_3$	In_5Se_4TeBr	420°C, 5d	$In_5Se_{(5-x)}Te_xBr$
22	In, Te, $InCl_3$	In_5Te_5Cl	350°C (A), 1w 400°C (A), 1w Q, 230°C, 20d	InTe, InCl In_2Te_3, In_3Te_4, InCl InTe, In_7Te_{10}
23	In, Te, $InBr_3$	In_5Te_5Br	Q, 350°C (A), 1w Q, 400°C (A), 1w 400°C, 1w	InTe In_2Te_3, In_9Te_{11}, InBr InTe, In_7Te_{10}
	Experiments for partly and fully substitution of Cl^- and Br^-			

24	In, S, $InCl_3$, $InBr_3$	$In_5S_5Cl_{0.5}Br_{0.5}$	400°C, 10d 500°C, 10d	$In_5S_5Cl_xBr_{(1-x)}$
25	In, Se, InCl, InBr	$In_5Se_5Cl_{0.5}Br_{0.5}$	400°C, 10d 500°C, 10d	$In_5Se_5Cl_xBr_{(1-x)}$
26	In, S, I_2 In_2S_3, InS, InI (pell)	In_5S_5I	Tp(1°C/h) 500°C, 2d 500°C, 6d	In_6S_7, In_2S_3, InI In_6S_7, InI
27	In, Se, I_2	In_5Se_5I	500°C, 10d Tp(1°C/h) 500°C, 2d	In_2Se_3, InI In_6Se_7, In_2Se_3, InI
	Experiments for further substitutions			
28	In, Te, I_2	In_5Te_5I	350°C, 1w	In_2Te_3, InTe, InI
29	Ga, S, $GaCl_3$	Ga_5S_5Cl	500°C, 3w	GaS, Ga_2S_3
30	Ga, Se, $GaCl_3$	Ga_5Se_5Cl	500°C, 3w	GaSe
31	Al, In, Te, $InBr_3$	$Al_2In_3Te_5Br$	500°C, 4w	In_7Te_{10}
32	TlCl, Ga, Se	$TlGa_4Se_5Cl$	450°C, 3d Q, 600°C (A), 1w	$TlGaSe_2$, Ga_2Se_3 Ga_2Se_3

Abbreviations: A = annealed, Q = quenched, d = day, w = week

Mixed crystals: Composition, characteristics and their lattice constants

Table 8.15: Composition, characteristics and lattice constants of several mixed crystals determined by structure solution and refinement from single crystal data.

Composition	**Characteristics / Space group**	**a /Å**	**b /Å**	**c /Å**	**β /°**	**V /Å^3**
$In_5S_5Cl_{0.55}Br_{0.45}$	Multiple twinned $Pmn2_1$	3.925(1)	9.052(2)	14.889(3)		528.0(2)
$In_5Se_5Cl_{0.61}Br_{0.39}$	Multiple twinned $P2_1/m$	9.258(2)	4.108(1)	15.377(3)	92.42(3)	584.3(8)
$In_5S_{2.49}Se_{2.51}Cl$	Multiple twinned $P2_1/m$	9.074(2)	4.008(1)	15.188(3)	93.46(3)	551.0(1)
$In_5S_{2.56}Se_{2.44}Br$	Multiple twinned $Pmn2_1$	4.022(1)	9.217(2)	15.112(3)		560.2(2)

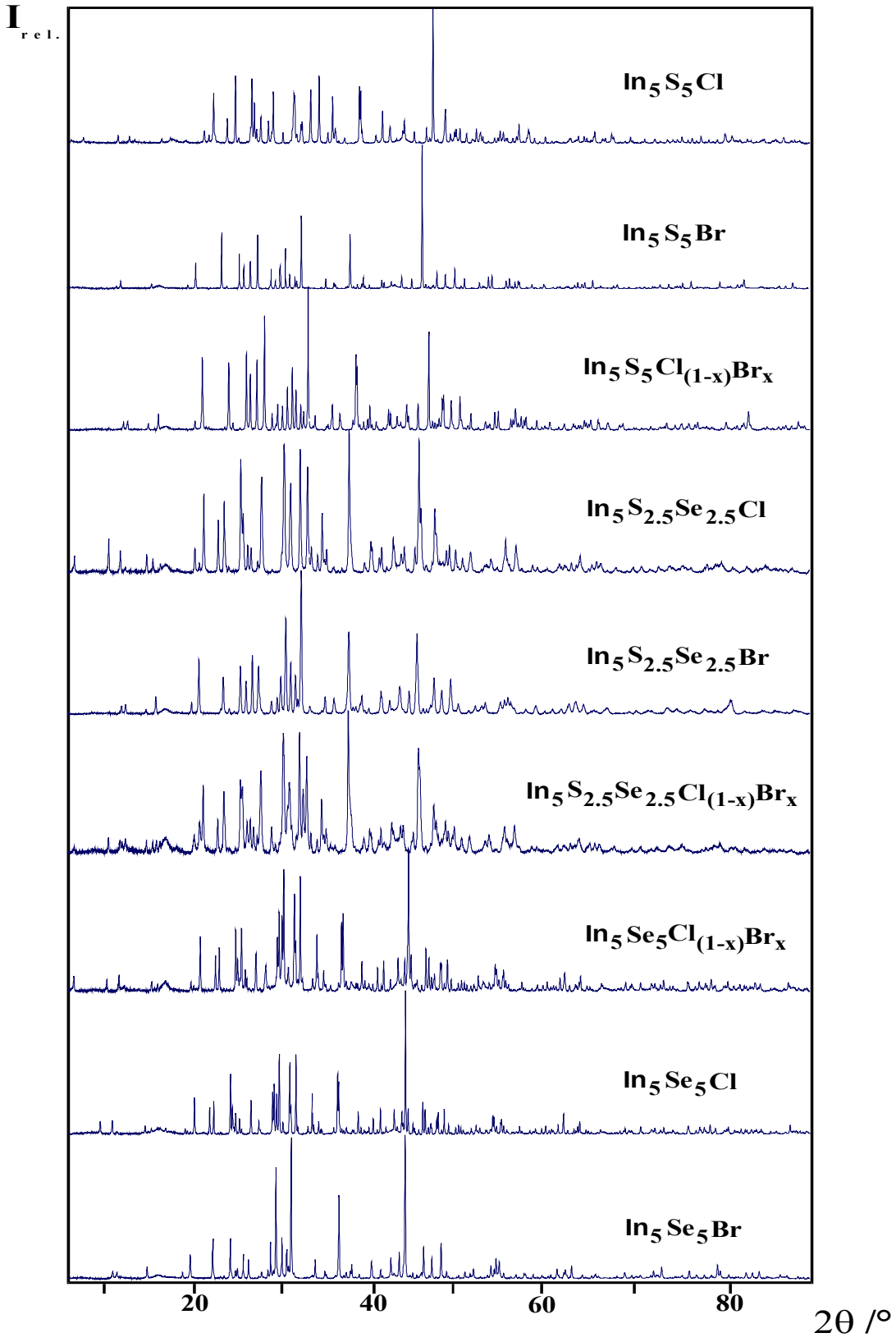

Fig. 8.6: Powder diffraction of the mixed valence compounds and their mixed crystals.

8.6 Data for the compounds $TlIn_4Ch_5Cl$ (Ch = S, Se)

Table 8.16: Important parameters for the X-ray single crystal investigation of $TlIn_4Se_5Cl$.

Sum formula	**$TlIn_4Se_5Cl$**
Formula weight /gmol^{-1}	M = 1093.90
Temperature /K	T = 293(2)
Wavelength /Å	Mo$K\alpha$, γ = 0.71073
Space group	$P2_1/m$ (No. 11)
Crystal dimension /mm	0.37 x 0.04 x 0.02
Cell dimensions /Å, /°	a = 9.222(2) b = 4.123(1) c = 15.221(3) β = 92.84(3)
Volume /Å^3	V = 578.0(2)
Formula units per unit cell	Z = 2
Density (calculated) /gcm^{-3})	ρ = 6.285
Absorption coefficient /mm^{-1}	μ = 37.662
F(000)	928
Diffractometer	IPDS (Stoe), oriented graphite monochromator
Scan type	φ
Measured θ range /°	$3.39 \leq \theta \leq 31.74$
Index ranges	$-13 \leq h \leq 13$ $-5 \leq k \leq 6$ $-22 \leq l \leq 20$
Measured reflections	2754
Number of reflections with $I_0 > 2\sigma$	1038
Completeness to θ /%	69.4
Absorption correction	Numerical [P8, P10]
Structure solution	Direct methods [P11]
Structure refinement	Full-matrix least-squares on F^2 [P12]
Data/restraints/parameters	1528 / 0 / 69
Goodness-of-Fit on F^2	1.296
R values [$I \geq 2\sigma$ (I)]	R_1 = 0.1356, wR_2 = 0.3371
R values (all data)	R_1 = 0.1666, wR_2 = 0.3730
Final Fourier residuals / eÅ^{-3}	$\rho_{max.}$ = 7.181, $\rho_{min.}$ = -6.855

Table 8.17: Anisotropic displacement parameters (U_{ij} /Å ^{2}) for $TlIn_4Se_5Cl$. The highlighted atoms show a greater difference of thermal displacement parameters.

Atom	U_{11}	U_{22}	U_{33}	U_{23}	U_{13}	U_{12}
In1	0.0128(7)	0.0195(8)	0.0196(7)	0	-0.0002(6)	0
In2	0.0302(9)	0.0220(9)	0.0223(8)	0	-0.0197(7)	0
In3	0.0140(7)	0.0231(8)	0.0286(9)	0	0.0019(6)	0
In4	0.0114(7)	0.0229(8)	0.0161(7)	0	-0.0047(6)	0
Se1	0.0090(9)	0.021(1)	0.0128(9)	0	-0.0073(7)	0
Se2	0.0091(9)	0.021(1)	0.017(1)	0	-0.0061(8)	0
Se3	0.0120(9)	0.016(1)	0.015(1)	0	-0.0046(8)	0
Se4	0.018(1)	0.022(1)	0.016(1)	0	-0.0061(9)	0
Se5	0.016(1)	0.021(1)	0.017(1)	0	-0.0048(9)	0
Cl	0.025(3)	0.038(4)	0.012(2)	0	-0.005(2)	0
In5	**0.0256(6)**	**0.0340(7)**	**0.0356(7)**	**0**	**-0.0036(5)**	**0**
Tl	**0.0256(6)**	**0.0340(7)**	**0.0356(7)**	**0**	**-0.0036(5)**	**0**

8.7 Data for the high temperature X-ray investigations

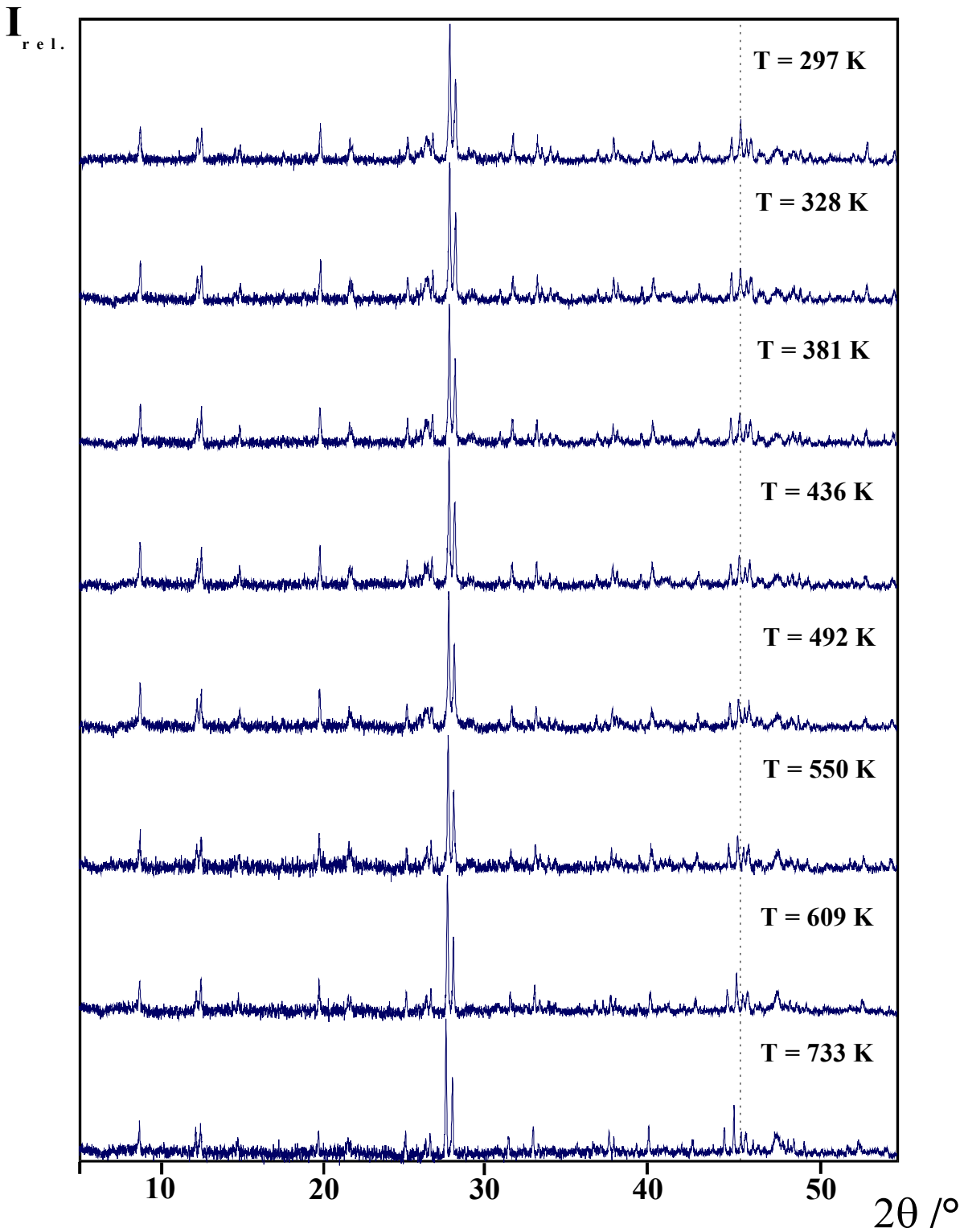

Fig. 8.7: Powder diffraction patterns of $K_2In_{12}Se_{12}Te_7$ measured at different temperatures. The dashed line reveals the displacement of the chosen reflection to lower 2θ - values with temperature increase.

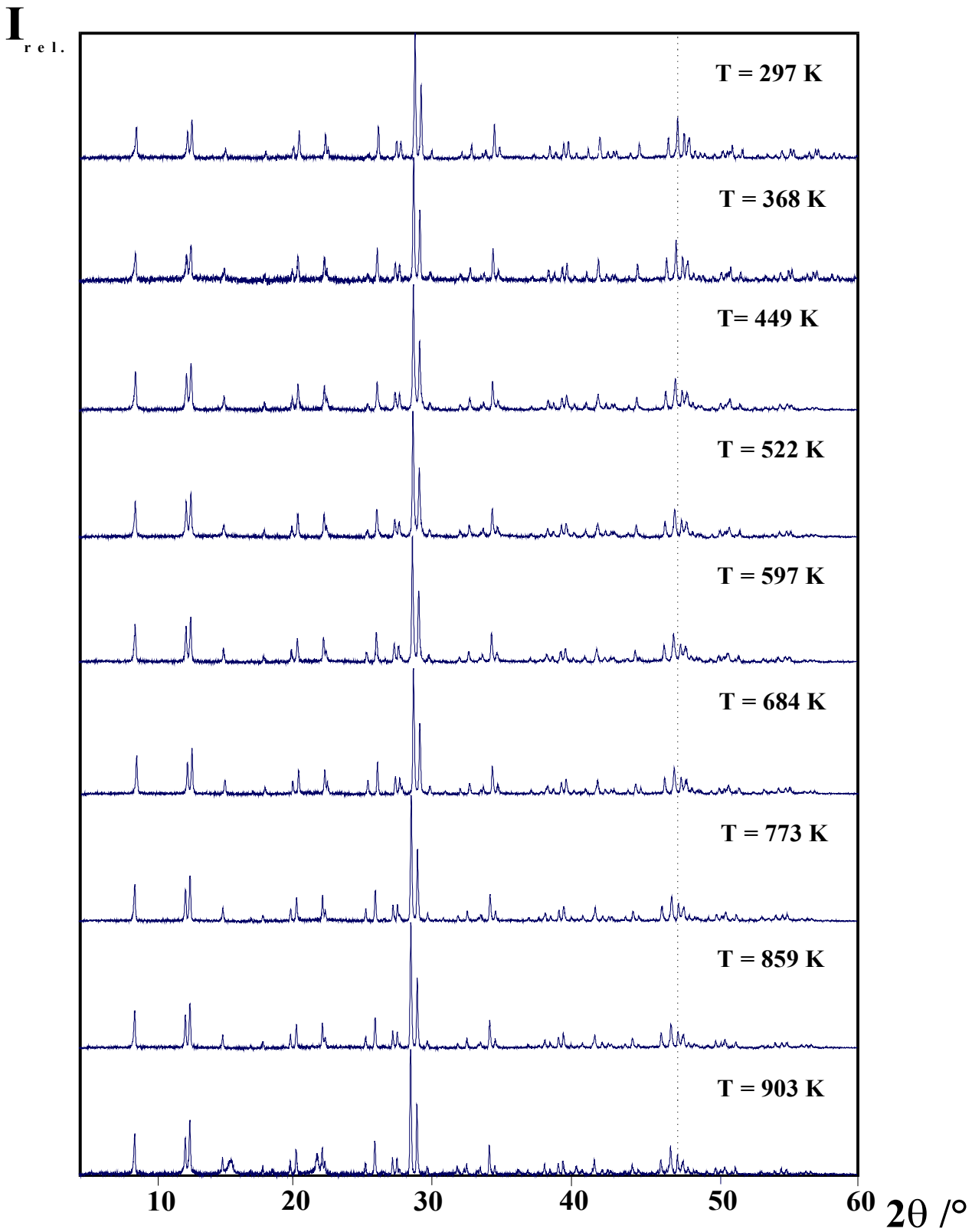

Fig. 8.8: Powder diffraction patterns of $K_2In_{12}Se_{19}$ measured at different temperatures. The dashed line reveals the displacement of the chosen reflection to lower 2θ - values with temperature increase.

Table 8.18: The coefficients of thermal expansion for $K_2In_{12}Se_{19}$ calculated at different temperatures.

T /K	α_a x 10^{-5} /K^{-1}	α_c x 10^{-5} /K^{-1}	α_V x 10^{-5} /K^{-1}
297 (4)	0.5(4)	1.02(3)	1.1(1)
320 (4)	0.29(4)	1.19(3)	1.8(1)
368 (4)	0.73(3)	1.50(2)	2.99(9)
412 (4)	1.07(3)	1.72(2)	3.92(8)
449 (4)	1.30(2)	1.87(1)	4.56(6)
485 (4)	1.49(2)	1.98(1)	5.06(5)
522 (4)	1.63(1)	2.059(6)	5.44(3)
559 (4)	1.727(8)	2.099(2)	5.70(2)
597 (4)	1.779(3)	2.103(2)	5.821(6)
640 (4)	1.779(3)	2.060(6)	5.80(1)
684 (4)	1.714(9)	1.96(1)	5.59(3)
728 (5)	1.58(1)	1.82(2)	5.20(4)
773 (5)	1.38(2)	1.61(2)	4.61(6)
829 (5)	1.04(3)	1.28(3)	3.61(8)
859 (5)	0.81(3)	1.07(3)	2.95(9)
880 (6)	0.63(4)	0.91(3)	2.4(1)
903 (6)	0.42(4)	0.72(3)	1.8(1)

Table 8.19: Fitting parameters for the equations 23 and 24.

In_5S_5Cl	P1	P2	P3	P4	χ^2	R^2
a	8.9391(7)	$1.2(2) \times 10^{-4}$	$5(1) \times 10^{-7}$	$-9(1) \times 10^{-10}$	0.48434	0.99937
b	3.9164(8)	$4.0(8) \times 10^{-5}$	$1.8(5) \times 10^{-7}$	$-3.1(8) \times 10^{-10}$	0.19995	0.99894
c	14.984(2)	$2.10(9) \times 10^{-4}$	-	-	2.14819	0.9902
V	523.5 (1)	$2.63(6) \times 10^{-2}$			3.41683	0.99676
In_5Se_5Cl						
a	9.231(1)	$1.4(6) \times 10^{-4}$	-	-	2.06725	0.98443
b	4.0923(3)	$5.0(2) \times 10^{-5}$			0.57631	0.99262
c	15.278(1)	$-6(2) \times 10^{-5}$	$1.1(1) \times 10^{-6}$	$-1.8(2) \times 10^{-9}$	0.25097	0.99469
V	576.54 (1)	$1.95(8) \times 10^{-2}$			3.77768	0.98964
In_5S_5Br						
a	3.9310(6)	$2(1) \times 10^{-5}$	$2.1(8) \times 10^{-7}$	$-4(1) \times 10^{-10}$	0.47289	0.99181
b	9.073(2)	$1.60(6) \times 10^{-4}$			2.50596	0.98889
c	14.831(2)	$3(2) \times 10^{-5}$	$1.4(5) \times 10^{-7}$		0.56997	0.9776
V	529.0(1)	$1.73(5) \times 10^{-2}$			2.10885	0.99327
In_5Se_5Br						
a	4.099(1)	$3(3) \times 10^{-5}$	$2(2) \times 10^{-5}$	$-4(2) \times 10^{-10}$	1.90396	0.99095
b	9.338(2)	$2.1(1) \times 10^{-4}$	-	-	8.17607	0.98499
c	15.248(3)	$8(5) \times 10^{-5}$	$-3.2(3) \times 10^{-7}$	$7(4) \times 10^{-10}$	0.59153	0.98072
V	583.5(1)	$2.45(6) \times 10^{-2}$	-	-	3.33993	0.99679

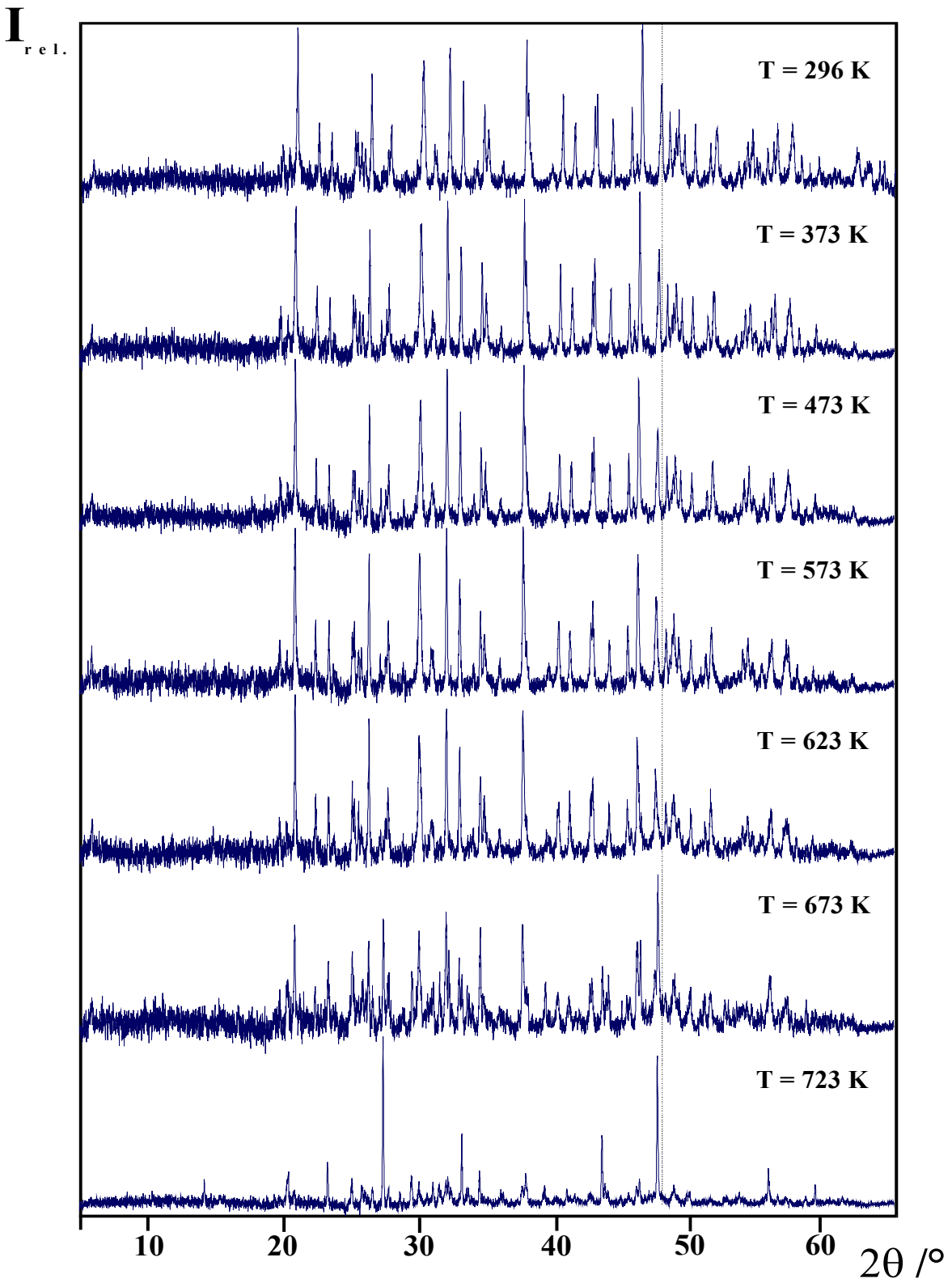

Fig. 8.9: Powder diffraction patterns of In_5S_5Cl measured at different temperatures. The dashed line reveals the displacement of the chosen reflection to lower 2θ - values with temperature increase.

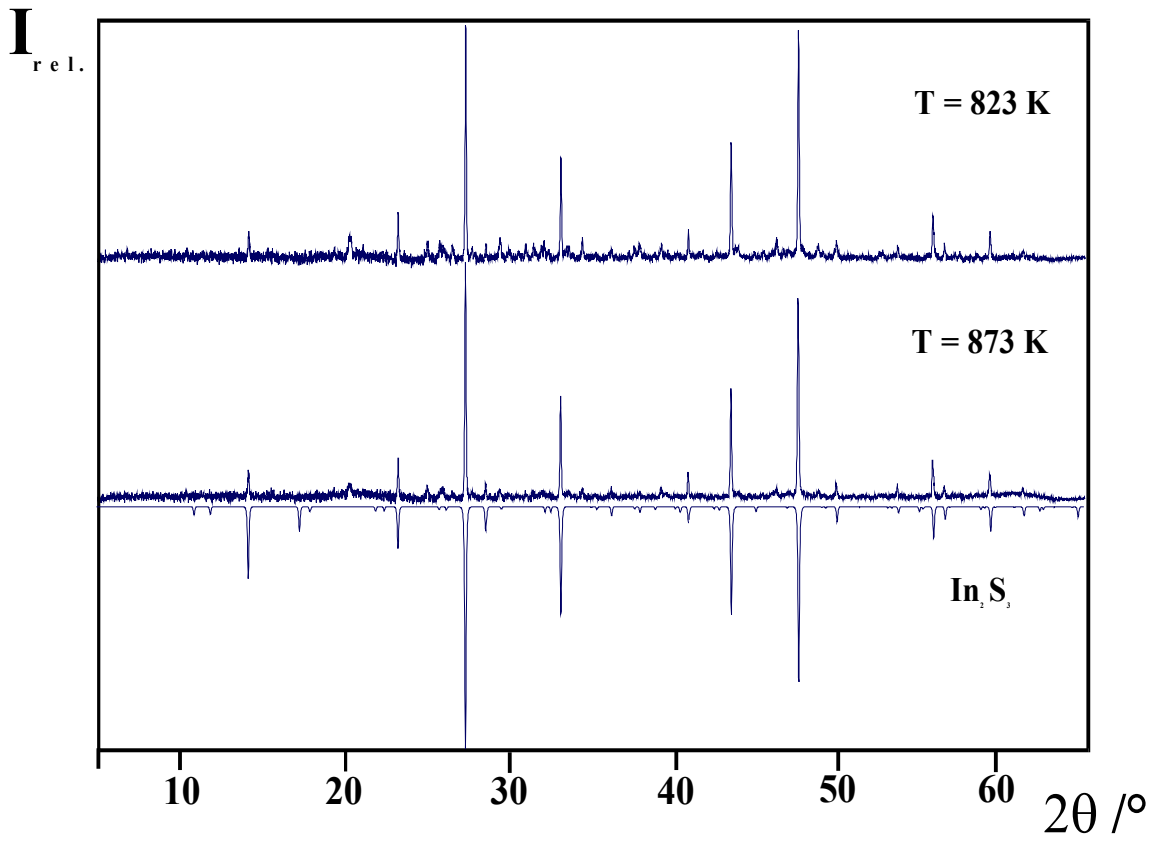

Fig. 8.10: Comparison of the measured diffraction patterns of In_5S_5Cl measured at 823 and 873 K with the calculated diffraction pattern of In_2S_3.

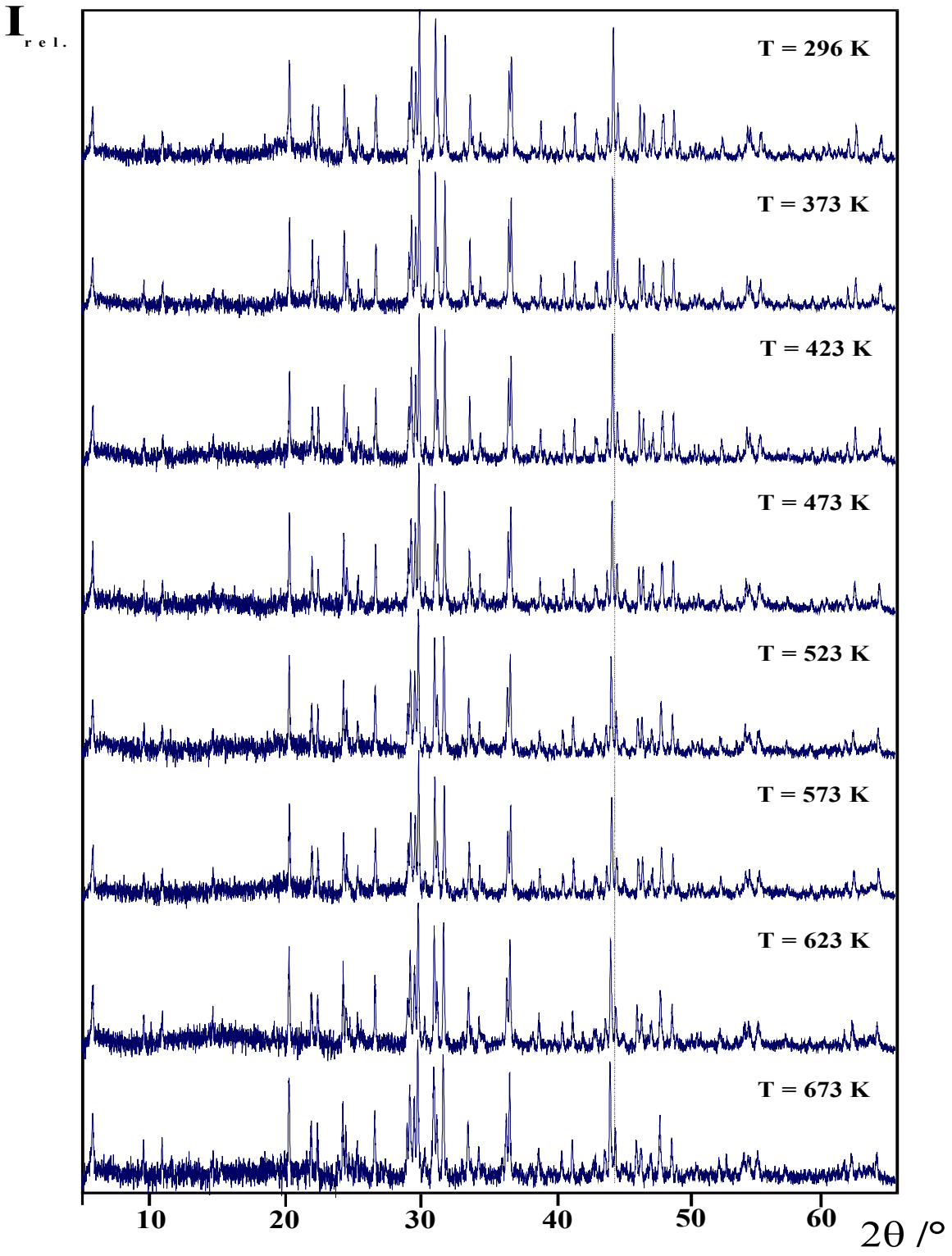

Fig. 8.11: Powder diffraction patterns of In_5Se_5Cl measured at different temperatures. The dashed line reveals the displacement of the chosen reflection to lower 2θ - values with temperature increase.

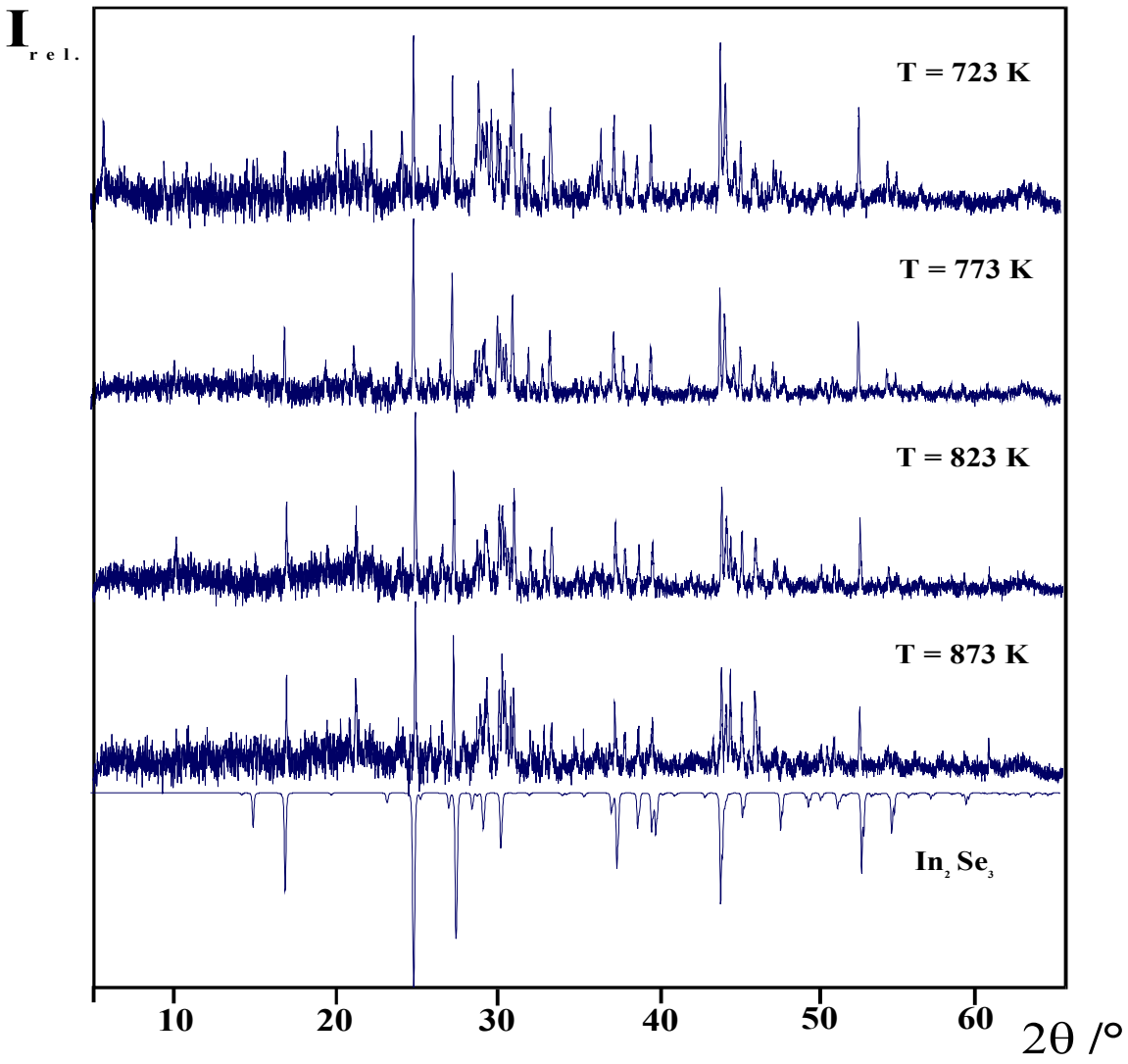

Fig. 8.12: The stepwise decomposition of In_5Se_5Cl starting approximately at 723 K. Comparison of the powder pattern recorded at high temperatures with the calculated diffraction pattern of In_2Se_3.

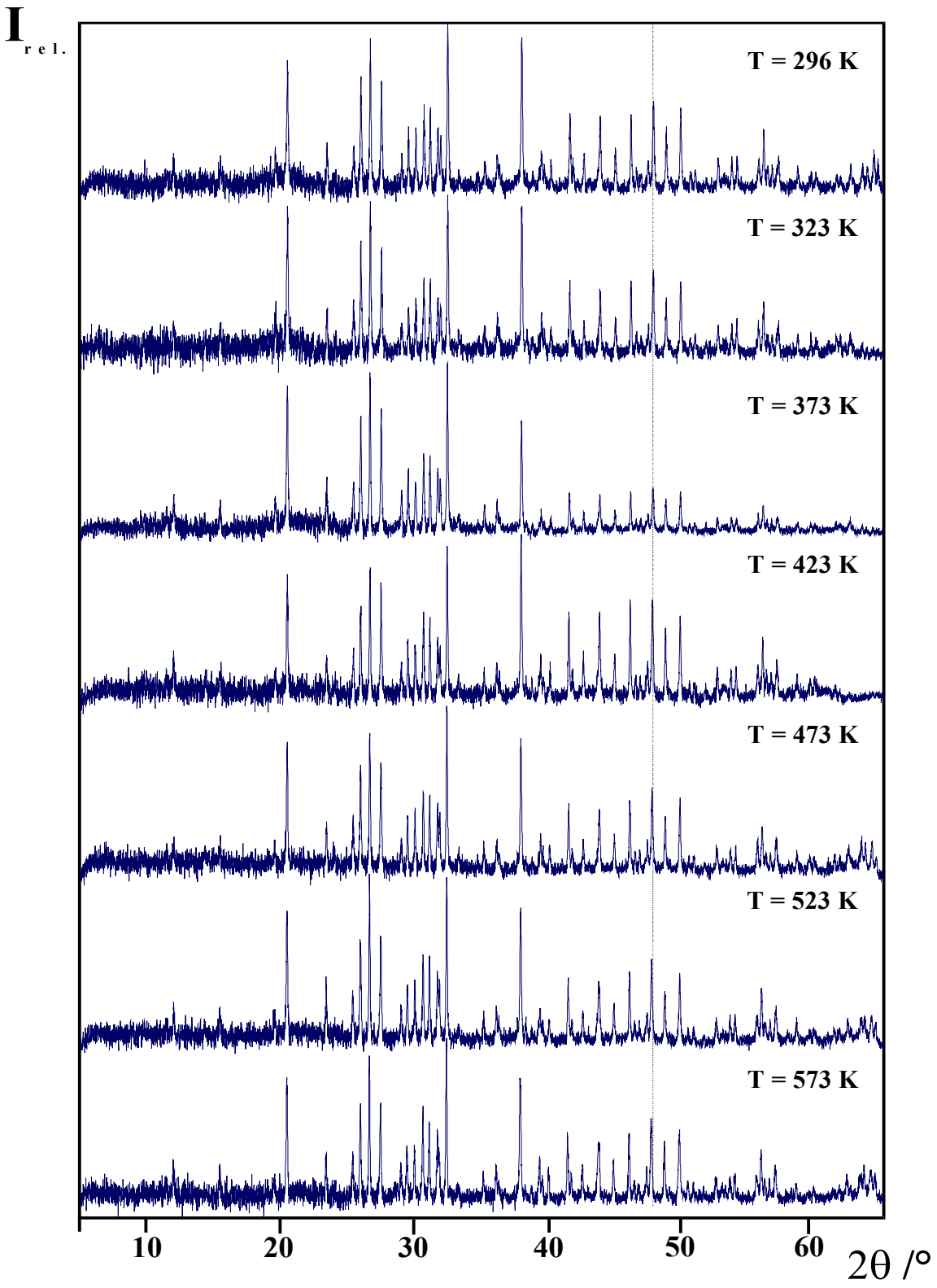

Fig. 8.13: Powder diffraction patterns of In_5Se_5Br measured at different temperatures. The dashed line reveals the displacement of the chosen reflection to lower 2θ - values with temperature increase.

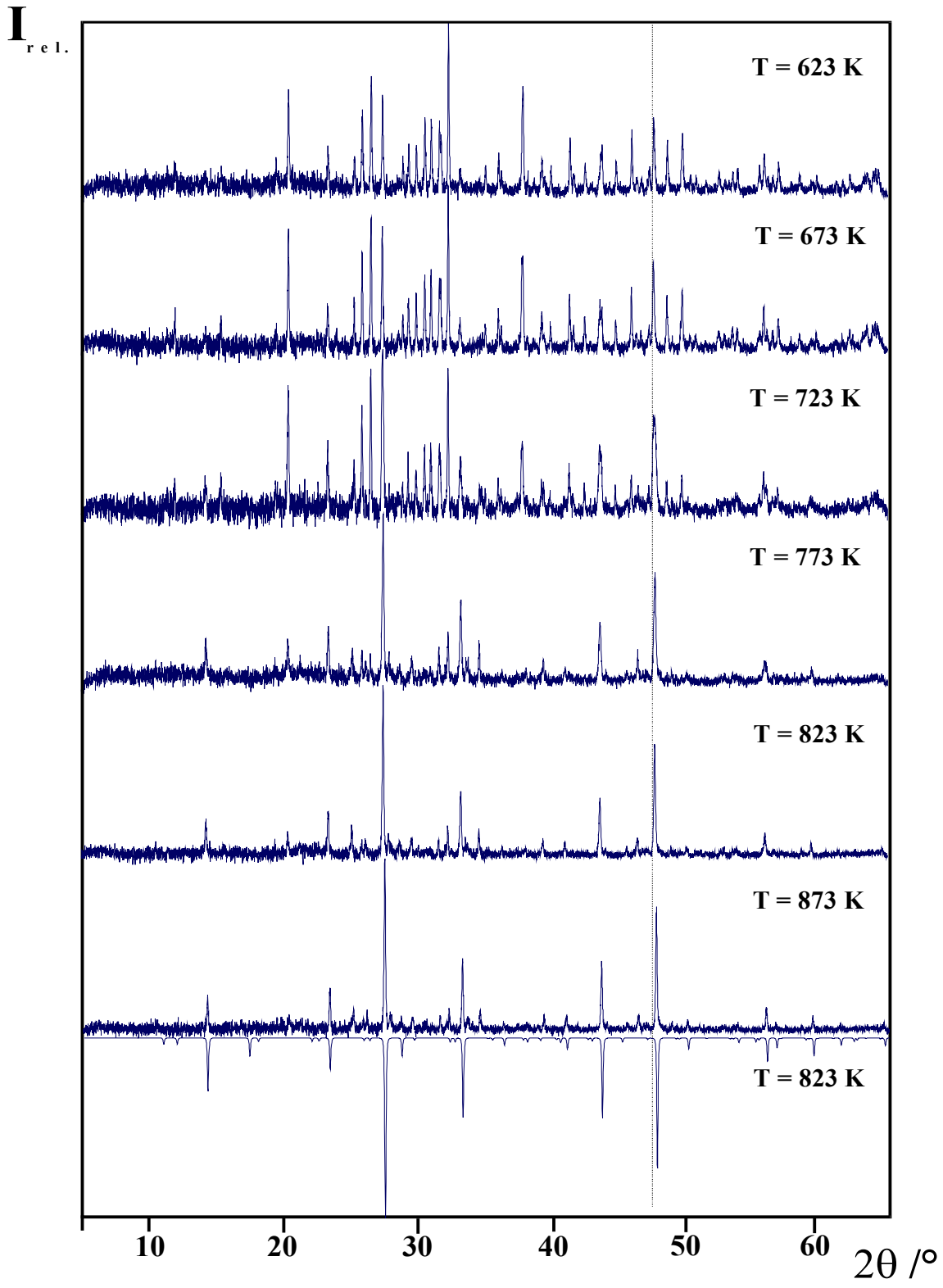

Fig. 8.14: The stepwise decomposition of In_5S_5Br starting approximately at 723 K. Comparison of the powder pattern recorded at high temperatures with the calculated diffraction pattern of In_2S_3.

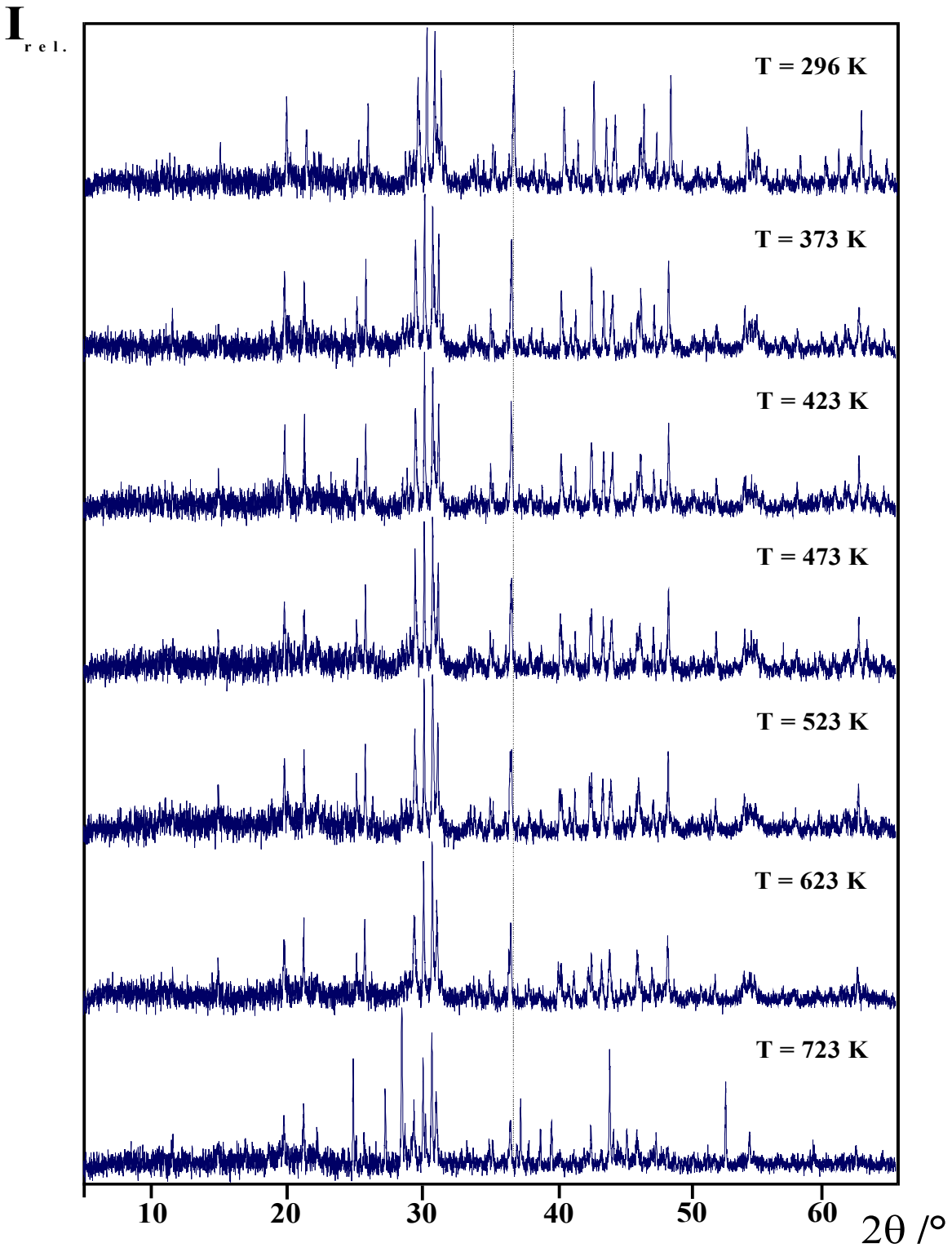

Fig. 8.15: Powder diffraction patterns of In_5Se_5Br measured at different temperatures. The dashed line reveals the displacement of the chosen reflection to lower 2θ - values with temperature increase.

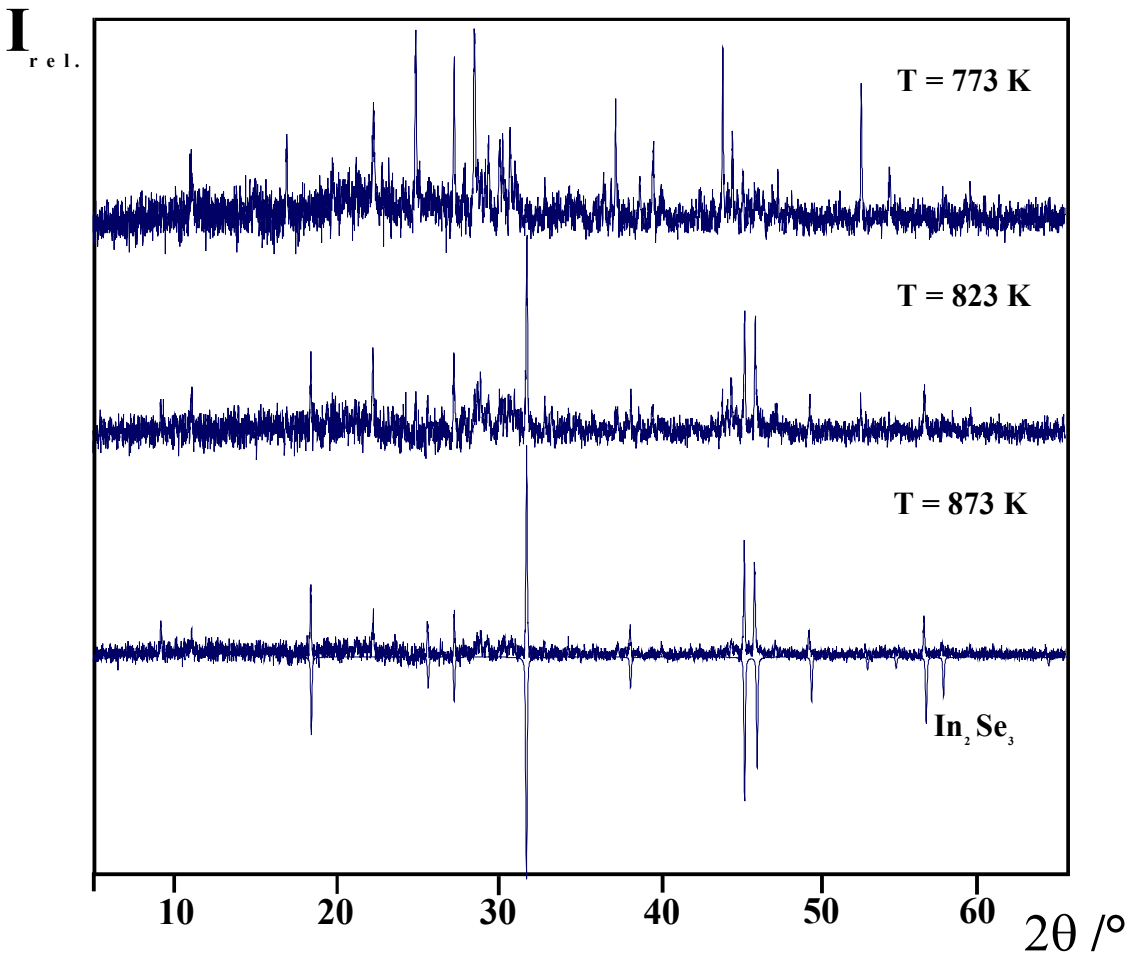

Fig. 8.16: The stepwise decomposition of In_5Se_5Br starting approximately at 723 K. Comparison of the powder pattern recorded at high temperatures with the calculated diffraction pattern of In_2Se_3.

8.8 Publications and posters

1. L. Kienle, O. Oeckler, H. Mattausch, V. Duppel, A. Simon, C. Reiner, M. Schlosser, K. Xhaxhiu, H. J. Deiseroth:
   Real Structure of Partially Ordered Crystals.
   Mater. Sci. in Semicond. Process. **2003**, *6(5-6)*, 393-396.

2. H.-J. Deiseroth, C. Reiner, K. Xhaxhiu, M. Schlosser, L. Kienle:
   X-Ray and Transmission Electron Microscopy Investigations of the new Solids In_5S_5Cl, In_5Se_5Cl, In_5S_5Br, In_5Se_5Br.
   Z. Anorg. Allg. Chem. **2004**, *630*, 2319-2328.

Poster

9^{th} European Conference on Solid State Chemistry with the title:
New Mixed Valence Chalcogenide Halides In_5Ch_5X (Ch: Chalcogenide, X: Halide) with Indium, Stuttgart 2003.